



University of Kentucky
UKnowledge

University of Kentucky Doctoral Dissertations

Graduate School

2010

Measurement of Single Spin Asymmetries in Semi-Inclusive Deep Inelastic Scattering Reaction $n \uparrow (e, e\pi^+)X$ at Jefferson Lab

Kalyan C. Allada

University of Kentucky, kalyan.allada@gmail.com

[Right click to open a feedback form in a new tab to let us know how this document benefits you.](#)

Recommended Citation

Allada, Kalyan C., "Measurement of Single Spin Asymmetries in Semi-Inclusive Deep Inelastic Scattering Reaction $n \uparrow (e, e\pi^+)X$ at Jefferson Lab" (2010). *University of Kentucky Doctoral Dissertations*. 31.
https://uknowledge.uky.edu/gradschool_diss/31

This Dissertation is brought to you for free and open access by the Graduate School at UKnowledge. It has been accepted for inclusion in University of Kentucky Doctoral Dissertations by an authorized administrator of UKnowledge. For more information, please contact UKnowledge@lsv.uky.edu.

ABSTRACT OF DISSERTATION

Kalyan C. Allada

The Graduate School
University of Kentucky

2010

Measurement of Single Spin Asymmetries in Semi-Inclusive Deep Inelastic Scattering
Reaction $n^\uparrow(e, e'\pi^+)X$ at Jefferson Lab

ABSTRACT OF DISSERTATION

A dissertation submitted in partial fulfillment of the
requirements for the degree of Doctor of Philosophy
at the University of Kentucky

By

Kalyan C. Allada

Lexington, Kentucky

Director: Dr. Wolfgang Korsch, Professor of Physics and Astronomy

Lexington, Kentucky

2010

Copyright © Kalyan C. Allada 2010

ABSTRACT OF DISSERTATION

Measurement of Single Spin Asymmetries in Semi-Inclusive Deep Inelastic Scattering
Reaction $n^\uparrow(e, e'\pi^+)X$ at Jefferson Lab

What constitutes the spin of the nucleon? The answer to this question is still not completely understood. Although we know the longitudinal quark spin content very well, the data on the transverse quark spin content of the nucleon is still very sparse. Semi-inclusive Deep Inelastic Scattering (SIDIS) using transversely polarized targets provide crucial information on this aspect. The data that is currently available was taken with proton and deuteron targets.

The E06-010 experiment was performed at Jefferson Lab in Hall-A to measure the single spin asymmetries in the SIDIS reaction $n^\uparrow(e, e'\pi^\pm/K^\pm)X$ using transversely polarized ^3He target. The experiment used the continuous electron beam provided by the CEBAF accelerator with a beam energy of 5.9 GeV. Hadrons were detected in a high-resolution spectrometer in coincidence with the scattered electrons detected by the BigBite spectrometer. The kinematic coverage focuses on the valence quark region, $x = 0.19$ to 0.34 , at $Q^2 = 1.77$ to 2.73 (GeV/c) 2 . This is the first measurement on a neutron target. The data from this experiment, when combined with the world data on the proton and the deuteron, will provide constraints on the transversity and Sivers distribution functions on both the u and d-quarks in the valence region. In this work we report on the single spin asymmetries in the SIDIS $n^\uparrow(e, e'\pi^+)X$ reaction.

Kalyan C. Allada

June 15, 2010

Measurement of Single Spin Asymmetries in Semi-Inclusive Deep Inelastic Scattering
Reaction $n^\uparrow(e, e'\pi^+)X$ at Jefferson Lab

By

Kalyan C. Allada

Dr. Wolfgang Korsch

(Director of Dissertation)

Dr. Joseph W. Brill

(Director of Graduate Studies)

June 15, 2010

(Date)

DISSERTATION

Kalyan C. Allada

The Graduate School
University of Kentucky

2010

Measurement of Single Spin Asymmetries in Semi-Inclusive Deep Inelastic Scattering
Reaction $n^\uparrow(e, e'\pi^+)X$ at Jefferson Lab

DISSERTATION

A dissertation submitted in partial fulfillment of the
requirements for the degree of Doctor of Philosophy
at The University of Kentucky

By

Kalyan C. Allada

Lexington, Kentucky

Director: Dr. Wolfgang Korsch, Professor of Physics and Astronomy

Lexington, Kentucky

2010

Copyright © Kalyan C. Allada 2010

To my parents

Surya Lakshmi and Rama Rao Allada

ACKNOWLEDGEMENTS

I thank my supervisor, Wolfgang Korsch, for suggesting me to work on this very exciting thesis topic. Without his constant support for all these years, and particularly during the time that I spent away from the University to work at Jefferson Lab, it is impossible to finish this thesis. When I first started my research as a graduate student, he got me involved in the target work at Kentucky, taught me experimental techniques, and basics of the physics involved in these kinds of experiments. I will always be grateful to him for all the help and being a wonderful guide, and also host to many thanksgiving dinners. I sincerely appreciate his help in correcting the draft of this thesis in short time.

I would like to thank Jian-ping Chen for being my supervisor at Jefferson Lab. His enthusiasm and deep understanding of physics always helped me learn new things from the discussions that we had together. His constructive criticism during the weekly analysis meetings helped all of us to improve the overall quality of the data analysis. I am looking forward to work with him in the future.

My appreciation goes to Xiaodong Jiang for being very active spokesperson of this experiment. His ability to pay attention to details, while running the experiment or during the data analysis, is simply amazing. And he always encouraged me to do the same. I will always be thankful to him for his continuing support and encouragement.

I thank other spokesperson of this experiment, Evaristo Cisbani, J.C. Peng and H. Gao for all their support during and after the experiment, and for several important physics discussions.

Many thanks to Susan Gardner for going through my thesis, discussing the implications of the results, and suggesting corrections. Thanks to Renee Fatemi for serving on my committee on a short notice.

This experiment was run by fairly large group of people and I had an opportunity to work and make friends with many of them. I thank Xin Qian for working very closely with me – starting from setting up the detectors in the test lab to running the experiment, and finally finishing our thesis around the same time. He has been a great help, especially in coming up with ideas for data analysis and developing software tools. My appreciation goes to the target team consisting of Yi Qiang, Chiranjib Dutta, Jin Huang, Joe Katich, Yi Zhang for all their efforts and hard work in building an excellent target system. I thank all of them for being great colleagues and friends. I have to particularly thank C. Dutta for

being good friend and sharing house during my stay in Newport News. Thanks to Diana Parno, Yawei Zhang for taking many expert shifts and all the help during the experiment.

I want to thank post-docs who worked on this experiment - Brad Sawatzky, Bryan Moffit, Vince Sulkosky and Alexander Camsonne and Yi Qiang. I particularly appreciate the help that B. Sawatzky and B. Moffit have given me in setting up the detectors and data acquisition system during the experiment.

I sincerely appreciate the help extended by Bob Michaels in designing and setting up the DAQ system for the experiment. He taught me all the basics of the data acquisition and how to identify the problems when the experiment is running. Thanks to Doug Higinbotham for his valuable help in setting up the BigBite spectrometer. Thanks to Sergey Abrahamyan for helping me with calibrations of the BigBite spectrometer.

I have to thank all my friends in the social group at Jefferson Lab who made life a bit more exciting. Thanks to Aji Daniel and Narbe Kalantarians for playing tennis with me. Many thanks to Xin Qian and J.P.Chen for inviting me to the soccer matches. Thanks to Daria Sokhan, Tim Ngo, Brandon Craver for their friendship and all the good time. Many thanks to Ameya Kolarkar for all his help and tips about living and working in the Newport News. And thanks to the amazing group of people who are always ready for an evening at the restaurant - Bryan Moffit, Alexander Camsonne, Chiranjib Dutta, Brad Sawatzky, Vince Sulkosky, Mark Dalton, Dustin McNulty, Wouter Deconinck, Rupesh Silwal, Megan Friend, Seamus Riordan, Jonathan Miller, and Fatiha Benmokhtar.

Finally I would like to thank my mother, Surya Lakshmi, and my dad, Rama Rao, for all their support and understanding in whatever I choose to do in life. Many thanks to my brother, Srinivas, and my sister, Sarala, for their constant encouragement and support throughout the time that I spent away from home.

TABLE OF CONTENTS

Acknowledgements	iii
List of Tables	viii
List of Figures	ix
CHAPTER 1: INTRODUCTION	1
1.1 Structure of the Visible Matter	1
1.2 Spin Structure of the Nucleon	2
1.3 Outline of the Thesis	3
CHAPTER 2: THE SPIN STRUCTURE OF THE NUCLEON	5
2.1 Deep Inelastic Scattering	5
2.1.1 DIS Cross Section	6
2.2 Naïve Quark Parton Model	9
2.3 QCD Improved Parton Model	11
2.4 Transversity Distribution	14
2.5 Transverse Momentum Dependent PDFs	16
2.6 Semi-Inclusive DIS	18
2.6.1 Semi-Inclusive DIS cross-section	21
2.7 Single Spin Asymmetries and Azimuthal Moments	24
2.7.1 Collins Effect	25
2.7.2 Sivers Effect	26
2.7.3 Recent SIDIS Data With Transversely Polarized Targets	27
CHAPTER 3: E06-010 EXPERIMENT IN HALL A	30
3.1 Experimental Technique	30
3.2 Experimental Setup	32
3.2.1 CEBAF at Jefferson Lab	32
3.2.2 Hall A Beamline	33
3.2.3 Polarized ^3He Target	37
3.2.4 High Resolution Spectrometer	48
3.2.5 BigBite Spectrometer	51
3.3 Trigger and Data Acquisition Setup	54
3.3.1 Trigger and Electronics for BigBite Spectrometer	57
3.3.2 Trigger and Electronics for High Resolution Spectrometer	60
3.3.3 Coincidence Trigger	61
3.3.4 Scaler Setup	63

CHAPTER 4: DETECTOR AND TARGET CALIBRATIONS	68
4.1 Target Polarization Analysis	68
4.1.1 NMR Calibration	69
4.2 BigBite Spectrometer	69
4.2.1 Multi-Wire Drift Chambers	70
4.2.2 Preshower and Shower	77
4.3 High Resolution Spectrometer	85
4.3.1 Vertical Drift Chambers	86
4.3.2 Gas Čerenkov Detector	87
4.3.3 Aerogel Detector	88
4.3.4 Lead-glass Detector	89
4.4 Coincidence Time-of-Flight	89
4.4.1 HRS and BigBite Single Arm Timing Calibrations	91
4.4.2 Coincidence Time Between Two Arms	92
4.5 Data Quality Checks	93
4.5.1 Scaler Checks	94
4.6 Deadtime Measurement	95
CHAPTER 5: ASYMMETRY ANALYSIS	98
5.1 Flow of the Data Analysis	98
5.2 Track Reconstruction and Optics Cuts in the BigBite Spectrometer	100
5.3 PID in the BigBite Spectrometer	102
5.3.1 Electrons	103
5.3.2 Positrons	104
5.3.3 Hadrons	104
5.3.4 Photon-Like Events	105
5.4 PID in the HRS	105
5.4.1 Pions	106
5.4.2 Protons	107
5.4.3 Electrons	107
5.5 Coincidence Time as PID	108
5.6 SIDIS Event Selection	109
5.6.1 Kinematical Phase Space	109
5.7 Contamination of the DIS Electron Sample in the BigBite Spectrometer	110
5.7.1 Negative Pion Contamination	111
5.7.2 Charge Symmetric Background	114
5.8 Single Target-Spin Asymmetries	117
5.8.1 Asymmetry Using Local Spin Pairs	118
5.9 Target Polarization and Spin Direction	120
5.10 Dilutions to the Asymmetry	122
5.10.1 Nitrogen Dilution	122
5.11 ^3He Nuclear Corrections - Extraction of Neutron Information	124

CHAPTER 6: RESULTS AND OUTLOOK	127
6.1 HRS Inclusive Hadron Single Spin Asymmetries	127
6.2 BigBite Inclusive Hadron Single Spin Asymmetries	128
6.3 Single Spin Asymmetry Results for Semi-Inclusive DIS in the $n^\uparrow(e, e'\pi^+)X$ Reaction	131
6.3.1 Angular Modulation: Extraction of Asymmetry Moments	132
6.3.2 Nitrogen Dilution Correction	133
6.3.3 Systematic Uncertainties	134
6.3.4 Single Spin Asymmetries Results for ^3He	137
6.3.5 Preliminary SSA on the Neutron	138
6.4 Summary and Future Studies	144
 APPENDIX A: CONVENTIONS	 145
 Bibliography	 146
 Vita	 151

LIST OF TABLES

2.1	DIS Kinematic variables	6
3.1	BCM calibration constants for both upstream and downstream signals determined during two different measurements. They are expressed in the units of counts/ μA	34
3.2	BCM scaler offsets for both upstream and downstream signals determined during two different measurements. They are expressed in the units of counts/ μA	35
3.3	Various triggers constructed during E06-010 experiment.	64
5.1	Coincidence TOF cuts for various channels. Here the subscript on HRS(BB) indicates the corresponding particle detected in that spectrometer. h refers to hadron.	110
5.2	Random coincidence time cuts for various channels. Here the subscript on HRS(BB) indicates the corresponding particle detected in that spectrometer. h refers to hadron.	110
5.3	Table showing the summary of the kinematical cuts used for selecting SIDIS events.	111
5.4	Negative pion contamination in the BigBite electron sample for different momentum bins.	116
5.5	Photon-induced electron contamination in the BigBite electron sample for different momentum bins.	118
5.6	The filling densities of ^3He and N_2 in the target cells. The uncertainty for ^3He was 2% and for N_2 it was 5% (relative).	124
6.1	A summary of the systematic uncertainties due to exclusion of other angular terms in the fit to extract the Collins and Sivers moments. The neutron asymmetries(second column) were estimated using the preliminary proton results. The ^3He asymmetries were estimated using combined neutron and proton results. The effect of different angular terms for the Collins/Sivers moments are shown in the last two columns.	138
6.2	Systematic uncertainties associated with the various sources in the $^3\text{He}e^\uparrow(e, e'\pi^+)X$ reaction. σ_{stat} is the statistical uncertainty and "relative" indicates uncertainties with respect to the central value.	139
6.3	A summary of the statistical and systematic errors in each Bjorken x bin for the Collins (columns 2 and 3) and Sivers moments (columns 4 and 5). . . .	143

LIST OF FIGURES

2.1	Feynman diagram of deep inelastic scattering.	6
2.2	Proton structure function F_2 measured with electromagnetic scattering of positron on proton (collider experiments ZEUS and H1), and for electron (SLAC) and muons (BCDMS, E665, NMC) on a fixed target. The data are plotted as a function of Q^2 in the bins of fixed x . For the purpose of plotting, F_2 has been multiplied by 2^{i_x} , where i_x is the number of x bins, ranging from $i_x = 1(x = 0.85)$ to $i_x = 28(x = 0.000063)$. This figure is reproduced from [1]	8
2.3	The spin-dependent structure function xg_1 of the proton, deuteron, and neutron (from ^3He target) measured in deep inelastic scattering of polarized electrons/positrons. This figure is reproduced from Ref.[1]	10
2.4	Handbag diagram for inclusive DIS	12
2.5	The three quark–nucleon helicity amplitudes.	15
2.6	Forward Compton scattering diagram of the forbidden helicity flip amplitude.	15
2.7	Probabilistic interpretation of the leading-twist, transverse-momentum-dependent parton distribution functions, where U, L, and T indicate unpolarized, longitudinally polarized, and transversely polarized spins respectively. This figure is reproduced from [2].	17
2.8	Semi-inclusive deep-inelastic scattering.	19
2.9	Diagram contributing to semi-inclusive DIS at LO. Figure reproduced from Ref.[3].	20
2.10	Definition of azimuthal angles for semi-inclusive deep inelastic scattering in the target rest frame. $P_{h\perp}$ and S_{\perp} are the transverse part of P_h and S with respect to the photon momentum.	21
2.11	Collins amplitudes obtained from the SIDIS data on a transversely polarized proton target [4] as a function of x , z and p_T . The error bars indicate the statistical uncertainty, and there is an additional 8% scale uncertainty. The curves are fit to the data as described in Ref. [5]. The figure is taken from Ref. [5].	28
2.12	Collins amplitudes obtained from the SIDIS data on a transversely polarized deuteron target [6] as a function of x , z , and p_T . The error bar indicates the statistical uncertainty. The curves are fit to the data as described in [5]. The Figure is taken from Ref. [5].	28
2.13	Sivers amplitudes obtained from the SIDIS data on transversely polarized proton target [4] as a function of x , z and p_T . The error bar indicates the statistical uncertainty and there is an additional 8% scale uncertainty. The curves are fit to the data as described in [5]. The Figure is taken from [5].	29
2.14	Sivers amplitudes obtained from the SIDIS data on transversely polarized deuteron target [6] as a function of x , z and p_T . The error bar indicates the statistical uncertainty. The curves are fit to the data as described in [5]. The Figure is taken from [5].	29
3.1	Layout of Continuous Electron Beam Accelerator Facility [7]	33
3.2	Panel on the left(right) shows the current (BCM downstream scaler counts) vs. time for different current settings in the calibration run.	35
3.3	Downstream BCM x3 scaler counts vs current. The slope of this plot gives the BCM calibration constant.	36

3.4	Contribution from different ground state wavefunctions to the ^3He nucleus. The Big (small) arrows indicate the polarization direction of the nucleus (nucleons).	38
3.5	Panel (a) shows the optical pumping process in the Rb states. Panel (b) shows the two-step spin exchange process. This figure is reproduced from [8].	39
3.6	Target cell showing two separate regions - pumping region and target region [8].	40
3.7	Target coils setup [9].	41
3.8	NMR signal generated using the <i>frequency sweep</i> method and fitted with the square root of a Lorentzian shape [10].	45
3.9	EPR spectrum showing the ^3He spin states when they are anti-parallel ($\vec{B} - \Delta\vec{B}$) and parallel($\vec{B} + \Delta\vec{B}$) to the holding field direction [10].	46
3.10	Schematic of the automatic target spin-flip system during E06-010 [11]. . .	47
3.11	Layout of the magnets in the High Resolution Spectrometer [7].	49
3.12	Arrangement of the detectors in High Resolution Spectrometer during the E06-010 experiment. The figure is reproduced from [12]	50
3.13	Layout of the BigBite spectrometer [13].	52
3.14	Orientation on U, V, and X wire planes in BigBite wire chambers.	53
3.15	Geometry of the BigBite preshower, scintillator, and shower detectors. . . .	55
3.16	Example of CODA configuration using read-out controllers.	56
3.17	Total sum of preshower and shower	58
3.18	BigBite spectrometer trigger logic diagram.	59
3.19	Re-timing circuit for the BigBite trigger	60
3.20	Trigger Logic for the Left HRS.	62
3.21	Schematic diagram of coincidence trigger setup between the two spectrometers	63
3.22	Coincidence timing between BigBite and HRS.	64
3.23	Scaler setup and gating scheme using target spin and beam helicity.	65
3.24	Beam helicity sequence during E06-010 experiment.	66
3.25	Timing sequence for the target spin state [11].	67
4.1	^3He target polarization measured by EPR when the target is in <i>transverse</i> direction. This plot is reproduced from [14].	68
4.2	^3He target polarization measured by EPR when the target is in <i>vertical</i> direction. This plot is reproduced from [14].	69
4.3	History of target polarization during the E06-010 experiment. The x-axis show the number of spin-flips (20 minutes each) [15].	70
4.4	Drift time spectrum for the 100th wire in the x plane of the third chamber [12].	71
4.5	The residual peak for the U-plane of the front chamber[12].	72
4.6	Reconstructed vertex for the multi-foil carbon target at a particle momentum of 0.9 GeV [12].	74
4.7	Reconstructed vertex for the muti-foil carbon target at a particle momentum of 1.2 GeV [12].	75
4.8	A lead sieve slit plate with a thinkness of 1.5".	75
4.9	The left panel shows the reconstructed sieve pattern with first order optics model. The middle panel shows the sieve pattern after adding offsets. The right panel shows the sieve pattern after applying higher order corrections. The red points indicates where the sieve holes/slots are actually located [12].	76

4.10	Final momentum resolution achieved with two beam energies: left panel is for $E_0 = 1.23$ GeV and right panel is for $E_0 = 2.39$ GeV [12].	77
4.11	BigBite optics check: The left side top(bottom) panels show the reconstructed missing mass peak of the proton and other resonances for beam energies of 1.23 GeV (2.39 GeV). The right side panels show the momentum vs. scattering angle θ correlations at the beam energies of 1.23 GeV and 2.39 GeV [12].	78
4.12	Momentum resolution for positive optics data at 1.23 GeV [12].	79
4.13	Reconstructed vertex for the multi-foil carbon target using positive optics data [12].	80
4.14	Event display for an uncalibrated(left) and calibrated(right) shower. The colors shows the strength of the ADC amplitude.	81
4.15	Shower ADC amplitudes fitted with a Gaussian+Landau distribution tail shape.	82
4.16	Peak of the ADC amplitudes of the preshower and the shower detector blocks after a rough alignment using the high voltage.	83
4.17	Preshower and shower detector calibration coefficients.	86
4.18	Reconstructed energy of electron in the preshower+shower detector signal at two incident beam energies.	87
4.19	Energy divided by momentum of the electrons in the preshower+shower at two incident beam energies	87
4.20	Preshower energy spectrum showing a clear separation between pions and electrons. The minimum ionizing pions peak around channel 180 and electron like events peak around channel 700.	88
4.21	Reconstructed vertex z_{react} for a multi-foil carbon target with a BeO target mounted in the front [16].	89
4.22	ADC sum of the gas Čerenkov detector.	90
4.23	ADC sum of the Aerogel detector for data taken at various times during the experiment [17].	91
4.24	Energy divided by momentum for the two-layer lead-glass detector shows a clear separation between pions and electrons.	92
4.25	Panel on the left (right) shows the timing resolution achieved by the single arm timing detectors in the HRS (BigBite spectrometer) [16].	93
4.26	Coincidence time-of-flight spectrum for $(e, e'\pi)$ where a clear separation between protons, kaons and pions is seen [16].	93
4.27	Preshower peak vs. run number before and after correction.	95
4.28	E/p peak value vs. run number before and after correction.	96
5.1	Data analysis flow for the E06-010 experiment.	99
5.2	Plot showing beam trip cuts for one run. The black points are excluded from the analysis [12].	100
5.3	χ^2/N_{dof} for the fit to the track in the BigBite spectrometer.	101
5.4	Event cut on reconstructed vertex in the BigBite spectrometer.	101
5.5	The BigBite optics valid cut shown in red. The black points indicate all the events before the cut [12].	102

5.6	Vertical position versus vertical slope in the first wire chamber shows a clear separation between oppositely bending particles. The events below the blue(red) boundary indicate negative(positive) particles. The black points include all particles.	103
5.7	The left(right) panel shows the difference between $x(y)$ coordinate of tracks projected on the shower counter and the reconstructed shower $x(y)$ position.	104
5.8	Energy deposited in the preshower vs. total energy divided by the particle's momentum shows a clear separation between electrons and pions.	105
5.9	Red points shows the HRS acceptance cut for the Pb-glass detector.	106
5.10	The 2D acceptance cuts based on the target kinematical variables θ_{tgt} , ϕ_{tgt} , y_{tgt} , and δp [16].	107
5.11	Event cut on reconstructed vertex in the HRS spectrometer.	108
5.12	Difference between BigBite and HRS reconstructed vertices.	109
5.13	Coincidence time-of-flight spectrum in the HRS positive mode. There is a clear separation between protons(P), π^+ , and K^+ mesons.	109
5.14	Phase space of kinematical variables x , z , Q^2 and P_T along with their binning.	112
5.15	Phase space of kinematical variables shown in 2D for all events passing the $N(e, e'\pi)X$ cuts.	113
5.16	Angular coverage of ϕ_h and ϕ_s in different x bins.	114
5.17	A Gaussian function that is convoluted with a Landau function is fitted to the preshower spectrum in different BigBite momentum bins. The red line shows the cut used for calculating the pion contamination.	115
5.18	Left(right) panel shows the π^- yield suppression factor as defined in Eq. (5.3) when HRS is in positive(negative) mode.	116
5.19	The top left(right) panel shows the BigBite singles photon-induced e^+ yield in red and the e^- yield in black, when the HRS polarity is positive(negative). The bottom left(right) panel shows the coincidence yield of positrons in the BigBite spectrometer and the $\pi^+(\pi^-)$ in the HRS in red, and the e^- yield in the BigBite and the $\pi^+(\pi^-)$ yield in the HRS in black	117
5.20	The left(right) panel shows the beam charge asymmetry with the local pair method (super local pair method) [12].	119
5.21	Raw ^3He asymmetry for different runs. There is a clear reversal of the asymmetry sign when the beam half-wave plate(BHWP) is inserted in the beamline [14].	121
5.22	^3He elastic asymmetry obtained from the constant fit to the run-by-run asymmetry at $E_0 = 1.23$ GeV and a spectrometer angle of 16° [14].	122
5.23	Raw ^3He asymmetry in the Δ resonance region for different runs. Transverse(+) and Transverse(-) indicate regions with the two opposite target spin directions. The asymmetry changes sign with the change in the target spin direction [14].	123
5.24	The left(right) plot shows the model calculation of the neutron Collins(Sivers) asymmetry for π^- meson (solid curve). The dashed curve shows the asymmetry extracted from Eq.(5.20) and dotted curve shows result when the proton polarization is ignored in Eq.(5.20). This figure is reproduced from Ref. [18]	125
6.1	The left(right) panel shows the transverse(vertical) target spin configurations, where the incoming electron (\vec{k}_1), the outgoing hadron(\vec{k}_2), and the spin vectors(\vec{S}_T) are shown.	128

6.2	The left(right) panel shows the inclusive hadron asymmetry in the HRS for "vertical"("transverse") spin configuration corrected for the target polarization. These asymmetries are not corrected for N ₂ dilution. The error bars indicate the statistical uncertainty. The study of the systematic uncertainties is currently underway.	129
6.3	The two panels show the asymmetries in the inclusive ${}^3\text{He}^\uparrow(e, h^-)X$ reaction. Corrections due to N ₂ dilution have not been applied.	130
6.4	The two panels shows the asymmetries in the inclusive ${}^3\text{He}^\uparrow(e, h^+)X$ reaction. Corrections due to N ₂ dilution have not been applied.	131
6.5	BigBite singles asymmetries obtained from the angular modulation $\langle \sin(\phi_S^h) \rangle$ for negative(left) hadrons, positive(center) hadrons, and photons(right). The error bars represent the statistical uncertainty. The systematic errors are not shown as they are currently under study.	132
6.6	HRS singles asymmetries obtained from the angular modulation $\langle \sin(\phi_S^h) \rangle$ for π^+ and π^- mesons and protons, at $P_h=2.35$ GeV. The error bars represent the statistical uncertainty. The systematic errors are not shown.	133
6.7	The left (right) panel shows the measured SSA in the ${}^3\text{He}(e, e'\pi^+)X$ channel when target spin is vertical (transverse). Different colors indicate the same data but with variations in the PID and acceptance cuts. "pass-4" is the most recent data used for the analysis. The error bars show only the statistical uncertainty [12].	134
6.8	${}^3\text{He}^\uparrow(e, e'\pi^+)X$ asymmetry moments obtained from fitting the Collins (left), Sivers(right), and Pretzelocity(right) angular modulations to the measured raw asymmetry. The error bars represent the statistical uncertainty.	135
6.9	Nitrogen dilution factors are shown in each x bin. Different colors indicate the dilution factors for the three different target cells [12].	136
6.10	The left(right) panel shows the SSA in ${}^3\text{He}^\uparrow(e, \pi^-\pi^+)X$ channel in vertical(transverse) target spin configuration.	137
6.11	The left(right) panel shows the SSA in the ${}^3\text{He}^\uparrow(e, \gamma\pi^+)X$ channel in the vertical(transverse) target spin configuration.	137
6.12	Preliminary results for the Collins and Sivers moments obtained for π^+ mesons on ${}^3\text{He}$. The error bars represent the statistical uncertainty and the red band shows the total systematic uncertainty. A theory prediction is shown by the solid curve [19][20].	140
6.13	Theory calculations for proton and neutron Collins and Sivers moments by Anselmino <i>et al.</i> [19][20]	141
6.14	Preliminary results on the Collins and Sivers moments obtained for π^+ on the neutron. The error bars represent the statistical uncertainty and the red band shows the systematic errors. The solid magenta curve is a theory prediction from Anselmino <i>et al.</i> [19][20], the solid black curve is a prediction from Ma <i>et al.</i> [21], and the red curve is from Pasquini [22]	142

CHAPTER 1: INTRODUCTION

1.1 Structure of the Visible Matter

Observational evidence from astrophysical objects suggests that only 4% of our visible universe is made of matter that we know, the rest is in unknown form. Of this tiny fraction, protons and neutrons, together known as *nucleons*, account for almost all the mass in the visible universe. Therefore it is necessary to understand the internal structure of the nucleons in terms of their constituents, quarks and gluons, and more importantly their dynamics, to account for the mass of the nucleon and thus for the matter that we know. Initially it was thought that all mesons and baryons, together known as *hadrons*, were point-like particles with no internal structure. But it was soon realized that this was not the case, particularly looking at the large variety of hadrons discovered in 1950's and 60's in the accelerator based experiments. In order to explain this zoo of particles, almost half a century ago it was postulated [23][24] that the hadrons, of which nucleon is the most prominent one, are composed of point-like particles called "quarks". Quarks have a spin-1/2, a fractional charge, and a new degree of freedom, known as *flavor*. This postulate was tested in late 1960's at Stanford Linear Accelerator Center (SLAC) by performing Deep Inelastic Scattering (DIS) experiments. In these experiments, a high-energy lepton beam scatters off of a proton target (such as hydrogen), transferring large amounts of energy and momentum to the system, causing it to disintegrate. By measuring the scattering cross sections as a function of momentum transfer, the information on the inner structure of the nucleon can be obtained. From these experiments it was discovered that the scattering cross sections are weakly dependent on the momentum transfer, a property known as *scaling* [25]. This was interpreted as an evidence of point-like particles inside the nucleon. And the DIS process is thought to be sum of incoherent scattering of electrons off these point-like particles called *partons* [26]. Later it was realized that the charged partons were quarks and the neutral partons were "gluons" which bind the two quarks together. This binding of quarks was explained by the field theory of strong interactions known as Quantum Chromodynamics (QCD).

1.2 Spin Structure of the Nucleon

One of the most important aspects of understanding the nucleon structure is the question of nucleon spin and its origin. We know that nucleon is spin-1/2 particle, and since it has inner structure, the contributions from the partons must be responsible for its spin. Deep inelastic scattering experiments with polarized beams and polarized targets have provided most of our present knowledge of the nucleon spin structure. The quantity that usually characterizes the contribution of the quark spin to the nucleon spin is the helicity distribution (δq) of individual quark flavors. The sum of helicity distributions of all quark flavors gives the total contribution of quark spin ($\Delta\Sigma$) to the nucleon spin. In the “infinite” momentum frame, where the nucleon is moving with a very large speed, and the nucleon spin is along the direction of its motion, the helicity distribution is given by the difference of the number of partons with their spins aligned and anti-aligned with respect to the nucleon spin. Therefore it measures the net *longitudinal* spin contribution of the quark in the nucleon. Experiments done at SLAC and CERN first suggested that this quantity contributes only about 30% to the spin of the proton [27][28]. So the rest of the contribution to the nucleon spin must come from the spin of the gluons and the orbital angular momentum of the quarks and gluons. Currently there is no clear picture of the exact gluon spin contribution, although, experiments using proton-proton collisions suggest that it may be small. For an example refer to the global data on gluon spin contribution (ΔG) in [29]. If this is the case, then most of the nucleon spin might be due to the orbital angular momentum of the partons, which has not been measured yet.

Earlier we mentioned the helicity distribution of the quarks which measures the longitudinal spin contribution. Similarly, there can be *transversity distribution* of the quarks which reveals the transverse spin structure of the nucleon. In the infinite momentum frame, and when the spin of the nucleon is transverse to the direction of its motion, transversity is defined as the numbers of partons with their spins aligned and anti-aligned to the nucleon spin. It is important to note that although the transversity looks similar to the helicity distribution, an interpretation is only possible in the infinite momentum frame where the rotational symmetry is broken by the direction of the motion. Moreover, due to the conservation of helicity, the gluon transversity cannot exist. So, in addition to the longitudinal spin we have to consider the contribution from the transverse spin to the overall nucleon

spin.

Transversity was first introduced by J. Ralston and D. Soper [30] in 1979 and it still remains an unknown quantity experimentally. This is due to the fact that it decouples from the inclusive DIS process because of its chiral-odd nature. In order to access this quantity we need another chiral-odd object. One way to access this quantity is to use the semi-inclusive DIS process where the leading hadron is detected in coincidence with the scattered electron. In this case, the transversity distribution combined with a chiral-odd “Collins” fragmentation function gives rise to observable effects (Collins asymmetry). The semi-inclusive DIS process not only gives access to transversity, but a whole new class of distributions which depend on the intrinsic transverse momenta of the quarks, these are known as the Transverse Momentum Dependent (TMD) distribution functions. One such function relevant to this thesis is the *Sivers distribution* function. Sivers distribution together with the unpolarized fragmentation function produces a left-right asymmetry of the produced hadron. It is particularly interesting due to its connection with the quark orbital angular momentum. A non-zero Sivers asymmetry indicates a non-vanishing orbital angular momentum of the quarks [31][32]. There has been a rapid development, both theoretical and experimental, to understand this new class of distribution functions. The initial experimental indications from HERMES [33] suggest that the Sivers asymmetry is not small. At the moment the only data available on Collins and Sivers moment comes from two experiments - HERMES at DESY using proton target [34][33] and COMPASS at CERN using both proton and deuteron target [35][36]. This thesis focuses on measurement of the Collins and Sivers asymmetries using the SIDIS process on a neutron target (^3He) for the first time. This will help to constraint the transversity and Sivers distribution functions extracted from a global fit to the world data.

1.3 Outline of the Thesis

In Chapter 2 the basic formalism for deep inelastic scattering is discussed with focus on the transversity distribution function and ways to measure it using semi-inclusive DIS. Also, the concept of TMDs are discussed with particular attention to the Sivers function. The Collins and Sivers moments along with the method of single-spin asymmetry is defined at the end. Chapter 3 introduces the Jefferson Lab E06-010 experiment in Hall-A. An extensive description of the detectors, data acquisition (DAQ), and the target used in this

experiment is given. In chapter 4 the techniques used for calibrating the detectors and target are discussed along with the problems encountered during the experiment. The physics analysis including the selection of SIDIS events, forming the single-spin asymmetries, and extraction of neutron asymmetries are shown in Chapter 5. Finally, in Chapter 6 the Collins and Sivers moments are shown for $n^\uparrow(e, e'\pi^+)X$ SIDIS reaction along with the description of the sources of systematic uncertainties and their estimation.

CHAPTER 2: THE SPIN STRUCTURE OF THE NUCLEON

Deep Inelastic Scattering (DIS) has played an important role in understanding the internal structure of the nucleon. First evidence of the point-like structures inside the nucleon, so called *partons*, came from the DIS experiments conducted in late 1960's. Since then we have learned a great deal about the momentum and spin structure of the nucleon in terms of how these point-like constituents contribute to the overall structure.

In this chapter a formal introduction to the inclusive DIS is presented along with the quark-parton model which connects the structure functions to the quark distribution functions. The main focus of this thesis, Transversity and Sivers distribution functions, are discussed along with the Collins fragmentation function, as well as ways to measure them using single-spin asymmetries in semi-inclusive DIS process. The mathematical notation and convention used in this chapter are defined in Appendix A. Throughout this thesis natural units are used, i.e., $\hbar = c = 1$.

2.1 Deep Inelastic Scattering

In a Deep Inelastic Scattering (DIS) process, an incoming lepton with energy E interacts with a nucleon via exchange of a virtual boson, as shown in Figure 2.1. During this process the momentum transfer involved is so large that the nucleon breaks up and forms a hadronic final state X . The energy (E') and direction of the scattered lepton is measured with a detector system, but the final hadronic state(X) is not detected experimentally. In the lab frame, the four momentum of the incoming and the outgoing lepton is given by $l = (E, \vec{l})$ and $l' = (E', \vec{l}')$ respectively. Where $\vec{l} = (0, 0, E)$, neglecting the lepton mass, and $\vec{l}' = (E', E' \sin \theta \cos \phi, E' \sin \theta \sin \phi, E' \cos \theta)$. In fixed target experiments such as, for example, at Jefferson Lab, the four momentum of the nucleon is given by $P = (M, \vec{0})$, where M is the mass of the nucleon.

The relevant kinematic variables for the inclusive DIS are summarized in table 2.1. The cross-section for inclusive DIS is usually expressed in terms of two independent variables – the squared momentum transfer to the target, Q^2 , which is the measure of the spatial resolution in the scattering process, and a dimensionless Bjorken scaling variable, x , which describes the inelasticity of the process. In DIS processes, Q^2 is large enough to resolve the constituents of the nucleon. In the elastic scattering process, the mass is conserved, i.e.,

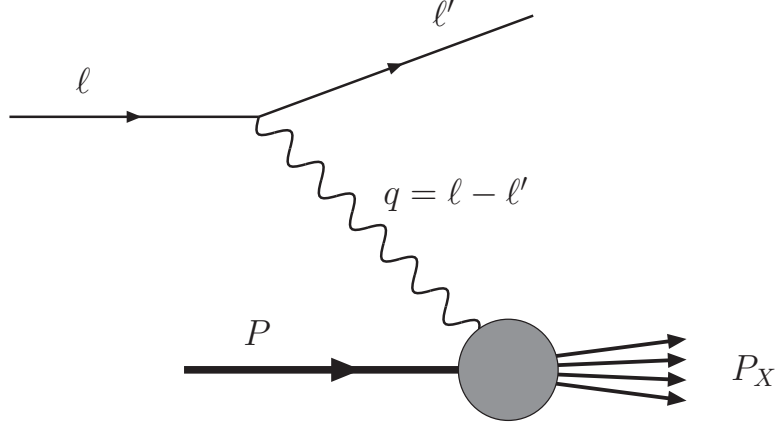


Figure 2.1: Feynman diagram of deep inelastic scattering.

$W^2 = M^2$ implying $x = 1$, whereas in inelastic processes, the squared mass of final hadronic state becomes larger than the nucleon mass, and consequently, $0 < x < 1$.

Table 2.1: DIS Kinematic variables

$q = l - l'$	four-momentum of the virtual photon
$\nu = E - E' = P \cdot q/M$	the energy loss of the lepton
$y = \nu/E = P \cdot q/P \cdot l$	the fractional energy loss of the lepton
$Q^2 = -q^2 = 2EE'(1 - \cos \theta) = 4EE' \sin^2 \frac{\theta}{2}$	negative four-momentum transfer squared
$x = Q^2/2M\nu = Q^2/2P \cdot q = Q^2/2MEy$	Bjorken scaling variable
$W^2 = (P + q)^2 = M^2 + 2M\nu - Q^2$	squared invariant mass of final hadronic state
$\omega = 1/x$	

2.1.1 DIS Cross Section

In the rest frame of the target the inclusive DIS cross section can be written in the form [37]

$$\frac{d^2\sigma}{dE'd\Omega} = \frac{\alpha^2}{2MQ^4} \frac{E}{E'} L_{\mu\nu} W^{\mu\nu}, \quad (2.1)$$

where α is the electromagnetic coupling constant and $L_{\mu\nu}$ and $W^{\mu\nu}$ are the leptonic and hadronic tensors, respectively. By interchanging the Lorentz indices μ and ν the leptonic tensor can be further decomposed into symmetric(S) and anti-symmetric(A) parts,

$$L_{\mu\nu} = L_{\mu\nu}^S(l, l') + iL_{\mu\nu}^A(l, s; l'), \quad (2.2)$$

where s is the spin four vector of the incoming lepton. The spin-independent symmetric part and the spin-dependent anti-symmetric parts are written as

$$L_{\mu\nu}^S = 2(l_\mu l'_\nu + l_\nu l'_\mu - g_{\mu\nu}(l^\sigma l'_\sigma - m^2)), \quad (2.3)$$

$$L_{\mu\nu}^A = 2m\epsilon_{\mu\nu\alpha\beta}s^\alpha(l^\beta - l'^\beta) \quad (2.4)$$

Here, $g_{\mu\nu}$ is the metric tensor, $\epsilon_{\mu\nu\alpha\beta}$ is the Levi-Civita tensor and m is the mass of the lepton. The leptonic tensor is easy to calculate using QED formalism since leptons are pointlike fermions.

The hadronic tensor in eq. (2.1) is more complicated to calculate directly using first principles because of the complex structure of the nucleon. Therefore this quantity is generally parametrized in terms of structure functions. Like the leptonic tensor, hadronic tensor can also be split into symmetric and anti-asymmetric parts:

$$W_{\mu\nu} = W_{\mu\nu}^S(q, P) + iW_{\mu\nu}^A(q; P, S) \quad (2.5)$$

where S is the spin four vector of the target nucleon in the target rest frame. In terms of the structure functions, the hadronic tensor is written as

$$W_{\mu\nu}^S = 2(-g_{\mu\nu} + \frac{q_\mu q_\nu}{q^2})F_1(x, Q^2) + \frac{2}{P \cdot q}(P_\mu - \frac{P \cdot q}{q^2}q_\mu)(P_\nu - \frac{P \cdot q}{q^2}q_\nu)F_2(x, Q^2) \quad (2.6)$$

$$W_{\mu\nu}^A = \epsilon_{\mu\nu\alpha\beta}\frac{2Mq^\alpha}{P \cdot q}[S^\beta g_1(x, Q^2) + (S^\beta - \frac{S \cdot q}{P \cdot q}P^\beta)g_2(x, Q^2)] \quad (2.7)$$

Eqns. (2.6) and (2.7) are electromagnetically gauge invariant. The dimensionless quantities F_1 and F_2 are known as *unpolarized structure functions*, as they do not depend on the spin of the nucleon, whereas g_1 and g_2 are spin-dependent quantities and are therefore known as *polarized structure functions*. These quantities are functions of DIS variables x and Q^2 , and by measuring these quantities experimentally, one can obtain knowledge of the internal structure of the nucleon. In the Bjorken limit,

$$\nu, Q^2 \rightarrow \infty, \quad x = \frac{Q^2}{2M\nu} \text{ fixed}, \quad (2.8)$$

the structure functions F_1 , F_2 , g_1 , g_2 scale approximately, i.e., they depend only on x and are approximately Q^2 independent.

Using Eqns. (2.2) and (2.5), we can write the differential cross section as

$$\frac{d^2\sigma}{dE'd\Omega} = \frac{\alpha^2}{2MQ^4} \frac{E}{E'} [L_{\mu\nu}^{(S)} W^{\mu\nu(S)} - L_{\mu\nu}^{(A)} W^{\mu\nu(A)}], \quad (2.9)$$

where the terms with opposite symmetry vanish due to the parity conservation of the electromagnetic interaction.

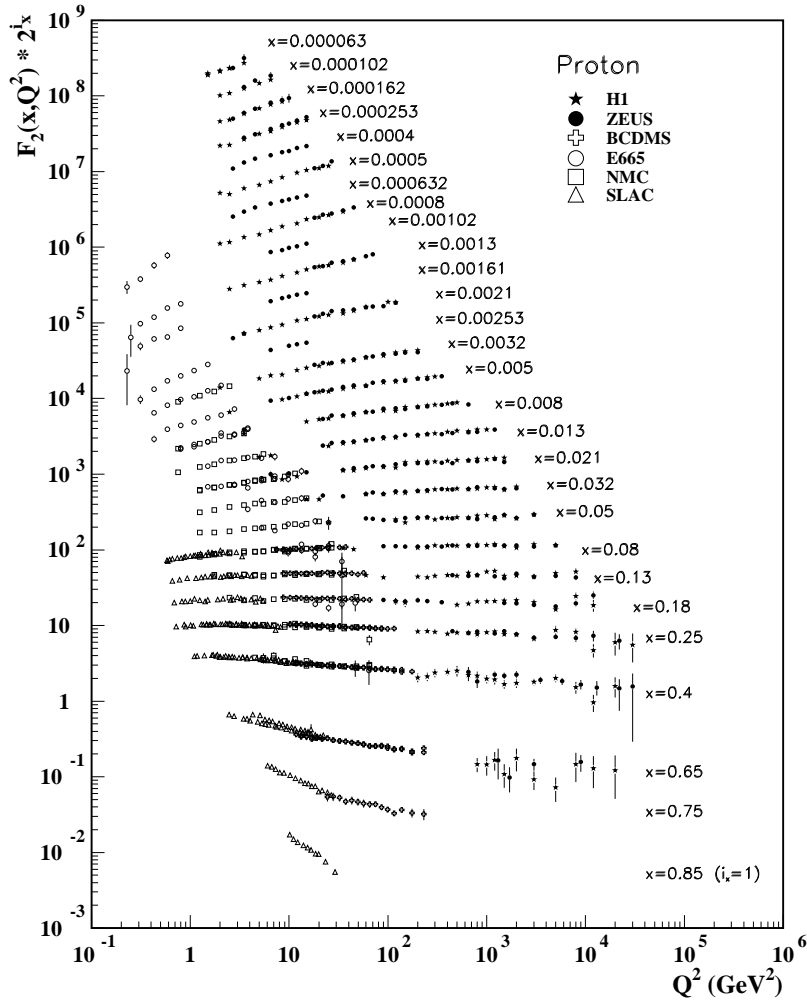


Figure 2.2: Proton structure function F_2 measured with electromagnetic scattering of positron on proton (collider experiments ZEUS and H1), and for electron (SLAC) and muons (BCDMS, E665, NMC) on a fixed target. The data are plotted as a function of Q^2 in the bins of fixed x . For the purpose of plotting, F_2 has been multiplied by 2^{i_x} , where i_x is the number of x bins, ranging from $i_x = 1(x = 0.85)$ to $i_x = 28(x = 0.000063)$. This figure is reproduced from [1]

Unpolarized cross section: The unpolarized cross section is obtained by averaging over all the spins of the incoming leptons, which leaves only the spin-independent symmetric part of the differential cross-section intact and we obtain,

$$\frac{d^2\sigma^{unpol}}{dxdy} = \frac{4\pi\alpha^2 s}{Q^4} [xy^2 F_1(x, Q^2) + (1 - y - \frac{xyM^2}{s}) F_2(x, Q^2)], \quad (2.10)$$

where $s = (P + l)^2$ is the center-of-mass energy. Figure 2.2 shows the world data on F_2 as a function of Q^2 at different values of x .

Polarized cross section: The polarized cross section depends on spins of both the lepton and the nucleon. The difference of the cross sections with opposite target nucleon spins probe the antisymmetric part of the lepton and hadronic tensors.

$$\frac{d\sigma(+S)}{dE'd\Omega} - \frac{d\sigma(-S)}{dE'd\Omega} = -\frac{\alpha^2}{2MQ^4} \frac{E'}{E} 2L_{\mu\nu}^{(A)} W^{\mu\nu(A)}. \quad (2.11)$$

When the target is *longitudinally polarized* (i.e, polarized along the incoming beam direction), then in terms of g_1 and g_2 , the above spin asymmetry takes the form

$$\frac{d\sigma(+S)}{dxdyd\varphi} - \frac{d\sigma(-S)}{dxdyd\varphi} = -\frac{4\alpha^2}{Q^2} \left[(2 - y)g_1(x, Q^2) \cos\theta_S^l + \frac{4Mx}{Q} \sqrt{1 - y}(g_1 + g_2) \sin\theta_S^l \cos\phi_S^l \right] \quad (2.12)$$

where θ_S^l is the angle between the spin of the nucleon S and the virtual photon momentum q , and ϕ_S^l is the azimuthal angle between the lepton plane and the plane formed by the incoming lepton direction (l) and the nucleon spin vector(S).

When the target spin is perpendicular to the virtual photon momentum direction in the plane formed by l and l' (i.e., $\theta_S^l = \pi/2$) then the difference in the cross-section reduces to

$$\frac{d\sigma(+S_\perp)}{dxdyd\varphi} - \frac{d\sigma(-S_\perp)}{dxdyd\varphi} = -\frac{4\alpha^2}{Q^2} \left[\frac{4Mx}{Q} \sqrt{1 - y}(g_1 + g_2) \right] \cos\phi_S^l. \quad (2.13)$$

In this process DIS probes the combination $g_1 + g_2$. Therefore when the incoming lepton and the target spin are longitudinally polarized the cross section is mainly dominated by the g_1 structure function (the second term in Eq. (2.12) is suppressed by $1/Q$), whereas if lepton beam is longitudinally polarized and the target spin is transversely polarized, then the cross section is sensitive to the combination $g_1 + g_2$. Figure 2.3 shows the world data on g_1 structure function using various targets.

2.2 Naïve Quark Parton Model

To connect the previously mentioned structure functions to the quark content (parton distribution functions) in the nucleon, we need to consider the Quark Parton Model (QPM). In

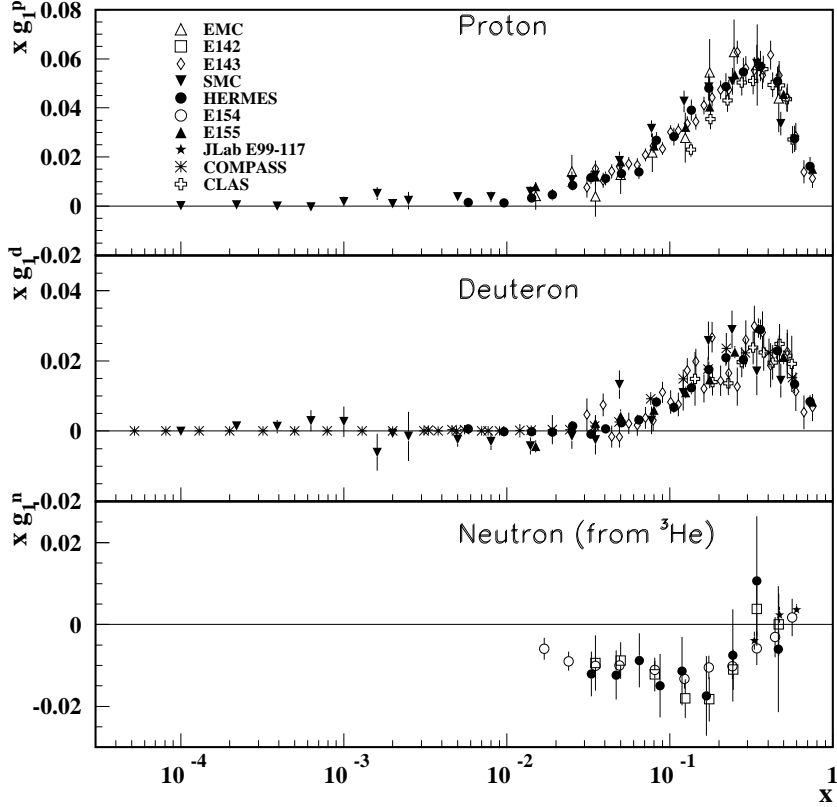


Figure 2.3: The spin-dependent structure function xg_1 of the proton, deuteron, and neutron (from ${}^3\text{He}$ target) measured in deep inelastic scattering of polarized electrons/positrons. This figure is reproduced from Ref.[1]

the QPM, the basic assumption is that at large Q^2 and ν , the photon interacts incoherently with the free partons (quarks and anti-quarks) inside the nucleon. This is true if the ν and Q^2 are large enough to resolve the internal structure of the target ($Q^2 > M^2$).

Here, it is convenient to consider a reference frame where the nucleon is moving with infinite momentum in z direction. In this frame we can express the nucleon momentum in light-cone coordinate system: $P = (P^+, P^-, P_T)$, and similarly the quark momentum is expressed as $p = (p^+, p^-, p_T)$ (see Appendix A for conventions). In such a frame the target momentum is much larger than its mass and the three momentum can be written as $p = xP + p_T$, where P is the nucleon momentum, p_T is the quark momentum transverse to the z -direction. Here it is assumed that as $P \rightarrow \infty$, p_T becomes negligible at short interaction times.

If $q(x)$ is the probability of finding a parton carrying a fraction x of the target's momentum in this frame, then we can relate this to the structure functions as [38],

$$F_1(x, Q^2) = \sum_{q\bar{q}} e_q^2 q(x) \quad (2.14)$$

and

$$F_2(x, Q^2) = \sum_{q\bar{q}} x e_q^2 q(x). \quad (2.15)$$

Where $q(x)$ is the unpolarized quark distribution function and e_q is the electric charge of the quark. If we consider a helicity basis¹ then one can construct both spin-independent and spin-dependent quark distribution function

$$q(x) = q^{\rightarrow}(x) + q^{\leftarrow}(x) \quad (2.16)$$

and

$$\Delta q(x) = q^{\rightarrow}(x) - q^{\leftarrow}(x), \quad (2.17)$$

where $q(x)$ is summed over all the quarks spin and $\Delta q(x)$ is the helicity distribution function, which can be defined as the net difference in the distribution of the quarks with opposite helicity states. Here \rightarrow and \leftarrow indicate the opposite helicity states of the quark in a longitudinally polarized nucleon². $\Delta q(x)$ can be related to spin-dependent structure g_1 function as follows,

$$g_1(x, Q^2) = \frac{1}{2} \sum_{q\bar{q}} e_q^2 \Delta q(x) \quad (2.18)$$

and g_2 is zero, as it describes the transverse spin of the quarks inside the nucleon, which vanishes in the QPM.

2.3 QCD Improved Parton Model

In the QCD improved parton model the distribution functions not only depends on x but also on Q^2 *i.e.*, $q(x) \rightarrow q(x, Q^2)$ and $\Delta q(x) \rightarrow \Delta q(x, Q^2)$. This dependence on Q^2 is related to the fact that quarks and gluons interact, and the number of partons the external probe "sees" depends on Q^2 and x . At large Q^2 and small x , the resolution of the electromagnetic probe (virtual photon) increases and therefore there is an enhancement of partons

¹In a helicity basis, the spin is quantized along the axis in the direction of motion of the particle.

²The longitudinal polarization means the nucleon spin pointing along its momentum direction. In the lab frame it is interpreted as nucleon spin pointing along the incoming lepton beam direction.

(quarks and gluons), all sharing the total nucleon momentum, as seen in Figure 2.2. The Q^2 dependence of the parton distribution functions is described by the DGLAP evolution equations [39][40][41][42]. Due to this Q^2 dependence, the structure function g_2 is non-zero and thought to arise from quark-gluon interactions.

If we consider the inclusive DIS process in the QCD improved quark parton model, the scattering process is described as an elastic scattering between quarks and the lepton, where the quarks behaves like quasi-free particles and any interaction between struck quark and the target remnant is ignored. This process can be represented by a handbag diagram (Figure 2.4). Here the momentum of the nucleon is P and initial momentum of the struck quark is p and final momentum of the outgoing quark is k . The hadronic tensor can then be written as

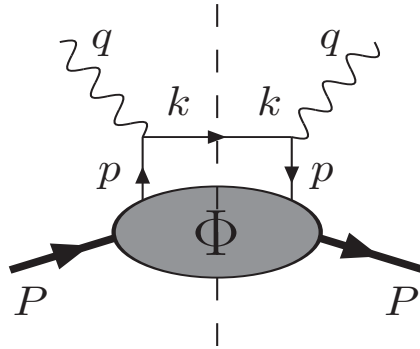


Figure 2.4: Handbag diagram for inclusive DIS

$$W^{\mu\nu} = \sum_{q,\bar{q}} e_q^2 \int \frac{d^4 p}{2\pi} \delta((p+q)^2) Tr[\Phi \gamma^\mu (\not{p} + \not{q}) \gamma^\nu] \quad (2.19)$$

where γ^μ and γ^ν are Dirac matrices, and Φ is the quark-quark correlator. The hadronic tensor can be split into a hard QED part describing quark-photon scattering and a non-perturbative QCD part described by a quark-quark correlator. The quark-quark correlator can be written as a bilocal, bilinear operator acting on the initial nucleon state, integrated over all possible separations ξ of the second quark spinor, so that

$$\Phi_{ij}(p, P, S) = \int d^4 \xi e^{ip \cdot \xi} \langle PS | \bar{\psi}_j(0) \psi_i(\xi) | PS \rangle, \quad (2.20)$$

where ψ is the quark spinor and i, j are the Dirac indices. Here the summation over the color is not shown but it is implicit. ψ can be decomposed in the basis of Dirac matrices, $\mathbb{1}$, γ^μ , $\gamma^\mu \gamma_5$, $i\gamma_5$, and $i\sigma^{\mu\nu} \gamma_5$, and can be written as

$$\Phi(p, P, S) = \frac{1}{2} [\mathcal{S} \mathbb{1} + \mathcal{V}_\mu \gamma^\mu + \mathcal{A}_\mu \gamma_5 \gamma^\mu + i\mathcal{P}_5 \gamma_5 + \frac{1}{2} i \mathcal{T}_{\mu\nu} \sigma^{\mu\nu} \gamma_5]. \quad (2.21)$$

where \mathcal{S} (scalar), \mathcal{V}_μ (vector), \mathcal{A}_μ (axial vector), \mathcal{P}_5 (pseudo-scalar), and $\mathcal{T}_{\mu\nu}$ (tensor) are the quantities which depend on p , P and S . In leading twist³, neglecting the transverse momentum of the quarks inside the nucleon, only vector, axial, and tensor terms survive in the above equation. Then the quark-quark correlation matrix, satisfying hermiticity, parity, and time-reversal invariance, can be written in terms of real functions $A_i(p^2, p \cdot P)$ as [3]

$$\Phi(p, P, S) = \frac{1}{2}[A_1 \not{P} + A_2 \lambda_N \gamma_5 \not{P} + A_3 \not{P} \gamma_5 \not{S}_\perp], \quad (2.22)$$

where nucleon spin is given by $S \simeq \lambda_N P^\mu / M + S_\perp^\mu$ with λ_N being the nucleon helicity. The approximate equality sign indicate that we are neglecting terms suppressed by $(P^+)^{-2}$. Integrating A_1 , A_2 and A_3 over p and using the constraint $x \simeq p^+ / P^+$, one obtains the three leading-twist quark distribution functions (DFs), namely,

$$q(x) = \int \frac{d^4 p}{(2\pi)^4} A_1(p^2, p \cdot P) \delta(x - \frac{p^+}{P^+}), \quad (2.23)$$

$$\Delta q(x) = \int \frac{d^4 p}{(2\pi)^4} A_2(p^2, p \cdot P) \delta(x - \frac{p^+}{P^+}), \quad (2.24)$$

and

$$\delta q(x) = \int \frac{d^4 p}{(2\pi)^4} A_3(p^2, p \cdot P) \delta(x - \frac{p^+}{P^+}). \quad (2.25)$$

A complete description of the nucleon momentum and spin structure, at leading-twist, can be obtained from these three parton distribution functions (PDFs). The first two DFs, $q(x)$ and $\Delta q(x)$, were discussed in section 2.2. The third one, $\delta q(x)$, is known as the *transversity distribution function*. While the first two DFs have been measured to a very high accuracy to several orders of magnitude in x and Q^2 , very little is known about $\delta q(x)$, because it decouples from inclusive DIS due to its chiral-odd in nature, and is highly suppressed for light quark masses via a fraction of (m_q/Q^2) [45]. This quantity is accessible, however, through other reactions such as semi-inclusive DIS or the Drell-Yan process, and are discussed in section 2.6. The following section addresses the properties of and ways to measure this distribution function.

³A leading twist is the leading order term in the $1/Q$ expansion of the hadronic tensor in terms of local operators as shown in Ref. [43][44]. The terms in the expansion are proportional $(Q/M)^{2-t}$, where $t = \text{twist} = d - n = \text{dimension} - \text{spin}$. The leading order term is given by $\text{twist}=2$.

2.4 Transversity Distribution

The transversity distribution $\delta q(x)$ is defined in Eq. (2.25). The quark-quark correlator in terms of these leading-twist distribution functions, integrated over p reads,

$$\Phi(x) = \frac{1}{2}[q(x) \not{P} + \lambda_N \Delta q(x) \gamma_5 \not{P} + \delta q(x) \not{P} \gamma_5 \not{S}_\perp]. \quad (2.26)$$

Integrating $q(x)$, $\Delta q(x)$ and $\delta q(x)$ over all x and combining the quark and anti-quark distributions gives the axial (g_V), vector (g_A), and tensor charge (g_T), respectively. That is,

$$q = \int_0^1 [q(x) - \bar{q}(x)] dx = g_V, \quad (2.27)$$

$$\Delta q = \int_0^1 [\Delta q(x) + \Delta \bar{q}(x)] dx = g_A, \quad (2.28)$$

and

$$\delta q = \int_0^1 [\delta q(x) - \delta \bar{q}(x)] dx = g_T. \quad (2.29)$$

Since the vector and tensor charges contain the difference of the quark and antiquark distributions, these charges correspond to the valence quark content of the nucleon. The tensor charge has been calculated using different theoretical models, such as the MIT bag model [46][47] and the chiral quark soliton model [48][49], and also using lattice calculations [50][51].

In the quark helicity basis, the distribution functions can be expressed in terms of quark-nucleon forward scattering amplitudes $A_{Hh,H'h'}$ where $h(h')$ and $H(H')$ represent the initial(final) quark and nucleon helicity states, respectively. Three amplitudes $A_{++,++}$, $A_{+-,+-}$, $A_{+,-,+}$ survive after applying helicity, parity conservation, and time-reversal invariance conditions, and these are related to $q(x)$, $\Delta q(x)$, and $\delta q(x)$, respectively. The first two amplitudes conserve helicity and can have probabilistic interpretation in the helicity basis, whereas the third one flips the helicity of both nucleon and struck quark, and thus is not diagonal in the helicity basis, so that it has no probabilistic interpretation (see Fig 2.5). However, in the transverse spin eigenstates ($|\perp\rangle$ and $|\top\rangle$), which are constructed using linear combinations of the helicity eigenstates,

$$|\perp\rangle = \frac{1}{2}(|+\rangle + i|-\rangle), \quad |\top\rangle = \frac{1}{2}(|+\rangle - i|-\rangle) \quad (2.30)$$

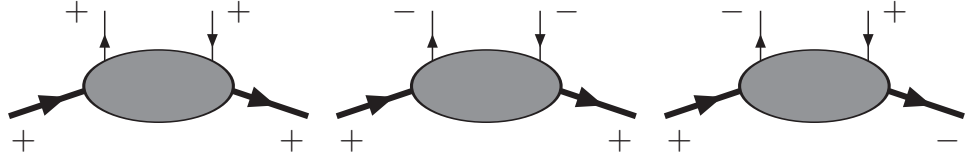


Figure 2.5: The three quark–nucleon helicity amplitudes.

$\delta q(x)$ can have probabilistic interpretation. In this case it is the probability of finding a quark aligned(\uparrow) or anti-aligned(\downarrow) to the nucleon spin (\uparrow), when the nucleon is transversely polarized:

$$\delta q(x) = q^{\uparrow\uparrow}(x) - q^{\uparrow\downarrow}(x). \quad (2.31)$$

Here $q^{\uparrow\uparrow}(x)$ is the probability of finding a quark with its spin aligned along a transversely polarized nucleon. Likewise, $q^{\uparrow\downarrow}(x)$ is the probability of finding a quark with its spin opposite to that of the transversely polarized nucleon. Because of this helicity flip, upon neglecting

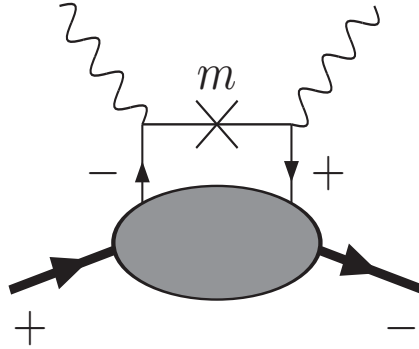


Figure 2.6: Forward Compton scattering diagram of the forbidden helicity flip amplitude.

quark masses in the infinite momentum frame, the transversity distribution is chiral odd. Since all strong and electromagnetic interactions conserve chirality (with corrections of order of m/Q), transversity decouples from the inclusive DIS process or single particle inclusive annihilation, $e^+e^- \rightarrow hX$. For non-relativistic quarks, $\delta q(x) = \Delta q(x)$, since simple boosts and rotations transform transverse spin eigenstates to helicity eigenstates. Therefore any difference between $\delta q(x)$ and $\Delta q(x)$ provides information about the relativistic nature of the quarks moving inside the nucleon. Furthermore, due to the helicity flip amplitude and conservation of helicity in leading twist, transversity does not mix with gluons for spin-1/2 targets. Therefore the transversity distribution has a completely different Q^2 evolution compared to the helicity and momentum distributions.

There are important inequalities that follow from the definitions of the leading-twist

quark distribution functions. Since $\Delta q(x)$ and $\delta q(x)$ are differences of probabilities, the following two trivial inequalities can be formed,

$$|\Delta q(x)| \leq q(x), \quad |\delta q(x)| \leq q(x). \quad (2.32)$$

The third bound, the Soffer inequality[52], follows from the positivity properties of the helicity amplitudes

$$2|\delta q(x)| \leq q(x) + \Delta q(x), \quad (2.33)$$

which is more complicated since all three quantities are not diagonal in the same basis.

2.5 Transverse Momentum Dependent PDFs

Until now in our discussions the transverse motion of the quarks inside the nucleon was ignored in the calculations of the quark distribution functions. However, it is necessary to consider the transverse momentum p_T of the quarks, as it can influence the momentum of the outgoing hadron in the semi-inclusive DIS process (section 2.6) and can result in a non-zero single-spin asymmetries observed in many recent experiments. In the leading-twist, considering a non-zero p_T , there are eight different transverse momentum dependent (TMD) quark distributions functions as shown in Figure 2.7. If we integrate over p_T , only three out of eight distribution functions survive, namely, $q(x)$, $\Delta q(x)$ and $\delta q(x)$, which were introduced earlier:

$$q(x) = \int d^2\vec{p}_T q(x, p_T^2), \quad (2.34)$$

$$\Delta q(x) = \int d^2\vec{p}_T \Delta q(x, p_T^2), \quad (2.35)$$

$$\delta q(x) = \int d^2\vec{p}_T \left\{ h_{1T}^q(x, p_T^2) + \frac{p_T^2}{2M} h_{1T}^{\perp q}(x, p_T^2) \right\} \equiv \int d^2\vec{p}_T \delta q(x, p_T^2). \quad (2.36)$$

Figure 2.7 shows the illustration of the leading-twist TMDs along with their probabilistic interpretation. Big (small) circles represent the nucleon (quark) along with their spin orientations shown in arrows. The virtual photon direction is assumed to be going from the left side of the figure to the right side. If we consider a transversely (T) polarized nucleon, there is a certain probability of finding quarks with their spins aligned along the same direction of nucleon ($\delta q(x, p_T^2)$), or along a different direction ($h_{1T}^{\perp q}(x, p_T^2)$). In this case, it is also possible to have quarks longitudinally polarized ($g_{1T}^{\perp}(x, p_T^2)$). Similarly, other

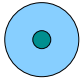
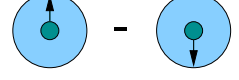
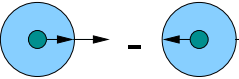
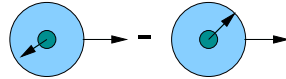
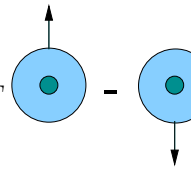
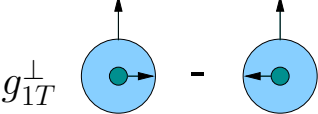
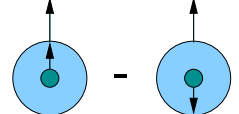
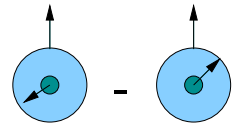
		quark		
		U	L	T
nucleon	U	q 		h_1^\perp 
	L		Δq 	h_{1L}^\perp 
	T	f_{1T}^\perp 	g_{1T}^\perp 	δq  h_{1T}^\perp 

Figure 2.7: Probabilistic interpretation of the leading-twist, transverse-momentum- dependent parton distribution functions, where U, L, and T indicate unpolarized, longitudinally polarized, and transversely polarized spins respectively. This figure is reproduced from [2].

situations are possible when the nucleon is either unpolarized or longitudinally polarized. All these different situations are possible due to non-vanishing \vec{p}_T .

In section 2.3 the derivation of the parton distribution function assumed time-reversal invariance. But if we relax this condition, then two additional terms in the vector (\mathcal{V}_μ) and axial (\mathcal{A}_μ) components of Φ arise, and these terms give rise to two p_T dependent T-odd distribution functions: f_{1T}^\perp , the *Sivers function*, and h_1^\perp , the *Boer-Moulders function*. The Sivers function is particularly interesting since it is related to the orbital angular momentum of the quarks inside the nucleon. It was first proposed by Sivers [53] to explain the non-zero single-spin asymmetries observed in the pion production in proton-proton scattering in which one of the proton beams was transversely polarized. It was shown in [31][32] that a non-zero Sivers function requires a non-vanishing orbital momentum of the quarks inside the nucleon. Time reversal-violating effects have not been observed in QCD, but the existence of quantities such as Sivers function, f_{1T}^\perp , are possible even though they are naïvely T-odd.

The time-reversal operation requires following condition on the quark-quark correlation

matrix, Φ [3]

$$\Phi^*(p, P, S) = \gamma_5 C \Phi(\tilde{p}, \tilde{P}, \tilde{S}) C^\dagger \gamma_5, \quad (2.37)$$

where $C = i\gamma^2\gamma^0$ and tilde four-vectors are defined as $p^\mu = (p^0, -\vec{p})$. A T-odd function would interchange initial and final state by changing the sign on the left hand side of Eq (2.37), which is not allowed in QCD. But inserting a path dependent gauge link operator \mathcal{L} between the quark fields in Φ would allow the existence of T-odd distribution functions.

$$\Phi_{ij}(p, P, S) = \int d^4\xi e^{ip\cdot\xi} \langle PS | \bar{\psi}_j(0) \mathcal{L}(0, \xi) \psi_i(\xi) | PS \rangle \quad (2.38)$$

This gauge link \mathcal{L} itself is required to satisfy the gauge invariance of the Φ . It is a bilocal operator connecting the quark fields in two different points in space and time,

$$\mathcal{L}(0, \xi) = \mathcal{P} \exp \left(-i\sqrt{4\pi\alpha_s} \int_0^\xi ds^\mu A_\mu(s) \right), \quad (2.39)$$

where \mathcal{P} indicates the path-ordering of the integral over gauge field A_μ . The gauge link acts through a soft-gluon exchange causing a final state interaction (FSI) between the struck quark and the target remnant [31]. Due to these interactions, the transformation back from final state to initial state is not trivial and cannot be achieved by imposing the condition in Eq (2.37). Therefore, T-odd simply means that the condition in Eq (2.37) is not satisfied, and not imply the violation of the time-reversal invariance. This is often referred to as a *naïvely T-odd* effect. While the standard time-reversal condition reverses the sign of both momentum(P) and spin(S) of the nucleon state, the naïve time-reversal only reverses the sign of the nucleon spin, keeping the momentum direction intact. However, unlike standard time-reversal, naïve time-reversal does not interchange the initial and final states. Hence any T-odd function, such as Sivers distribution function, can be non-zero due to this effect.

2.6 Semi-Inclusive DIS

In a semi-inclusive DIS process the electron scatters off a nucleon target via exchange of a photon with a high virtuality. As a result of this hard collision, the target breaks up and the final state consists of two well separated “regions” of particles - one consists of hadrons formed due to the hard interaction with the photon, known as *current fragments*, and the other consists of remnants of the target, known as *target fragments*. In semi-inclusive DIS, one of the outgoing hadrons from the current fragmentation region is detected in coincidence

with the scattered electron. This process is shown in Figure 2.8, where P_h and P_X are the momentum of the outgoing hadron(h) and rest of the target remnants (X) respectively. The fraction of energy transfer (ν) carried by the struck quark fragmenting to a hadron is given by

$$z = \frac{P \cdot P_h}{P \cdot q} = \frac{E_h}{\nu}, \quad (2.40)$$

and the magnitude of the transverse momentum (with respect to the virtual photon) is

$$P_{h\perp} \equiv \frac{|\vec{P}_h \times \vec{q}|}{|\vec{q}|}. \quad (2.41)$$

Ideally, in semi-inclusive DIS the energy fraction z of the detected hadron should be high enough to make sure that the hadron is in the current fragmentation region. There were reports of the cross section measurement in the inclusive electroproduction reaction, $e^- + p \rightarrow e^- + \pi^\pm + X$, and the measurement of hadron production in quark-fragmentation region, in experiments conducted more than three decades ago [54] [55]. These were some of the first measurements performed in this type of reactions and provided data for checking the predictions of the quark-parton model.

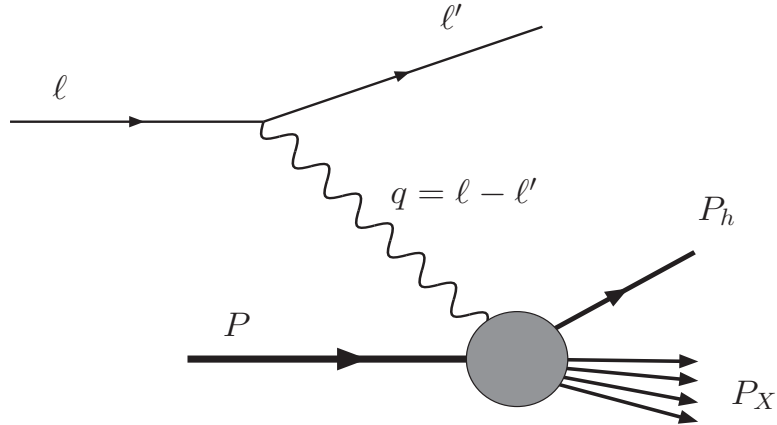


Figure 2.8: Semi-inclusive deep-inelastic scattering.

In the parton model this process can be described by an extended handbag diagram shown in Figure 2.9. The leptonic vertex of the SIDIS process is identical to that of the DIS process, therefore there is no change in the leptonic tensor ($L_{\mu\nu}$). However, the hadronic tensor ($W^{\mu\nu}$) now contains a new quark-quark correlation matrix $\Xi_{ij}(k, P_h, S_h)$, which is a function of struck quark's momentum (k), momentum (P_h) and spin (S_h) of the produced

hadron. We have

$$W^{\mu\nu} = \sum_{q\bar{q}} e_q^2 \int \frac{d^4 p}{(2\pi)^4} \int \frac{d^4 k}{(2\pi)^4} \delta^4(p+q-k) \text{Tr}[\Phi(p, P, S) \gamma^\mu \Xi(k, P_h, S_h) \gamma^\nu] \quad (2.42)$$

where

$$\Xi_{ij}(p, P_h, S_h) = \sum_X \int d^4 \xi e^{ik \cdot \xi} \langle 0 | \psi_i(\xi) | P_h S_h, X \rangle \langle P_h S_h, X | \bar{\psi}_j(0) | 0 \rangle \quad (2.43)$$

contains information about the *fragmentation* process in which the struck quark hadronizes into a final state particle that is detected. This is represented by the upper blob of the extended handbag diagram in Figure 2.9. Using the Dirac matrices introduced in section 2.3, the correlation function $\Xi(p, P_h, S_h)$ can be decomposed into fragmentation functions that depends on energy fraction z . However, in order to study the $P_{h\perp}$ distribution of the outgoing hadron, one has to account for the dependence of transverse momentum of the struck quark (k_T) in the fragmentation functions. Since, most of the time, the spin of the produced hadron is not measured we can sum over the spin (S_h) of the hadron, which results in two fragmentation functions – one is the unpolarized fragmentation function $D_1(z, z^2 k_T^2)$ and the other is the Chiral-odd Collins fragmentation function $H_1^\perp(z, z^2 k_T^2)$ [56].

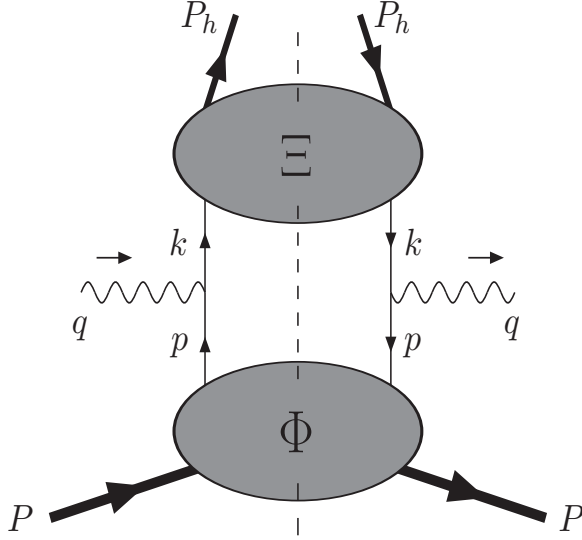


Figure 2.9: Diagram contributing to semi-inclusive DIS at LO. Figure reproduced from Ref.[3].

In terms of a probabilistic interpretation, $D_1(z, z^2 k_T^2)$ can be interpreted as the probability of a struck quark with transverse momentum k_T to fragment into a hadron with energy fraction z . Similarly the Collins function describes the fragmentation of a transversely polarized quark into an unpolarized hadron. The unpolarized fragmentation function is

chiral-even and T-even, whereas the Collins function is both chiral-odd and T-odd. Fragmentation functions can be T-odd due to the final-state interactions in the upper part of the extended handbag diagram shown in Fig 2.9.

2.6.1 Semi-Inclusive DIS cross-section

In general, the differential cross-section of the semi-inclusive DIS process depends on six different variables:

$$\frac{d^6\sigma}{dx dy dz d\phi_h d\phi_S dP_{\perp}^2} = \frac{\alpha^2 y}{8zQ^4} 2MW^{\mu\nu} L_{\mu\nu}, \quad (2.44)$$

where $P_{h\perp}$ is the transverse momentum of the produced hadron, ϕ_h is the azimuthal angle between the scattering plane, and hadron plane and ϕ_S is the azimuthal angle around the virtual photon between the target spin S_T and the scattering plane as shown in Fig 2.10. The angles are defined according to the Trento conventions [57]. These angles are very important in extracting different terms in the measured asymmetries.

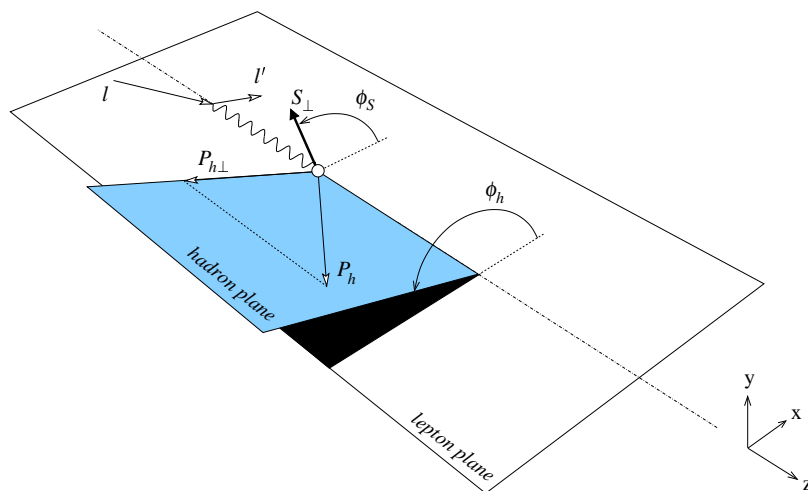


Figure 2.10: Definition of azimuthal angles for semi-inclusive deep inelastic scattering in the target rest frame. $P_{h\perp}$ and S_{\perp} are the transverse part of P_h and S with respect to the photon momentum.

In the single photon-exchange approximation, the lepton-hadron cross-section for semi-inclusive deep inelastic scattering can be expressed in terms of structure functions in a

model-independent way [58]:

$$\begin{aligned}
\frac{d\sigma}{dx dy d\psi dz d\phi_h dP_{h\perp}^2} = & \frac{\alpha^2}{xyQ^2} \frac{y^2}{2(1-\varepsilon)} \left(1 + \frac{\gamma^2}{2x}\right) \left\{ F_{UU,T} + \varepsilon F_{UU,L} + \sqrt{2\varepsilon(1+\varepsilon)} \cos\phi_h F_{UU}^{\cos\phi_h} \right. \\
& + \varepsilon \cos(2\phi_h) F_{UU}^{\cos 2\phi_h} + \lambda_e \sqrt{2\varepsilon(1-\varepsilon)} \sin\phi_h F_{LU}^{\sin\phi_h} \\
& + S_{\parallel} \left[\sqrt{2\varepsilon(1+\varepsilon)} \sin\phi_h F_{UL}^{\sin\phi_h} + \varepsilon \sin(2\phi_h) F_{UL}^{\sin 2\phi_h} \right] \\
& + S_{\parallel} \lambda_e \left[\sqrt{1-\varepsilon^2} F_{LL} + \sqrt{2\varepsilon(1-\varepsilon)} \cos\phi_h F_{LL}^{\cos\phi_h} \right] \\
& + |S_{\perp}| \left[\sin(\phi_h - \phi_S) \left(F_{UT,T}^{\sin(\phi_h - \phi_S)} + \varepsilon F_{UT,L}^{\sin(\phi_h - \phi_S)} \right) \right. \\
& + \varepsilon \sin(\phi_h + \phi_S) F_{UT}^{\sin(\phi_h + \phi_S)} + \varepsilon \sin(3\phi_h - \phi_S) F_{UT}^{\sin(3\phi_h - \phi_S)} \\
& \left. + \sqrt{2\varepsilon(1+\varepsilon)} \sin\phi_S F_{UT}^{\sin\phi_S} + \sqrt{2\varepsilon(1+\varepsilon)} \sin(2\phi_h - \phi_S) F_{UT}^{\sin(2\phi_h - \phi_S)} \right] \\
& + |S_{\perp}| \lambda_e \left[\sqrt{1-\varepsilon^2} \cos(\phi_h - \phi_S) F_{LT}^{\cos(\phi_h - \phi_S)} + \sqrt{2\varepsilon(1-\varepsilon)} \cos\phi_S F_{LT}^{\cos\phi_S} \right. \\
& \left. + \sqrt{2\varepsilon(1-\varepsilon)} \cos(2\phi_h - \phi_S) F_{LT}^{\cos(2\phi_h - \phi_S)} \right] \left. \right\}, \tag{2.45}
\end{aligned}$$

where the structure functions depend on x , Q^2 , z , and $P_{h\perp}^2$. The angle ψ is the azimuthal angle of ℓ' around the lepton beam axis with respect to an arbitrary fixed direction, which in the case of a transversely polarized target is the direction of S . For DIS kinematics $d\psi \equiv d\phi_S$. The first and second subscripts in the structure functions, $F_{UU,T}$, $F_{UU,L}$ and $F_{UT,T}^{\sin(\phi_h - \phi_S)}$, $F_{UT,L}^{\sin(\phi_h - \phi_S)}$ are beam and target polarization, respectively, while the third subscript indicates the polarization of the virtual photon. Also, λ_e denotes the helicity of the lepton beam, and ε is the ratio of the longitudinal to transverse photon fluxes, namely,

$$\varepsilon = \frac{1 - y - \frac{\gamma^2 y^2}{4}}{1 - y + \frac{y^2}{2} + \frac{\gamma^2 y^2}{4}}. \tag{2.46}$$

The structure functions appearing in Eq.(2.45) can be extracted by comparing them with the full expression of the cross section in Eq. (2.44) after substituting the expressions for the leptonic and hadronic tensors. In this experiment the beam is unpolarized, and the target is transversely polarized. From Eq.(2.45) we can see that a total of five terms are

associated with this situation (terms with subscript UT). In leading twist only three terms survive. The expressions for these structure functions are shown below:

$$F_{UT}^{\sin(\phi_h + \phi_S)} = \mathcal{C} \left[-\frac{\hat{P}_{h\perp} \cdot \vec{k}_T}{M_h} \delta_q H_1^\perp \right], \quad (2.47)$$

$$F_{UT,T}^{\sin(\phi_h - \phi_S)} = \mathcal{C} \left[-\frac{\hat{P}_{h\perp} \cdot \vec{p}_T}{M} f_{1T}^\perp D_1 \right], \quad (2.48)$$

and

$$F_{UT}^{\sin(3\phi_h - \phi_S)} = \mathcal{C} \left[\frac{2(\hat{P}_{h\perp} \cdot \vec{p}_T)(p_T \cdot \vec{k}_T) + p_T^2(\hat{P}_{h\perp} \cdot \vec{k}_T) - 4(\hat{P}_{h\perp} \cdot \vec{p}_T)^2(\hat{P}_{h\perp} \cdot \vec{k}_T)}{2M^2 M_h} h_{1T}^\perp H_1^\perp \right], \quad (2.49)$$

where $\hat{P}_{h\perp} = \frac{P_{h\perp}}{|P_{h\perp}|}$. Here the following notations is introduced [2]:

$$\mathcal{C}[\mathcal{W} dF] = x \sum_{q\bar{q}} e_q^2 \mathcal{I}[\mathcal{W} dF], \quad (2.50)$$

where

$$\mathcal{I}[\mathcal{W} dF] = \int d^2\vec{p}_T d^2\vec{k}_T \delta^{(2)}(\vec{p}_T - \vec{k}_T - \vec{P}_{h\perp}/z) \mathcal{W}(\vec{p}_T, \vec{k}_T) d_q(x, p_T^2) F_q(z, z^2 k_T^2) \quad (2.51)$$

\mathcal{W} is an arbitrary function and d_q and F_q are the distribution and fragmentation functions, respectively. The expressions for the other structure functions associated with different combinations of beam and target polarization terms are given in Ref.[58].

Now substituting the expressions for structure functions from Eq.(2.47) through Eq.(2.49) (and the ones with different combinations of beam and target polarization that are not shown here), the expression for differential cross-section, Eq.(2.45), can be rewritten as

$$d^6\sigma = d^6\sigma_{UU} + d^6\sigma_{LU} + d^6\sigma_{UL} + d^6\sigma_{LL} + d^6\sigma_{UT} + d^6\sigma_{LT}. \quad (2.52)$$

In principle, by using different combinations of beam and target polarizations, each term⁴ in the above differential equation can be measured. The two terms most relevant to this thesis are the ones with unpolarized beam and transversely polarized target and we will consider this combination for the rest of the discussion, namely,

$$d^6\sigma_{UT} = \frac{2\alpha^2}{sxy^2} |\vec{S}_T| B(y) \sin(\phi_h + \phi_S) \sum_{q\bar{q}} e_q^2 \mathcal{I} \left[\frac{\vec{k}_T \cdot \hat{P}_{h\perp}}{M_h} \delta_q(x, p_T^2) H_1^{\perp q}(z, z^2 k_T^2) \right] \quad (2.53)$$

⁴U = Unpolarized, L = Longitudinally polarized, and T = Transversely polarized, so that UT means an unpolarized beam and transversely polarized target.

where

$$B(y) = \left(1 - y - \frac{y^2\gamma^2}{4}\right) \frac{1}{1 + \gamma^2}. \quad (2.54)$$

Note that the product of transversity and the Collins fragmentation function has a $\sin(\phi_h + \phi_S)$ modulation. The other term is,

$$d^6\sigma_{UT} = \frac{2\alpha^2}{sxy^2} |\vec{S}_T| A(y) \sin(\phi_h - \phi_S) \sum_{q\bar{q}} e_q^2 \mathcal{I} \left[\frac{\vec{p}_T \cdot \hat{P}_{h\perp}}{M_h} f_{1T}^{\perp q}(x, p_T^2) D_1^q(z, z^2 k_T^2) \right], \quad (2.55)$$

where

$$A(y) = \left(1 - y + \frac{y^2}{2} - \frac{y^2\gamma^2}{4}\right) \frac{1}{1 + \gamma^2}. \quad (2.56)$$

The product of the Sivers distribution function and the unpolarized fragmentation function is modulated by $\sin(\phi_h - \phi_S)$.

2.7 Single Spin Asymmetries and Azimuthal Moments

In order to study the azimuthal distribution of the detected hadron, whose spin is not measured, it is convenient to measure the semi-inclusive DIS cross section asymmetries instead of absolute cross-sections. When the difference of cross sections is measured with opposite target spin states, for example, many uncertainties associated with the detectors cancel out. We have already seen that in the equation for $d\sigma_{UT}$, the Collins and Sivers functions are modulated by $\sin(\phi_h + \phi_S)$ and $\sin(\phi_h - \phi_S)$, respectively. This can cause an observable *Single Spin Asymmetry* (SSA) which is defined as the difference in the count rate of produced hadrons in opposite target spin states divided by the sum. For example, for an unpolarized beam and a transversely polarized target,

$$A_{UT} = \frac{1}{\langle P \rangle} \frac{d\sigma_{U\uparrow}^6 - d\sigma_{U\downarrow}^6}{d\sigma_{U\uparrow}^6 + d\sigma_{U\downarrow}^6}, \quad (2.57)$$

where $\langle P \rangle$ is the average target polarization and the arrows indicate opposite target spin directions. This asymmetry is usually expressed as azimuthal moments, for example, for the Collins moment it reads,

$$\langle \sin(\phi_h + \phi_S) \rangle_{UT}^h = -|\vec{S}_T| \frac{\frac{1}{xy^2} B(y) \sum_{q\bar{q}} e_q^2 \int d^2\vec{P}_{h\perp} \left[\frac{\vec{k}_T \cdot \hat{P}_{h\perp}}{M_h} \delta q(x, p_T^2) H_1^{\perp q}(z, z^2 k_T^2) \right]}{2 \frac{1}{xy^2} A(y) \sum_{q\bar{q}} e_q^2 q(x) D_1^q(z)}, \quad (2.58)$$

and for the Siver moment it is,

$$\langle \sin(\phi_h - \phi_S) \rangle_{UT}^h = -|\vec{S}_T| \frac{\frac{1}{xy^2} A(y) \sum_{q\bar{q}} e_q^2 \int d^2 \vec{P}_{h\perp} \mathcal{I} \left[\frac{\vec{p}_T \cdot \vec{P}_{h\perp}}{M_h} f_{1T}^{\perp q}(x, p_T^2) D_1^q(z, z^2 k_T^2) \right]}{2 \frac{1}{xy^2} A(y) \sum_{q\bar{q}} e_q^2 q(x) D_1^q(z)}. \quad (2.59)$$

Both these moments can be non-zero and these are known as the *Collins effect* and the *Sivers effect*, respectively. Note that the kinematical term $\frac{1}{xy^2} A(y)$ does not cancel because both the numerator and denominator are integrated separately over certain x and y ranges.

To obtain information on the products $\delta q(x, p_T^2) H_1^{\perp q}(z, z^2 k_T^2)$ and $f_{1T}^{\perp q}(x, p_T^2) D_1^q(z, z^2 k_T^2)$ in Eqs. (2.58) and (2.59), the convolution integral \mathcal{I} has to be factorized, which is not possible due to the factors $\mathcal{W} = \vec{k}_T \cdot \vec{P}_{h\perp}/M_h$ for the Collins function and $\mathcal{W} = \vec{p}_T \cdot \vec{P}_{h\perp}/M$ for the Sivers function. In order to factorize this integral one has to assume transverse momentum dependence of the distribution and fragmentation functions. Usually a Gaussian distribution is assumed for both p_T and K_T , where $\vec{K}_T = -z\vec{k}_T$ [59]. Therefore,

$$\delta q(x, p_T^2) \approx \frac{\delta q(x)}{\pi \langle p_T^2(x) \rangle} e^{-\frac{p_T^2}{\langle p_T^2(x) \rangle}} \quad H_{1T}^{\perp}(z, K_T^2) \approx \frac{H_{1T}^{\perp}(z)}{\pi \langle K_T^2(z) \rangle} e^{-\frac{K_T^2}{\langle K_T^2(z) \rangle}}, \quad (2.60)$$

where $\langle p_T^2(x) \rangle = \int d^2 \vec{p}_T p_T^2 q(x, p_T^2)/q(x)$ and $\langle K_T^2(z) \rangle = \int d^2 \vec{K}_T K_T^2 D_1(z, K_T^2)/D_1(z)$, and the integration yields the following expressions for the Collins and Sivers moments:

$$\langle \sin(\phi_h + \phi_S) \rangle_{UT}^h = -\frac{|\vec{S}_T|}{\sqrt{1 + z^2 \langle p_T^2 \rangle / \langle K_T^2 \rangle}} \frac{\frac{1}{xy^2} B(y) \sum_{q\bar{q}} e_q^2 \delta q(x) H_1^{\perp(1/2)q}(z)}{\frac{1}{xy^2} A(y) \sum_{q\bar{q}} e_q^2 q(x) D_1^q(z)}, \quad (2.61)$$

and

$$\langle \sin(\phi_h - \phi_S) \rangle_{UT}^h = -\frac{|\vec{S}_T|}{\sqrt{1 + \langle K_T^2 \rangle / (z^2 \langle p_T^2 \rangle)}} \frac{\frac{1}{xy^2} A(y) \sum_{q\bar{q}} e_q^2 f_{1T}^{\perp(1/2)q}(x) D_1^q(z)}{\frac{1}{xy^2} A(y) \sum_{q\bar{q}} e_q^2 q(x) D_1^q(z)}. \quad (2.62)$$

2.7.1 Collins Effect

As mentioned in section 2.4 the transversity distribution is a chiral-odd object and cannot be measured in inclusive DIS processes. We need another chiral-odd object, like the Collins function, to make the product of the two a chiral-even (Eq. (2.58)) quantity, which gives rise to the observable effects. When a transversely polarized quark fragments into a hadron, the structure of the outgoing jet is sensitive to the polarization of the quark. In particular, the Collins function can lead to an azimuthal asymmetry of the detected hadrons around

the direction of the transversely polarized quark. Thus the combination of the transversity and the Collins function gives rise to a correlation between the transverse target spin and the transverse momentum of the produced hadron. Also, the associated asymmetries are proportional to $\sin(\phi_h + \phi_S)$, which can be used to extract the product of transversity and the Collins fragmentation. In order to extract the transversity distribution function itself, the knowledge of the fragmentation function is required. Fragmentation functions are expected to be universal, *i.e.*, independent of both the process and target [60]. For example, the distribution of the hadrons in the jets produced in $e^+e^- \rightarrow \text{hadrons}$ is described by the same fragmentation functions that describe the jets in DIS. Therefore, we can extract transversity using the knowledge of the Collins fragmentation function from the $e^+e^- \rightarrow \text{hadrons}$ process.

2.7.2 Siverts Effect

An entirely different mechanism, known as the Siverts effect (introduced in section 2.5), can also contribute to the azimuthal asymmetries in semi-inclusive DIS. In particular, it arises from the correlations between the transverse spin of the target nucleon (S_T) and the intrinsic transverse momentum (p_T) of the unpolarized quark inside the nucleon. Both these quantities are in the transverse direction with respect to the nucleon momentum (\hat{P}) in the infinite momentum frame. Note that \hat{P} is a unit vector opposite to the direction of the virtual-photon direction. Thus, the Siverts function is proportional to term $(P \times p_T) \cdot S_T$, which makes it naïvely T-odd so that it would vanish in the naïve parton model. But it was realized that a final state interaction (FSI) mediated by soft gluon(s) between the struck quark and the remainder of the target nucleon, before the quark fragments into hadron, could avoid this restriction [31] [61] and produce a non-zero single-spin asymmetry. It has also been shown that the quark Siverts function in the SIDIS process and in the Drell-Yan (DY) processes must have opposite signs, a time-reversal modified universality [61], namely,

$$f_{1T}^\perp(x, p_T^2)_{SIDIS} = -f_{1T}^\perp(x, p_T^2)_{DY}. \quad (2.63)$$

In [62] this relation was derived for both quark and gluon Siverts function from the parity and time-reversal invariance of QCD. The asymmetry in DY processes arises from initial state interactions (ISI) between the incoming antiquark and the target. If this relation is experimentally verified, it provides a test of the current understanding of the Siverts function

within QCD.

2.7.3 Recent SIDIS Data With Transversely Polarized Targets

Currently there is very limited data on the semi-inclusive DIS measurements with transversely polarized targets. The first measurement was reported by HERMES experiment [34][33]. They used positron beams on proton targets to measure the SIDIS cross section difference and extracted the Sivers and Collins moments. The other measurement is from the COMPASS experiment, which used a higher energy muon beam on deuteron and proton targets [36] [35].

Figure 2.11 shows a clear non-zero signal for the Collins moment measured by the HERMES experiment. Moreover, the π^+ and π^- asymmetries have an opposite signs. In contrast to this, the Collins moment measured by COMPASS is consistent with zero (Figure 2.12). Apparently the contributions from proton and neutron in the deuteron target cancels and results in a zero asymmetry.

The HERMES Sivers moment is shown in Figure 2.13 for both pions and kaons. There is a clear positive and non-zero signal for π^+ and K^+ , whereas the for negatively charged mesons it is zero. In the case of COMPASS deuteron target, all the amplitudes are consistent with zero as shown in Figure 2.14.

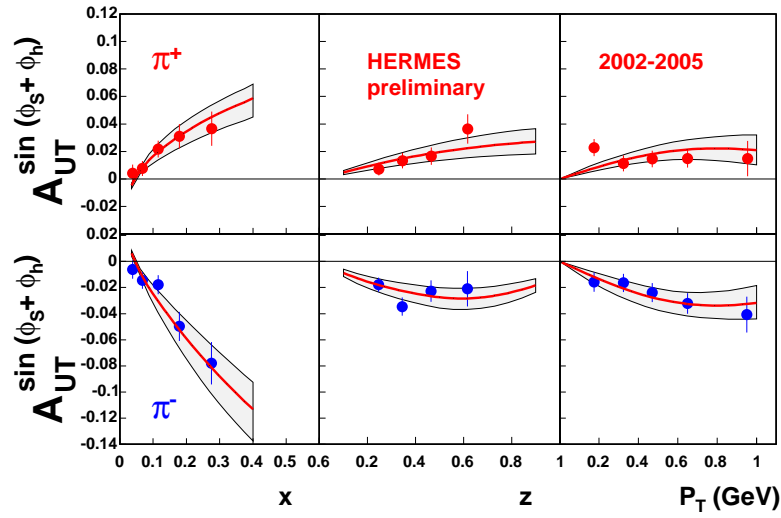


Figure 2.11: Collins amplitudes obtained from the SIDIS data on a transversely polarized proton target [4] as a function of x , z and p_T . The error bars indicate the statistical uncertainty, and there is an additional 8% scale uncertainty. The curves are fit to the data as described in Ref. [5]. The figure is taken from Ref. [5].

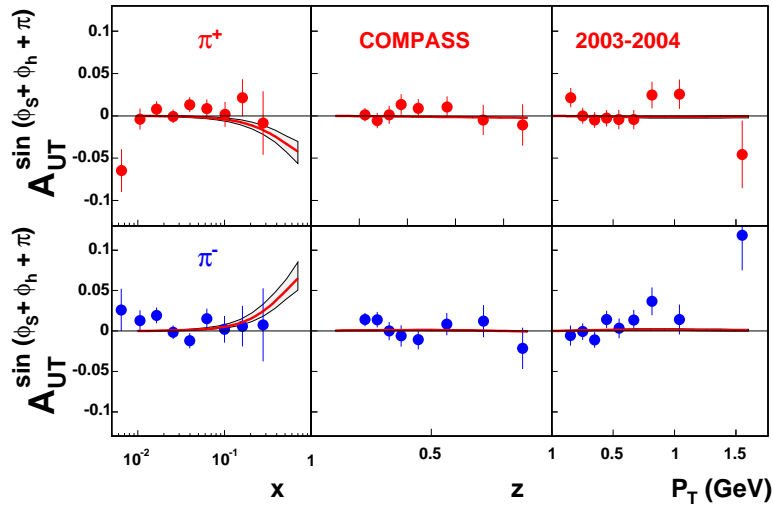


Figure 2.12: Collins amplitudes obtained from the SIDIS data on a transversely polarized deuteron target [6] as a function of x , z , and p_T . The error bar indicates the statistical uncertainty. The curves are fit to the data as described in [5]. The Figure is taken from Ref. [5].

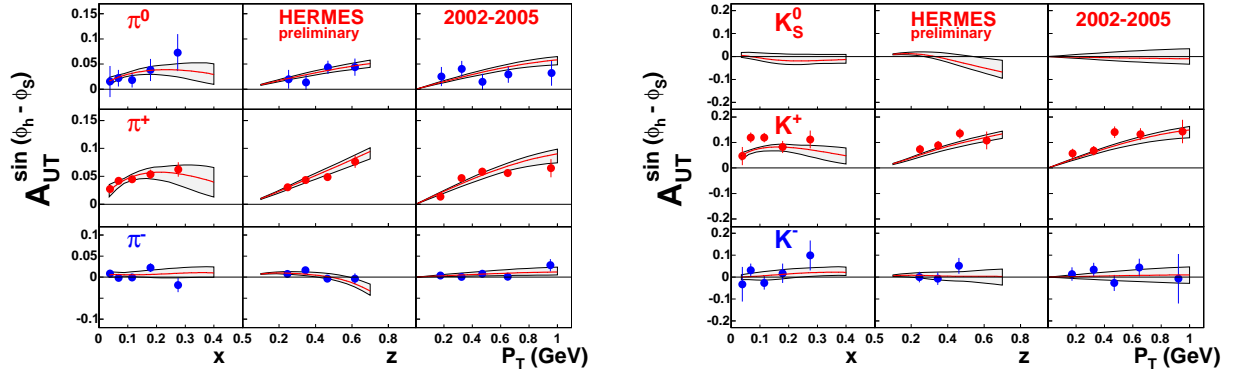


Figure 2.13: Sivers amplitudes obtained from the SIDIS data on transversely polarized proton target [4] as a function of x , z and p_T . The error bar indicates the statistical uncertainty and there is an additional 8% scale uncertainty. The curves are fit to the data as described in [5]. The Figure is taken from [5].

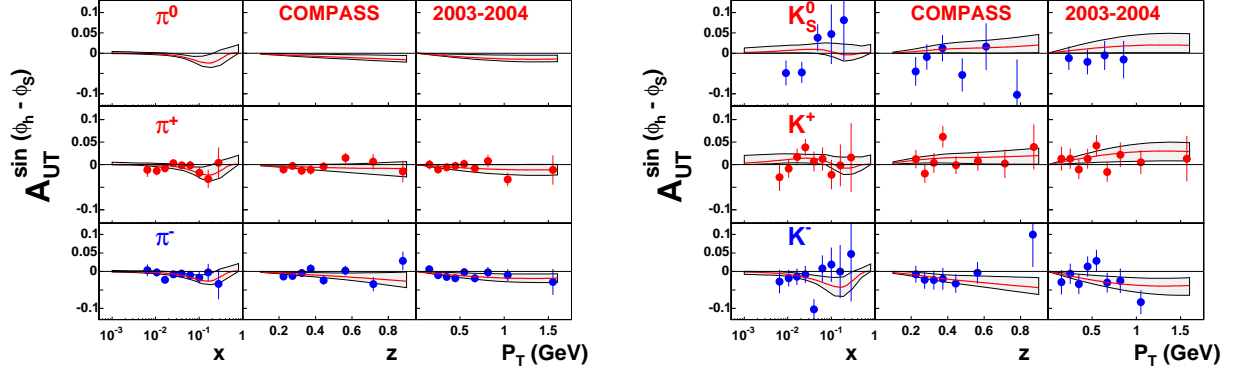


Figure 2.14: Sivers amplitudes obtained from the SIDIS data on transversely polarized deuteron target [6] as a function of x , z and p_T . The error bar indicates the statistical uncertainty. The curves are fit to the data as described in [5]. The Figure is taken from [5].

CHAPTER 3: E06-010 EXPERIMENT IN HALL A

Experiment E06-010 was performed in Hall A at Jefferson Lab, which is located in Newport News, Virginia. This experiment took data during the time period lasting from September 2008 to Feb 2009. The aim of the experiment was to measure single target-spin asymmetries in $n^\uparrow(e, e'\pi^{+/-}/K^{+/-})X$ semi-inclusive DIS reactions using a transversely polarized ^3He target. The ^3He target served as an effective neutron target. By looking at the ϕ_S and ϕ_h angular dependence of these measured asymmetries, one can extract the Sivers and Collins moments. This thesis will report on the extraction of these moments for single spin asymmetries (SSA) in the $n^\uparrow(e, e'\pi^+)X$ channel. A 5.9 GeV beam was used for this experiment. E06-010 is a coincidence experiment where two particles are detected in coincidence in two spectrometers placed on either side of the target. The scattered electrons were detected using a large acceptance BigBite spectrometer and the outgoing hadrons (π/K) were detected in the High Resolution Spectrometer(HRS), which has a smaller acceptance. Polarized ^3He gas was used as the target, with an ability to rotate the spin of the ^3He in all four mutually perpendicular directions with respect to the incoming beam direction, thereby increasing the angular coverage.

In this chapter the description of the experimental technique along with detailed setup of the experimental apparatus is discussed. This will also cover the methods involved in polarizing the target, description of the detector setup, and the data acquisition system used for the experiment.

3.1 Experimental Technique

In leading twist, the differential cross section for a SIDIS reaction $n(e, e'h)X$ is given by the sum of beam and target spin dependent and spin independent terms, as shown in Eq.(2.52). The unpolarized beam and transversely polarized target term (σ_{UT}) can be split further into three terms in the leading order (neglecting higher-twist terms),

$$d^6\sigma_{UT} = d^6\sigma_{UT}^{\sin(\phi_h+\phi_S)} + d^6\sigma_{UT}^{\sin(\phi_h-\phi_S)} + d^6\sigma_{UT}^{(3\phi_h-\phi_S)}. \quad (3.1)$$

Each of these terms in the above equation can be written as a convolution of the parton density and a fragmentation function, which are functions of x and z , respectively.

$$d\sigma_{UU} = \frac{4\pi\alpha^2 s}{Q^2} (1 - y + \frac{y^2}{2}) \sum_q e_q^2 [f_1^q \otimes D_1^q] \quad (3.2)$$

$$d\sigma_{UT}^{\sin(\phi_h + \phi_S)} = \frac{4\pi\alpha^2 s}{Q^2} |S_T| (1 - y) \sin(\phi_h + \phi_S) \sum_q e_q^2 [h_1^q \otimes H_1^{\perp q}] \quad (3.3)$$

$$d\sigma_{UT}^{\sin(\phi_h - \phi_S)} = \frac{4\pi\alpha^2 s}{Q^2} |S_T| (1 - y + \frac{y^2}{2}) \sin(\phi_h - \phi_S) \sum_q e_q^2 [f_{1T}^{\perp q} \otimes D_1^q] \quad (3.4)$$

$$d\sigma_{UT}^{(3\phi_h - \phi_S)} = \frac{4\pi\alpha^2 s}{Q^2} |S_T| (1 - y) \frac{P_{h\perp}^2}{6z^2 M_N^2} \sin(3\phi_h - \phi_S) \sum_q e_q^2 [h_{1T}^{\perp q} \otimes H_1^{\perp q}], \quad (3.5)$$

where the the symbol \otimes represents the convolution over the transverse momentum of the initial quark (k_T) and final quark (p_T) fragmenting into a hadron with appropriate weighting [3].

a target single spin asymmetry can be defined as,

$$A_{UT} = \frac{1}{|S_T|} \frac{d\sigma(\phi_h, \phi_S) - d\sigma(\phi_h, \phi_S + \pi)}{d\sigma(\phi_h, \phi_S) + d\sigma(\phi_h, \phi_S + \pi)}, \quad (3.6)$$

where the angles are defined as shown in Figure 2.10. By rotating the spin of the target by 180° and taking the cross section difference between the two states (ϕ_S and $\phi_S + \pi$) normalized by the sum of the cross sections, one can measure the above asymmetry. Since each term in Eqs. (3.3) to (3.5) has a different angular dependence, we can separate them by binning the asymmetry in two dimensions of ϕ_h and ϕ_S angles and performing a simultaneous two-dimensional fit using all three spin terms,

$$A_{UT}(\phi_h, \phi_S) = A_{UT}^{\sin(\phi_h + \phi_S)} \sin(\phi_h + \phi_S) + A_{UT}^{\sin(\phi_h - \phi_S)} \sin(\phi_h - \phi_S) + A_{UT}^{\sin(3\phi_h - \phi_S)} \sin(3\phi_h - \phi_S) \quad (3.7)$$

Since this experiment has limited angular coverage, the target spin is rotated into two configurations - *vertical* and *transverse*. The target is "vertical" when the polarization direction is normal to the scattering plane (pointing upwards or downwards) and it is "transverse" when the polarization direction is 90° in-plane (either left or right side).

This type of measurement assumes the leading order naïve x - z separation in the SIDIS reaction. It has been proved by X. Ji *et al.* [63] that QCD factorization works for a hadron emitted in the current fragmentation region with low transverse momentum $P_{\perp h} \ll Q$. QCD factorization for spin-dependent cross-sections in SIDIS has also been proved for the

low $P_{\perp h}$ case [64]. Also, recent data from JLab suggest that the assumption of leading order naïve x - z separation, where the parton distributions and fragmentation functions are factorized, works reasonably well at 6 GeV beam energy for $z < 0.65$ [65]. In our experiment the average z value is about 0.5.

3.2 Experimental Setup

This experiment used a 5.9 GeV polarized electron beam provided by the electron accelerator at Jefferson Lab. Although, this experiment does not require a polarized beam since it is measuring A_{UT} , the data were taken with a polarized beam to accommodate other parasitic measurements looking for A_{LT} asymmetries. This section describes the experimental setup used for E06-010 with a detailed description of the spectrometers and the polarized target.

3.2.1 CEBAF at Jefferson Lab

The Continuous Electron Beam Accelerator Facility (CEBAF) at Jefferson Lab delivers a continuous electron beam with very high polarization (usually around $\sim 85\%$) into three experimental Halls A, B, and C. The total beam current can reach more than $100 \mu\text{A}$, but usually Halls A and C run with high currents and Hall B runs at a current of less than 100 nA . The accelerator consists of two superconducting radio frequency linear accelerators joined by magnetic recirculating arcs (Figure 3.1).

Polarized electrons are produced by shining a circularly polarized laser light on a gallium arsenide (GaAs) photo-cathode. The photons from the laser excite the electrons in the valence band to the conduction band of the GaAs. These electrons from the conduction band are extracted by applying a voltage of -100 kV to the photo-cathode. The electrons enter the injector where they are accelerated to about 67 MeV before entering the North Linac. At the end of the North Linac, the electron beam is deflected by 180° using bending magnets to South Linac. Each Linac consists of 20 superconducting cryomodules and the beam gains about 600 MeV energy passing through one Linac. At the end of South Linac beam is bent again by 180° to enter the North Linac again. This recirculation of the beam can be done up to five times in order to achieve a maximum of beam energy of $\sim 6 \text{ GeV}$. After each pass (one fully circulated beam), the radio frequency separator located in the beamline can be activated to extract every third beam bunch, sending one pulse to each of

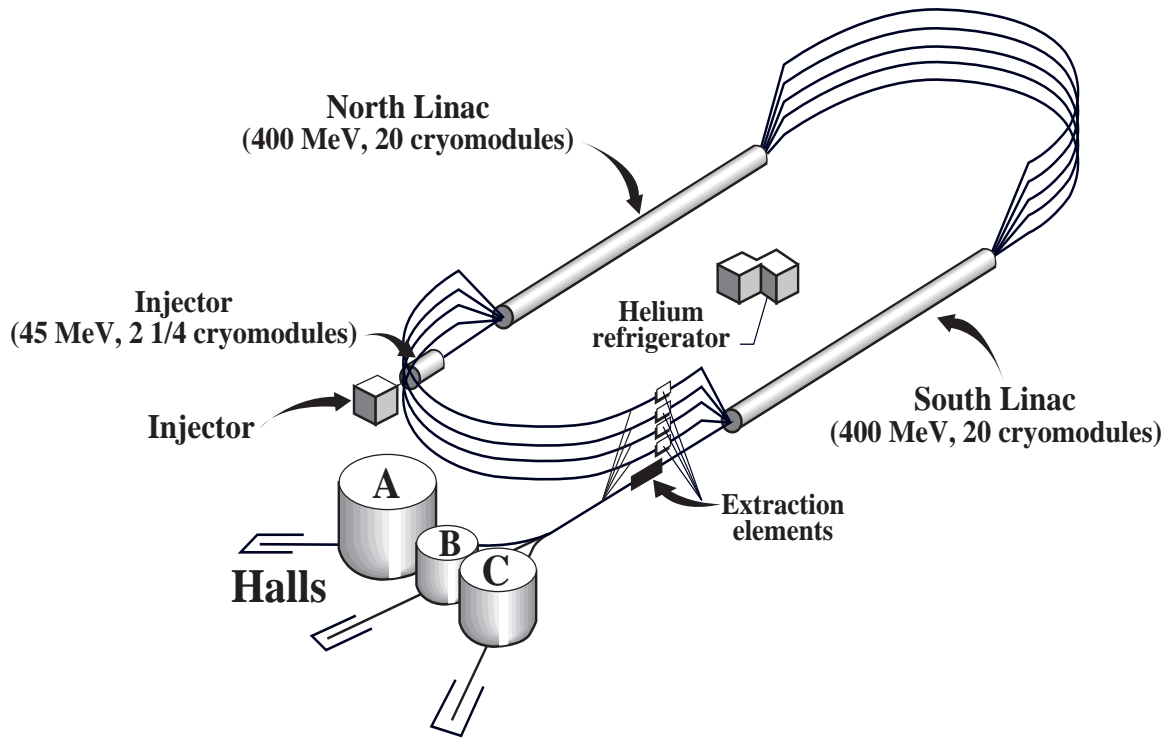


Figure 3.1: Layout of Continuous Electron Beam Accelerator Facility [7]

the three experimental halls.

3.2.2 Hall A Beamline

Beam Current Monitors

Beam Current Monitors (BCMs) are used for determining the current and integrated charge over a period of time. These monitors consist of RF cavities that are tuned to the beam pulse frequency (1497 MHz)[7]. The output of the cavities is an RF signal which is then converted to a voltage signal proportional to the beam current. They are located 25 m upstream of the target. An Unser monitor, to measure the absolute current, is situated between the two BCM cavities. This can be used to calibrate the BCMs, but due to drift in the Unser signal over a period of time, it is usually not used. Instead a Faraday cup is used to calibrate the BCMs [66]. The output of the RF cavities is a voltage signal, which is sent to a Voltage-to-Frequency(V-to-F) converter and also to a high precision voltmeter for continuous updating (monitoring) and recording of the current. The signal coming out of the V-to-F converter is a frequency signal which is sent to three different sets of amplifiers (with gains of 1, 3, and 10). The amplified signal is sent to a high frequency VME scaler.

The VME scaler records the counts from these frequency signals. The corresponding output from the scaler is proportional to the accumulated charge during that run.

The calibration of the BCM signals involves finding the relation between the scaler counts corresponding to a particular BCM signal (1X, 3X, or 10X gain) and the actual beam current.

$$\text{Avg_current} = \frac{\frac{\text{scaler_counts}}{\text{time}} - \text{offset}}{\text{constant}} \quad (3.8)$$

This can be done by special BCM runs where the beam current is stepped up many times within a run. During this run, the beam current value provided by the accelerator group (known as OLO2 current) and the corresponding scaler counts for every BCM signal are recorded in the datastream. There are two BCM monitors, one located upstream of the target and other downstream of the target. Figure 3.2 shows an example plot for the downstream BCM signal with a gain factor of three. The left side panel shows the OLO2 current values at various times during the run, and right side panel shows the corresponding scaler counts for each of those beam currents. Once this information is known, a straight line is fitted to the scaler counts vs. OLO2 current values (Figure 3.3). The slope of this fit gives the BCM calibration *constant*. The scaler *offset* can be found by recording the scaler count rate when there is no beam. The *time* in Eq. 3.8 is the total time duration for the run. Tables 3.1 and 3.2 show the BCM calibration constants and scaler offsets obtained during two calibration runs taken during the experiment. The signal on the upstream BCM with a gain of ten was missing during the October 2008 run.

Table 3.1: BCM calibration constants for both upstream and downstream signals determined during two different measurements. They are expressed in the units of counts/ μA

Date	U1	U3	U10	D1	D3	D10
Feb 2009	2101.87	6464.39	19718.30	2147.88	6645.89	20952.00
Oct 2008	2077.56	6390.79	-	2162.85	6696.15	21120.68

Beam Position Monitors

Beam position information is recorded using two Beam Position Monitors (BPMs) located about 7.5 m and 1.3 m upstream of the target. Each monitor consists of four wire antennae parallel to the direction of the beam and tuned to the beam RF frequency. These wires are

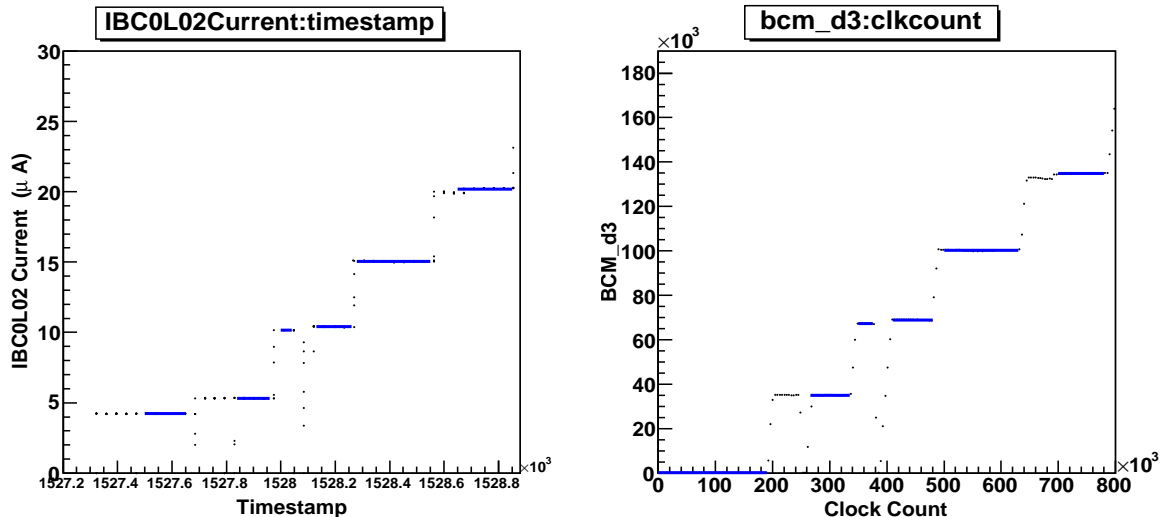


Figure 3.2: Panel on the left(right) shows the current (BCM downstream scaler counts) vs. time for different current settings in the calibration run.

Table 3.2: BCM scaler offsets for both upstream and downstream signals determined during two different measurements. They are expressed in the units of counts/ μA

Date	U1	U3	U10	D1	D3	D10
Feb 2009	395.80	453.40	770.52	154.58	133.32	293.46
Oct 2008	369.84	406.98	-	157.80	111.66	307.73

positioned at $\pm 45^\circ$ relative to the horizontal and vertical direction in the Hall. The signal induced in these wires by the beam is recorded in ADCs. This signal is inversely proportional to the distance of the wire from the beam position. By looking at the difference in the signal from two wires, the relative beam position can be determined at a level of $100 \mu\text{m}$. Signals from BPMs can be calibrated using harps (wire scanners). These are situated adjacent to the BPMs. A harp scan is an invasive procedure where the wires are scanned across the electron beam resulting in scattered particles, which are detected. Since the harps are surveyed, their positions are known and thus the BPMs can be calibrated with the harps.

Raster

The beam is rastered in order to avoid any local overheating of the target cell. It involves producing small deviations (few millimeters) in the beam position at the target. This is achieved by two raster dipole magnets (horizontal and vertical) located 23 m upstream

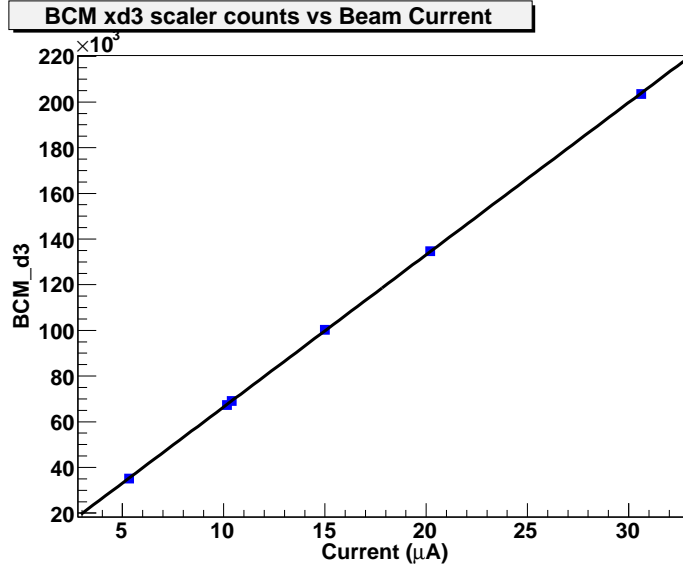


Figure 3.3: Downstream BCM x3 scaler counts vs current. The slope of this plot gives the BCM calibration constant.

of the target. They produce a small transverse magnetic field which the beam passes through. This results in small deviations in the beam position in both directions at the target location. The magnet currents are recorded in the datastream for each event. These currents are useful in extracting the the exact beam positions from the recorded data.

BPMs are slow in measuring the position of the beam at the time when the electron actually hits the target. They have a delay of the order of a few microseconds. The raster magnets have much smaller delay, and can be used to determine the positions directly. The calibration of raster involves finding the transformation coefficients and offsets for converting the raster currents to actual beam positions. This is done using the averaged beam position information from BPMs and raster currents recorded in the ADCs.

Beam Energy

The Beam energy information was provided by the accelerator group. It is determined using arc energy measurements [67]. The basic idea is to measure the deflection angle of the beam in the 40 m arc section of the beamline in a known magnetic field. The momentum of the electron deflected by the magnetic field is related to the field integral of the dipoles and the angle of deflection through the arc by the following Eq:

$$p = k \frac{\int \vec{B} \cdot d\vec{l}}{\theta}, \quad (3.9)$$

where $k = 0.299792 \text{ GeV rad T}^{-1} \text{ m}^{-1}/c$ and the nominal bend angle in the arc section is about 34.3° . There is non-invasive way to monitor the beam energy using a Tiefenbach energy measurement [68]. This method uses the relation between the field integral value and the set current in the dipole magnets in the arc section of the accelerator. The energy from this method is accurate to a level of $5 \times 10^{-4} \text{ GeV}$.

3.2.3 Polarized ^3He Target

Free neutrons are unstable and decay quickly (885.7 ± 0.8 seconds¹) into a proton [1], electron and an electron anti-neutrino, known as beta decay. Therefore it is necessary to find an alternative source of neutron targets with sufficient density for performing scattering experiments. One such candidate is helium-3 (^3He). When a ^3He gas is polarized, about $\sim 90\%$ of the polarization is carried by the symmetric S state of the neutron, about $\sim 1.5\%$ is carried by the S' state, and $\sim 8\%$ is carried by the D state. Figure 3.4 shows the contribution of the different states to the spin of the ^3He nucleus. In the S state, the two protons, being in opposite spin states, cancel their spins and the neutron effectively carries the ^3He spin. Therefore, most of the time a polarized ^3He nucleus acts as an effective neutron target. However, there is a small contribution from proton polarization of about $\sim 3\%$ which must be taken into account in the calculation of the asymmetries from the SIDIS event sample. The polarization of the target is measured using two standard techniques - Nuclear Magnetic Resonance (NMR) and Electron Paramagnetic Resonance (EPR). Polarized ^3He targets have been previously used in many experiments around the world. For example, Hall A experiments at JLab, the HERMES experiment at DESY, at SLAC, and at MAMI (Mainz). This section describes the basic principles involved in polarizing the ^3He target and methods to measure the polarization, along with target setup during the E06-010 experiment.

Polarization Method

The polarization of the ^3He gas was achieved by the Hybrid Spin Exchange Optical Pumping (HSEOP) method. This is a three step process where first, Rb atoms are polarized using circularly polarized laser light of 795 nm wavelength, corresponding to the $^5S_{1/2} \rightarrow ^5P_{1/2}$ (D1) transition of the Rb atoms. Second, the polarization of Rb atoms is transferred to

¹Recently Serebrov *et al.*, have reported a more accurate result of the neutron lifetime. They obtained a value of $878.5 \pm 0.7_{stat} \pm 0.3_{sys}$ [69].

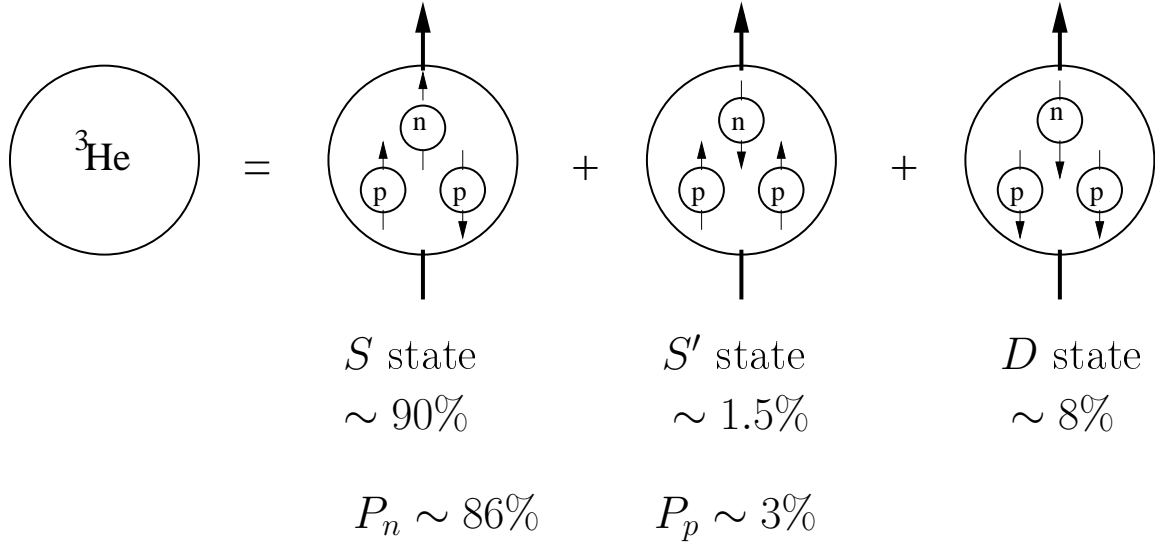


Figure 3.4: Contribution from different ground state wavefunctions to the ${}^3\text{He}$ nucleus. The Big (small) arrows indicate the polarization direction of the nucleus (nucleons).

potassium atoms through spin-exchange in binary collisions, and finally the polarization is transferred to the ${}^3\text{He}$ nuclei via hyperfine interaction between Rb/K electrons and the ${}^3\text{He}$ nuclei.

Optical Pumping

Figure 3.5 shows the optical pumping process in the Rb atom. This process is governed by angular momentum selection rules. If we ignore the effects of the nuclear spin of the Rb atom, the energy levels of the Rb atom placed in a magnetic field are given by, $N^{2s+1}L_j$. Where N is the electron shell, S is the electron spin, L is the orbital angular momentum, and J is the total angular momentum, $J = L + S$. Right circularly polarized laser light of 795 nm wavelength will induce transitions from the $5^2S_{1/2}$ ($m = -1/2$) ground state to the $5^2P_{1/2}$ ($m = +1/2$) excited state, according to the selection rule $\Delta L = +1$. The excited electrons decay back with equal probabilities to both $m = +1/2$ and $m = -1/2$ states. But they can only be excited back again from $m = -1/2$ state. Therefore, as this process continues, the $m = +1/2$ state gets populated. In order for this process to work perfectly there should not be any relaxation processes. The excited electrons decay to the ground state by emitting photons which usually have different polarization states. Therefore, in dense targets these photons can limit the efficiency of the pumping process. To avoid this kind of reduction in efficiency, a small amount of N_2 gas is added to the cell which allows a non-radiative decay of the electrons by absorbing the emitted photons into their rotational

and vibrational degrees of freedom [70].

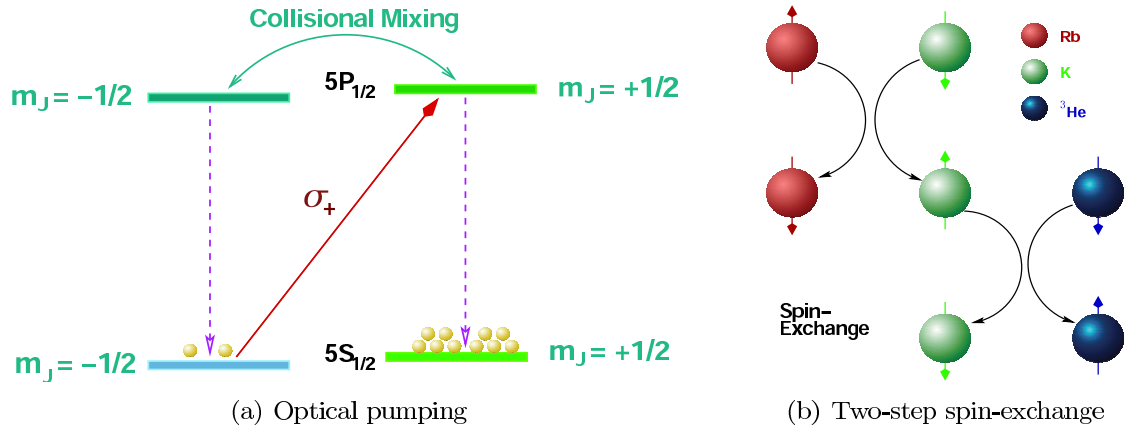


Figure 3.5: Panel (a) shows the optical pumping process in the Rb states. Panel (b) shows the two-step spin exchange process. This figure is reproduced from [8].

Spin Exchange

The ^3He "hybrid" target cells used in experiment E06-010 contained two kinds of alkali vapors, Rb and K. Due to the large collisional cross-section of the Rb-K atoms, the spin exchange between Rb and K takes place very quickly [71]. And this results in equal polarization (P_A) of Rb and K atoms, as they reach a spin-temperature equilibrium. Rb and K atoms undergo spin-exchange collisions and transfer their spin orientations to ^3He atoms and thus polarizing the ^3He nucleus. It turns out that this process is a lot more efficient than just having one alkali species, like Rb, to polarize ^3He . The amount of time required to polarize the gas, known as "spin-up time", is of the order of 15 hours for cell with one alkali species like Rb. But this time reduces significantly to about 3-5 hours for "hybrid" cells. It is very important for the experiment to have faster spin-up times so that one can maintain a stable target polarization, despite beam and polarization measurement induced depolarization effects.

Target Setup

The target setup in E06-010 consisted of several components which are listed below

- **Target Cells:** Figure 3.6 shows a target cell used in this experiment. It consisted of three regions - a pumping chamber of approximately 3 inch diameter on the top, a target chamber of about ~ 2 cm diameter and 40 cm long tube, where the particle interaction takes place, and finally, a transfer tube connecting both regions. The target

cells were hand-blown by Mike Souza at Princeton University. They were filled with ^3He gas and characterized at the University of Virginia and the College of William and Mary. The characterization of a cell includes, measuring the polarization, gas density, wall thickness of the cell, and spin-up time. In addition to this the ratio of Rb to K in the cell is also an important parameter that needs to be optimized. Apart from polarized ^3He target cells, an empty cell was used during the experiment which could be filled with various gases like N_2 , H_2 and ^3He . This allowed us to determine the dilutions factors due to various gases present in the target cell.

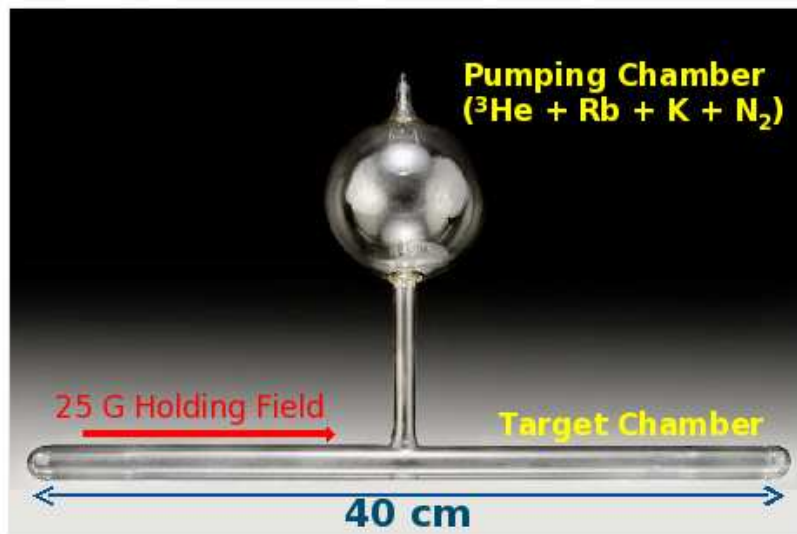


Figure 3.6: Target cell showing two separate regions - pumping region and target region [8].

- Target Oven and Ladder System:** The pumping chamber of the target cell must be kept at high temperature of 230°C in order to reach a significantly high K vapor pressure. For this, the entire pumping chamber was mounted inside an oven system with constant flow of compressed hot air. The flow of air was controlled by a PID feedback system to keep the temperature constant. A number of Resistive Temperature Devices (RTDs) were attached to the cell inside the oven to measure the cell temperature. A target ladder system which could be controlled remotely is a vertically moving system. It consists of different targets and can position a target in the right place with respect to the beam, as needed by the experiment. In this experiment we had four different targets - the primary ^3He target, a multiple carbon foil target for detector optics calibration purposes, an empty target (no target) for beam tuning

purposes, and finally a reference cell target which was filled with either N_2 , H_2 , or 3He as needed for the calibration and determining dilution factors needed for the data analysis.

- **Target Coils:** The holding field for the 3He target was provided by a set of three pairs of Helmholtz coils mounted in mutually orthogonal directions around the target. Figure 3.7 shows the target coils setup (red) used during the experiment. The pair of coils providing a magnetic field in the vertical direction were larger than the other two pairs. A holding field of approximately 25 G was generated by these coils. A second set of coils (blue) was used for generating RF signals transverse to the holding field direction for NMR and EPR measurements. An additional set of coils, mounted very close to the target and pumping chamber of the cell, was used as pick-up coils for the NMR signals.

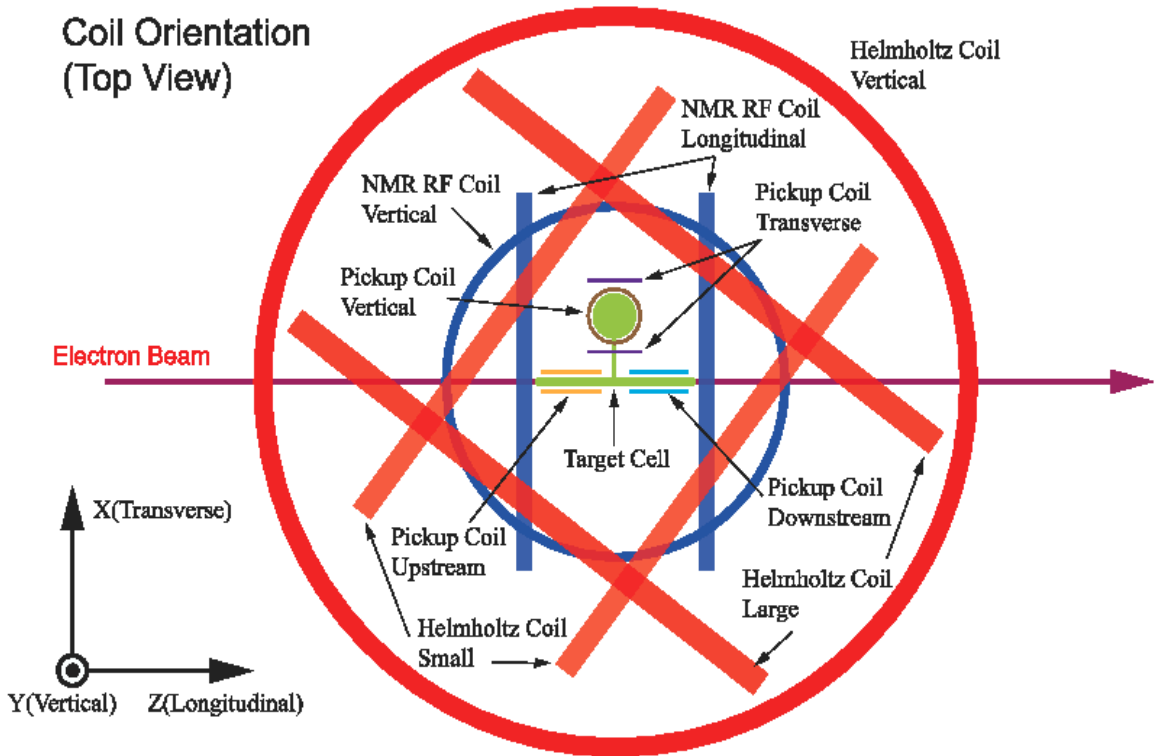


Figure 3.7: Target coils setup [9].

- **Lasers and Optics Setup:** The optical pumping in the hybrid cell was done using new narrow bandwidth COMET lasers which have a linewidth of about 0.2 nm. Because of the very narrow linewidth, almost all the laser light is absorbed by the atoms

in the cell, thereby increasing the efficiency of the optical pumping. Using these new lasers one can achieve relatively high polarization values within a short period of time about (3 to 5 hours), compared to the previous system, which used FAP lasers with much broader linewidth (~ 2 nm). A total of three lasers, each with a power of 25 W, were used in this experiment. The lasers were installed outside of the experimental hall and therefore each laser was connected to a 75 m long fiber going into the hall. The light from all three lasers was combined using a 5-to-1 combiner, and an optics assembly was used for the single output to generate right(left) circularly polarized light which was directed towards the cell. The optics assembly was designed to polarize the target in all three directions - transverse(sideways), vertical (normal) and longitudinal(parallel) to the beam direction. For this experiment the transverse and vertical optics lines were used.

Polarization Measurement

The polarization of the target was measured using two methods. One was using NMR, which is a relative measurement, and the other was using EPR, which yielded an absolute measurement of the polarization. EPR can be used to calibrate the NMR signal. In addition, NMR measurements were done with a water sample to cross-check the calibration. The polarization of the protons in water, when placed in a known magnetic field, can be calculated exactly and thus the water NMR signal can also be used to calibrate the ^3He signal. In addition to this, the target spin automatically flipped every 20 mins during the experiment. For each flip of the target spins, an NMR signal was recorded and thus the polarization is known for every spin state of the target. In the following we describe the basic principles of both the NMR and the EPR methods.

Nuclear Magnetic Resonance (NMR)

This method uses the Adiabatic Fast Passage (AFP) technique to measure the polarization of the ^3He gas. In this technique, the spins of the ^3He nuclei, which are initially aligned along the holding field direction, are rotated to the opposite direction using a radio-frequency (RF) field. This can be done in two ways - by keeping the RF field constant and slowly changing the holding field, known as *field sweep*, or by changing the RF field while the holding field is kept constant, this is known as *frequency sweep*. There are two conditions that need to be satisfied in order for the AFP method to work. If we consider the *frequency sweep* method,

then the change in the RF field should be fast enough such that the spins do not have enough time to relax, and it should be slow enough so that they can follow the frequency sweep and change to the opposite direction.

In a classical picture, the precession of a nucleus with spin \vec{I} and magnetic moment \vec{M} , kept in a constant magnetic field \vec{H}_0 , is described by the following equation in the laboratory frame [72],

$$\frac{d\vec{M}}{dt} = \gamma\vec{M} \times \vec{H}_0, \quad (3.10)$$

where γ is the gyro-magnetic ratio. It is much simpler to consider a rotating frame of reference which is rotating at an angular velocity of $\vec{\omega}$. Then the rate of change in the magnetic moment is given by

$$\frac{d\vec{M}}{dt} = \frac{\partial\vec{M}}{\partial t} + \vec{\omega} \times \vec{M} \quad (3.11)$$

where $\frac{\partial\vec{M}}{\partial t}$ is the rate of change of magnetic moment in the rotating frame of reference. Using Eq. (3.10) in Eq. (3.11) one can write down an expression for this rate of change as,

$$\frac{\partial\vec{M}}{\partial t} = \gamma\vec{M} \times \left(\vec{H}_0 + \frac{\vec{\omega}}{\gamma}\right) \quad (3.12)$$

Eq. (3.12) is similar to Eq. (3.10) except that the holding field \vec{H}_0 in the lab frame is replaced by an effective \vec{H}_e in the rotating frame of reference, where

$$\vec{H}_e = \vec{H}_0 + \frac{\vec{\omega}}{\gamma}. \quad (3.13)$$

Here, if a frequency is chosen such that $\vec{\omega} = -\gamma\vec{H}_0$ then the motion of magnetic moment will vanish. This frequency ω_0 is called *Larmour frequency*. Consider a situation when the target gas is polarized in vertical direction (against gravity) where the holding field \vec{H}_0 is pointing in x direction, and an RF field \vec{H}_{RF} applied in z direction (parallel to the beam direction), then the effective field in rotating frame of reference can be written as,

$$\vec{H}_e = \left(H_0 + \frac{\omega}{\gamma}\right)\hat{i} + H_{RF}\hat{k}, \quad (3.14)$$

where \hat{i} and \hat{k} are the unit vectors in the direction of the holding field and the RF field, respectively. In order to satisfy the AFP conditions, the frequency of the RF field was swept from 77 kHz to 85 kHz at a rate of 4 kHz/sec, and back. The sweep passed through the resonance frequency of $\omega_0=81$ kHz. As the frequency sweep occurs, the ^3He spins go from being aligned with the holding field to anti-aligned. The following condition needs to be

satisfied for the *frequency sweep* method to work [8]

$$\frac{|\gamma H_{RF}|}{T_2} \ll |\dot{\omega}| \ll \gamma^2 H_{RF}^2. \quad (3.15)$$

where $\gamma = 3.224$ kHz/G (gyro-magnetic ratio of ^3He) and T_2 is the transverse ^3He spin relaxation time. When resonance happens, the motion of the spins generate a large EMF signal in a pair of pick-up coils placed very close to the cell. The amplitude of the signal is proportional to the transverse component of the magnetization, which in turn is proportional to the polarization of the target up to some constants. These constants can be experimentally determined.

In addition to *frequency sweep* NMR, *field sweep* NMR was also performed to cross-check the calibration procedure. For this, the field was swept between 25 G to 32 G at a rate of 1.2 G/sec. The resonance occurred at 28 G at an applied RF frequency of 91 kHz. A sample NMR signal recorded during a *frequency sweep* is shown in Figure 3.8. The signal is fitted with the square root of a Lorentzian shape. The height of the signal is proportional to the polarization of the ^3He in the cell. Since this is a relative measurement, the NMR signal height has to be calibrated with an absolute polarization given by an Electron Paramagnetic Resonance (EPR) measurement. The EPR measurement is described in the following section.

Electron Paramagnetic Resonance

Electron Paramagnetic Resonance is used to determine the absolute polarization of the target by measuring the Zeeman splitting in the energy levels of the electrons when placed in an external magnetic field. The energy levels of the Rb and K atoms present in the target chamber are split when the target is placed in a magnetic holding field. For Rb, the $F=3$ ground state splits into seven sub-levels $m_f = -3, -2, ..2, 3$. Here F is the total angular momentum quantum number. The splitting corresponds to a frequency which is proportional to the holding field, $\nu_0 = \gamma B_0$, with $\gamma = 0.466\text{MHz/G}$ for Rb atom. A shift in this frequency occurs due to the small effective magnetic fields created by the spin exchange mechanism of Rb-K and K- ^3He , and also due to the polarization of ^3He nuclei itself. This shift in frequency is known as the EPR frequency shift ($\Delta\nu_{EPR}$).

We can measure the contribution of ^3He spins to the shift in the EPR frequency by reversing the direction of the ^3He spins. This can be done by sweeping the RF field at AFP conditions at constant holding field. The shift in frequency due to ^3He spins is of

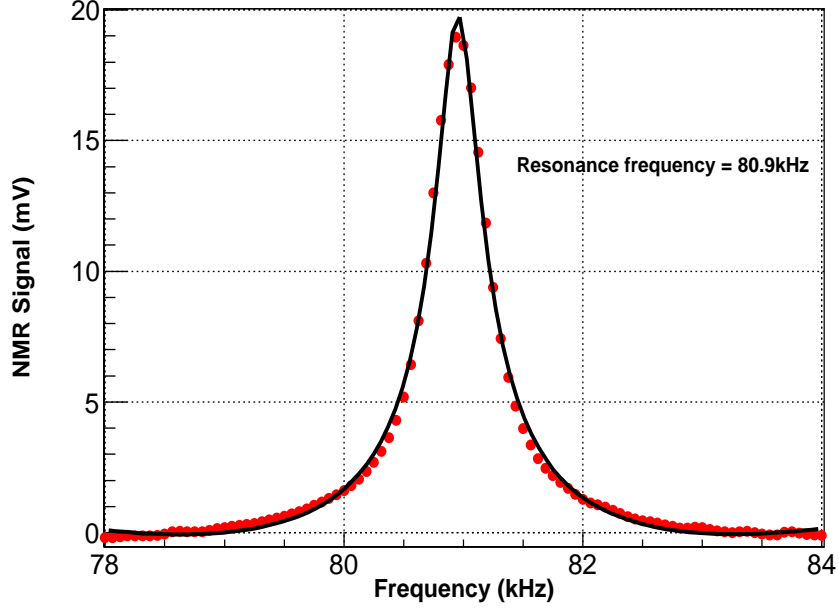


Figure 3.8: NMR signal generated using the *frequency sweep* method and fitted with the square root of a Lorentzian shape [10].

the order of few tens of kiloHertz in our case, and can easily be measured. The following equations (Eqs. (3.16) to (3.18)) show various contributions to the EPR frequency shift in two opposite states and how the difference in EPR frequency is related to only the ^3He contribution.

$$\Delta\nu_+ = \Delta\nu_{He} + \Delta\nu_{SE} + \Delta\nu_B \quad (3.16)$$

$$\Delta\nu_- = -\Delta\nu_{He} + \Delta\nu_{SE} + \Delta\nu_B \quad (3.17)$$

$$\Delta\nu_+ - \Delta\nu_- = 2\Delta\nu_{He} \quad (3.18)$$

where $\Delta\nu_{He}$ is contribution from ^3He spins, $\Delta\nu_{SE}$ is the spin-exchange contribution and $\Delta\nu_B$ is the contribution from the holding field to the frequency splitting, $\Delta\nu$. This change in the frequency is related to the polarization of the ^3He by the following equation [73]

$$\Delta\nu_{EPR} = \frac{8\pi}{3} \frac{d\nu_{EPR}}{dB} \kappa_o \mu_{He} \eta_{He} P, \quad (3.19)$$

where $\kappa_o \equiv \kappa_o(T) = \kappa_{oo}(T_{ref}) + \kappa_{oT}(T - T_{ref})$ is a dimensionless quantity for spin-exchange that depends on the geometry and temperature of the cell. $\frac{d\nu_{EPR}}{dB}$ can be calculated from the Breit-Rabi equation. P is the polarization of the ^3He in the cell, η_{He} is the ^3He density, and $\mu_{He} = 6.706984 \times 10^{-14} \text{MeV/T}$. The value of κ_{oT} is known at temperatures around 170° . This

value is extrapolated to the operating temperature of 255° , resulting in large uncertainties. Therefore κ_{oT} presents the largest uncertainty in the polarization measurement using EPR.

In order to measure $\Delta\nu_{EPR}$ of Rb, an RF field corresponding to the energy difference between $m_F = -3$ to $m_F = -2$ ground state sublevels has to be applied to the target. This increases the number of electrons in the $m_F = -2$ sublevel. Since they absorb the photons from the circularly polarized laser light, these electrons get excited to the $P_{1/2}$ state. As they decay back to the ground state ($S_{1/2}$), there is an increase in the number of photons emitted which can be detected by a photodiode. This is the D_1 transition with a wavelength of 795 nm. Whereas the energy difference between $S_{1/2}$ and $P_{3/2}$ is called D_2 (780 nm) transition. A thermal mixing between energy levels can cause electrons in the $P_{1/2}$ state to mix with the $P_{3/2}$ state and later decay back to $S_{1/2}$ state as a D_2 transition. This will release some D_2 light. A D_2 filter is used in front of the photodiode to separate D_2 light from D_1 light. For an EPR measurement, the ^3He spins are flipped by sweeping the RF field (typically used for an NMR sweep) through resonance and measuring the change in the EPR frequency. A typical EPR spectrum is shown in Figure 3.9.

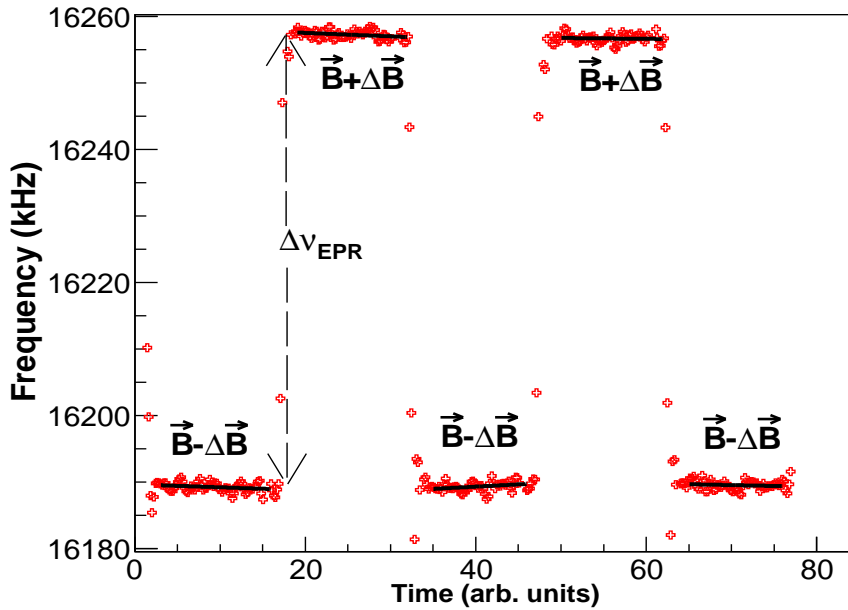


Figure 3.9: EPR spectrum showing the ^3He spin states when they are anti-parallel ($\vec{B} - \Delta\vec{B}$) and parallel ($\vec{B} + \Delta\vec{B}$) to the holding field direction [10].

Spin-Flip System

During the experiment the spin of the ^3He target was flipped every 20 min to keep any systematic uncertainties associated with the target as low as possible. Also, to remove any biases related to the DAQ, these regular flips of the target spins were performed independent of the data acquisition. In order to perform this job, an automatic target spin-flip system was developed by J. Huang (MIT). It recorded the NMR signal generated during the spin-flip. Therefore the polarization of the target is known for every state. The system also generates a spin-flip signal to gate the scalers on the basis of the target spin. Target-spin gated scalers provide the accumulated charge and triggers in each spin state, which are later used for normalizing the experiment. Details of the scaler gating system is discussed in section 3.3.4. A robust error handling was also part of this system. During the spin-flip, the circular polarization of the pumping laser directed towards target cell had to be reversed, as well. This was achieved by remotely rotating the quarter wave plate by 90° while the spin was flipped. The spin-flip system continuously monitored the quarter wave plate position and reported any error to the user. A general schematic of the system is shown in Figure 3.10.

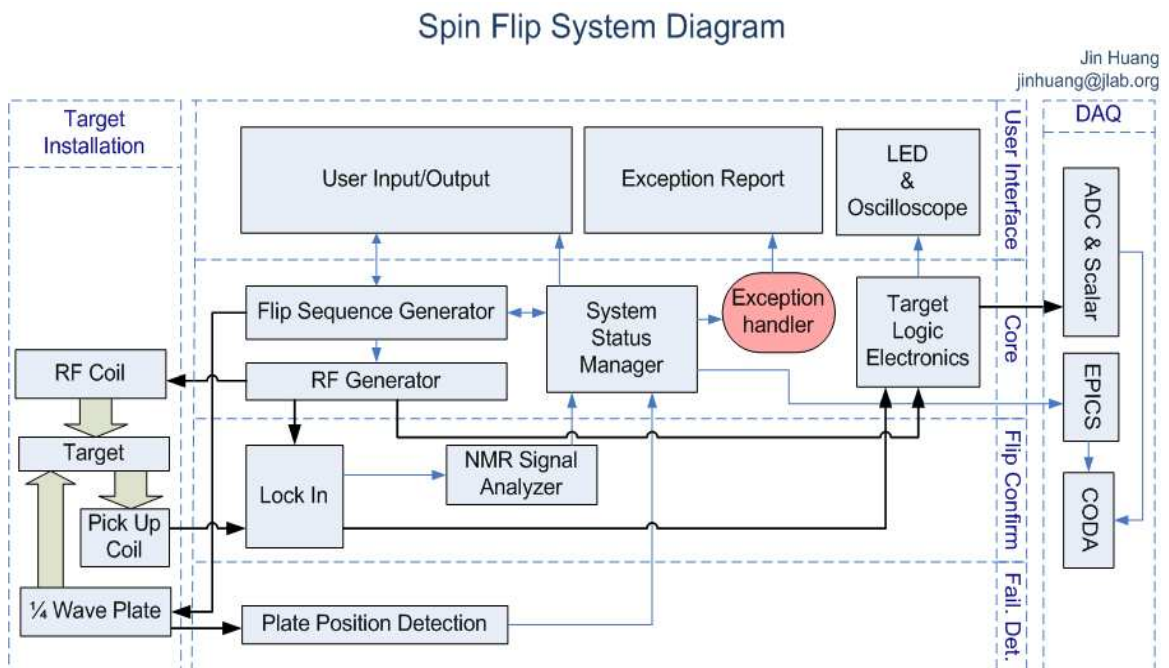


Figure 3.10: Schematic of the automatic target spin-flip system during E06-010 [11].

Measurement of Holding Field Direction

In this experiment the ^3He nuclei are polarized either in vertical (normal) or transverse (sideways) directions with respect to the scattering plane (formed by the vectors representing incoming and scattered lepton). Therefore it is necessary to accurately measure the direction of the holding field generated by the Helmholtz coils in the target region. By knowing the direction of the magnetic field due Helmholtz coils at the level of 0.5° , one can infer the direction of the ^3He spins, since they align with the magnetic field direction.

Two different methods were used to determine the direction of the magnetic field in the target region - one for transverse direction and one for vertical direction. For measuring the transverse field direction, a bar magnet was placed near the target region and the angles were surveyed by the Jefferson Lab survey group. Using this information combined with the values of exact currents in the Helmholtz coils, the transverse field direction was determined. For measuring the vertical field direction, a vertical compass was designed and constructed at the University of Kentucky. This is a flotation device, consisting a magnetic cylinder with an ability to float on air when pressurized air flows through the system. An optical encoder was attached to the cylinder to record the rotations. First, the compass assembly was placed in the target region and nitrogen gas was allowed to flow into the system so that the magnetic cylinder floats. Then the vertical field was turned on and value of the encoder readings were recorded. This procedure was repeated after rotating the entire assembly to 180° . Using this information the vertical field direction was determined [14].

3.2.4 High Resolution Spectrometer

The High Resolution Spectrometer(HRS) is part of the standard equipment in Hall A. There are two identical HRSs in the Hall, one on either side of the beam line. For this experiment, the left HRS was used for detecting the outgoing hadrons. The HRS consists of three quadrupole and one dipole magnets in a QQDQ configuration [7]. The layout of the magnets in the HRS is shown in Figure 3.11. It focuses the charged particles within a small momentum and angular range to the detectors. The relative momentum resolution can reach up to $\sim 10^{-4}$ and the central momentum in the spectrometer is determined by the magnetic field of the dipole. The detector package in the HRS consists of the following detectors whose arrangement is shown in Figure 3.12

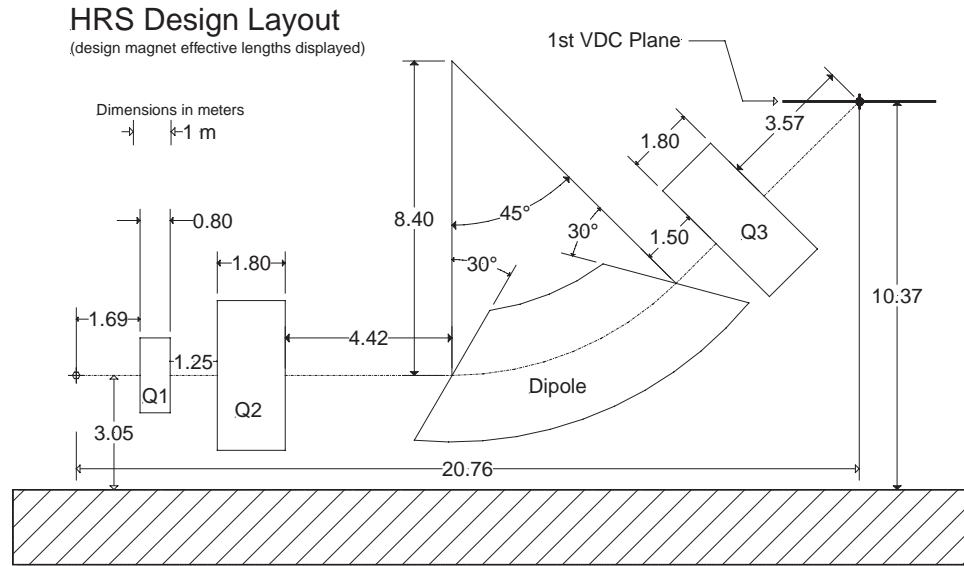


Figure 3.11: Layout of the magnets in the High Resolution Spectrometer [7].

- Vertical Drift Chambers:** The tracking information was provided by the Vertical Drift Chambers (VDCs). There are two chambers in the HRS and each chamber has two wire planes, U and V, at an angle of 45° with respect to the dispersive and non-dispersive directions. The VDC is designed in such a way that the particle traversing the VDCs at 45° will fire about five wires per plane providing accurate reconstruction of the particle's track. The track is reconstructed using the timing information given by the Time-to-Digital Converter (TDC) for each wire. This timing is used for determining the drift distances for each wire. The cross-over point of the track is then determined by a linear fit of drift distances versus wire position. The position and angle of the track reconstructed using this method has a resolution of about $100 \mu\text{m}$ and 0.5 mrad , respectively.
- S1 and S2m Scintillators:** These are two plastic scintillator planes (S1 and S2m) separated by a distance of 2 m. The S1 plane consists of six scintillator paddles with two Photo-Multiplier Tubes (PMTs) on each side of one paddle. Similarly, the S2m plane consists of 16 scintillator paddles with two PMTs on each side of a paddle. They are primarily used for triggering the hadron arm (HRS) and to provide the timing information for the coincidence time-of-flight calculations. The S2m scintillators provided the timing information. The trigger setup for the HRS is discussed in section 3.3.2.

- Gas Čerenkov Detector:** The Gas Čerenkov counter consists of ten spherical mirrors arranged in five rows and two columns. Each mirror is coupled to one PMT where the incoming light is converted into an electronic signal which was recorded in an ADC. A Gas Čerenkov detector is a threshold detector and is used to differentiate between pions and electrons. Since the aim is to detect a hadron, electrons are considered as background. One can separate electrons from pions by looking at the total sum of the signals from all the PMTs. Hadrons will leave a one photo-electron peak in the spectrum, whereas electrons will leave more than one (usually up to 6 photo-electrons). Therefore this counter works as a good particle identification detector.

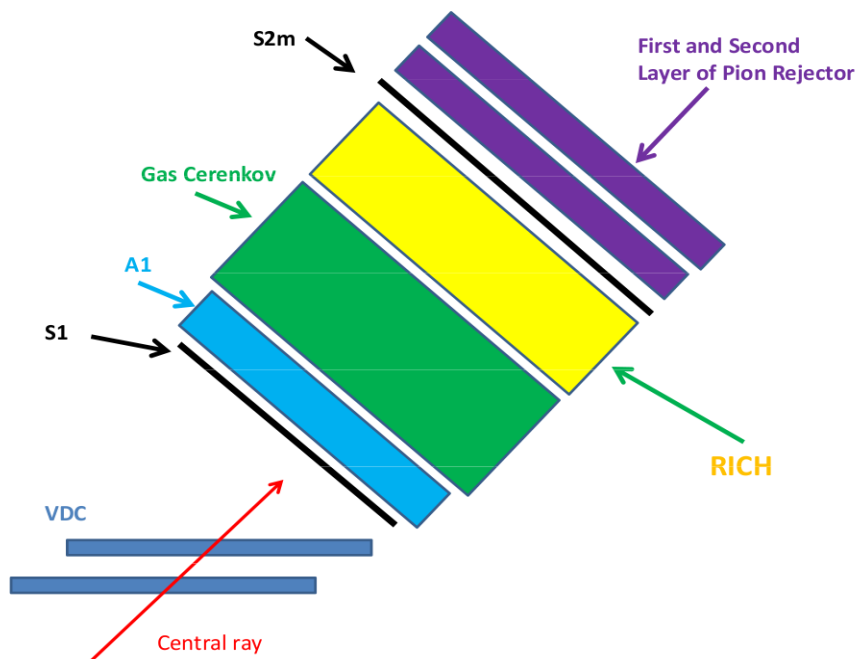


Figure 3.12: Arrangement of the detectors in High Resolution Spectrometer during the E06-010 experiment. The figure is reproduced from [12]

- Aerogel Detector:** Due to the requirements for good particle identification, another threshold detector was used. The refractive index of aerogel is 1.015. At the 2.35 GeV momentum setting of the spectrometer, only pions can trigger the Aerogel(A1) detector. Kaons and protons cannot be directly detected by the produced Čerenkov light. Therefore, this can also be used to identify kaons, by requiring that the Aerogel

counter does not trigger, in addition to the coincidence time-of-flight method. This detector consists of 24 PMTs, 12 on each side of the detector. The sum of the signals from all the PMTs is used to determine the cuts needed to separate kaons and protons from pions.

- **Lead-Glass Detector:** This detector consists of two layers of lead-glass blocks, each layer consists of 17 short blocks and 17 long blocks. They are arranged in two columns (2×17). The signal from each PMT is recorded with an ADC. This detector is used as additional particle identification for pions and electrons. We can identify pions from this detector as they leave a minimum ionization peak, whereas electrons leave a large signal due to an electromagnetic shower. By using a cut on the gas Čerenkov, to reject electrons, one can cleanly identify all the pions in this detector.

3.2.5 BigBite Spectrometer

The BigBite spectrometer was used as an electron detector in this experiment. The aim was to accurately determine the direction and momentum of the scattered electrons. Unlike the HRS, it is an open geometry spectrometer where both charged and uncharged particles can hit the detectors. It consists of a large dipole magnet which produces a field of about 1.2 T. The front face of the magnet was located at a distance of 1.5 m from the target center which provided an angular acceptance of about 64 msr. The spectrometer consists of several detectors - a set of three drift chambers for position and momentum reconstruction, a scintillator plane for timing information, and finally a calorimeter for particle identification and trigger purposes (Figure 3.13). In this section we describe the details of the hardware for each detector.

Definition of Coordinate Systems

The coordinate systems relevant to the BigBite spectrometer are defined below.

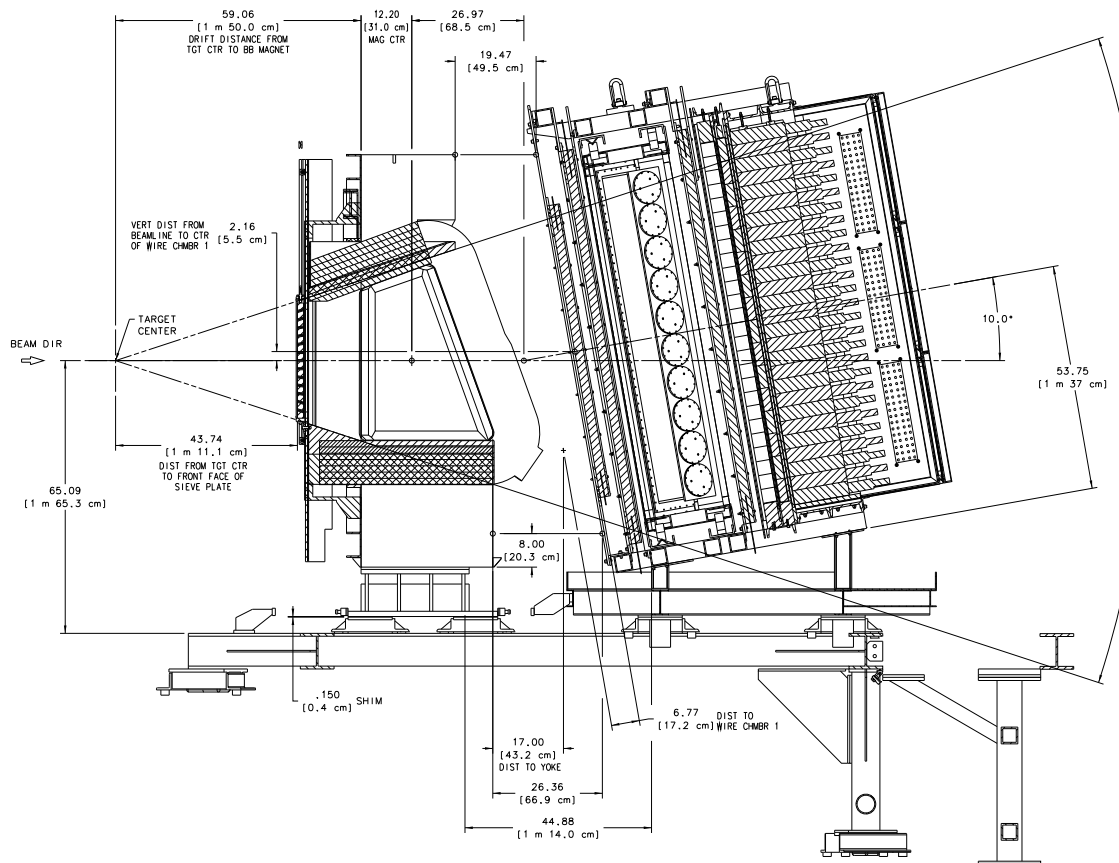
- **Lab coordinate system:**

z is along the beam direction

y is against gravity

x is to the left when looking in the beam direction

- **Magnet coordinate system:**



BIG BITE SPECTROMETER
 (SECTION CUT THRU CENTER)
 TRANSVERSITY - EXP E06-010
 A06010-15-02-0000
 29 OCT 08
 SCALE 1:10

Figure 3.13: Layout of the BigBite spectrometer [13].

x is to the right when facing the magnet

y is against the gravity

z is $x \times y$

- **Detector coordinate system:** The origin is specified by the center of first wire chamber.

x is pointing down from the center of the chamber

z is the nominal direction of the particle passing through the detector

y is $z \times x$

Multi-Wire Drift Chambers

Three drift chambers were used to accurately reconstruct the particles track going into the BigBite spectrometer. There are three types of wire planes, U, V, and X and their orientation is shown in Figure 3.14. The X plane is parallel to the y_{det} axis in the detector coordinate system and V and U planes are oriented $\pm 30^\circ$ with respect to this axis. Each chamber has two sets of these planes (total 6 wire planes). In each plane, the sense wires are spaced 1 cm apart, with a field wire in between a pair of sense wires. A cathode plane is inserted 3 mm above and below each wire plane. The chamber is filled with a gas composed of a mixture of 50% argon + 50% ethane, which is first bubbled through alcohol at 0°C . The signal generated by the charged particle passing through the chamber is amplified before it is fed into a TDC for recording the time. The drift time, the amount of time it takes for free ions to drift from track position to the sense wire, is then converted to a drift distance. This information gives the hit position of the track in each plane, which is then used to fit a straight line to reconstruct the original track.

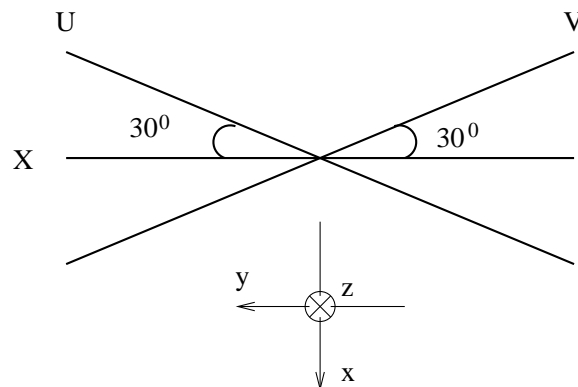


Figure 3.14: Orientation on U, V, and X wire planes in BigBite wire chambers.

BigBite Scintillators

The BigBite scintillator plane consists of 13 bars. The dimensions of each bar is $17 \times 64 \times 4$ cm³. Each bar is connected to two PMTs, one on each side. The entire scintillator plane is mounted between the preshower and shower detectors (see Figure 3.15). The signal from each PMT is amplified 10 times and then sent to a discriminator which makes a logic pulse. This pulse is recorded in a TDC for timing information. The BigBite scintillators provided an accurate timing information of the particles entering the detector, which is used together

with the corresponding timing of the S2m scintillators to get the coincidence time-of-flight in the HRS. In other words the difference in the time of hit of a particle in the BigBite and the corresponding hit in the HRS gives the coincidence time-of-flight in the HRS. This is very crucial for the particle identification in the hadron spectrometer, as there is a slight difference (on the order of few ns) between different particles traveling 26 m length in the HRS, before hitting the detector.

Preshower and Shower

The preshower and shower detectors provide the electron particle identification (PID) in the BigBite. They also provide the trigger for the BigBite spectrometer. A detailed description of the BigBite trigger is given in section 3.3.1. The preshower blocks are made of TF-5 lead-glass blocks, each measuring $8.5 \text{ cm} \times 34 \text{ cm} \times 8.5 \text{ cm}$ in the X, Y, and Z directions, respectively. There are 54 preshower blocks arranged in two columns of 27 rows each. It has an active area of $210 \times 74 \text{ cm}^2$, with 8.5 cm (3 radiation lengths) along the particle's direction. The shower blocks are made of TF-2 lead-glass material, each measuring $8.5 \text{ cm} \times 8.5 \text{ cm} \times 34 \text{ cm}$ in the X, Y, and Z directions, respectively. It covers an active area of $221 \times 85 \text{ cm}^2$, with 34 cm (13 radiation lengths) in along the particle's direction. There are 189 shower blocks arranged in 7 columns of 27 rows each (Figure 3.15).

The particle entering the lead-glass block generate electromagnetic showers and leave a large signal in the PMT, which is amplified and sent to the summing modules for making a trigger. The signals are also recorded in ADCs. The combined ADC information from both preshower and shower detector gives the total energy deposited by the particle. The reconstructed energy has a resolution of about $\sigma_{\Delta E/E} = 8\%$. The signal generated by the electron is rather large compared to the hadrons. Based on this difference in the response of the different particles in the detector we can cleanly separate hadrons and electrons.

3.3 Trigger and Data Acquisition Setup

In this section we describe the trigger and data acquisition(DAQ) setup for experiment E06-010. A detailed description of the trigger setup in both spectrometers is given along with the coincidence trigger setup. Scalers, which are needed to normalize the experiment, are also described towards the end of this section. There are several software and hardware

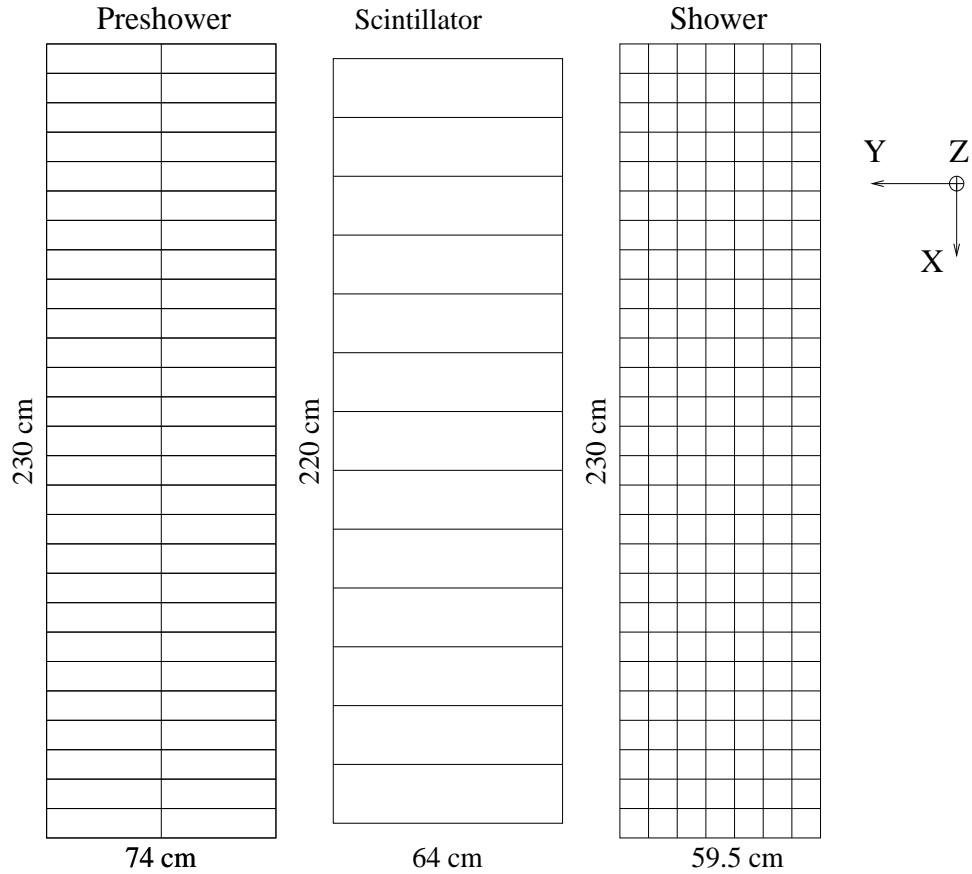


Figure 3.15: Geometry of the BigBite preshower, scintillator, and shower detectors.

components to the DAQ setup, which include

1. **The Trigger Supervisor(TS):** This is the central control point for the data acquisition activity. It is the link between the experiment specific triggering system and the read-out controllers (ROCs), which handle the event-by-event retrieval of the data recorded from the detectors. The hardware is a 9U multi-functional VME board and has several ECL inputs. External triggers are accepted through the eight input channels, usually known as T1 to T8. It accepts and prescales multiple triggers and maintains the *"system busy"* signal while a trigger is being processed. From the accepted triggers it generates a signal, for gating and timing of the front-end electronics (ADCs and TDCs), known as level-1 accept (L1A). The status of the ROCs are exchanged directly with the TS using a dedicated RS432 flat cable daisy-chained to all the ROCs in the configuration, which allows the TS to monitor the ROCs that are busy. During this time no additional triggers are accepted until all the ROCs are finished processing the data. This way the TS maintains synchronization between the ROCs [74].

2. **CODA(CEBAF Online Data Acquisition)**: This is the standard data acquisition software toolkit developed at Jefferson Lab and used by experiments in all three Halls - A, B, and C. It provides several software tools for monitoring and recording the data from the experiment. The main component of this system is called *RcServer* which is responsible for storing and initializing the chosen configuration. It also periodically checks the status of all the components and ensures that the recorded data are correct. Depending on the necessity we can create several CODA configurations using various combinations of the ROCs. All the configurations and the status of the components involved are stored in a MiniSQL database server.

Figure 3.16 shows the general flow for a simple CODA configuration. The L1A generated

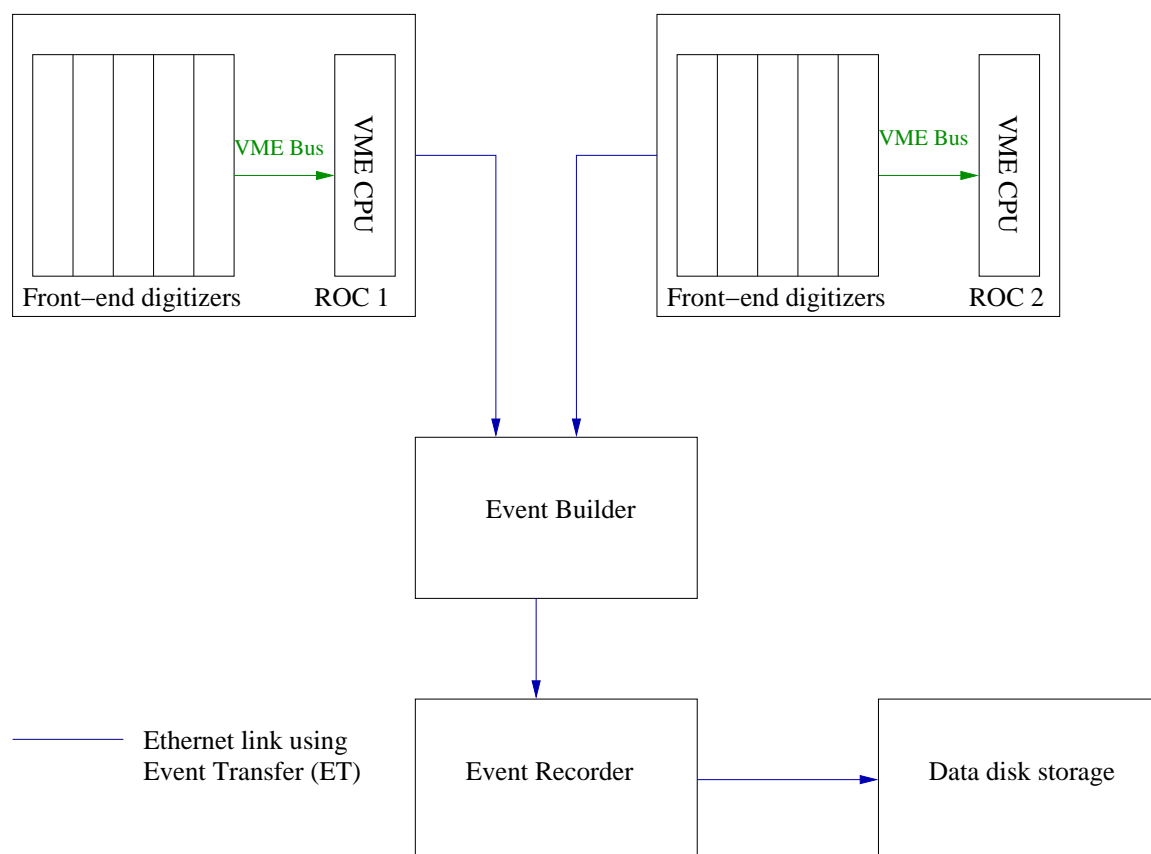


Figure 3.16: Example of CODA configuration using read-out controllers.

from the trigger supervisor causes the front-end electronics to digitize the detector signals and read out the crates. This is achieved by set of C routines called CODA readout list (crl) which can be programmed by the user. Data from each crate is then transmitted to

the Event Builder (EB). The Event Builder collects the data from different crates and sorts them into events putting them into the structured CODA event. This constructed event is then recorded as a CODA file in the disk by the Event Recorder (ER). The transfer of the data from all the components takes place using the Event Transfer (ET) library.

3. **EPICS and slow controls:** The Experimental Physics and Industrial Control System (EPICS) system provides information on the beam, magnets, power supplies, and various other instruments in the accelerator and in the Hall. The information such as beam position, beam current, beam energy, and magnet status, etc., are gathered and written to the CODA datastream every few seconds. It was also used to retrieve target information such as target oven temperature from the polarized ^3He target system. In additions to this, the slow controls were used to set/adjust high voltages of the photo-multiplier tubes on the detectors. A LeCroy 1458 high voltage mainframe was used over the ethernet connection to adjust the high voltages.

3.3.1 Trigger and Electronics for BigBite Spectrometer

The BigBite spectrometer was used in this experiment to detect the scattered electrons from DIS reactions, therefore the trigger was designed to select electrons by measuring the total energy deposited by the particles entering the spectrometer. For this purpose a full calorimeter made of lead-glass was used. It consists of two detectors, preshower and shower. A detailed description of BigBite spectrometer and its detectors is given in section 3.2.5. In order to measure the total energy deposited by a particle in the lead-glass detector, a total hardware sum (TSUM) of the two overlapping rows of preshower ($2 \times 2 = 4$ blocks) and shower ($2 \times 7 = 14$ blocks) was formed (see Figure 3.17). This is done by first summing the signals from two rows of preshower blocks using LeCroy 428F modules, and then summing the signals from two rows of shower blocks using custom built summing modules. Later these two signals (preshower sum and shower sum) are combined together to form a total sum signal. The preshower signal is amplified five times and shower signal is amplified ten times before the total sum (TSUM) signal is formed.

The TSUM signal is proportional to the total energy deposited by the particle in the calorimeter. This analogue signal then goes through a discriminator. The threshold of this discriminator is controlled remotely and can be adjusted according to the experiment's

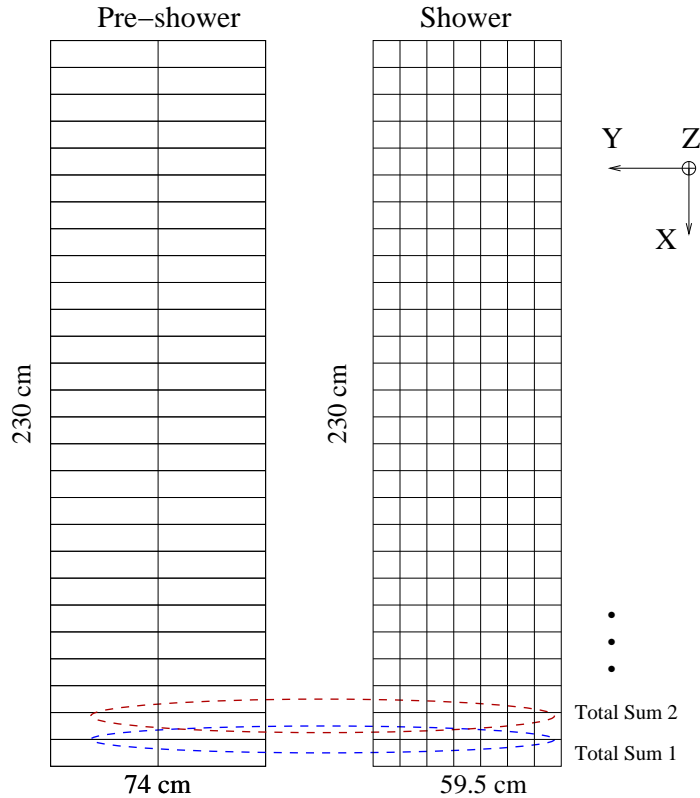


Figure 3.17: Total sum of preshower and shower

requirements. This trigger in the BigBite was known as T1. The detailed trigger logic can be found in Figure 3.18.

Apart from the T1 trigger, other triggers were constructed in the BigBite spectrometer for use in parasitic experiments. Here we just describe the basic triggers without going into the details of the construction of the individual triggers. The T6 trigger was formed similar to T1 trigger, but with a higher threshold on the TSUM signal. The T7 trigger was formed with Čerenkov signals only and T2 was formed with an overlap of Čerenkov, preshower and shower signals. It is appropriate to mention here that the BigBite Čerenkov detector was not used for this experiment, as it was under commissioning and testing during the data taking period of E06-010.

The BigBite detector signals were read out using both FASTBUS and VME electronics. The timing information from the individual wires in the drift chambers were read out using LeCroy 1877 TDCs. The scintillator time was recorded using F1 TDCs, which were designed at the Jefferson Lab. These are common-stop multihit TDCs with a resolution setting of either 120 ps or 60 ps. For this experiment it was set to 60 ps, since it is necessary

to determine the coincidence time-of-flight of the particle in the HRS with high accuracy, in order to improve particle identification. LeCroy 1881 ADCs were used to read all the PMT signals in the calorimeter and scintillators. The ADC gate width was set to 240ns.

BigBite Trigger Logic for Hall A Transversity (E06-010) Experiment

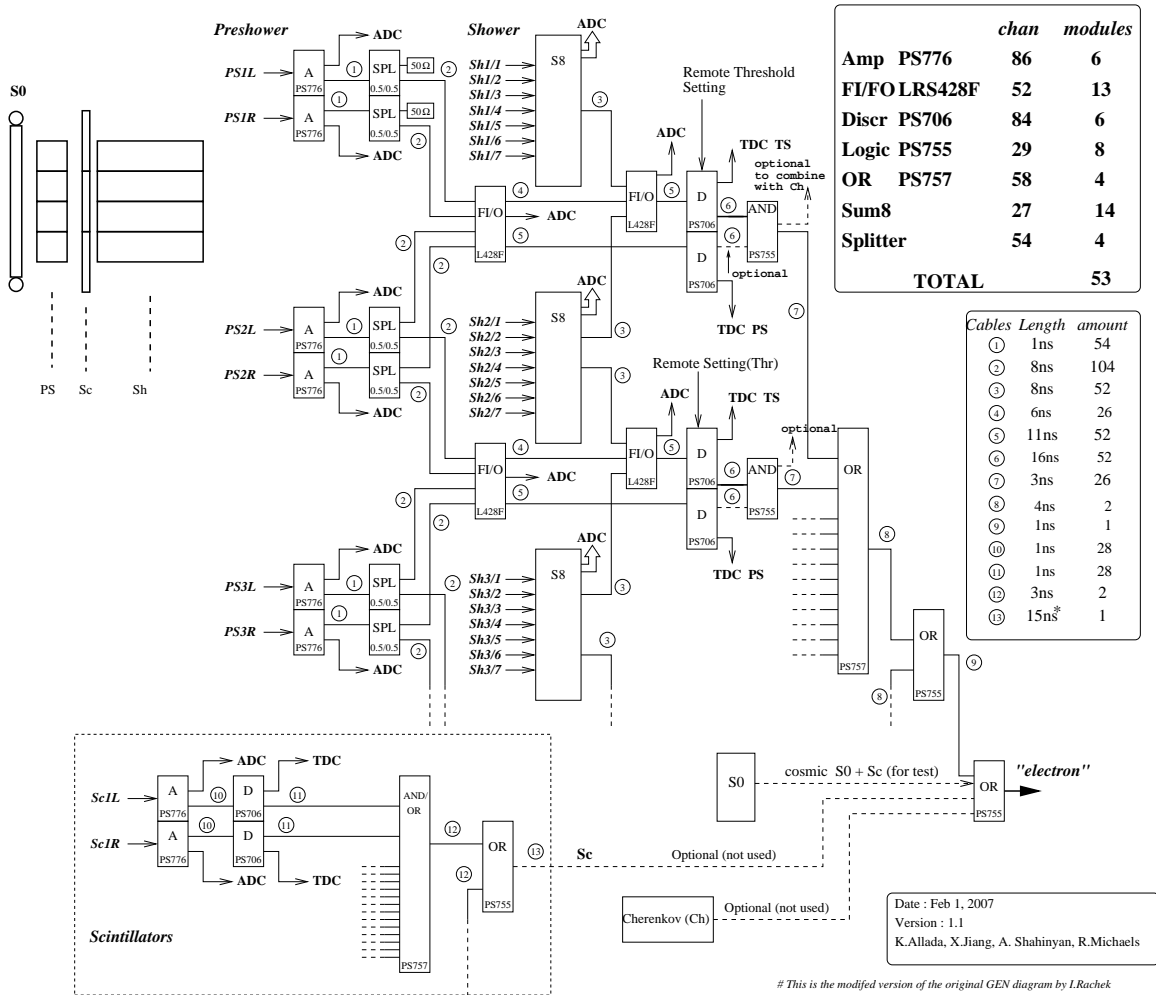


Figure 3.18: BigBite spectrometer trigger logic diagram.

Retiming in the BigBite When multiple triggers, constructed in different spectrometers, are used in the trigger supervisor, it is necessary to keep the reference timing of the recorded TDC signal in a particular spectrometer constant with respect to the trigger generated in that spectrometer. To achieve this, a re-timing circuit was employed in the BigBite trigger setup to gate the ADCs and TDCs. Figure 3.19 shows the re-timing circuit. The basic idea of the re-timing circuit in the BigBite spectrometer is that it makes sure

that the L1A generated by the TS has a corresponding T1 trigger by performing an AND logic between T1 and L1A. This way the reference time for the ADC and TDC gates is tied to the T1 trigger. And since the timing for the coincidence trigger (T5) is always given by the leading edge of the T1 trigger, this ensures that all the gates for the T5 trigger have a common reference time. If for some reason there is no T1 for a particular L1A (for example, if the accepted trigger is from the HRS) then a delayed copy of the L1A gives the timing for the gates (see the timing diagram in Figure 3.19). The width of the T1 trigger was 40 ns and the timing for the ADC and TDC gates was tied to the leading edge of the T1 trigger.

Re-timing Circuit for the BigBite Trigger (E0-6010)

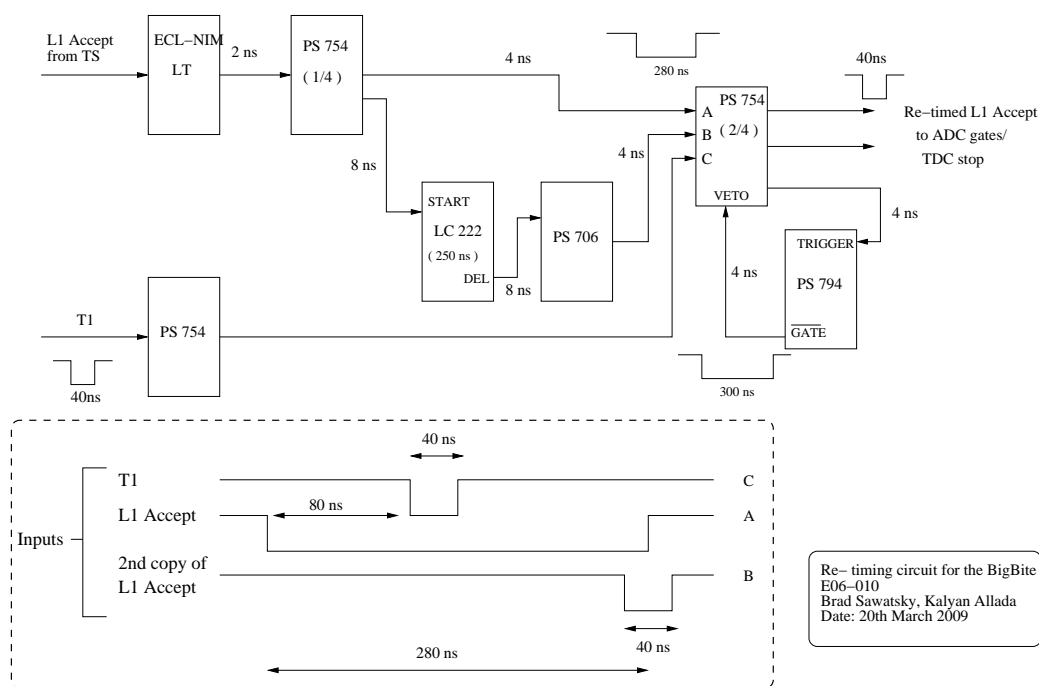


Figure 3.19: Re-timing circuit for the BigBite trigger

3.3.2 Trigger and Electronics for High Resolution Spectrometer

The High Resolution Spectrometer (HRS) consist of several types of detectors (see section 3.2.4) and were used in the standard Hall A configuration. For this experiment an upgraded Ring Imaging Cherenkov (RICH) detector was added to the spectrometer for identifying kaons. The trigger diagram for the HRS is shown in the Figure 3.20. The main trigger is formed by requiring that both S1 and S2m scintillator planes have a hit, i.e., one

paddle in S1 and one paddle in S2m have a hit on both sides (a total of four PMTs). In order to have a constant reference time, the timing of this trigger was tied to the leading edge of the right side PMT signal of the S2m scintillator paddles. This is usually known as T3 trigger in the spectrometer. Apart from this trigger, there was an additional trigger, T4, which is used as an efficiency trigger. This trigger is formed by requiring that 2 out of 3 detectors have a hit, where apart from S1 and S2m a third detector (Čerenkov) is used. Also, T4 requires that it is not a T3 trigger, i.e. excluding the coincidence between S1 and S2m planes. For this experiment, the T4 trigger was not used. A re-timing circuit was used to gate the ADCs and TDCs. The gates for ADCs and TDCs were generated using the L1A signal and the S2m PMT signals.

The signals from the detectors in the spectrometer were read out using FASTBUS electronics. The timing information from S1 and S2m scintillator planes were recorded using high resolution LeCroy 1875 TDCs with the resolution set to 50 ps. These are common-start single-hit TDCs. The signals from individual wires in the VDCs were recorded in common-stop multi-hit LeCroy 1877 TDCs which have a timing resolution of 0.5 ns. The timing information for other detectors like Aerogel(A1), Čerenkov, and the two-layer lead-glass detector were recorded using 1877 TDCs. The integrated charge of the signal coming out of the detector is recorded in ADCs. For this experiment LeCroy 1881 ADCs were used for all the detector signals in the spectrometer.

3.3.3 Coincidence Trigger

In this experiment scattered electrons were detected in the BigBite and hadrons were detected in the HRS. A coincidence trigger (T5) between BigBite (T1) and HRS (T3) was constructed by overlapping individual triggers in time. A sketch of coincidence trigger setup between two arms is shown in Figure 3.21.

In order to construct a coincidence trigger, two quantities should be known - the exact trigger formation time and the time-of-flight of particles, in both spectrometers. The trigger formation time was measured by injecting a fake electronic pulse at a point where a detector PMT signal goes into the trigger circuit, and measuring the time it takes to come out of the circuit. The exact time-of-flight of the particles in both spectrometers can be reconstructed from the kinematics (momentum) of the particle and the distance travelled

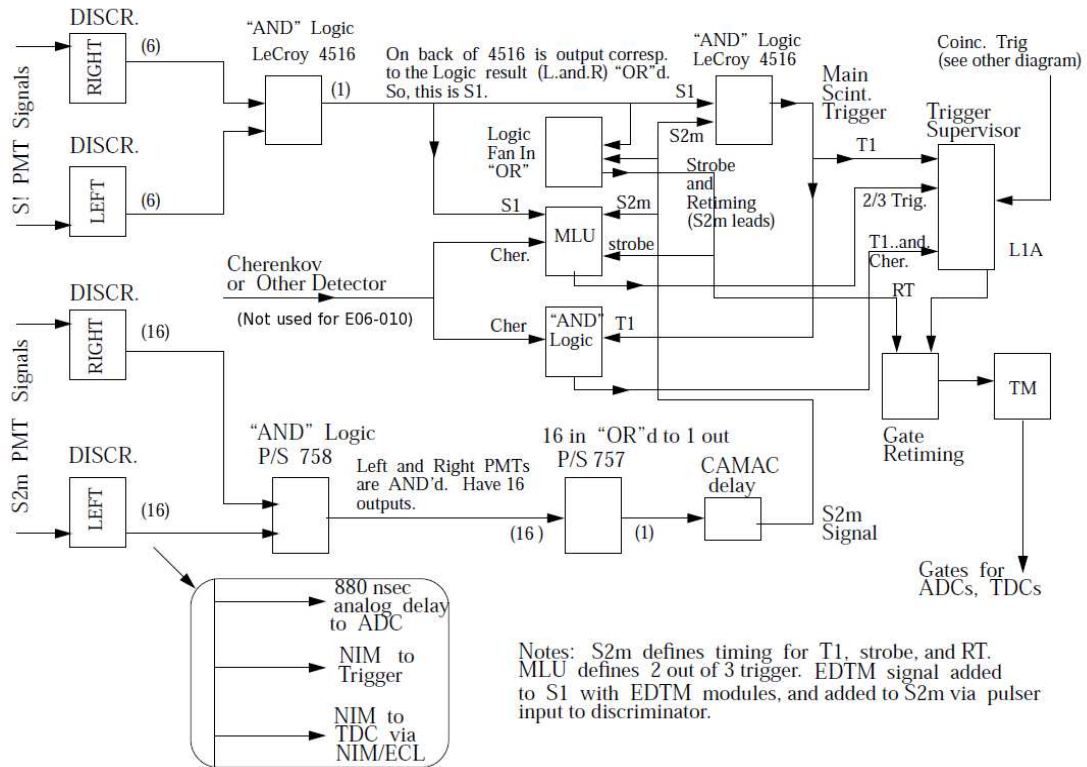


Figure 3.20: Trigger Logic for the Left HRS.

in the spectrometers. Once these two quantities are known, appropriate cable delays are set in the individual triggers (T1 and T3) such that there is an overlap between them. A logic AND between T1 and T3 defines the T5 trigger. The schematic timing diagram is shown in Figure 3.22. The timing of T5 is given by the leading edge of a T1 trigger. The cable delays are set such that T1 arrives 40 ns after T3. For this experiment the coincidence window was formed by T3 and the width was set to 140 ns. The width of T1 and T5 was set to 40 ns. During the commissioning of the experiment a full coincidence trigger was simulated using an electronic pulser with delays set close to the real experimental situation.

After the T5 signal is formed it is fed to the trigger supervisor (TS) which generates an L1A signal. This L1A signal is sent to both spectrometers where it is re-timed with the respective local trigger to form gates for TDCs and ADCs. Table 3.3 describes all the triggers that were used during the experiment E06-010.

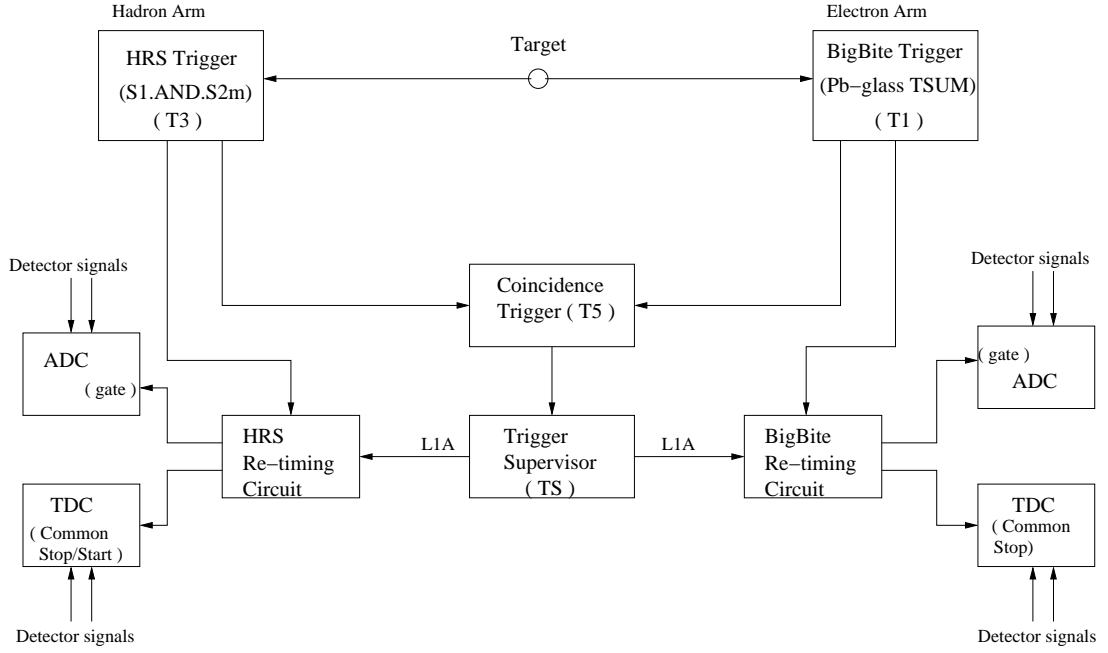


Figure 3.21: Schematic diagram of coincidence trigger setup between the two spectrometers

3.3.4 Scaler Setup

Scalers count raw signals generated from the PMTs on the detectors without any deadtime. They are used for getting information on the raw counts/rates for various triggers, which is needed to normalize the experimental data. Scalers are also used for counting the Beam Current Monitor(BCM) signal, which is basically a voltage signal converted to a frequency signal whose frequency is proportional to the beam current. This information from the scalers is very useful for real time monitoring of the trigger rates, beam current, and raw rates on the individual PMTs. Raw trigger counts are also used in the calculation of the DAQ deadtime. Section 4.6 describes the deadtime measurement in detail.

The scaler setup is shown in Figure 3.23. A set of five SIS38xx VME modules were used in 3800 mode. Each scaler has 32 input lines. The input signals, such as triggers, BCM signals, clock, etc., are daisy-chained using an RS432 flat cable. Therefore, all five scalers have copies of identical signals in their input lines. For the redundancy and cross-checking purposes, an identical scaler setup was constructed in both the spectrometers, BigBite and HRS.

For this experiment the knowledge of beam helicity is not a requirement, since the measurement uses an unpolarized beam and a polarized target. Although this experiment

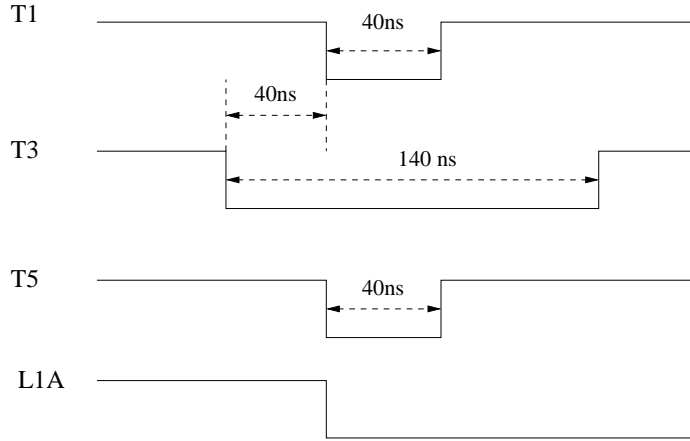


Figure 3.22: Coincidence timing between BigBite and HRS.

Table 3.3: Various triggers constructed during E06-010 experiment.

Trigger type	Description
1	Low threshold on BigBite lead-glass
2	BigBite gas Čerenkov singles
3	Left HRS singles (S1.AND.S2m)
4	Left HRS efficiency
5	Coincidence between BigBite and Left HRS (T1.AND.T3)
6	High threshold on BigBite lead-glass
7	BigBite Čerenkov and lead-glass overlap
8	1024 Hz clock

depends only on the target spin, the scalers were gated using both target spin and beam helicity. This was done due to the considerations of other parasitic measurements which required both beam helicity and target spin gated scalers. Four scalers were gated with target-spin and helicity combinations: Tar+ Hel+, Tar+ Hel-, Tar- Hel+, Tar- Hel-, and one was ungated. On the top of this all five scalers were also gated with a *run gate*, which allowed the scalers to count only during the period of run-start and run-stop. The *run gate* can be obtained from the trigger supervisor.

The scaler gating scheme is shown in Figure 3.23. It is formed by making a logical AND between three signals - run gate, target spin state, and beam helicity. Four gating signals were constructed separately using four combinations of target spin and beam helicity. These signals were then sent to the control bit on the SIS3800 scaler for gating purpose.

The beam helicity sequence is shown in Figure 3.24. There are three relevant signals

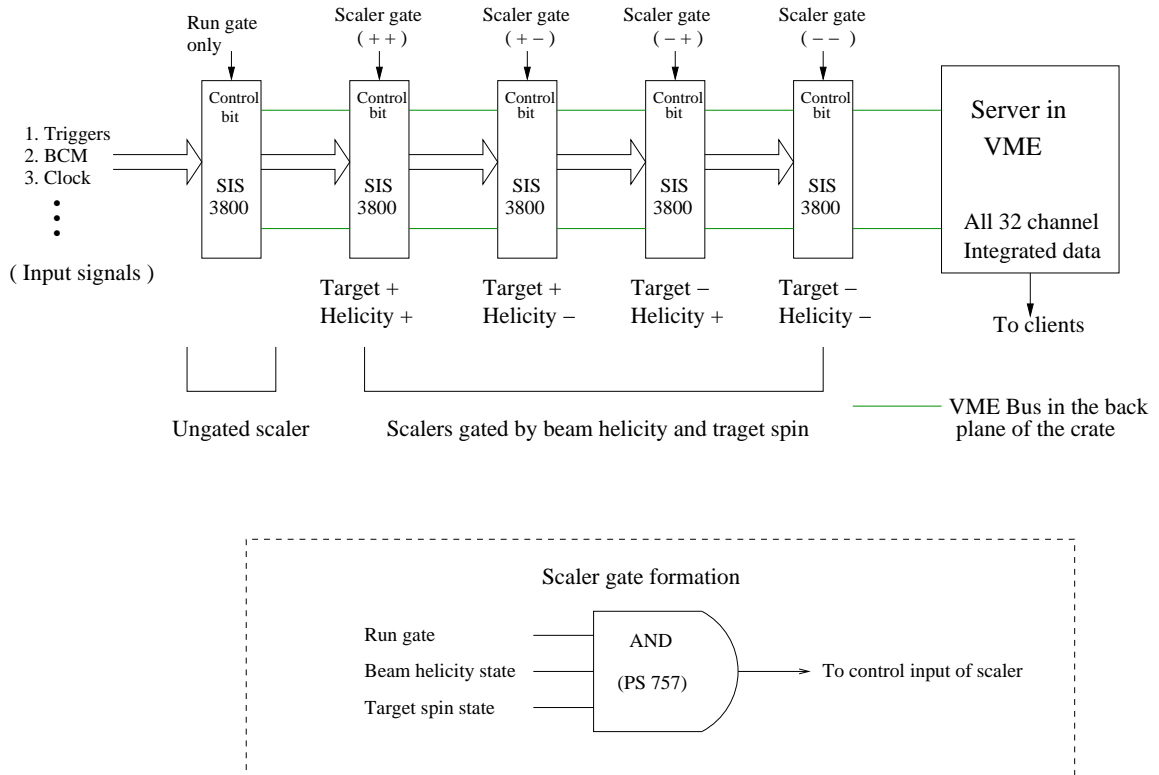


Figure 3.23: Scaler setup and gating scheme using target spin and beam helicity.

associated with the helicity:

- Quartet trigger (QRT) defines when a new random sequence of four helicity states has begun.
- The micro-pulse trigger (MPS) at 30Hz is defines the periods when the helicity is valid.
- The helicity sequence has quartet structure (either $+ - - +$ or $- + + -$).

Scaler gating requires two helicity state signals, Hel+ and Hel-. These signals can be constructed using the MPS and helicity signals shown in Figure 3.24. For example, the logical AND between the MPS and the helicity signals gives the Hel+ state, while the logical AND between the MPS and the inverse of helicity signals gives the Hel- state.

The target-spin timing sequence is shown in Figure 3.25. There are two inputs for the formation of the target spin signals. An analogue NMR signal recorded in the lock-in amplifier, when the target is flipped and the status signal (TTL) from the function generator which provides the RF field to the NMR. Using these two signals, a NIM level target spin

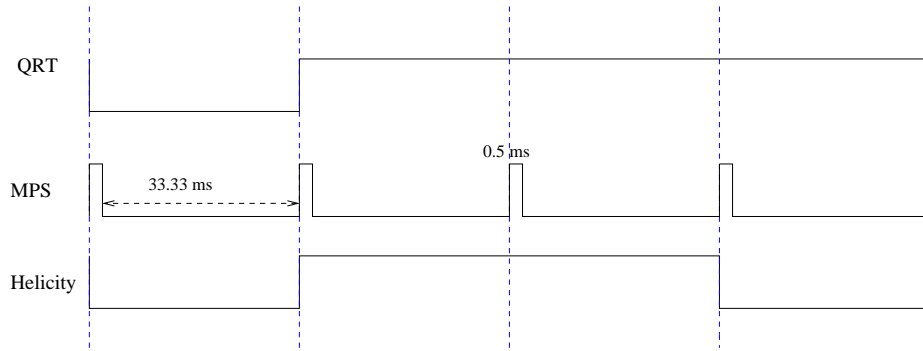


Figure 3.24: Beam helicity sequence during E06-010 experiment.

logic signal is constructed, one for each target state. The target spin-flip sequence is on a much longer time scale. A spin-flip happens every 20 minutes. There was an undefined period of about 5 seconds during the spin-flip.

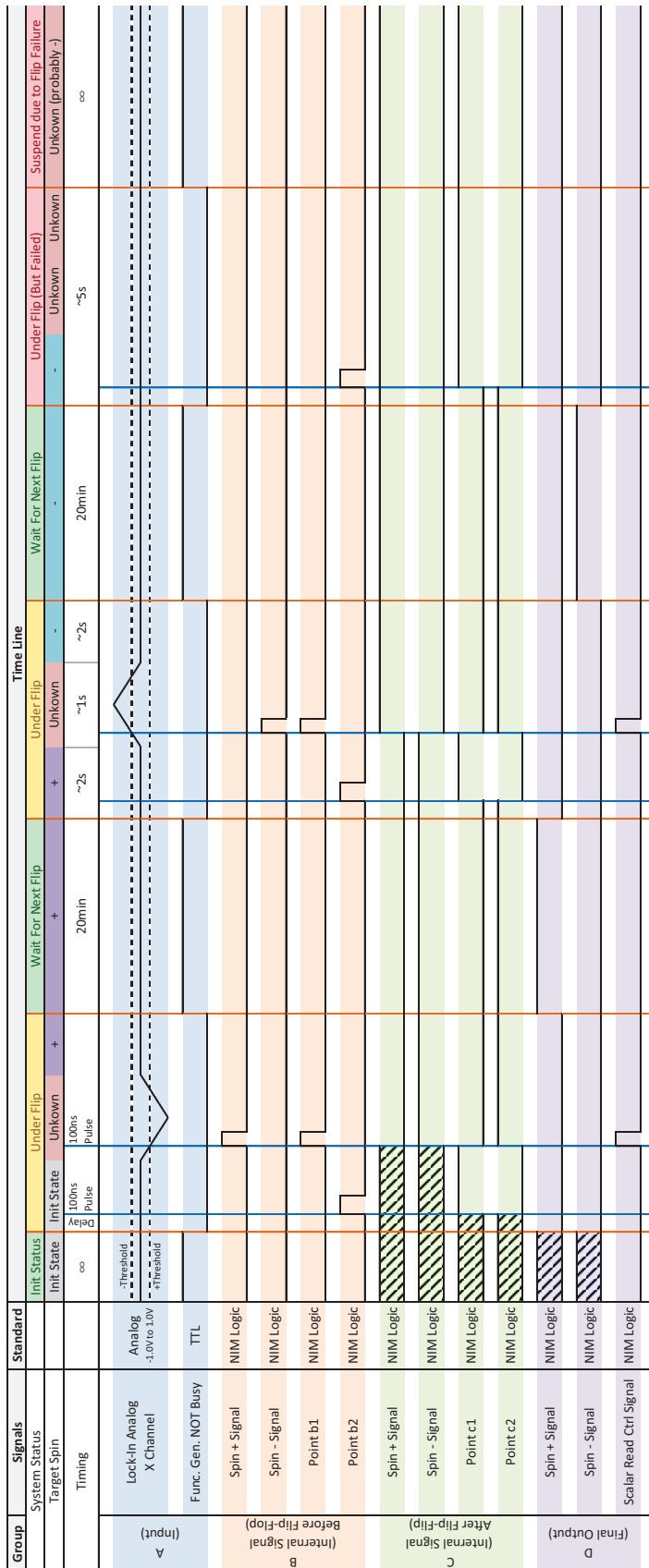
The scalers were read out from the VME server. There are several clients that read scaler information, which included:

- Online GUI display of the real time trigger rates, raw PMT rates, and beam current during the experiment.
- Event type 140 (integrated data) which was inserted into the datastream using the Event Transfer (ET) functionality of CODA. This was done asynchronous to the CODA event.
- Scaler read out from the ROC in-synch with CODA events. This type of read out was done for every 100 CODA events.
- Event-by-event read out. Some of the most important signals like primary triggers and BCM signals were read out every CODA event.
- Writing to a web based electronic log. At the end of each run the final reading of the scaler were written to an electronic log.

Figure 3.25: Timing sequence for the target spin state [11].

Spin Flip Signal Timing Diagram

By Jin Huang <jinhuang@jlab.org>



CHAPTER 4: DETECTOR AND TARGET CALIBRATIONS

This chapter describes the calibration of the detectors and the target. It covers the description of the methods involved in the calibration and the level of accuracy reached in each case.

4.1 Target Polarization Analysis

The polarized ^3He target system is discussed in section 3.2.3. Here we describe the calibration of the NMR signals with an EPR measurements, to determine the absolute polarization of the target. During the experiment the NMR signal was recorded for every 20 minutes spin-flip. An EPR measurement was performed once a week.

The EPR calibration was performed by C. Dutta of the University of Kentucky [14]. The procedure for measuring the target polarization using EPR is given in section 3.2.3. Here we show the polarization results obtained from all the EPR measurements done during the experiment. Figure 4.1 shows the target polarization measured at various times when the target spin were pointing in the "transverse" direction. Similarly, Figure 4.2 shows the polarization when target spins were pointing in the "vertical" direction. The statistical uncertainty is about 2% for most of the measurements, but there were a few measurements with larger uncertainty mostly due to large statistical fluctuations in the alkali Zeeman splitting frequency.

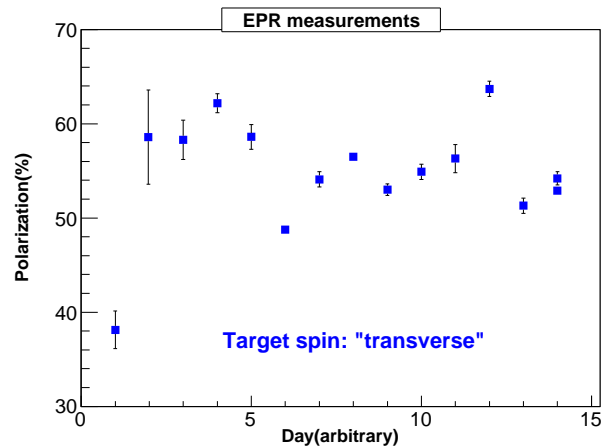


Figure 4.1: ^3He target polarization measured by EPR when the target is in *transverse* direction. This plot is reproduced from [14].

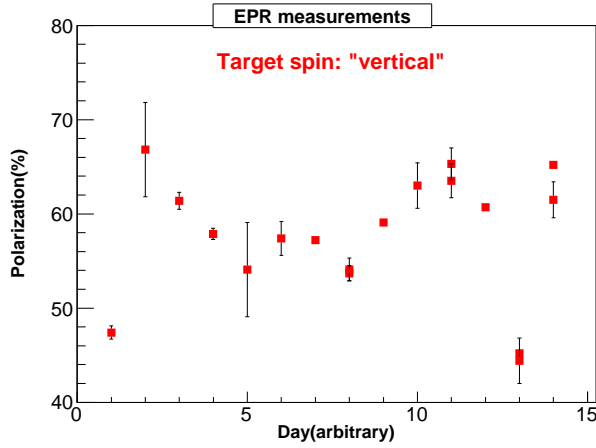


Figure 4.2: ^3He target polarization measured by EPR when the target is in *vertical* direction. This plot is reproduced from [14].

4.1.1 NMR Calibration

The calibration of the NMR signals involves performing an NMR AFP spin-flip followed by an EPR measurement and then another NMR measurement. Let the signal height of the first NMR be $S1$ and for second NMR be $S2$. And, if the absolute polarization obtained by the EPR frequency shift going from state $A \rightarrow B$ is $P1$ and from $B \rightarrow A$ is $P2$ (this can be determined using Eq. (3.9)). Then the proportionality constant between $P1$ and $S1$ gives the calibration between NMR and EPR,

$$P1 = c1 * S1. \quad (4.1)$$

Similarly, $c2$ can be determined from $P2$ and $S2$. The average of $c1$ and $c2$ gives the overall calibration constant. This way every NMR signal can be calibrated to give the absolute target polarization. The history of the target polarization for every 20 minutes spin-flip during the experiment is shown in Figure 4.3.

4.2 BigBite Spectrometer

The BigBite spectrometer provides the momentum and direction of the scattered electron to a very high accuracy. In this section the calibration of the BigBite spectrometer is discussed.

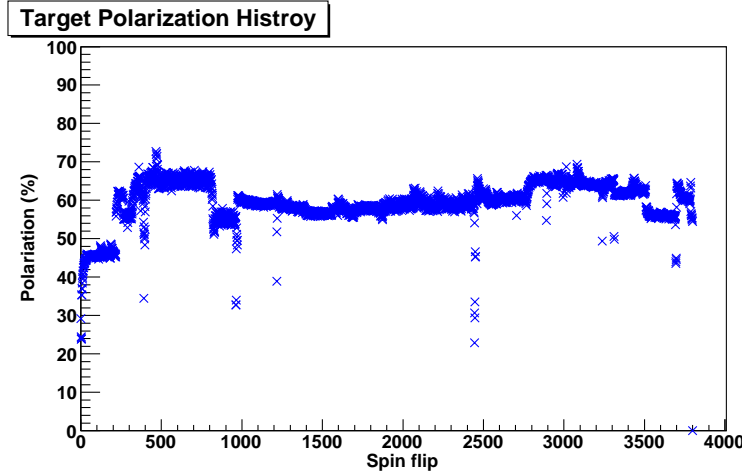


Figure 4.3: History of target polarization during the E06-010 experiment. The x-axis show the number of spin-flips (20 minutes each) [15].

4.2.1 Multi-Wire Drift Chambers

A set of multi-wire drift wire chambers (MWDCs) provided an accurate momentum reconstruction of the tracks of the particles passing through the BigBite spectrometer. In order to precisely reconstruct the tracks passing through the chambers, a number of calibration procedures had to be followed. This calibration was performed by X. Qian of Duke University [12]. The calibration steps included:

- t_0 calibration
- drift time to drift distance conversion
- determination of absolute wire position of individual wires.

The timing information of each wire in the MWDC was recorded in a TDC. This recorded time was the difference between the signal propagation from the wire to the TDC (t_{sig}) and the signal from the BigBite trigger (provided by the calorimeter) to the TDC (t_{trig}). As a particle hits the chamber, it produces an ionization and the resultant electrons drift to certain distance before producing a signal on the wire:

$$t_{sig} = t_{drift} + t_{delay}^1 \quad (4.2)$$

where t_{drift} is the drift time of the electrons and t_{delay}^1 is the propagation time of the signal from the wire to the TDC. t_{trig} is given by the following relation,

$$t_{trig} = t_{hit} + t_{path} + t_{delay}^2 + t_{tw} \quad (4.3)$$

where t_{hit} is the time of the hit, i.e., when the particle reaches the wire chamber. t_{path} is the time it takes for the particle to travel from the hit wire to the BigBite calorimeter, which provides the trigger. t_{delay}^2 is the time for the signal to propagate from the calorimeter to the TDC. t_{tw} is the trigger time-walk effect that needs to be corrected.

Therefore, the recorded TDC time for individual wire (after correcting for the trigger time-walk effect) can be written as,

$$t_{sig} - t_{trig} - t_{tw} = t_{drift} - t_{hit} + t_{delay}^1 - t_{path} - t_{delay}^2 \quad (4.4)$$

which can be approximated to be

$$t_{sig} - t_{trig} - t_{tw} \approx t_{drift} - t_{hit} + t_0. \quad (4.5)$$

Here t_{path} is found to be the same for all types of particles within the momentum range of interest. The effect is less than 1 ns, which is comparable to the resolution of the recorded time in the TDC. The value of the t_0 offset is determined for individual wires by identifying the rising edge of the drift time spectrum above the background events. Figure 4.4 shows a drift time spectrum for one wire in x-plane. This procedure is repeated for all the wires in the three wire chambers.

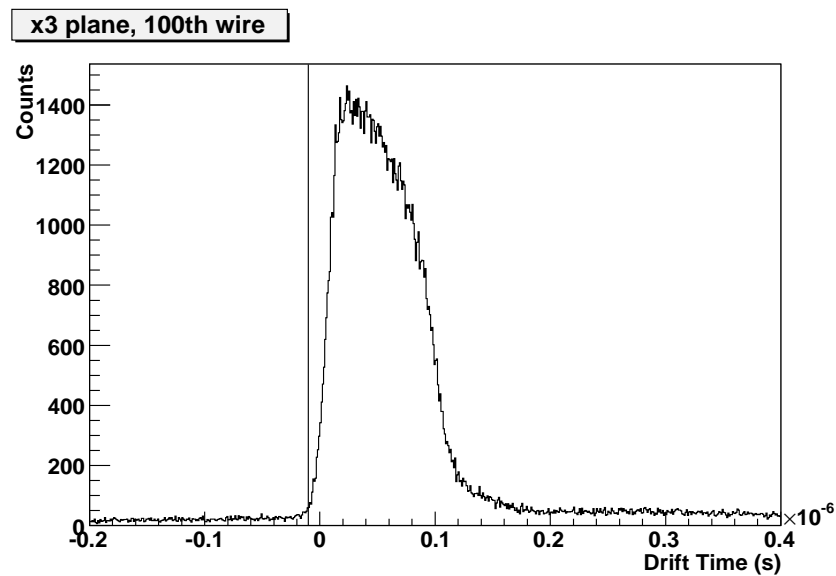


Figure 4.4: Drift time spectrum for the 100th wire in the x plane of the third chamber [12].

The reconstructed track provides the information on the position of the track in each wire plane. Using this information and the known position of the wire that got a hit, we can

calculate the drift distance. This distance is plotted against the drift time and an empirical formula with several polynomials is fitted to the data (see Figure 4.4). This procedure yields the time to distance conversion function.

The chamber position was surveyed before the experiment. The overall chamber position is known from the survey reports. The wire position of the individual wires in the chamber is calibrated by recording the reading from the wirechamber construction report and comparing it with the position of the reconstructed track. The distance between the reconstructed track and the hit wire position is given by a quantity known as track residual, shown in Figure 4.5. Each wire position can be shifted by the central value of the track residual spectrum. The resolution (σ) of the residual peak after calibration was about 180 μm .

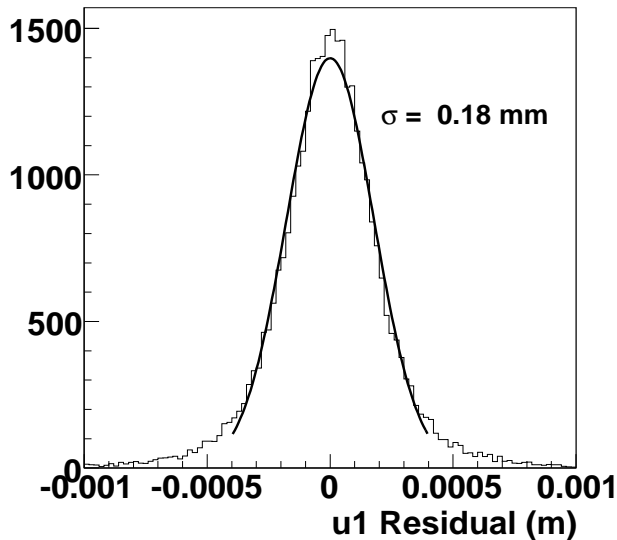


Figure 4.5: The residual peak for the U-plane of the front chamber[12].

BigBite Optics

The BigBite spectrometer optics was calibrated using two different beam energies: $E_0 = 1.23$ GeV and $E_0 = 2.39$ GeV. The momenta of the scattered particles from these two beam energy settings will cover the range of momenta that we are interested in, i.e., 0.8 GeV to 2.2 GeV. In order to perform optics calibrations several steps needed to be followed.

The target, the BigBite magnet, the sieve slit and the chamber positions were surveyed and recorded. The survey reports provided the position information. The position of the

chamber can be calibrated using the data taken with the BigBite magnet turned off. When there is no field in the BigBite magnet the particles hit the detectors without bending, which can be used to directly get the kinematics of the scattered particles from the target.

Before the full vertex and angle reconstruction is performed, a first order optics calibration is done to calculate the particle's momentum and interaction vertex. In first order expansion the optics of the BigBite spectrometer is treated as a perfect dipole and a virtual bending plane is assumed in the middle of the magnet from which particles are bent. The angle between the momentum vector of the particle and the magnet field vector is given by

$$\cos \phi = \frac{\mathbf{B} \cdot \mathbf{p}}{|\mathbf{B}| \cdot |\mathbf{p}|} \quad (4.6)$$

where ϕ is fixed. The naïve interaction vertex is constructed by looking at the intersection of the cone, formed by the fixed angle ϕ , with the beam line. The vector connecting this naïve vertex and the mid point of the the bending plane determines the first order scattering angle.

The first order momentum is given by

$$p = \frac{L}{2 \cdot \tan(\theta_{bend}/2) \cdot \sin(\phi)} \quad (4.7)$$

where L is the distance traveled by the particle inside the magnetic field. θ_{bend} is the particle's bend angle in the plane perpendicular to the magnetic field direction.

Vertex Reconstruction

After the reconstruction of the first order vertex, higher order corrections are applied by looking at the dependence of δz , the difference between the reconstructed vertex and the expected vertex position of the multi-foil carbon target. Various tracking variables like track hit positions in the first chamber tr_x and tr_y , track direction tr_{xp} and tr_{yp} , and the positions of the bend points in the magnet coordinate system, $bend_x$ and $bend_y$ are used. Here tr_{xp} and tr_{yp} are defined as,

$$tr_{xp} = \frac{dtr_x}{dtr_z}, \quad tr_{yp} = \frac{dtr_y}{dtr_z}. \quad (4.8)$$

Since the BigBite spectrometer covers a wide range of momenta, a momentum dependent vertex correction needs to be added to the reconstructed vertex. For this, the first order

momentum is used, based on Eq. 4.7. In addition to this, a fiducial volume cut is added in the magnetic mid-plane in order to exclude top and bottom regions of the magnet where the field is much weaker than in the central region. Figure 4.6 shows the final reconstructed vertex with a resolution of about 1 cm at a momentum of 0.95 GeV. In the momentum range of 0.8-2.0 GeV the average resolution is about 0.8 cm (see Fig 4.7).

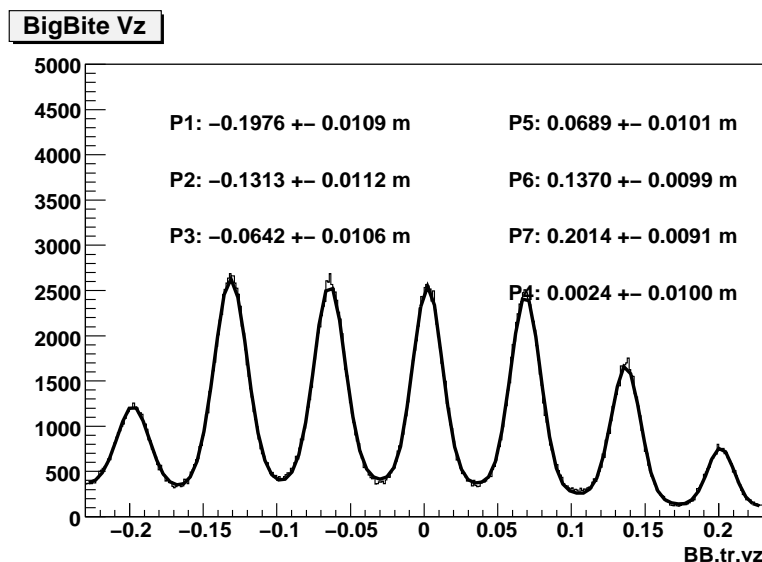


Figure 4.6: Reconstructed vertex for the multi-foil carbon target at a particle momentum of 0.9 GeV [12].

Angle Reconstruction

A lead sieve plate with different patterns and a thickness of 1.5", mounted in the front of the magnet, was used to reconstruct the scattering angle in the BigBite spectrometer. In first order the angle is reconstructed by connecting the reconstructed vertex with the middle point. Figure 4.8 shows the real sieve plate and Figure 4.9 shows the reconstructed sieve pattern. For higher order correction to the angle, a procedure similar to the one used for vertex reconstruction is adopted.

Momentum Reconstruction

The momentum calibration is done using elastic electrons scattered off a hydrogen target at two different beam energies: 1.23 and 2.39 GeV. Elastic electrons were selected by graphical cuts in the δp vs. $bend_x$ plot where δp is the difference between first order reconstructed

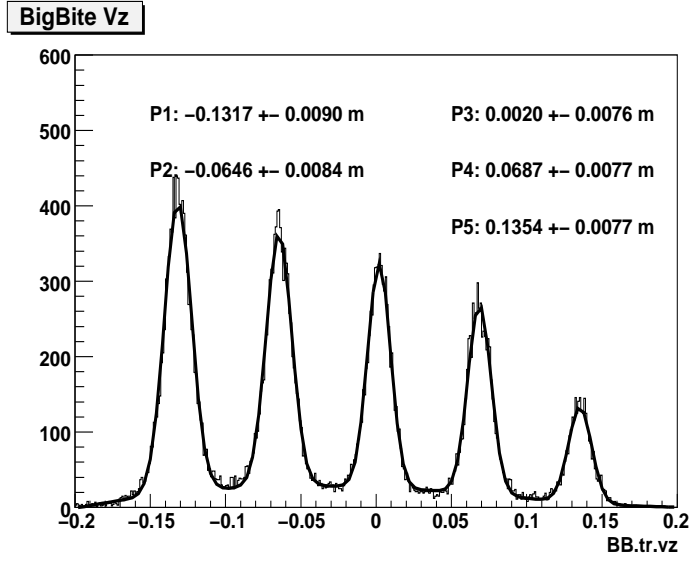


Figure 4.7: Reconstructed vertex for the multi-foil carbon target at a particle momentum of 1.2 GeV [12].



Figure 4.8: A lead sieve slit plate with a thickness of 1.5".

momentum and the expected momentum in elastic kinematics. Since the scattered electrons pass through various materials before hitting the chamber, energy loss effects are applied to both the beam and the scattered electrons. Using these events, a first order momentum is reconstructed and additional corrections were applied using a look-up table depending on the middle point position of the selected events. The corrections are given by,

$$p^{(1)} = z_0 \cdot p^{(0)} + z_1 + z_2 \cdot tr_x + z_3 / \theta_{bend} \quad (4.9)$$

where the z_0 , z_1 , z_2 , and z_3 are functions of the middle point position $bend_x$ and $bend_y$. Figure 4.10 shows the final resolution achieved using this procedure. An average resolution of 1% was obtained in the entire momentum range. Since the calibration was done at two

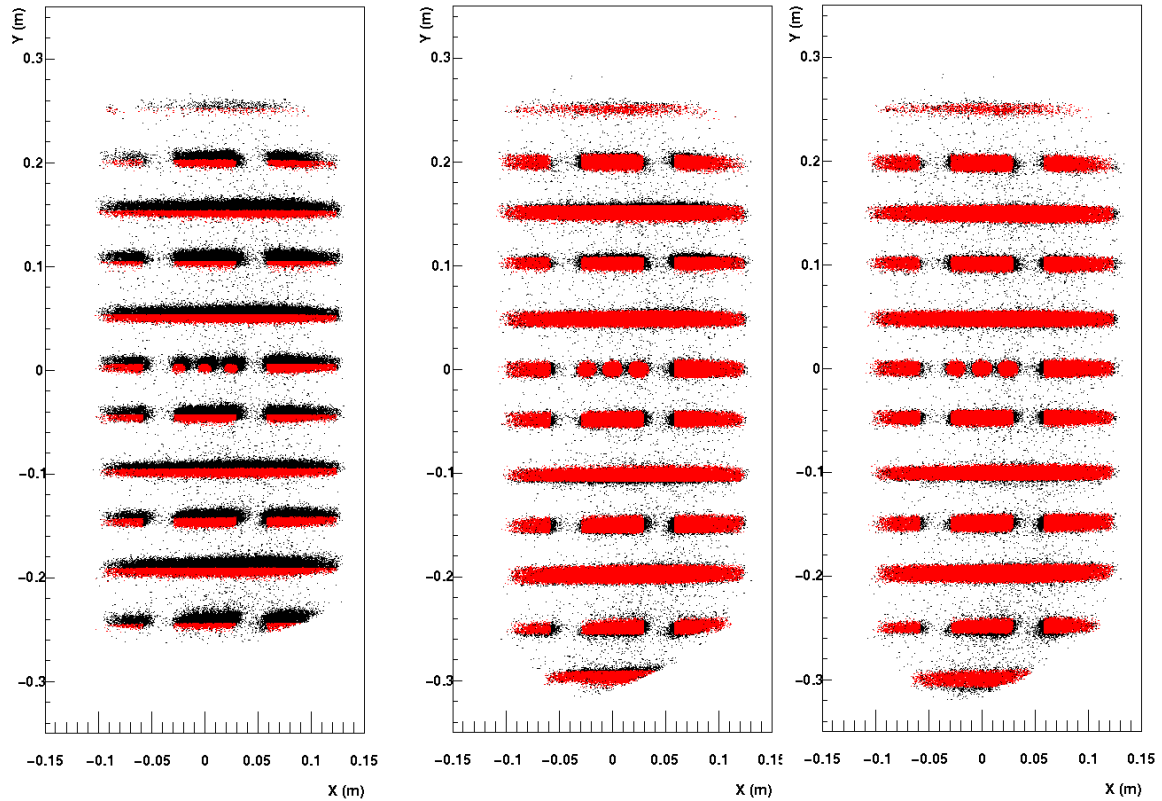


Figure 4.9: The left panel shows the reconstructed sieve pattern with first order optics model. The middle panel shows the sieve pattern after adding offsets. The right panel shows the sieve pattern after applying higher order corrections. The red points indicates where the sieve holes/slots are actually located [12].

momentum points, it is crucial to check the reliability of the optics in the range beyond these two points. This can be done by looking at the missing mass (W) spectrum and identifying the resonances. In Figure 4.11, the top(bottom) left panel shows the reconstructed missing mass spectrum for a beam energy of 1.23 (2.39) GeV where one can clearly see the $\Delta(1232)$ and higher mass resonances at the right values of W . The right side panels show the momentum vs. scattered angle correlations from which clear elastic events can be identified. Similarly, for momenta beyond 2.36 GeV, hydrogen elastic events from a 5-pass beam energy of 5.892 GeV were used to check the optics quality.

BigBite is an open geometry spectrometer and both positive and negative particles can reach the detectors, but they bend in opposite directions. Therefore it is necessary to calibrate the optics using the positive charged particles, too. A positive optics model was

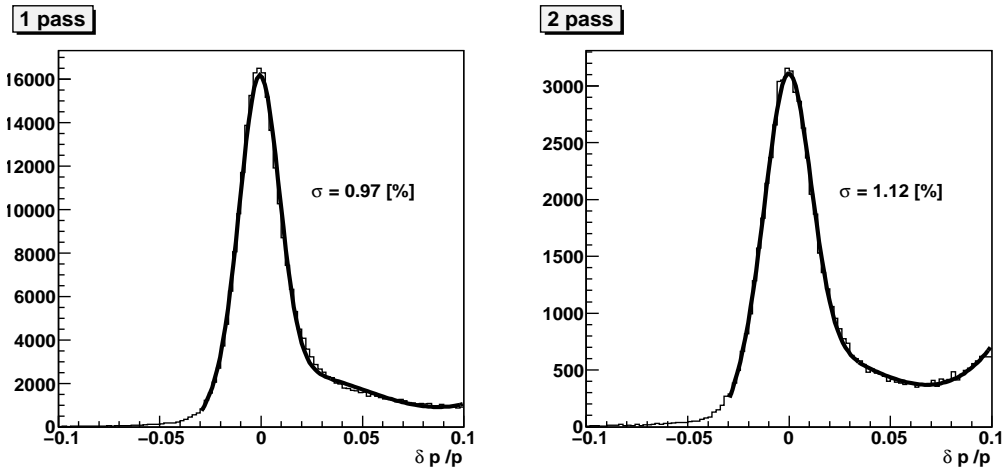


Figure 4.10: Final momentum resolution achieved with two beam energies: left panel is for $E_0 = 1.23$ GeV and right panel is for $E_0 = 2.39$ GeV [12].

developed using the data taken by reversing the magnet polarity. Due to some practical issues, the runs were taken at 45° instead of the usual BigBite spectrometer setting of 30° . The positive mode optics developed at 45° was applied to 30° and checked against the negative mode optics for both 30° and 45° . The model gives a good description of the reconstructed momentum, vertex, and angle. Figure 4.12 shows the momentum resolution achieved using positive optics. Figure 4.13 shows the vertex reconstruction.

4.2.2 Preshower and Shower

The BigBite calorimeter consists of a preshower detector and a shower detector, both made of lead-glass as described in Section 3.2.5. It was used for triggering the BigBite spectrometer and for particle identification of the scattered electrons. A detailed description of the BigBite trigger is given in Section 3.3.1. The total energy of the detected particles is roughly proportional to the sum of the cluster amplitudes in both the preshower and shower detectors. In order to accurately measure this quantity, the detectors have to be calibrated to a known energy of the incident particle. For this experiment, the elastic reaction, $H(e, e')X$, on a H_2 target was chosen with two different incident beam energies, $E_0 = 1.23$ GeV and $E_0 = 2.39$ GeV. Also, the preshower and shower detectors were initially gain matched with cosmic rays for a rough alignment of the ADC amplitudes by adjusting the high voltage on the PMTs. The calibration procedure using these two methods, using cosmic rays and elastic events, is described in the following sections.

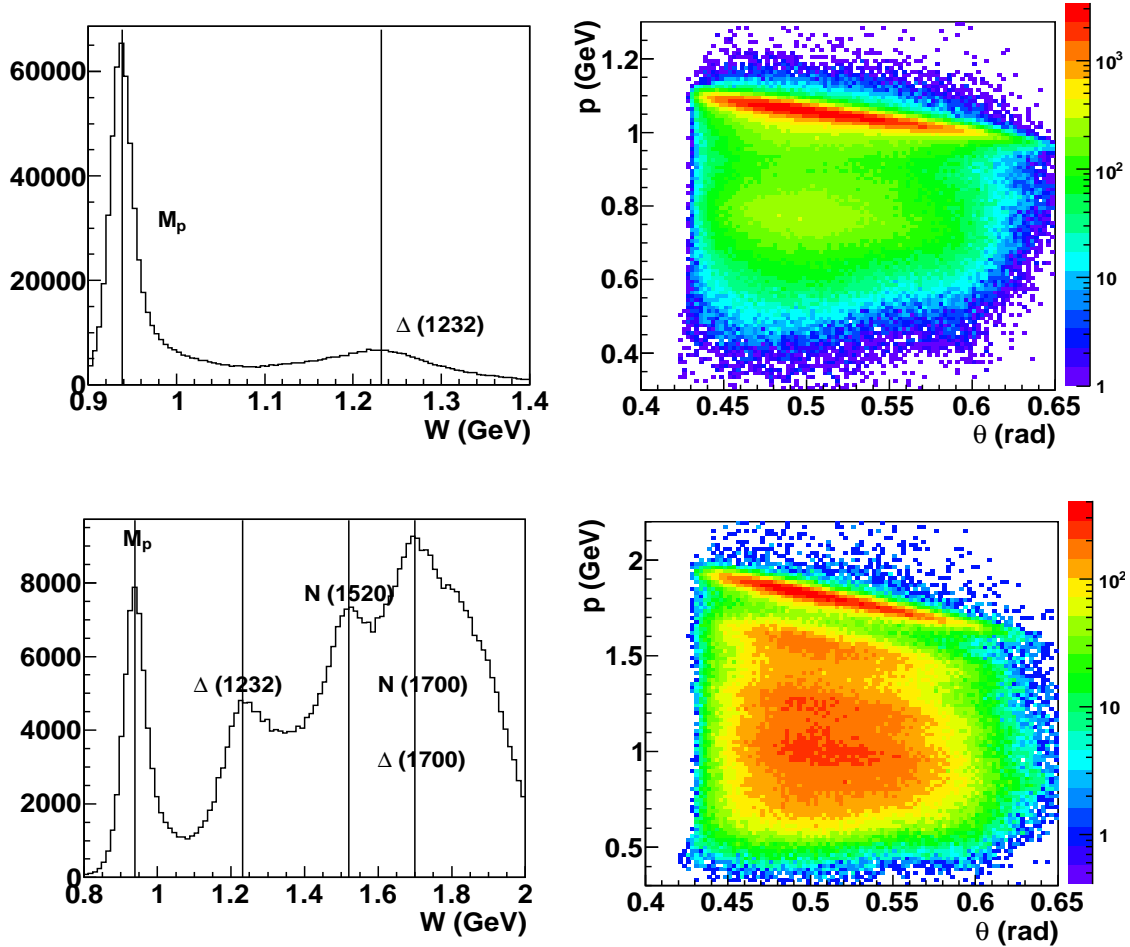


Figure 4.11: BigBite optics check: The left side top(bottom) panels show the reconstructed missing mass peak of the proton and other resonances for beam energies of 1.23 GeV (2.39 GeV). The right side panels show the momentum vs. scattering angle θ correlations at the beam energies of 1.23 GeV and 2.39 GeV [12].

Calibration Using Cosmic Rays

A scintillator trigger was set up in order to align the ADC amplitudes generated by the cosmic rays passing vertically through the lead-glass blocks. Two scintillators were mounted, one on the top and one on the bottom of the detector. Each scintillator had two PMTs, one on each side. A trigger was constructed by making a logical AND of all four PMTs, such that cosmic rays passing vertically through the detector were triggered. By making offline cuts, events passing vertically through the detector were selected. These high energy cosmic rays (mostly muons) leave minimum ionization in each block, giving a well defined energy loss peak in the ADC. These ADC peaks were then aligned by adjusting the high

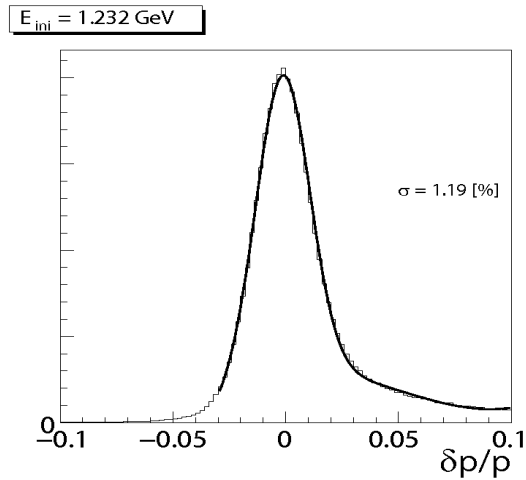


Figure 4.12: Momentum resolution for positive optics data at 1.23 GeV [12].

voltage on the PMTs in an iterative procedure. The preshower amplitude was aligned to ADC channel 240 and the shower amplitude was aligned to channel 120. Figure 4.14 shows an event display before and after aligning the amplitudes in all the blocks in the shower detector. Figure 4.16 shows the peak value in each block in both the shower and preshower detectors.

Shower Cluster Reconstruction

The aim of shower cluster reconstruction is to determine the energy and position of the particle, which generates an electromagnetic shower in the detector. A cluster is defined as a group of continuous shower blocks where the energy loss due to the electromagnetic shower is detected. The block that has maximum energy in the cluster is known as the central block. There can be more than one cluster per event in the shower and preshower detectors. The cluster reconstruction algorithm identifies all the clusters, with a lower cut off on the energy and saves the energy and position information for analysis. The basic steps in identifying a valid cluster in the shower and preshower are as follows:

- Search for the block where largest energy is deposited in the shower, known as central block.
- Sum over 8 blocks surrounding this central block to get the cluster energy in the shower.

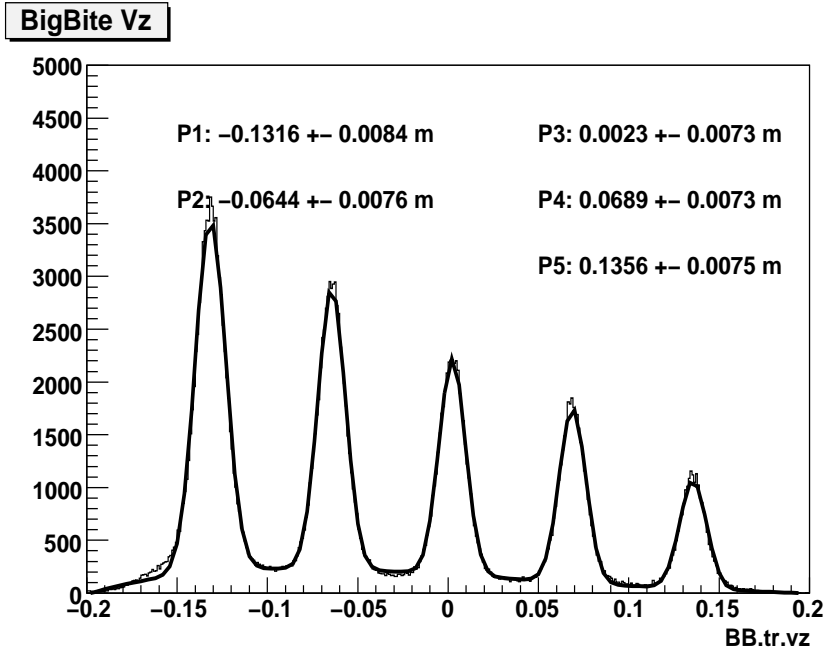


Figure 4.13: Reconstructed vertex for the multi-foil carbon target using positive optics data [12].

- This procedure is repeated to find additional clusters in decreasing order of the energy and saved.
- Corresponding to the largest cluster in the shower detector, find a matching cluster in the preshower detector within a certain distance. If not found, then this cluster is not valid, and the next cluster in the shower detector is chosen.
- If found, then sum over 6 blocks (3 in each row) in the preshower detector with maximum amplitude block at the center. This sum gives the cluster energy in the preshower detector.
- For the final validity of the clusters, the track projection on the shower X and Y coordinates is matched with the reconstructed position of the cluster within a certain distance (typically, size of 2 blocks). If no match is found then the procedure is repeated until all the above conditions are satisfied.
- If all of the above conditions are met, then position and energy information of the clusters in the preshower and shower detectors are stored for further analysis.
- Photon tracks are constructed in a similar fashion, but as they do not leave a signal

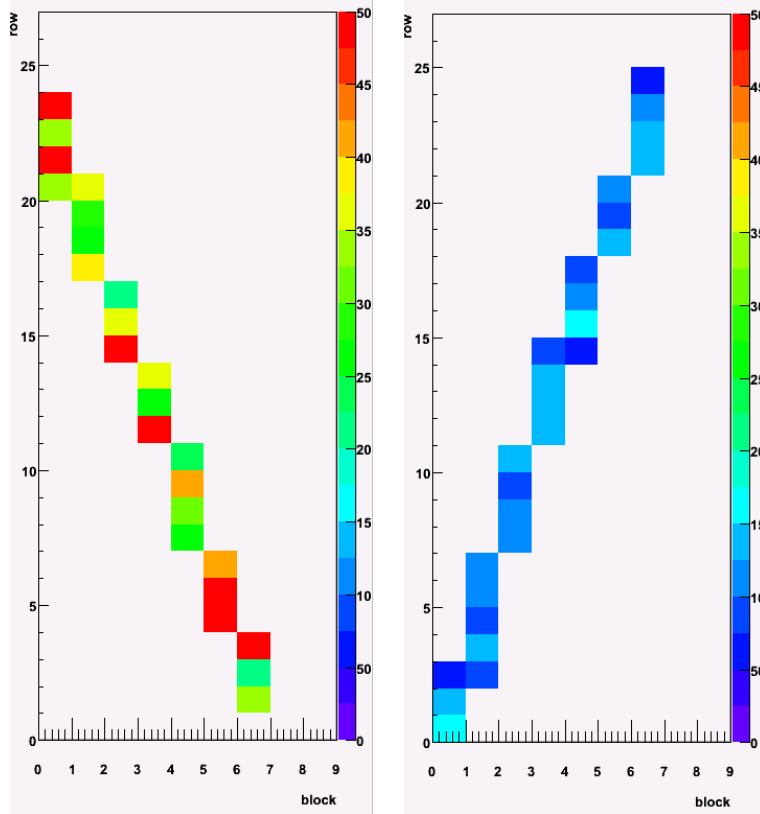


Figure 4.14: Event display for an uncalibrated(left) and calibrated(right) shower. The colors shows the strength of the ADC amplitude.

in the wire chambers, the position of the photon cluster cannot be matched with that of the projected track from the wire chamber.

The energy E of the cluster is calculated as the sum of the energies deposited in all the blocks in the cluster.

$$E = \sum_{i=1}^M E_i, \quad (4.10)$$

and the X and Y-coordinates are calculated using the energy weighting method.

$$X = \sum_{i=1}^M E_i \cdot X_i / E, \quad Y = \sum_{i=1}^M E_i \cdot Y_i / E, \quad (4.11)$$

where M is the number of blocks in the cluster.

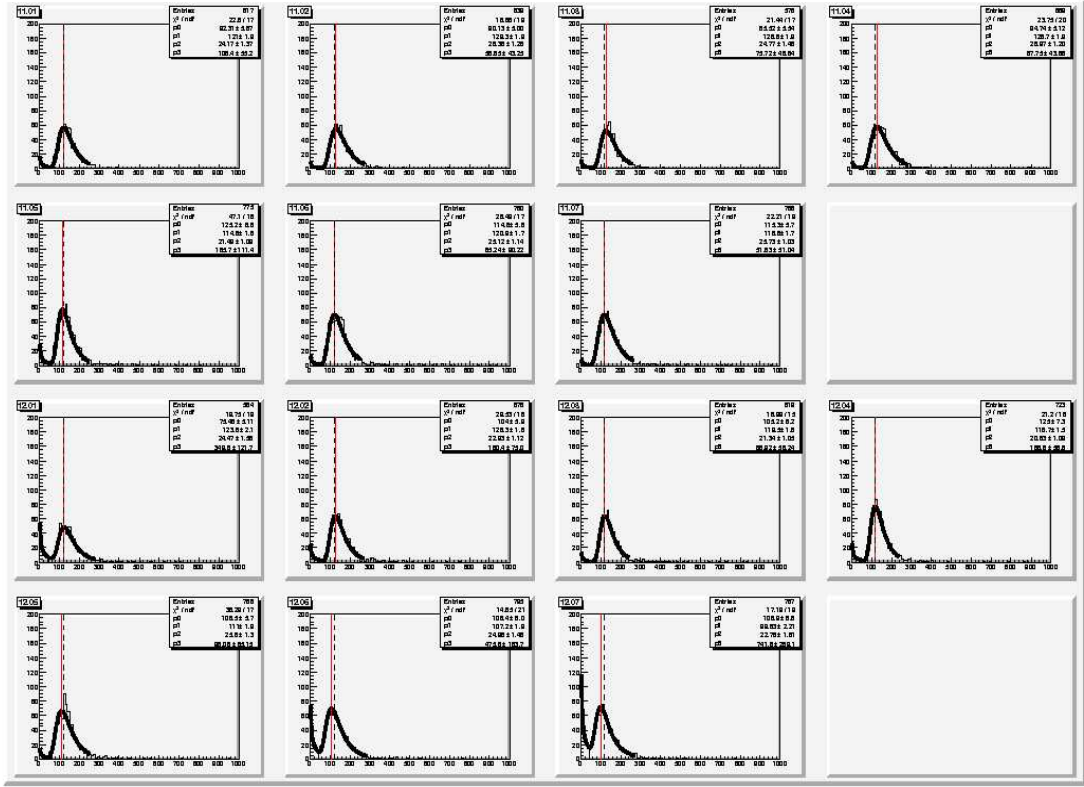


Figure 4.15: Shower ADC amplitudes fitted with a Gaussian+Landau distribution tail shape.

Preshower and Shower Gain Calibration Using Elastic Events from H_2 Target

The BigBite preshower and shower detectors were calibrated using events from the H_2 elastic reaction, $H(e, e')X$, with two different incident beam energies, $E_0 = 1.23$ GeV and $E_0 = 2.39$ GeV. The energy (momentum) of the scattered electron in this reaction can be calculated using the formula,

$$E_e = \frac{M_p E_b}{(M_p + E_b(1 - \cos\theta))}, \quad (4.12)$$

where M_p is the mass of the proton, E_b is the beam energy and θ is the scattered angle of the electron, which is given by the track of the event.

The calibration of the detector involves finding the coefficients C_i for every block which transform the ADC amplitudes to the energy deposited,

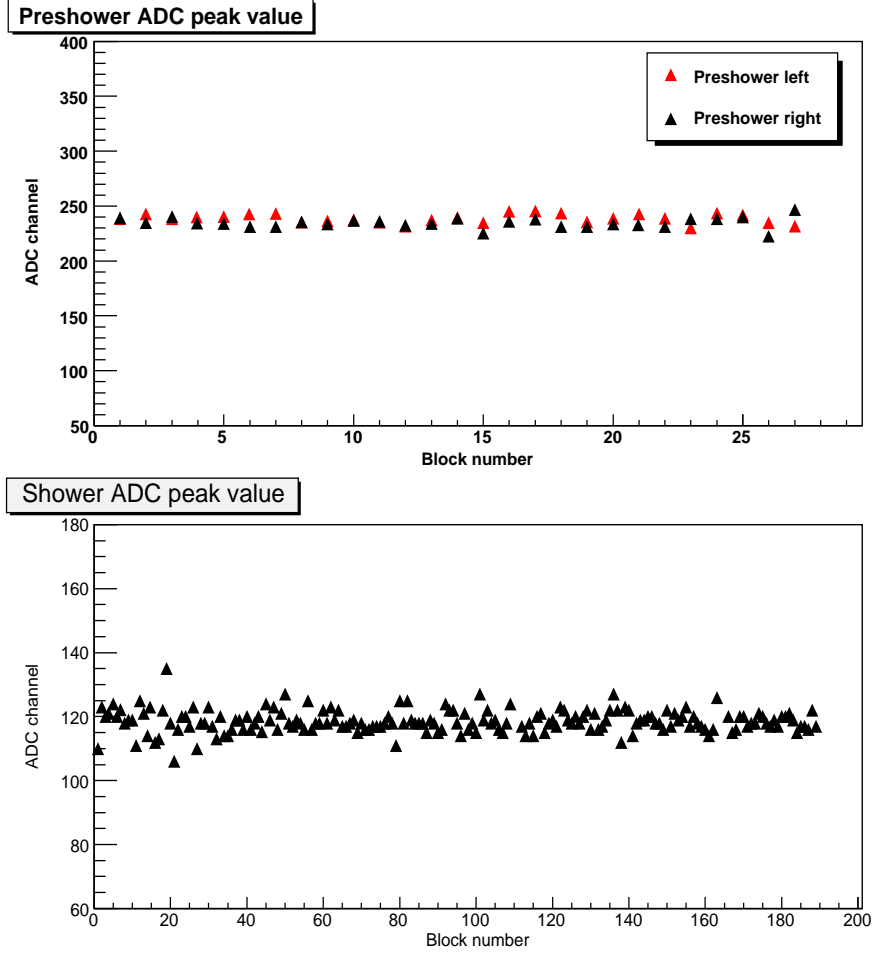


Figure 4.16: Peak of the ADC amplitudes of the preshower and the shower detector blocks after a rough alignment using the high voltage.

$$E_i = C_i \cdot (A_i - P_i) \quad (4.13)$$

A_i is the raw ADC amplitude, P_i is the pedestal, and E_i is the energy deposited in i^{th} block. This can be achieved by minimizing the χ^2 , which is defined as the squared difference between the particle's measured energy and calculated energy, summed over all elastic events. In order to achieve this, a linear minimization method was used to obtain the coefficients for every block. There are a total of 243 blocks (189 for the shower detector and 54 for the preshower detector) that needed to be calibrated. The procedure to minimize χ^2 is described below.

Let E_e be the energy of the scattered electron, as given by the tracking, C_k be the coefficient for k^{th} block, and A_k be the pedestal subtracted ADC amplitude measured in

the k^{th} block. For N elastic events the χ^2 is given by,

$$\chi^2 = \sum_{i=1}^N \left(E_e^i - \sum_{j=0}^M C_j A_j^i \right)^2 = \sum_{i=1}^N \left((E_e^i)^2 + \left(\sum_{j=0}^M C_j A_j^i \right)^2 - 2E_e^i \sum_{j=0}^M C_j A_j^i \right), \quad (4.14)$$

where M is total number of the blocks in a shower and preshower cluster. Here A_j is the pedestal subtracted ADC amplitude of the j^{th} block. By setting the derivative of χ^2 with respect to C_k to zero, a set of linear equations can be obtained:

$$\frac{\partial \chi^2}{\partial C_k} = 0, \quad (4.15)$$

$$2 \sum_{i=1}^N \left(\sum_{j=0}^M C_j A_j^i \right) A_k^i - 2 \sum_{i=1}^N E_e^i A_k^i = 0, \quad (4.16)$$

$$\sum_{j=1}^M \left(C_j \left(\sum_{i=0}^N A_j^i A_k^i \right) \right) = \sum_{i=1}^N E_e^i A_k^i, \quad (4.17)$$

The system of linear equations can be represented in matrix form,

$$MC = B \quad (4.18)$$

where

$$B = \begin{pmatrix} \sum_{i=1}^N E_e^i A_0^i \\ \cdot \\ \cdot \\ \cdot \\ \sum_{i=1}^N E_e^i A_M^i \end{pmatrix}, \quad (4.19)$$

$$C = \begin{pmatrix} C_0 \\ \cdot \\ \cdot \\ \cdot \\ C_M \end{pmatrix}, \quad (4.20)$$

and the matrix elements of the matrix M can be written as

$$M_{lm} = \sum_{i=1}^N A_l^i A_m^i. \quad (4.21)$$

By inverting the matrix and solving the linear system of equations the coefficients in the vector C can be obtained.

This calibration procedure was implemented using the combined data from two H_2 elastic runs, one taken with beam energy $E_0=1.23$ GeV and the other with $E_0=2.30$ GeV.

The momentum range of the scattered electrons covers roughly the range of interest (0.8 GeV - 2.0 GeV) for the semi-inclusive DIS events with the polarized ^3He target. The elastic events were selected by putting a cut on the momentum vs. scattered angle(θ) and selecting the elastic stripe (see Figure 4.11). In addition to this, cuts were placed on the deposited energy in the preshower detector to select the electrons. The events selected in this way were used to calibrate the preshower and shower detectors and a single set of calibration constants was obtained. One set of coefficients was used for the entire data of the E06-010 experiment.

Figure 4.17 shows the coefficients obtained for the preshower and shower blocks using this method. On average the coefficients are close to 0.5 but some of the blocks differ from this value. One reason is that the blocks on the edges do not have a large acceptance and the other reason is that, even though the gain was matched before the experiment, few blocks in the shower had very low amplitudes on their PMTs during the normal data-taking period, so the calibration coefficients for these PMTs were different than the average value.

The reconstructed energies in the calorimeter for the two different incident beam energies is shown in Figure 4.18. An energy resolution of about $\sigma_{E/p} = 8\%$ was achieved for the calorimeter. Figure 4.19 shows the plot of total energies divided by the momentum of the electrons for the two incident beam energies. The energy resolution in the case of higher momentum electrons is a little bit better than for the lower momentum electrons.

Particle identification can be done by examining the signal in the preshower detector. Hadrons (in this case mostly pions) leave a small signal in the preshower detector due to minimum ionization whereas electrons leave a large signal in the preshower (Figure 4.20). Electrons can be selected by placing a cut greater than channel 400 and hadrons can be selected by requiring that all the events generate a signal lower than channel 300. The detailed particle identification cuts are discussed in chapter 5.

4.3 High Resolution Spectrometer

One High Resolution Spectrometer(HRS) was used to detect the outgoing hadrons in coincidence with the electrons detected in the BigBite spectrometer. Unlike BigBite, which is an open geometry spectrometer, the HRS is a focusing spectrometer, where the magnet polarity can be changed to allow either positively or negatively charged particles to be focused on to the detectors. A brief description of the detector calibration procedures involved is

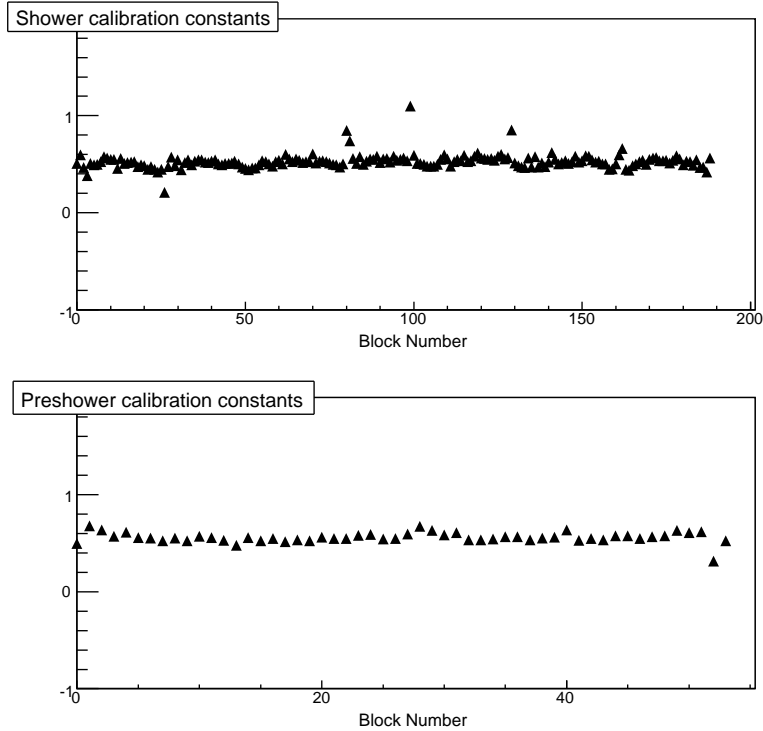


Figure 4.17: Preshower and shower detector calibration coefficients.

given in this section.

4.3.1 Vertical Drift Chambers

Vertical Drift Chamber (VDC) calibrations involve t_0 calibration and optimizing the optics calibrations for a good vertex and momentum reconstruction from a 40 cm long target. The optics calibrations were performed by J. Huang [17] (MIT). The calibration was performed with special elastic runs taken with different targets such as a 7-foil carbon target, ^3He , N_2 , and H_2 gas. The vertex calibration was done using the surveyed positions of the carbon foils along the target length. The positions of the reconstructed tracks from different carbon foils were aligned to the actual positions of the foils at the target. Figure 4.21 shows the vertex reconstruction plot. All 7 foils are aligned to their actual position and an average resolution of 6 mm was achieved for z_{react} . Also the coincidence BigBite and HRS vertexes agree at the level of 1 cm.

The out-of-plane angle (θ_{tg}) and the in-plane angle (ϕ_{tg}) were calibrated by minimizing the difference between the actual value and the reconstructed angle. Survey reports provide the information on the actual values of the angle.

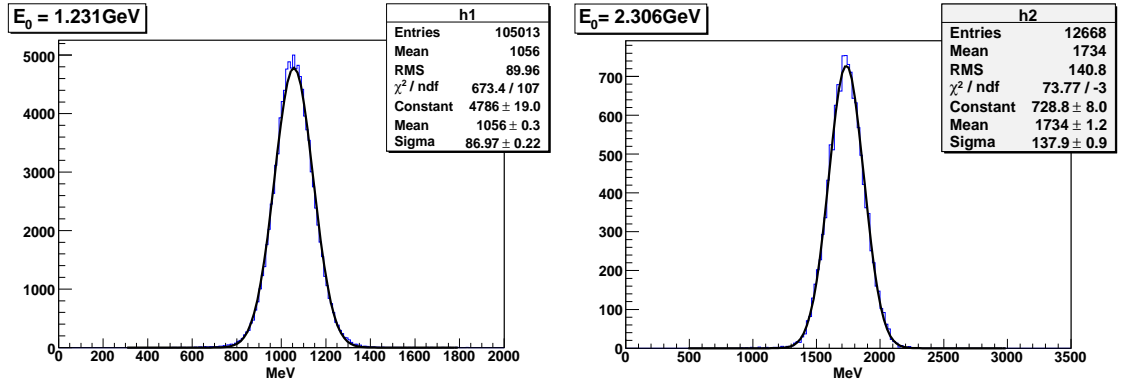


Figure 4.18: Reconstructed energy of electron in the preshower+shower detector signal at two incident beam energies.

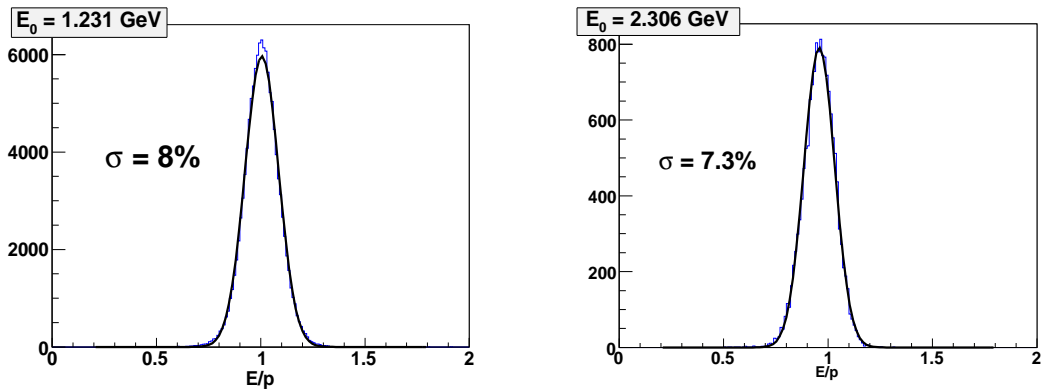


Figure 4.19: Energy divided by momentum of the electrons in the preshower+shower at two incident beam energies

The momentum of the outgoing particle was calibrated using the data taken with carbon target in elastic kinematics. A scan of the momentum was performed by moving the carbon elastic peak across the focal plane at $p_0 = 0\%, \pm 2\%$, and $\pm 4\%$. An optimization of the momentum was done by choosing the specific ground state and a specific excited state of the carbon nucleus [17]. A resolution of about $5 \cdot 10^{-4}$ was achieved using this procedure.

4.3.2 Gas Čerenkov Detector

A gas Čerenkov counter was used for particle identification. It was very useful for rejecting electrons, which was the primary background for the π^- and K^- detection in the negative polarity mode of the HRS. The calibration of this detector was performed by C. Dutta.

The calibration of the gas Čerenkov detector was performed by aligning the single photoelectron peak of each ADC spectrum to channel 200. This was done by fitting a Gaussian

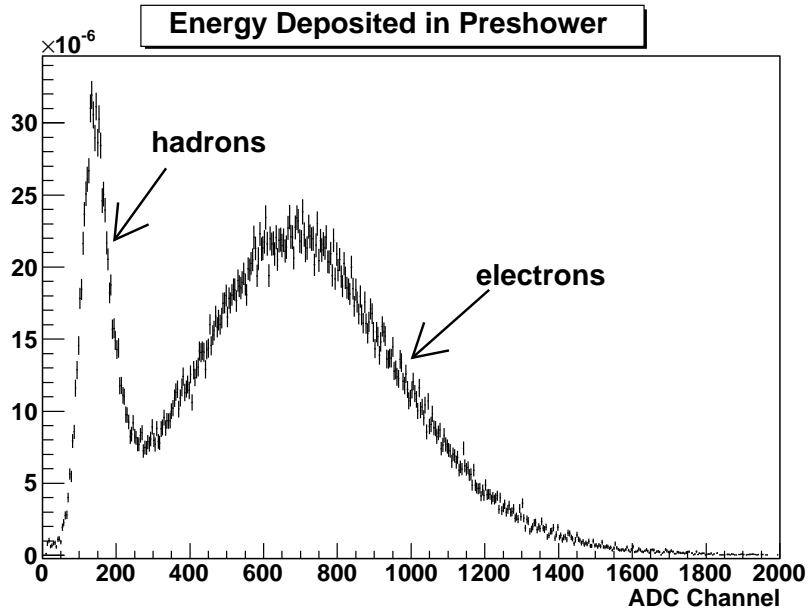


Figure 4.20: Preshower energy spectrum showing a clear separation between pions and electrons. The minimum ionizing pions peak around channel 180 and electron like events peak around channel 700.

shape to the individual photo-electron peaks and scaling the mean value to channel 200. Then the sum of all 10 ADCs was constructed with the single photo-electron peak aligned at channel 200. Since pions and other hadrons peak around one specific channel (200) in the ADC spectrum, whereas electrons generate large signal in the ADC, one can separate the particles by cutting on the ADC value. Figure 4.22 shows the ADC sum spectrum of the gas Čerenkov detector for a negative polarity run. After performing a detailed cut efficiency study a cut on the ADC sum less than 250 channels was used in the analysis. This will reject the electrons with an efficiency of 99%.

4.3.3 Aerogel Detector

This is a threshold aerogel Čerenkov detector which is used for detecting pions. Before the experiment a rough calibration was performed by aligning the single photo-electron peaks due to minimum ionizing cosmic rays. This was done by adjusting the high voltage on the PMTs. During the experiment the detector was calibrated using real data. The single photo-electron peaks were aligned to channel 100 in the ADC. Similar to the gas Čerenkov detector, an ADC sum is constructed using all 24 PMT signals. Figure 4.23 shows the spectrum of the ADC sum signal for a positive polarity run. The sharp peak at channel

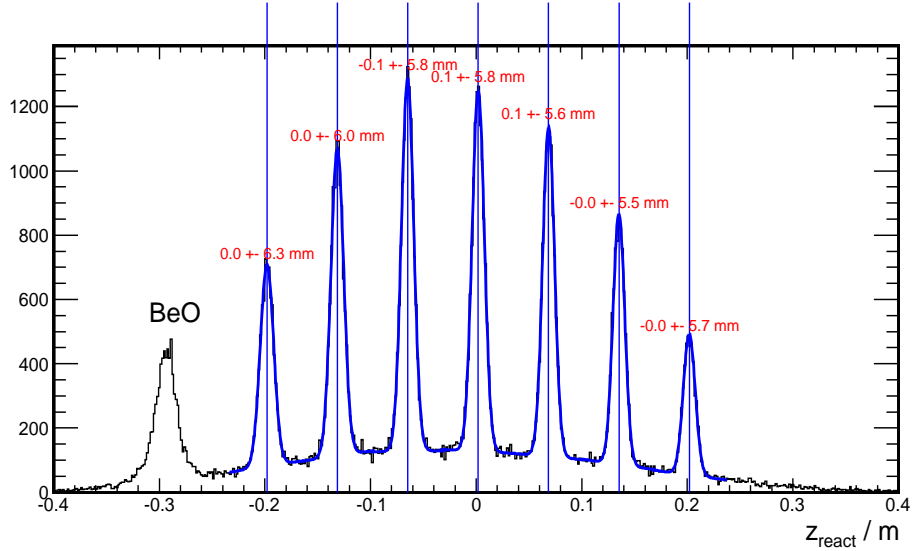


Figure 4.21: Reconstructed vertex z_{react} for a multi-foil carbon target with a BeO target mounted in the front [16].

100 is mostly due to protons. A cut on ADC sum < 150 channels rejects 97% of the pions. This cut was used for identifying kaons from the coincidence time-of-flight spectrum.

4.3.4 Lead-glass Detector

In the lead-glass detector the hadrons leave minimum ionization peaks and electrons leave large signals due to the electromagnetic showers. The calibration was performed by aligning the minimum ionization peak in each block to channel 100 in the ADC and making an ADC sum of all the blocks in the two-layered lead-glass detector. Figure 4.24 shows the energy divided by momentum (E/p) spectrum where a clear separation between pions and electrons is seen. A cut efficiency study was done and a cut on $E/p < 0.65$ was applied to choose the pions.

4.4 Coincidence Time-of-Flight

In this experiment two particles are detected in coincidence with each other - an electron in the BigBite spectrometer and a hadron in the HRS. Also, since the path length of the particles traveling through the HRS is about 25 m before they hit the detectors, we can calculate the coincidence time-of-flight (CTOF) of various particles. The detected time will be different for different particles, due to differences in their masses. The coincidence

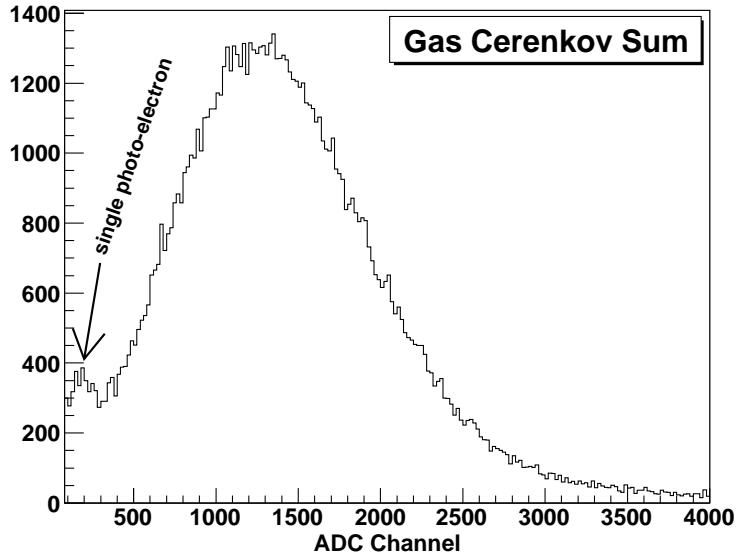


Figure 4.22: ADC sum of the gas Čerenkov detector.

time-of-flight is defined as the time difference between two particles that are created in the reaction. Therefore, ideally we should obtain a sharp peak centered around zero for a particular species of particle. If more than one particle is detected then the time difference will show up at different locations in the CTOF spectrum.

A good coincidence time-of-flight information will help to reduce background events and also help in particle identification. In our case, the kaon and proton peaks are separated by ~ 1.8 ns and ~ 6 ns, respectively, from the pion peak. The coincidence TOF can be separated into three parts [17][16].

$$t_{coin} = t_{HRS}^{RF} - t_{BB}^{RF} + \Delta t_{trigger} \quad (4.22)$$

where t_{coin} is the coincidence time, $\Delta t_{trigger}$ is the time difference between two single arm triggers, t_{HRS}^{RF} is the time difference between the vertex reaction and the single arm trigger for the HRS, similarly for BigBite it is t_{BB}^{RF} . Here $t_{HRS/BB}^{RF}$ include:

- Time-of-flight of the particle from reaction point to the scintillators.
- Detector response time including cable delays and processing by electronics.
- Difference in timing detector (BigBite Scintillator) signals and trigger signals (BigBite Calorimeter). These differences in time were recorded using high resolution (60 ps) TDCs.

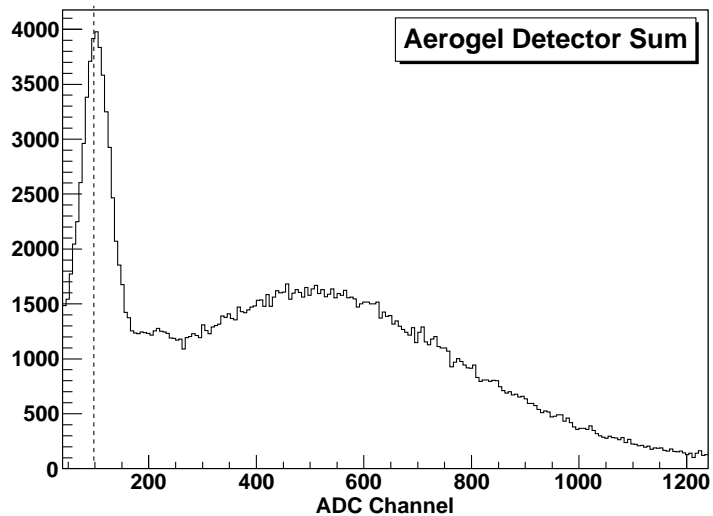


Figure 4.23: ADC sum of the Aerogel detector for data taken at various times during the experiment [17].

$t_{HRS/BB}^{RF}$ is calibrated in individual spectrometers by using the beam radio frequency (RF) signal. The beam RF signal provides the timing for each beam bunch (each electron beam bunch is separated by 2 ns). This signal is recorded in the TDC (t_{RF}). The difference of $t_{HRS/BB}^{RF}$ and t_{RF} is minimized in both spectrometers separately before calculating the coincidence time. In the following section we briefly describe the calibration of the single arm timing detectors before showing the results of the coincidence TOF.

4.4.1 HRS and BigBite Single Arm Timing Calibrations

The HRS timing was determined by the S2m scintillators. The goal was to reach below few hundred picoseconds resolution. Therefore it was necessary to perform various corrections on the scintillator timing, including pathlength correction, time-walk corrections, and scintillator timing offset corrections. Figure 4.25 shows the resolution of the S2m time for pion like events after all the corrections. A resolution of 140 ps was achieved for this detector.

In the BigBite spectrometer the scintillator plane was inserted between the preshower and shower counters. Therefore an electron coming from the target can induce a shower of secondary particles at the preshower which in turn can leave a signal in the scintillator, along with the primary electron. The calibration procedure involves two steps:

- Time-walk and bar offset correction: This is done by choosing the events with a hit

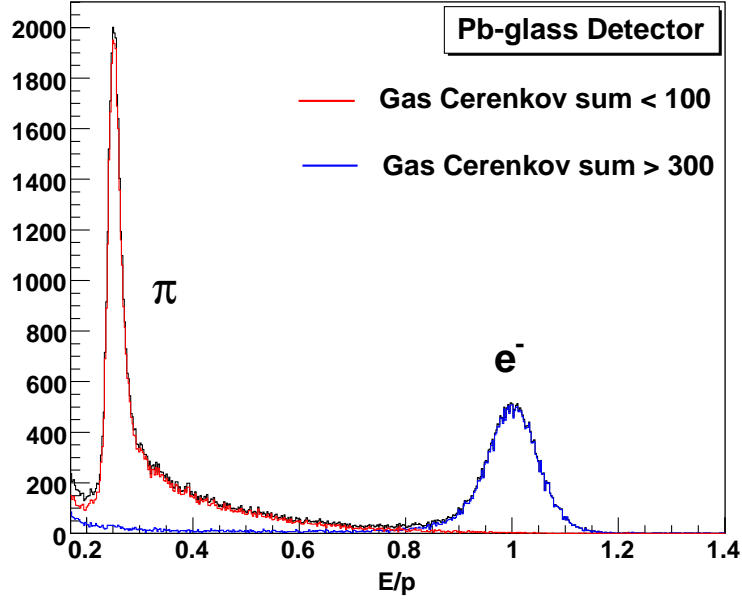


Figure 4.24: Energy divided by momentum for the two-layer lead-glass detector shows a clear separation between pions and electrons.

in two neighboring bars and minimizing the time difference between these two bars by applying time offset and time-walk corrections. The following formula is used for correcting the time-walk effect on all the PMTs:

$$\Delta t_{tw} = -17.9A_p^{-0.14}ns \quad (4.23)$$

where A_p is the pedestal subtracted amplitude measured in ADC channels.

- Pathlength calibration: This correction was done using the linear correlation between the pathlength difference and the tangent of the vertical track angle measured by the drift chambers, θ_{MWDC} , as shown below.

$$\Delta L_{tw}/c = 1.4\theta_{MWDC} \quad (4.24)$$

Figure 4.25 shows the resolution of RF time in the BigBite spectrometer which is about 270 ps.

4.4.2 Coincidence Time Between Two Arms

Once the RF time in the individual spectrometers is calibrated, the last term in Eq. (4.22) needs to be determined in order to calculate the coincidence time. For this experiment

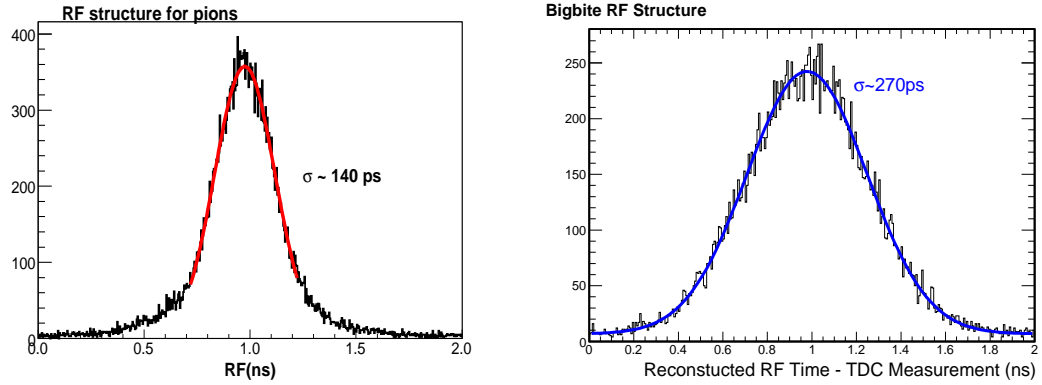


Figure 4.25: Panel on the left (right) shows the timing resolution achieved by the single arm timing detectors in the HRS (BigBite spectrometer) [16].

$\Delta t_{trigger}$ was measured in a TDC with 60 ps resolution. A final coincidence time spectrum is shown in Figure 4.26 calculated for the $(e, e'\pi)$ reaction. A resolution of $\sigma = 340$ ns was reached using this method.

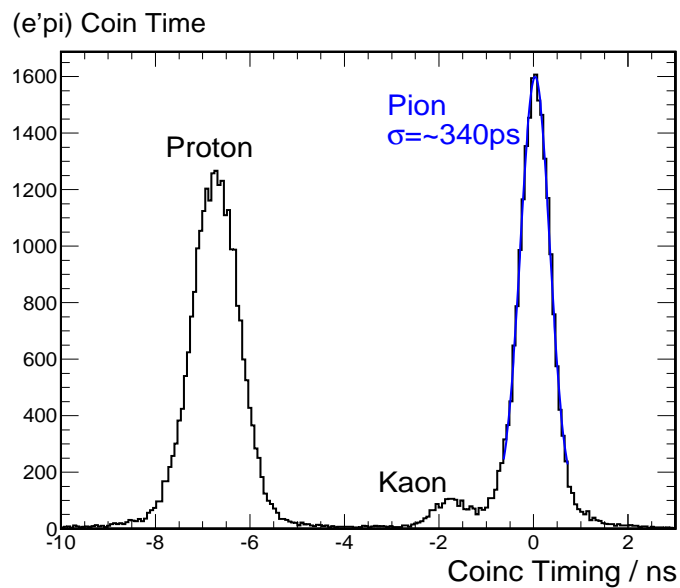


Figure 4.26: Coincidence time-of-flight spectrum for $(e, e'\pi)$ where a clear separation between protons, kaons and pions is seen [16].

4.5 Data Quality Checks

Problem related to flaky level-1 accept signal

During the running of this experiment, a very small portion of the data got affected due to

intermittent double pulsing of the level-1 accept (L1A) signal going to the left HRS DAQ. Since the level-1 accept signal was used for gating ADCs and TDCs, the events associated with a flaky gate signal were affected by this problem. These events were identified by doing various studies during the data analysis. Usually when a track passes through the detector, certain number of local PMTs have a signal, but it was found that for the problematic events almost all the PMTs on a detector had a hit. By looking at the distribution of number of PMTs that had a hit in a particular event, we could identify these kinds of problematic events. Also, by looking at the hit of the L1A signal in the TDC, one could identify the bad events. For every good event, the L1A signal had a hit in the TDC, but for a bad event, due to time-shift, there was no hit in the TDC. This way we could identify most of the bad events and assign them an event flag. These events were later cut away from the physics analysis.

Radiation damage in the BigBite preshower and shower detectors

A gain drop had been observed in the BigBite lead-glass detector signals due to high radiation, especially on the preshower detector because of its closeness to the beam line. Due to radiation the lead-glass blocks change color and become less transparent, and over time this reduces the signals observed on the PMTs attached to the blocks. A position dependent correction was applied to the preshower and shower signals to correct for the drop in the signals. For this correction the entire data set was divided into several run periods. Each run period was corrected by the slope of a linear fit to the preshower peak versus total accumulated charge. After this, a similar correction was applied to the shower signal by fitting a second order polynomial to the energy over momentum (E/p) spectrum vs total accumulated charge. Figure 4.27 shows the preshower peak value vs. run number. The top panel shows the data before the correction. There is a clear drop in the signal which was corrected as shown in the bottom panel. Similarly in Figure 4.28, the top panel shows the E/p peak vs. run number and the bottom panel the data after correction.

4.5.1 Scaler Checks

The scaler setup for this experiment is discussed in section 3.3.4. Scalers were used to record the signals from the Beam Current Monitors (BCMs), count raw and accepted triggers. A consistency check between two identical copies (one in the BigBite spectrometer and other

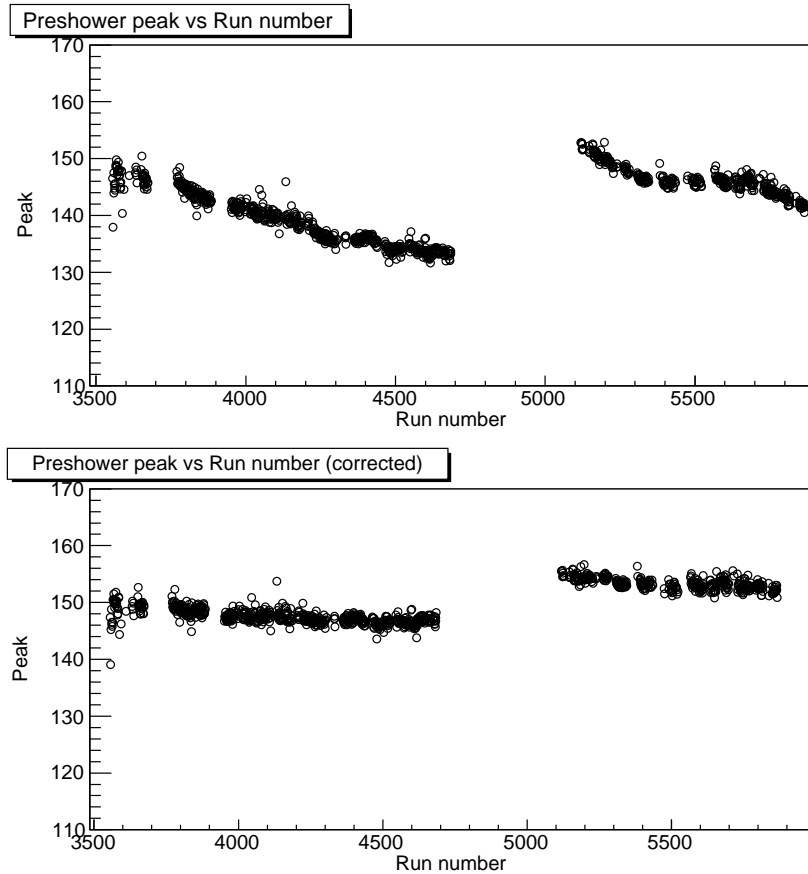


Figure 4.27: Preshower peak vs. run number before and after correction.

in HRS) of the scaler signals was done by M. Huang from Duke University. The goal was to find any possible hardware problems with the recorded signals. Although most of the gated scaler signals were found to be good, there were a few signals in the scaler with target spin and helicity combination of $Tar - Hel-$, which were found to be inconsistent between the left HRS and BigBite copies. Therefore ungated scalers, which are more reliable, were used to determine the target-spin dependent counts. This was done using the recorded target-spin state for every event in the datastream.

4.6 Deadtime Measurement

During the data acquisition some of the events are lost due to dead time in the DAQ system. This needs to be corrected in the analysis later. Dead time can be caused in two ways - one from the front-end electronics like discriminators or other logic modules which may lose some events in a high rate situation, called electronic dead time (EDT), and the other reason

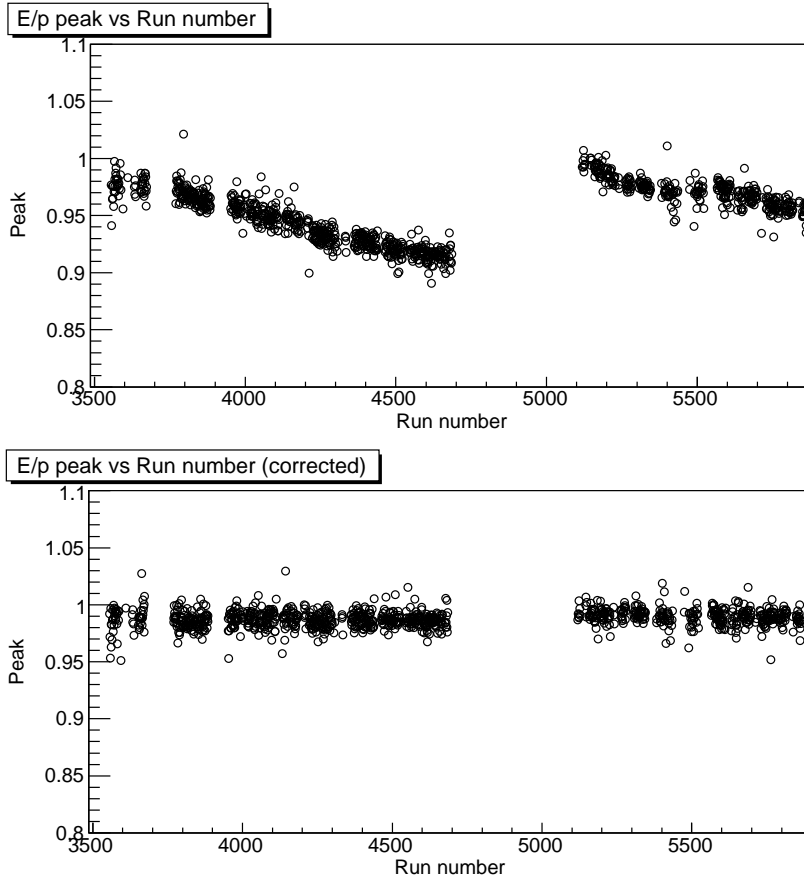


Figure 4.28: E/p peak value vs. run number before and after correction.

is due to the DAQ electronics, known as DAQ dead time. When an event occurs, the trigger supervisor accepts the trigger and sends an L1A signal to all the read-out controllers (ROCs) for retrieving the data from the ADCs and TDCs. The trigger supervisor maintains a *busy* state while all the ROCs are being read out. This *busy* state can last anywhere between $300 \mu\text{s}$ to $500 \mu\text{s}$, depending on the kind of modules used. This waiting period causes a loss of events that occurred during this period. Typically DAQ deadtime is much higher than the electronic dead time.

To measure the electronic dead time, a pulser of 12.5 Hz was sent to the front-end trigger electronics which formed a fake trigger. By measuring the number of pulses recorded by the DAQ compared to the number of pulses sent gives an estimation of the electronic dead time. The DAQ dead time is given by $1 - LT$, where LT is the livetime. The LT is measured by counting the number of events recorded (N_{rec}) by a particular trigger divided by the total number of events occurred (N_{tot}) in this trigger (given by the scaler reading). If the triggers

are prescaled, then the livetime is given by the following equation:

$$LT = \frac{ps \cdot N_{rec}^{data}}{N_{tot}^{scaler}}. \quad (4.25)$$

where ps is the prescaler factor. In the E06-010 experiment no prescale factor was used, as the coincidence trigger rate was very low.

To correctly account for the livetime, fake EDT pulse counts have to be subtracted from the real trigger counts, both for the recorded counts in the TDC and raw scaler counts. Therefore the livetime reduces to:

$$LT = \frac{ps \cdot (N_{rec}^{data} - N_{EDT}^{data})}{N_{tot}^{scaler} - N_{EDT}^{scaler}}. \quad (4.26)$$

The livetime was typically greater than 85% during this experiment.

CHAPTER 5: ASYMMETRY ANALYSIS

The main goal of this thesis is to measure the single spin asymmetry of positive pion electro-production in the SIDIS reaction, $n^\uparrow + e \rightarrow e' + \pi^+ + X$. After calibrating the detectors and checking the data quality, the physics analysis was performed by selecting the SIDIS events of interest and forming the asymmetries.

In this chapter, after describing the general flow of the analysis, the SIDIS event selection using particle identification in both spectrometers, and the kinematical phase space are discussed. Then the contamination from various background channels to the SIDIS event sample is discussed. This contamination introduces systematic uncertainties to the coincidence ${}^3\text{He}(e, e'\pi^+)X$ channel. Finally, a procedure to extract the neutron results from the measured ${}^3\text{He}$ asymmetries is shown.

5.1 Flow of the Data Analysis

A general analysis flow diagram for E06-010 is shown in Fig 5.1. The raw data are first processed using the standard "Hall-A analyzer". The Hall-A analyzer is an object oriented framework to decode and analyze the raw data. For this experiment, additional tools were developed for the BigBite optics and the coincidence TOF calculations. The raw data are decoded and filled into ROOT trees using a "run database", which store the information of the run conditions. These tree variables were then used for detector calibration purposes. Once all the detectors have been calibrated, the raw data are again decoded with the new calibration information and this time the physics variables are filled into ROOT trees. Once the physics variables have been obtained, a number of data quality checks are done in order to exclude any bad data. This is done through a "skim" process where a the previously generated ROOT trees are reduced in size by keeping only the essential variables, and also removing any unwanted regions of the data. The following cuts have been implemented as a part of data quality checks in the skimming process.

- **Beam trip cut:** For various reasons the electron beam in the accelerator trips several times during a run (which usually lasts for one hour). When the beam recovers from a trip, it slowly ramps to the set current value. Therefore it is essential to cut away the events within the beam-trip window (defined by a current threshold), since the

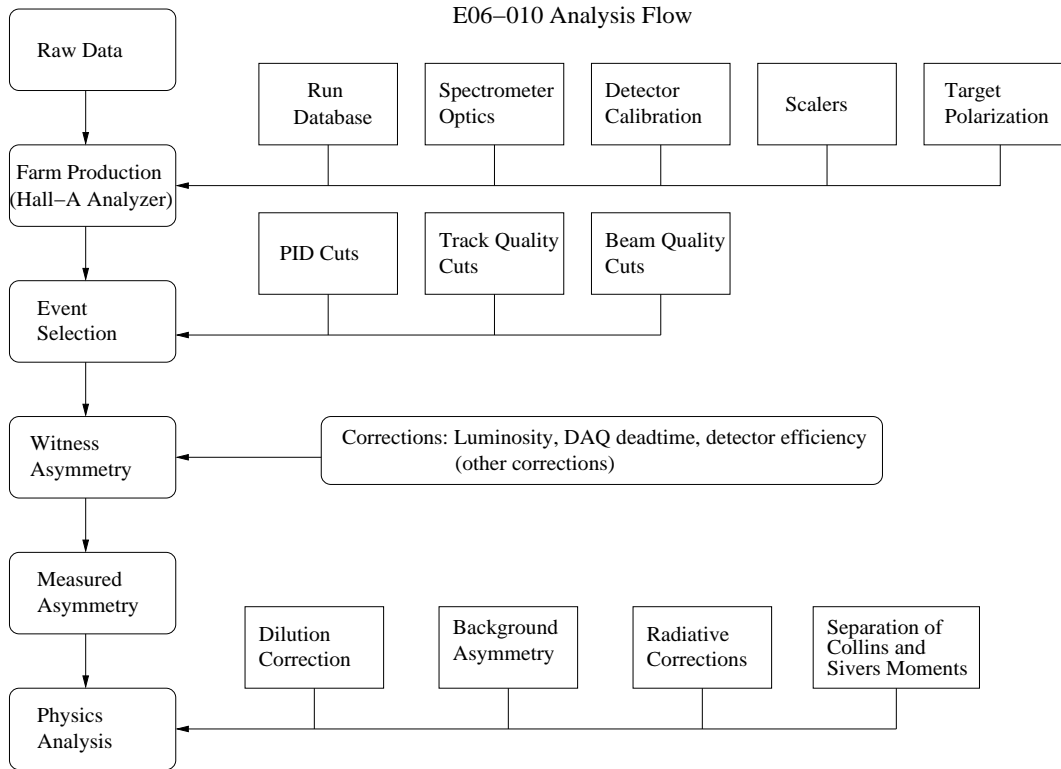


Figure 5.1: Data analysis flow for the E06-010 experiment.

beam charge monitors are not reliable with low beam current values. However, since the scalers are counting during this period, they have to be adjusted accordingly by identifying the counts before and after the beam-trip window and shifting them back for alignment with the real events. A typical run with a beam-trip is demonstrated in the Fig 5.2. The red points are when there is acceptable beam and the black points indicate the periods which were excluded.

- **BigBite wire chamber trip cut:** A small deflection in the beam positions can result in beam hitting the glass wall and producing high rates at the chamber. When this happens the high voltage on the wire chambers trips due to the high currents. The events from the data during this kind of trips were identified and excluded from the physics analysis.
- **Other cuts:** Apart from the above mentioned data quality checks, there were other situations when a tiny fraction of the data is effected due to either DAQ problems or the problems related to the detectors. During the skimming process, all these run periods were identified and excluded.

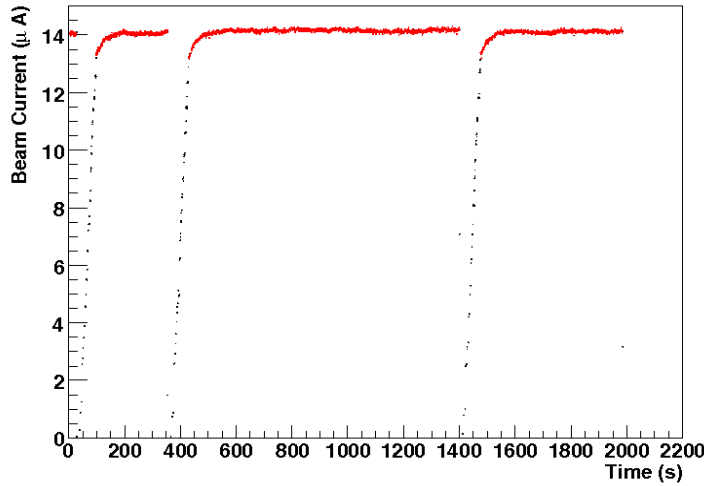


Figure 5.2: Plot showing beam trip cuts for one run. The black points are excluded from the analysis [12].

Once the data files were reduced in the size and all the necessary checks were performed, the event selection was done using the particle identification and quality cuts on the track reconstruction.

5.2 Track Reconstruction and Optics Cuts in the BigBite Spectrometer

The tracks reconstructed in the BigBite spectrometer have to pass through some quality checks before they are included in the physics analysis. The following cuts have been implemented for a track to be considered a valid track for a charged particle.

- **Track quality cut:** The quality of the reconstructed track is determined by the quantity χ^2/N_{dof} where χ^2 is defined as

$$\chi^2 = \sum_i \frac{(x_{reconst} - x_{track})^2}{R_i^2} \quad (5.1)$$

where $x_{reconst}$ is the reconstructed hit position and x_{track} is the projected hit position of the reconstructed track. N_{dof} is the number of degrees of freedom, which in this case is the number of wire planes used in the reconstruction. R_i is the intrinsic resolution used in the tracking software for each wire plane i . As shown in Figure 5.3, all the tracks with $\chi^2/N_{dof} > 2.4$ are excluded.

- **Reconstructed Vertex:** The ^3He target is made of a 40 cm long glass cell. During the experiment two collimators were used on the BigBite side to block events generated

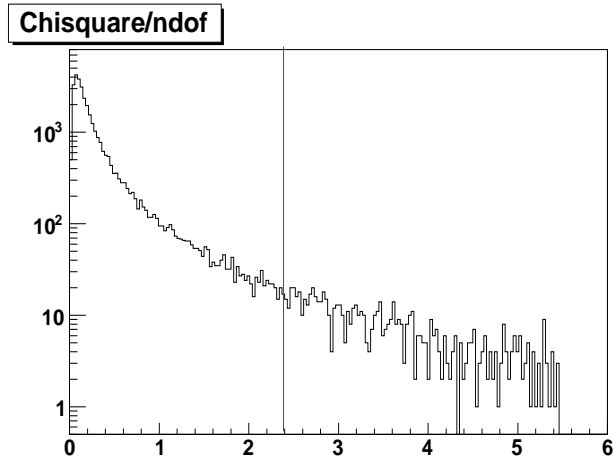


Figure 5.3: χ^2/N_{dof} for the fit to the track in the BigBite spectrometer.

by the glass windows of the cell. A typical reconstructed interaction vertex (v_z) along the z-direction is shown in Figure 5.4. A cut of $18.5 \text{ cm} < v_z < 18.5 \text{ cm}$ was used for the coincidence events (T5 trigger).

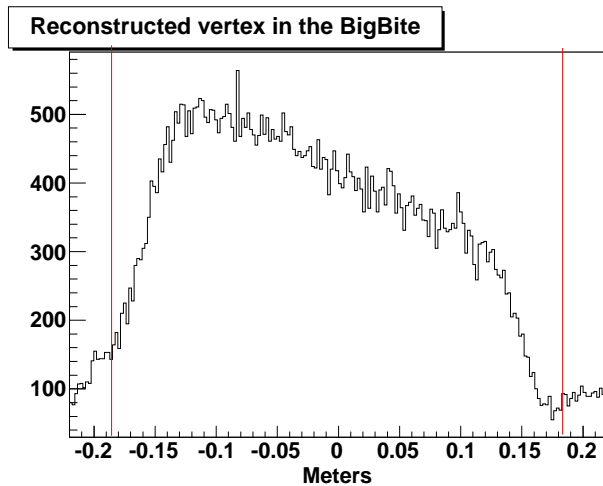


Figure 5.4: Event cut on reconstructed vertex in the BigBite spectrometer.

- **Valid Optics cut:** An optics validity cut was implemented to remove those regions of the BigBite magnet where the magnetic field was very weak. Usually the top and bottom of the magnet have much lower field than at the center, and the optics reconstruction fails in these extreme regions. Figure 5.5 shows the 2D graphic cut used to exclude the invalid region in the BigBite spectrometer.
- **Charge type:** The charge type of the reconstructed track can be identified by deter-

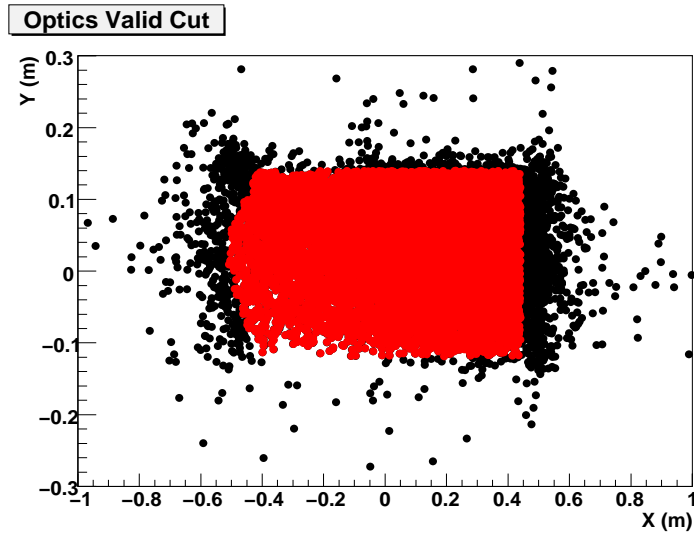


Figure 5.5: The BigBite optics valid cut shown in red. The black points indicate all the events before the cut [12].

mining the direction of the bend of the particles in the BigBite magnet. Since BigBite contains a dipole magnet only, it bends the charged particles in opposite directions. The negatively charged particles are bent upwards and positively charged particles are bent down. This allows us to clearly identify the charge type of the particles. The vertical position (X) as a function of the vertical slope in the first drift chamber shows a clear separation between two regions corresponding to the upwards and downwards bending particles (Figure 5.6).

- **Track matching with shower cluster:** In principle every reconstructed track should have a cluster associated with it in the shower detector. Therefore, the projected track positions are matched with the position of the center of the shower cluster. The difference between the position of the projected track and the cluster center is shown Figure 5.7. For different particles the width of this distribution is different, since the energy deposited in the cluster is different. Therefore a particle dependent cut is used which is discussed in the BigBite PID section.

5.3 PID in the BigBite Spectrometer

As described in the section 3.2.5, the BigBite is an open geometry spectrometer and both charged and uncharged particles can fall into the spectrometer acceptance. Therefore it

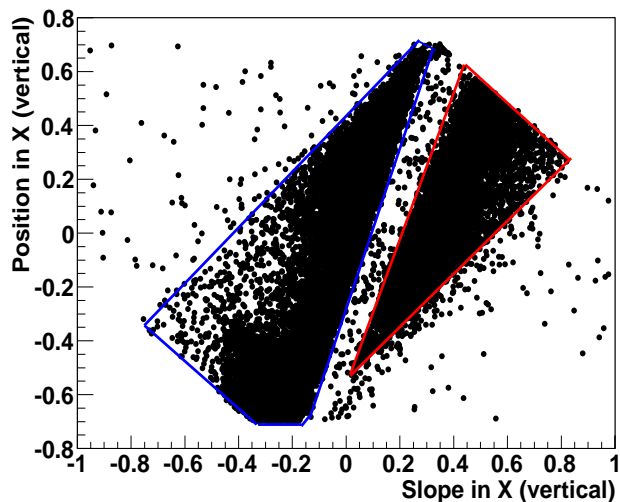


Figure 5.6: Vertical position versus vertical slope in the first wire chamber shows a clear separation between oppositely bending particles. The events below the blue(red) boundary indicate negative(positive) particles. The black points include all particles.

is important to separate the electrons from the other particles. Here we list the type of particles that can be identified using various cuts to the data in this spectrometer. The goal is to clearly identify the electrons scattered from the ^3He target. All the charged particle tracks pass through the cuts discussed in section 5.2 before being considered for particle identification.

5.3.1 Electrons

Electron-like events were identified using the following cuts:

- **Charge Particle Cut:** Negatively charged particles are selected using upwards bending tracks in the BigBite spectrometer.
- **Momentum Cut:** Momentum range is $0.6 \text{ GeV} < p < 2.5 \text{ GeV}$
- **Preshower Cut:** A cut on the energy deposited in the preshower, $E_{preshower} > 200 \text{ MeV}/c$, excludes almost all the pions (see Figure 5.8).
- **E/p Cut:** For electrons the ratio of total energy deposited in the calorimeter to its momentum should be close to 1.0. A momentum dependent cut is applied for this ratio. This was done by fitting a Gaussian shape to the E/p spectrum in different BigBite momentum ranges. For electrons $\mu_{E/p} \pm 2.5\sigma_{E/p}$ cut was used.

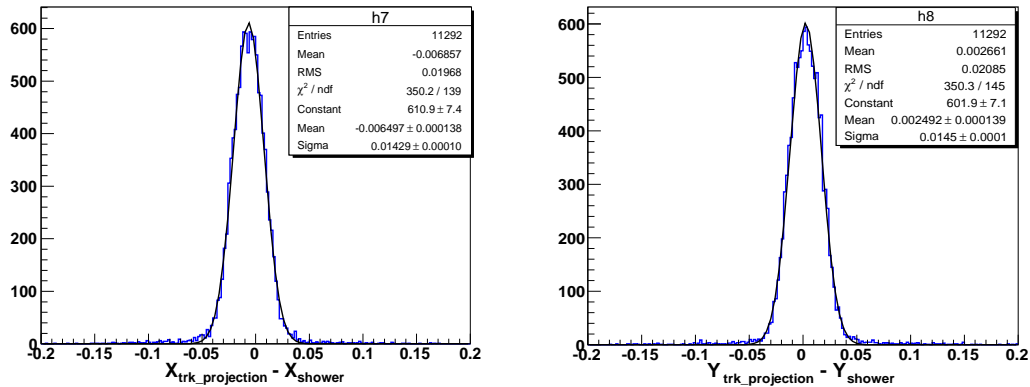


Figure 5.7: The left(right) panel shows the difference between x(y) coordinate of tracks projected on the shower counter and the reconstructed shower x(y) position.

- **Track Match with Shower Cut:** The difference of the projected track and shower cluster position is shown in Fig 5.7. A 3σ cut was used as a standard cut.

5.3.2 Positrons

Positrons were identified in the same way as electrons except that positively charged particles are selected (see Fig 5.6).

- Positive charge particle cut - downwards bending tracks.
- Preshower cut: $E_{preshower} > 225$ MeV/c was used.
- E/p cut : A 1.5σ cut was used.
- Track match cut: A 2.5σ cut was used.

5.3.3 Hadrons

In the BigBite spectrometer, different hadron species cannot be separated. Therefore, all hadrons are identified based only on their charge type. The following cuts are applied to identify hadron-like events.

- Charged particle cut for identifying positively and negatively charged hadrons.
- Preshower cut: $E_{preshower} > 150$ MeV/c was used.
- Track match cut: A 2.0σ cut was used.

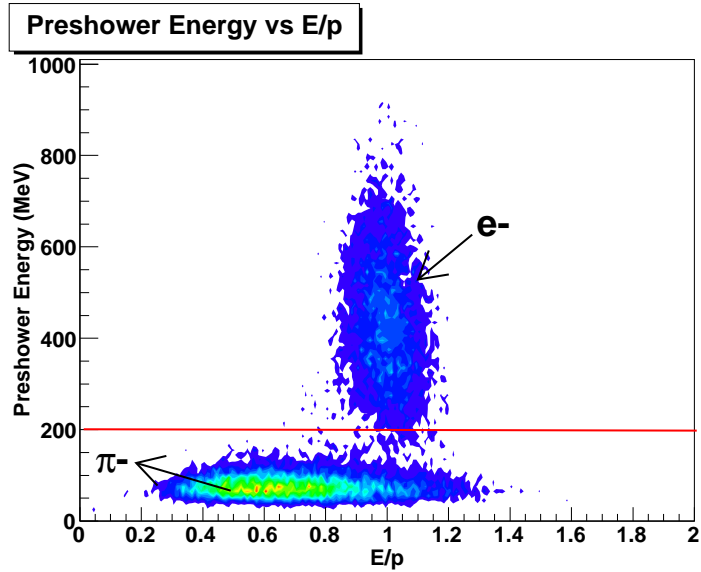


Figure 5.8: Energy deposited in the preshower vs. total energy divided by the particle's momentum shows a clear separation between electrons and pions.

5.3.4 Photon-Like Events

Photon-like events coming from the target region do not leave tracks in the drift chambers, therefore these events are identified using the following cuts.

- No track found in the BigBite Spectrometer.
- Preshower cut : $E_{preshower} > 200 \text{ MeV}/c$ was used.
- Shower cluster match with preshower cluster.
- Total energy cut: $0.6 \text{ GeV} < E_{sh+ps} < 2.5 \text{ GeV}$.

5.4 PID in the HRS

The high resolution spectrometer (HRS) was used for detecting the charged hadron produced from the SIDIS reaction. In order to separate the pions from other particles a number of particle identification(PID) detectors were used. Before moving to PID cuts, first, the acceptance and vertex cuts are discussed. Two types of acceptance cuts were used. First, a cut was implemented on both the dispersive(X) and non-dispersive(Y) positions of the track projected on the two layer Pb-glass calorimeter, as shown in Fig 5.9.

- Dispersive direction: $-1.5 \text{ m} < x < 1.0 \text{ m}$

- Non-dispersive direction: $-0.2 \text{ m} < y < 0.2 \text{ m}$

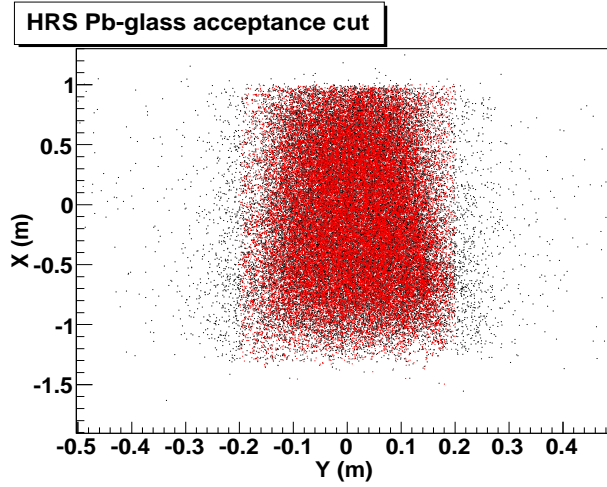


Figure 5.9: Red points shows the HRS acceptance cut for the Pb-glass detector.

The second acceptance cut was based on the target kinematical variables: θ_{tgt} , ϕ_{tgt} , y_{tgt} and δp . A set of six 2D graphic cuts was implemented using two of these four kinematic variables for every cut. Fig 5.10 shows all the six cuts.

The reconstructed vertex cut is shown in Fig 5.11. A vertex cut of $-0.185 \text{ cm} < v_z < 0.185 \text{ cm}$ was used for all coincidence events. In addition to these cuts, a single track event cut was used where all the multi-track events were rejected. In general, in the HRS, multi-track events are less than 2% of the single track events, and the false asymmetry due to this cut is of the order of 1×10^{-4} .

There are three PID detectors for identifying different types of particles - a light gas Čerenkov detector, an Aerogel detector(A1), and a two layered Pb-glass calorimeter. The following cuts were implemented to identify the particles.

5.4.1 Pions

- Aerogel cut: Pions fire the Aerogel detector, hence $A1 \text{ ADC_sum} > 150$ channel.
- Čerenkov cut: Pions do not fire the Cerenkov detector, hence $\text{Cerenkov ADC_sum} < 250$ channels.
- E/p cut: For pions the energy deposited in the Pb-glass calorimeter divided by its momentum is less than 1. Hence, $E_{calo}/p_{track} < 0.6$ was used.

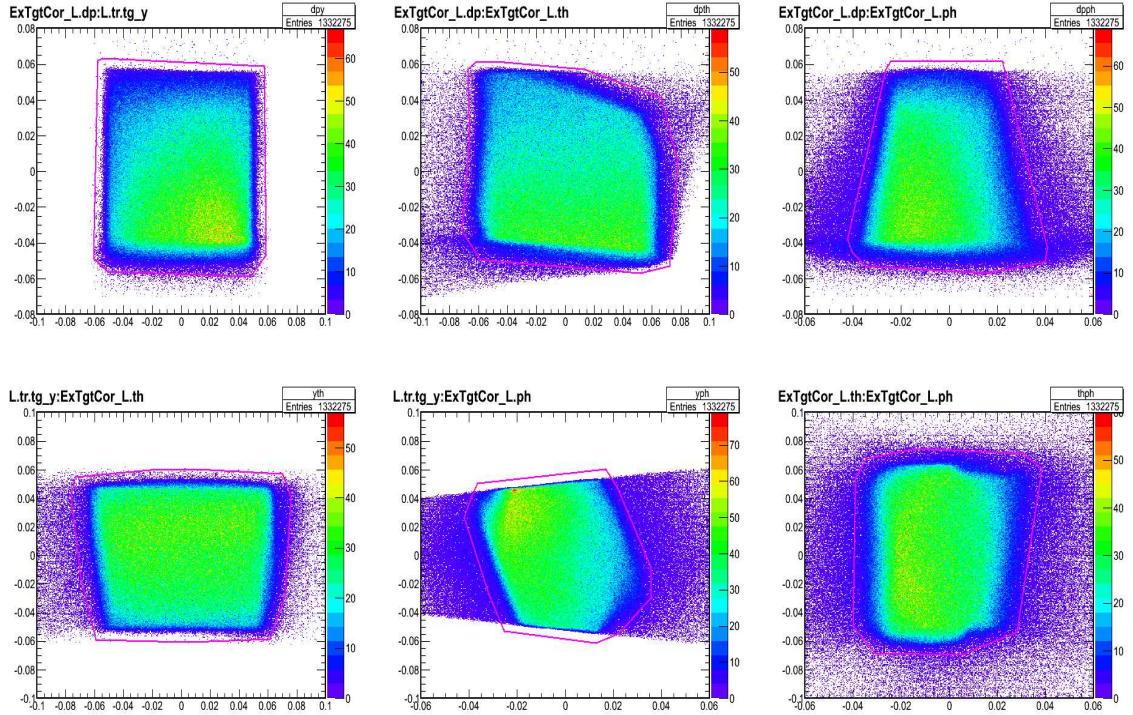


Figure 5.10: The 2D acceptance cuts based on the target kinematical variables θ_{tgt} , ϕ_{tgt} , y_{tgt} , and δp [16].

5.4.2 Protons

- Aerogel cut: $A1 \text{ ADC_sum} < 150$ channels.
- Cerenkov cut: $\text{ADC_sum} < 250$ channels.
- E/p cut : $E_{calo}/p_{track} < 0.6$.

5.4.3 Electrons

- Aerogel cut: $A1 \text{ ADC_sum} > 150$ channels.
- Cerenkov cut: $\text{ADC_sum} > 250$ channels.
- E/p cut: $E_{calo}/p_{track} > 0.7$.

In the detection of the positively charged pions, the main contamination comes from the protons and the positive kaons. Protons can be rejected completely using the coincidence time-of-flight information (see Fig 4.26), since they are several σ_{TOF} away from the pion

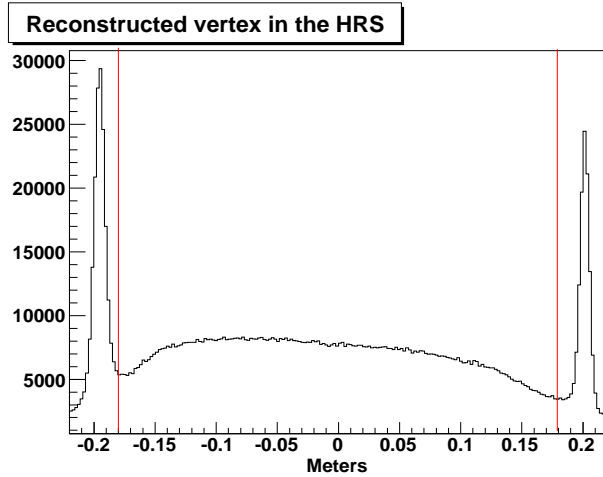


Figure 5.11: Event cut on reconstructed vertex in the HRS spectrometer.

peak. Kaons (and protons) do not fire Aerogel detector, therefore they can be rejected by placing a cut on the A1 ADC_sum < 150 . The aerogel Cerenkov detector gave a kaon/pion rejection factor of better than 10:1. Moreover, in this experiment the K^+/π^+ ratio is about 6%. Combining all this information the K^+ contamination to π^+ sample is less than 1%.

5.5 Coincidence Time as PID

The coincidence time between the two spectrometers gives an additional handle to identify different hadrons detected in the HRS. In addition to this, the coincidence vertex, which is the difference between the reconstructed vertices by the two spectrometers, reduces the background events very effectively. The coincidence vertex, shown in Figure 5.12, has a resolution of about 1.2 cm obtained by fitting a Gaussian function. A momentum dependent cut was implemented for the coincidence vertex using the functional form obtained by fitting the resolution vs. BigBite momentum.

The coincidence time-of-flight spectrum calculated using the pion mass when the HRS is in positive polarity mode is shown in Fig 5.13. Table 5.1 shows the cuts used for the coincidence time for various channels. Note that the time t in this table represents the coincidence time calculated for that particular channel. For example, for an electron in the BigBite spectrometer and a pion in the HRS, the coincidence TOF is calculated using the pion mass. Similarly t is calculated for other particles in the HRS. Table 5.2 shows the random coincidence cuts used for the analysis. Random coincidence background events,

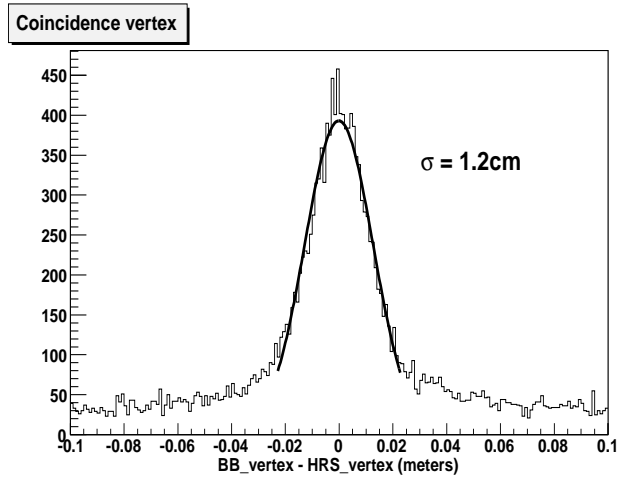


Figure 5.12: Difference between BigBite and HRS reconstructed vertices.

although very small in number, may induce its own single spin asymmetry. Therefore it is necessary to subtract the random coincidence background from the real coincidence events before forming the asymmetries.

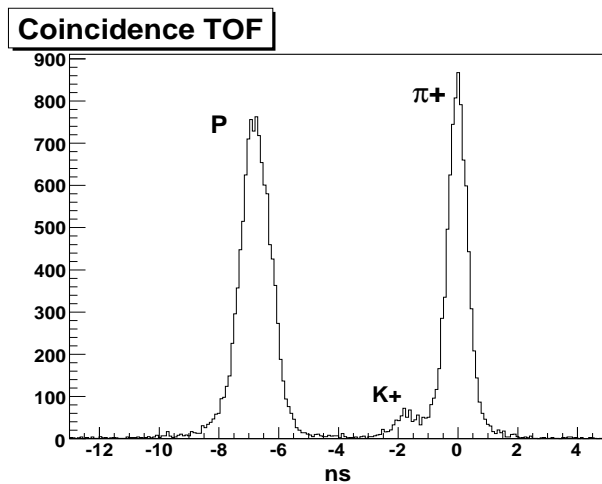


Figure 5.13: Coincidence time-of-flight spectrum in the HRS positive mode. There is a clear separation between protons(P), π^+ , and K^+ mesons.

5.6 SIDIS Event Selection

5.6.1 Kinematical Phase Space

The semi-inclusive DIS events are selected from the data using various kinematical cuts shown in Table 5.3. A four momentum transfer greater than 1.0 GeV^2 is used to select the

Table 5.1: Coincidence TOF cuts for various channels. Here the subscript on HRS(BB) indicates the corresponding particle detected in that spectrometer. h refers to hadron.

	HRS $_{\pi}$	HRS $_K$	HRS $_p$
BB $_e$	-3 ns < t < 3 ns	-1 ns < t < 1 ns	-3 ns < t < 3 ns
BB $_{\gamma}$	-3 ns < t < 3 ns	-1 ns < t < 1 ns	-3 ns < t < 3 ns
BB $_h$	-2.5 ns < t < 3.5 ns	-	-2.5 ns < t < 3.5 ns

Table 5.2: Random coincidence time cuts for various channels. Here the subscript on HRS(BB) indicates the corresponding particle detected in that spectrometer. h refers to hadron.

	HRS $_{\pi}$	HRS $_K$	HRS $_p$
BB $_e$	9 ns < t < 59 ns OR -69 ns < t < -19 ns	9 ns < t < 59 ns OR -73 ns < t < -43 ns	11 ns < t < 61 ns OR -73 ns < t < -23 ns
BB $_{\gamma}$	9 ns < t < 59 ns OR -69 ns < t < -19 ns	9 ns < t < 59 ns OR -73 ns < t < -43 ns	11 ns < t < 61 ns OR -73 ns < t < -23 ns
BB $_h$	-69.5ns < t < -19.5ns OR 9.5ns < t < 59.5ns	-	-73.5ns < t < -23.5ns OR 11.5ns < t < 61.5ns

scattering events are in the DIS region. In order to avoid any resonances, the invariant mass (W) of the final hadronic state is chosen to be greater than 2.0 GeV. In addition to this cut, the invariant mass of the hadronic system without the detected hadron (W') is selected to be greater than 1.5 GeV to avoid any contributions from the resonance production channels. To reasonably make sure that the detected hadron is in the current fragmentation region, the fraction of energy transfer is selected as follows: $0.4 < z < 0.7$.

The kinematics phase space covered by the ${}^3He^{\uparrow}(e, e'\pi)X$ SIDIS events in E06-010 is shown in Figure 5.14 and Figure 5.15. We can see that most of the SIDIS events peak at value of z of ~ 0.5 . The angular coverage of ϕ_h and ϕ_S is shown in the Fig 5.16.

5.7 Contamination of the DIS Electron Sample in the BigBite Spectrometer

There are two major sources of contamination to the DIS electron sample measured in the BigBite spectrometer. One, due negative pion production and the other due to charge

Table 5.3: Table showing the summary of the kinematical cuts used for selecting SIDIS events.

Kinematical variable	SIDIS cuts
Momentum transfer	$Q^2 > 1.0 \text{ GeV}^2$
Invariant mass	$W > 2.0 \text{ GeV}$
Invariant mass without detected hadron	$W' > 1.5 \text{ GeV}$
Fraction of energy transfer	$0.4 < z < 0.7$

symmetric background - electron-positron production from the neutral pion decay. The neutral pions produced in the target region decay quickly inside the target in a dominant decay mode (98.798%) to two photons ($\pi^0 \rightarrow 2\gamma$) [1]. These photons can interact with the glass cell of the target and any other material present in front of the spectrometer, before hitting the detectors. This can produce electron-positron pairs which are detected in the BigBite spectrometer. The other mechanism is $\pi^0 \rightarrow e^+e^-2\gamma$, where the neutral pion directly decays to one photon and one electron-positron pair. Both these mechanisms can, in principle, produce an electron which is indistinguishable from the DIS electron produced in the ${}^3\text{He}(e, e'\pi^+)X$ reaction. Therefore, it is necessary to estimate these types of contamination and resulting false asymmetries. In this section we describe a procedure for estimating both negative pion and charge symmetric background contamination.

5.7.1 Negative Pion Contamination

Negatively charged pions are the major source of background for the detected DIS electron sample. For the E06-010 experiment, a Pb-glass calorimeter made of preshower and shower blocks was the only particle identification detector used. Although pions and electrons are well separated in the preshower detector (see Fig 5.8), it is necessary to find the level of pion background in the electron sample.

We used two methods to determine the pion contamination in the coincidence $N(e, e'\pi^+)X$ event sample (T5 trigger). The first method, which is a direct method, is based on fitting the preshower energy spectrum with a Gaussian function that is convoluted with a Landau function. This allows us to estimate the background contamination. The second method is based on the suppression of the pion yield in the coincidence trigger (T5) relative to the

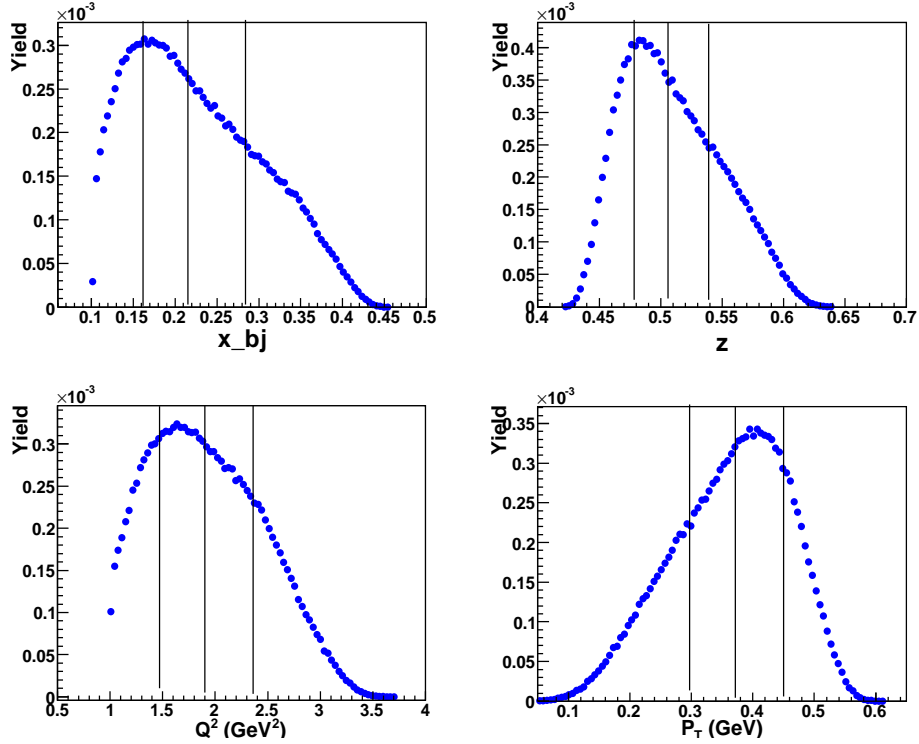


Figure 5.14: Phase space of kinematical variables x , z , Q^2 and P_T along with their binning.

singles trigger T1. This is possible due to the fact that the coincidence trigger T5 was constructed using the singles trigger T1 (see section 3.3.3). Both these methods are discussed in detail below.

Method I:

First, the data is divided into several momentum bins and the preshower spectrum is plotted using all the DIS cuts except the preshower cut. Pions leave a minimum ionization peak around ADC channel 200 and electrons peak at much larger ADC channels depending on the momentum bin. A Gaussian function that is convoluted with a Landau function ($f(x)$) is fitted to the pion peak and a separate Gaussian function is fitted to the electron peak. Fig 5.17 shows the preshower spectrum in different BigBite momentum bins described well with the above mentioned fitting function. The pion contamination ($k_{\pi^-}^{T5}$) is calculated using the following formula,

$$k_{\pi^-}^{T5} = \frac{\int_{400}^{\infty} f(x) dx}{N_{>400}^e} \quad (5.2)$$

where the function $f(x)$ is integrated from ADC channel 400 to some large value. Here $N_{>400}^e$ is the number of events in the electron peak with a cut greater than channel 400, up

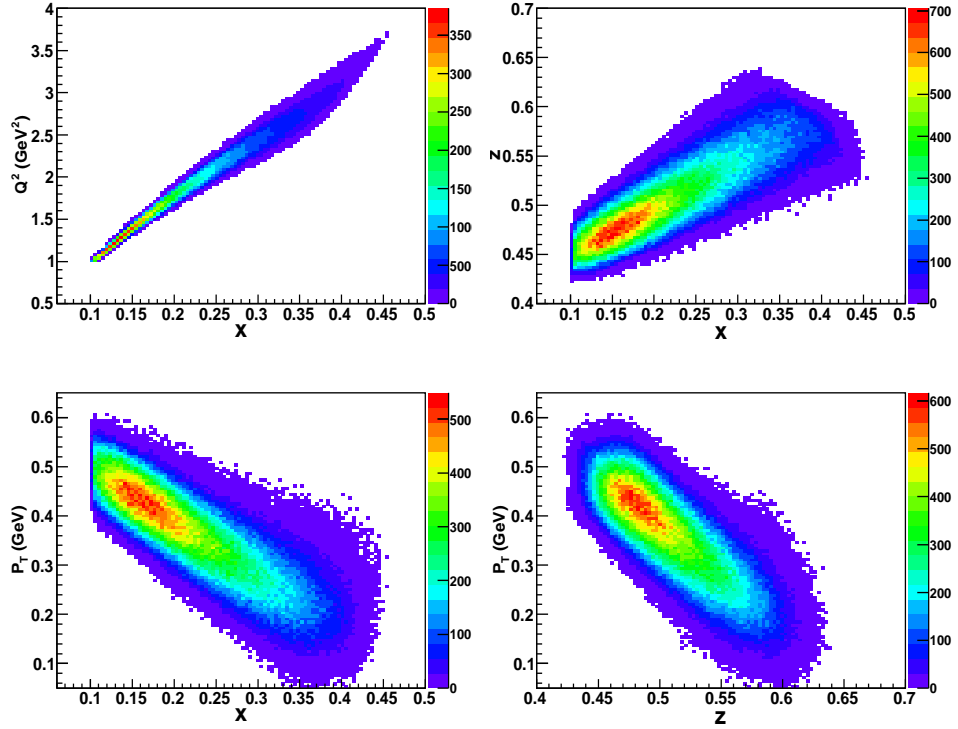


Figure 5.15: Phase space of kinematical variables shown in 2D for all events passing the $N(e, e'\pi)X$ cuts.

to some large number. Table 5.4 shows the contamination obtained using this method in different momentum bins.

Method II:

In this method we calculate the suppression factor (f_{sup}) which is defined as

$$f_{sup} = \frac{Y_{(\pi^-, \pi)}^{T5} / Y_{\pi^-}^{T1}}{Y_{(e^-, \pi)}^{T5} / Y_{e^-}^{T1}} \quad (5.3)$$

where $Y_{(\pi^-, \pi)}^{T5}$ is the yield for coincidence events when BigBite detects π^- mesons and the HRS detects π^\pm mesons. Similarly $Y_{(e^-, \pi)}^{T5}$ is defined for electrons in the BigBite spectrometer and pions in the HRS. This factor gives an estimation of the pion yield suppression in the coincidence (T5) channel relative to the singles (T1) pion yield, when compared to the corresponding electron yield (signal). This can be directly obtained from the data by taking the ratio of the yields. Fig 5.18 shows this factor plotted against the BigBite momentum when the HRS is in positive mode.

Once f_{sup} is known and the pion contamination in the BigBite spectrometer singles (T1 trigger) is known from the preshower fit ($k_{\pi^-}^{T1}$), then an estimation of the pion contamination

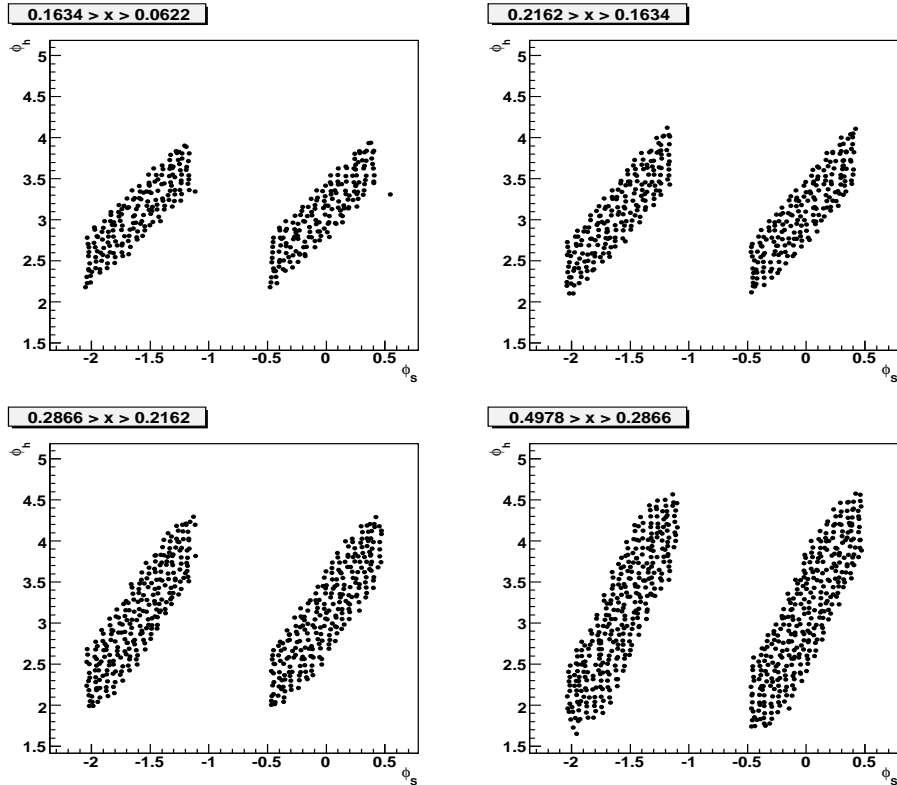


Figure 5.16: Angular coverage of ϕ_h and ϕ_s in different x bins.

in coincidence channel can be done using

$$k_{\pi^-}^{T5} = \frac{k_{\pi^-}^{T1}}{f_{sup}}. \quad (5.4)$$

Table 5.4 summarizes the negative pion contamination in the electron sample obtained from the two methods mentioned above. Any difference between these two methods gives an estimation of the systematic uncertainty present in the applied method. From the Table 5.4, it is clear that the pion contamination in the electron sample is less than 3% in the entire BigBite spectrometer momentum range.

5.7.2 Charge Symmetric Background

The mechanism by which the charge symmetric background, such as electron-positron pair production, can occur is discussed earlier in the section. For differentiating these pair produced electrons from DIS electrons, we refer to them as "*photon-induced electrons*" in all future references. In experiment E06-010, there was no direct way to separate the DIS electrons from the photon-induced electrons in the event sample. Since it is a charge

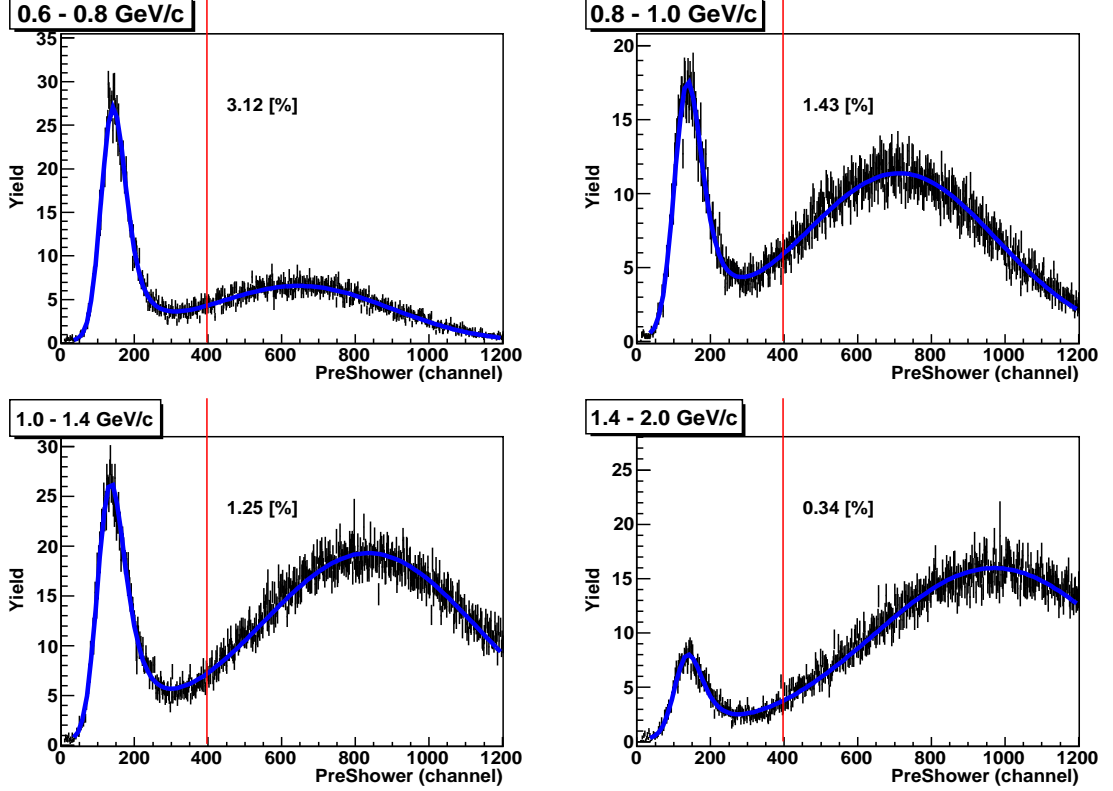


Figure 5.17: A Gaussian function that is convoluted with a Landau function is fitted to the preshower spectrum in different BigBite momentum bins. The red line shows the cut used for calculating the pion contamination.

symmetric background the kinematics of the photon-induced electrons and positrons are same. Therefore, by measuring the yield of the photon-induced positrons, we can deduce the corresponding electron contribution to the DIS sample. This was achieved by reversing the polarity of the BigBite magnet. With the reversal of the magnetic field in the BigBite, the positrons (dominated by pair production) bend in the same direction and cover the same acceptance as the electrons when the field was not reversed.

The photon-induced electron contamination (k_γ^{T1}) is given by the ratio of the positron yield (after subtracting the π^+ contamination) in the charge symmetric background to the total electron yield (after subtracting the π^- contamination). For the singles trigger T1,

$$k_\gamma^{T1} = \frac{Y_{e^+}^{T1}}{Y_{e^-}^{T1}} \quad (5.5)$$

and for the coincidence trigger T5 it is given by,

$$k_\gamma^{T5} = \frac{Y_{(e^+, \pi)}^{T5}}{Y_{(e^-, \pi)}^{T5}} \quad (5.6)$$

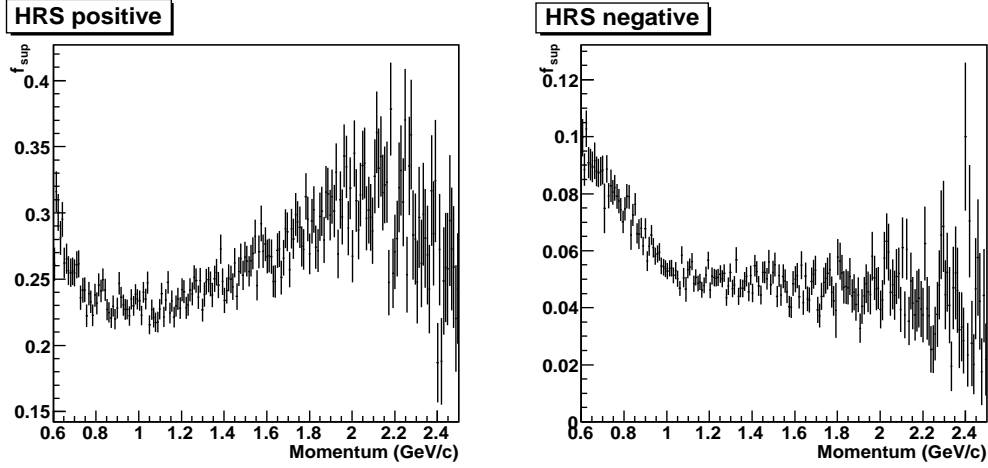


Figure 5.18: Left(right) panel shows the π^- yield suppression factor as defined in Eq. (5.3) when HRS is in positive(negative) mode.

Table 5.4: Negative pion contamination in the BigBite electron sample for different momentum bins.

Momentum range (GeV)	Contamination method I (%)	Contamination method II (%)
0.6 – 0.8	3.12	2.87
0.8 – 1.0	1.43	2.13
1.0 – 1.4	1.25	1.70
1.4 – 2.0	0.34	0.47

where $Y_{(e^+, \pi)}^{T5}$ and $Y_{(e^-, \pi)}^{T5}$ are the yields for electron or positron detection in the BigBite spectrometer in coincidence with a pion in the HRS.

Fig 5.19 shows the positron yield (red) versus the electron yield (black) for both singles and coincidence events, before subtracting the pion contamination from each of these channels. The π^+ contamination is subtracted from the positron sample by fitting the preshower spectrum as described in subsection 5.7.1. Table 5.5 shows the photon-induced electron contamination for the coincidence events obtained by this method.

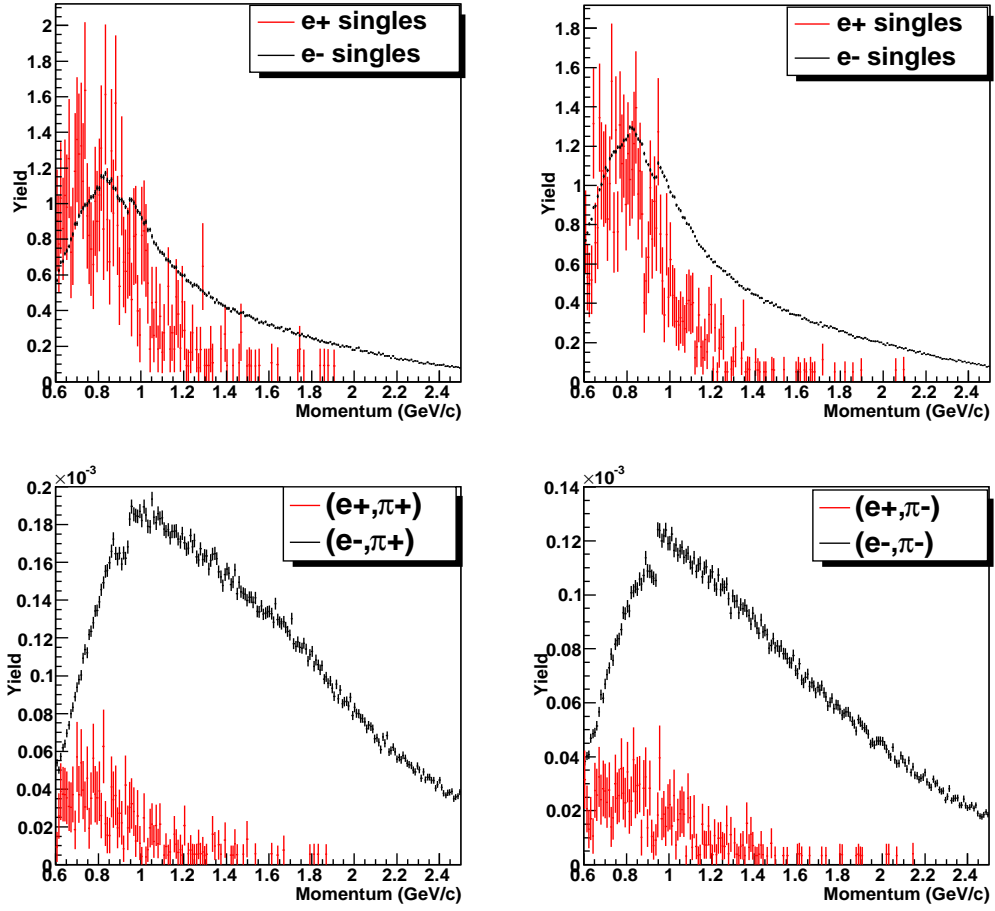


Figure 5.19: The top left(right) panel shows the BigBite singles photon-induced e^+ yield in red and the e^- yield in black, when the HRS polarity is positive(negative). The bottom left(right) panel shows the coincidence yield of positrons in the BigBite spectrometer and the $\pi^+(\pi^-)$ in the HRS in red, and the e^- yield in the BigBite and the $\pi^+(\pi^-)$ yield in the HRS in black

5.8 Single Target-Spin Asymmetries

The single spin asymmetry (SSA) is defined as,

$$A_{UT} = \frac{1}{|S_T|} \frac{d\sigma(\phi_h, \phi_S) - d\sigma(\phi_h, \phi_S + \pi)}{d\sigma(\phi_h, \phi_S) + d\sigma(\phi_h, \phi_S + \pi)} \quad (5.7)$$

and the measured raw asymmetry can be written as,

$$A_{raw} = \frac{1}{Pf} \frac{Y_+ - Y_-}{Y_+ + Y_-} \quad (5.8)$$

Table 5.5: Photon-induced electron contamination in the BigBite electron sample for different momentum bins.

Momentum range (GeV)	Contamination (%)
0.6 – 0.8	19.6
0.8 – 1.0	3.8
1.0 – 1.4	1.2
1.4 – 2.0	0.6

where P and f are the target polarization and the dilution factor, respectively, and $Y_{+/-}$ are the $N(e, e'\pi^+)X$ yields in opposite target spin states. The yield is defined as

$$Y_+ = \frac{N_+}{C_+L_+} \quad , \quad Y_- = \frac{N_-}{C_-L_-}. \quad (5.9)$$

where N is the number of events that pass the semi-inclusive DIS cuts in a particular spin state and C and L are the charge and livetime for the corresponding spin state. In principle L may consist of other corrections like target density, etc. Assuming L and N are statistically not correlated, the uncertainty of A_{raw} reduces to,

$$\delta A_{raw} = \frac{1}{Pf} \frac{2C_+C_-L_+L_-(N_- \delta N_+ + N_+ \delta N_-)}{(N_+C_-L_- + N_-C_+L_+)^2} \quad (5.10)$$

which can be written as,

$$\delta A_{raw} = \frac{1}{Pf} \frac{2Y_+Y_-}{(Y_+ + Y_-)^2} \sqrt{\frac{1}{N_+} + \frac{1}{N_-}}. \quad (5.11)$$

5.8.1 Asymmetry Using Local Spin Pairs

In experiment E06-010 the target spin was flipped every 20 minutes. Two consecutive and opposite target spin states are referred to as one spin-pair. During this experiment, there were several different experimental running conditions, such as different beam currents, change in high voltage settings, change in target cells, etc. Therefore, in order to avoid problems related to changes in experimental settings, the asymmetries were first formed locally and then combined together to get the final asymmetry. Local asymmetries also help to understand the data better. It will reveal, if any, problems related to the detectors at any given point of time. For example, if the local asymmetry in a given period behaves very

differently than the average asymmetry, then it indicates some problem in that particular period. Moreover, due to the radiation damage of the BigBite calorimeter, the yield was drifting over time. To avoid any false asymmetry due to this drift, it is essential to form local asymmetries.

We can further split one spin state into two halves and make two "super local pairs" out of one local spin pair (a pair of opposite spin states of 20 mins each). This method will increase the number of spin pairs and have definite advantage over just the local pair, since the coincidence yield was drifting during the experiment. This can be demonstrated by the width of the charge asymmetry, which becomes narrower for the super local pair method when compared to local pair method. Fig 5.20 shows the charge asymmetry obtained from both these methods. In principle, both methods can be used to form the asymmetries. In order to keep the systematic uncertainty due to yield drift low, we use the super local pair method. The method used to combine different local spin pairs is shown below [75].

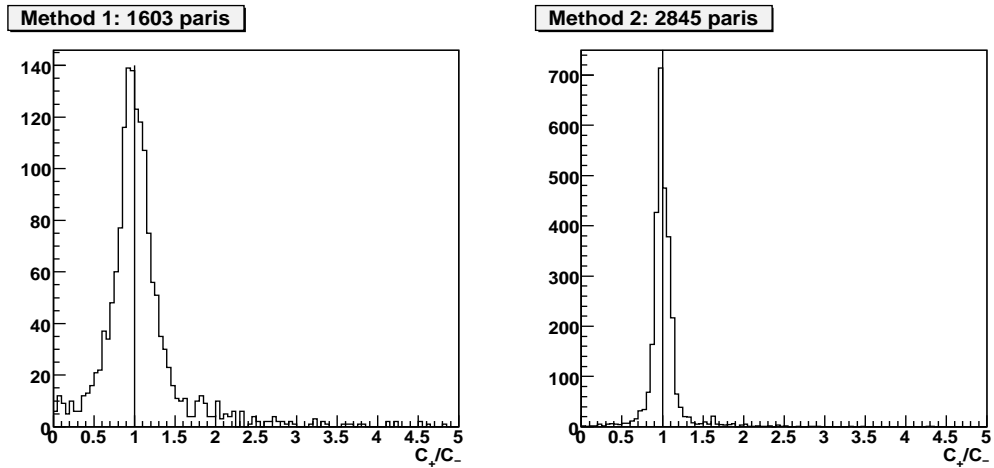


Figure 5.20: The left(right) panel shows the beam charge asymmetry with the local pair method (super local pair method) [12].

$$A_{raw} = \frac{\sum_i a_i (Y_{i+} - Y_{i-}) / P_i}{\sum_i a_i (Y_{i+} + Y_{i-})} \quad (5.12)$$

where P_i is the polarization in the i^{th} spin pair, and a_i is weighting factor. The weighting factor can be determined by the following condition,

$$\frac{\partial \delta A_{raw}}{\partial a_i} = 0 \quad (5.13)$$

This condition leads to a group of equations which is not easy to solve, therefore we make

the following approximation:

$$A_{raw} = \frac{\sum_i a_i (Y_{i+} - Y_{i-}) / P_i}{\sum_i a_i (Y_{i+} + Y_{i-})} = \frac{\sum_i a_i A_i (Y_{i+} + Y_{i-}) / P_i}{\sum_i a_i (Y_{i+} + Y_{i-})} \approx \frac{\sum_i b_i A_i}{\sum_i b_i}. \quad (5.14)$$

By solving Eq.(5.13), one can obtain the best b_i ,

$$b_i \sim \frac{1}{\delta A_i^2} \sim \frac{1}{\frac{1}{N_+} + \frac{1}{N_-}} \sim \frac{1}{\frac{1}{Y_+ L_+} + \frac{1}{Y_- L_-}}. \quad (5.15)$$

Therefore, using Eq.(5.14) we can write an expression for a_i as,

$$a_i = \frac{b_i}{Y_{i+} + Y_{i-}} \sim \frac{1}{\frac{1}{L_+} + \frac{1}{L_-}}. \quad (5.16)$$

5.9 Target Polarization and Spin Direction

Target polarization measurements were done using two methods - NMR and EPR. The absolute target polarization was measured using the EPR method and then this is used to calibrate the NMR signal obtained for every 20 min spin-flip. The details of target polarization analysis is described in section 4.1. It is also essential to know the direction of the target spin.

Target spin direction can be determined using different ways. One way is to use the EPR frequency signal. As mentioned in section 4.3.1, the measured EPR frequency is proportional to the effective magnetic field due to both the holding field and the ^3He spins ($\mathbf{B} + \Delta\mathbf{B}$). When the ^3He spins are flipped to the opposite direction, then the effective field becomes $\mathbf{B} - \Delta\mathbf{B}$. This change in the effective magnetic field is directly reflected in the measured EPR frequency difference. Using this information along with the absolute direction of the holding magnetic field (given by the compass measurement), one can determine the target spin direction.

Alternatively, the target spin direction can also be determined by performing double spin asymmetry measurements using the ^3He target in the elastic and the Δ resonance regions, and comparing the sign of the asymmetry with theoretical calculations [76][77]. For this experiment, the absolute sign of the ^3He elastic double spin asymmetry was first obtained using the standard Hall A SAMC (Single Arm Monte Carlo). The result from the SAMC was then compared to a measured ^3He elastic asymmetry, taking into account all the sign conventions.

From the SAMC result, A_{phys}^{MC} was positive for both target spin directions - one, along the beam direction and the other, opposite to beam direction. Whereas the measured ^3He

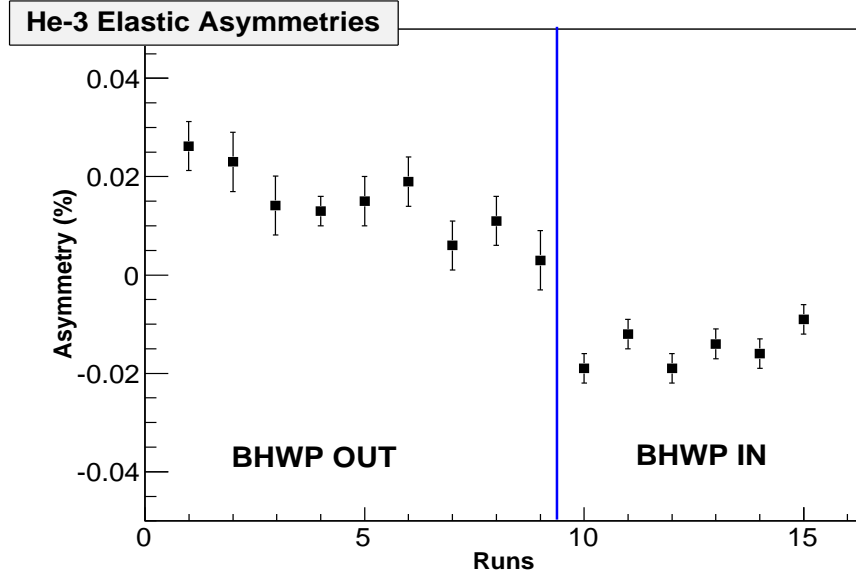


Figure 5.21: Raw ^3He asymmetry for different runs. There is a clear reversal of the asymmetry sign when the beam half-wave plate(BHWP) is inserted in the beamline [14].

raw elastic asymmetry was negative when the target spins were pointing along the beam direction (towards downstream) and positive when they are pointing in the 180° opposite to the beam direction. Therefore, an additional negative sign, due to the target polarization direction, makes the physics asymmetry positive when the spins are pointing along the beam direction.

Figure 5.21 shows the raw ^3He elastic asymmetries for different runs. The asymmetry reverses sign when the beam half-wave plate is inserted, which is expected as the electron helicity reverses. Similarly, Fig 5.23 shows the Δ asymmetry in two opposite target spin directions. Again, the asymmetry changes sign when target spin is reversed.

The magnitude of the measured ^3He elastic asymmetry is also compared with the SAMC result which was obtained in the same kinematic region. At an incoming beam energy of 1.23 GeV and a spectrometer angle of 16° the elastic asymmetry obtained from the constant fit (see Fig 5.22) is $A_{phy} = 0.04549 \pm 0.0031$. The Monte Carlo result yields $A_{phys}^{MC} = 0.0479$. The overall systematic uncertainty of the measured asymmetry was $\sim 4\%$ and for the simulation it was $\sim 1.6\%$. The full results of the ^3He elastic and Δ asymmetries are discussed in the [14].

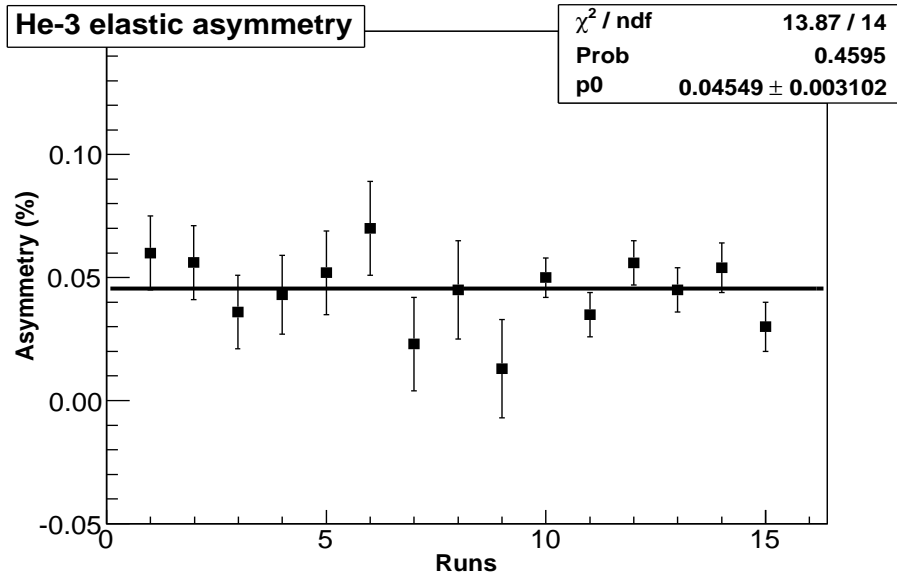


Figure 5.22: ^3He elastic asymmetry obtained from the constant fit to the run-by-run asymmetry at $E_0 = 1.23$ GeV and a spectrometer angle of 16° [14].

5.10 Dilutions to the Asymmetry

To extract the ^3He physics asymmetry from the measured raw asymmetry, the contamination from unpolarized material in the target region needs to be considered. There are two main sources of contamination. One, the small amount of N_2 gas in the target cell and second, the glass wall of the target cell itself. A study was done to determine the event rate due to the cell wall using the data from an empty reference cell. When all the $N(e, e'\pi)X$ SIDIS cuts were applied, this event rate was found to be zero. Therefore, for this experiment the contribution from the cell wall was zero. The contribution from the nitrogen gas in the target cell is discussed below.

5.10.1 Nitrogen Dilution

As discussed in section 3.2.3, a small amount of N_2 gas is added to the ^3He target cell to improve the rubidium polarization in the pumping chamber. There is no way to separate the semi-inclusive DIS events coming from the polarized ^3He gas and the events scattered from the N_2 molecules. Since the nitrogen cross-section is larger than the ^3He cross-section, there is a significant contribution to the unpolarized cross-section from the N_2 molecules. This will result in a dilution of the physics asymmetry of interest. This dilution needs to be

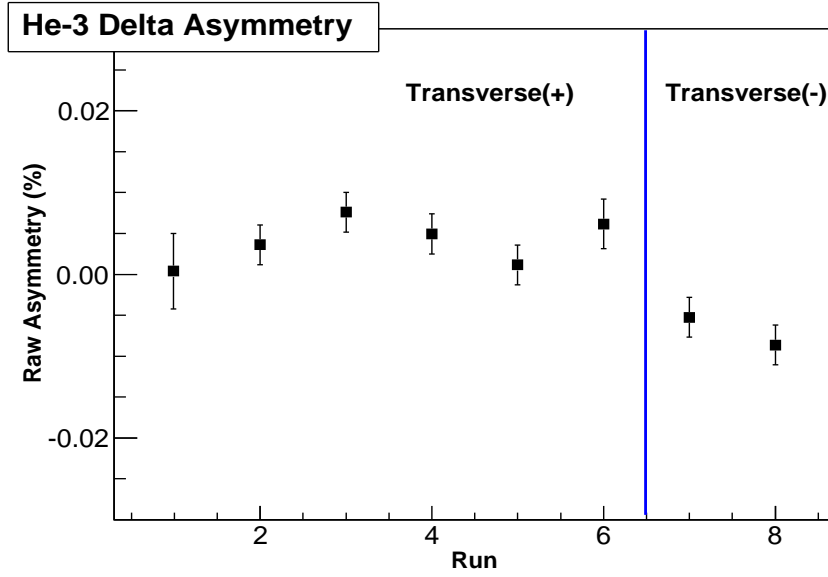


Figure 5.23: Raw ^3He asymmetry in the Δ resonance region for different runs. Transverse(+) and Transverse(-) indicate regions with the two opposite target spin directions. The asymmetry changes sign with the change in the target spin direction [14].

corrected for in order to extract the ^3He physics asymmetry. The dilution factor is defined as:

$$f_{N_2} = \frac{Y_{^3\text{He}}}{Y_{^3\text{He}} + Y_{N_2}} \quad (5.17)$$

$$f_{N_2} = \frac{n_{^3\text{He}}\sigma_{^3\text{He}}}{n_{^3\text{He}}\sigma_{^3\text{He}} + n_{N_2}\sigma_{N_2}} = \frac{1}{1 + \frac{n_{N_2}\sigma_{N_2}}{n_{^3\text{He}}\sigma_{^3\text{He}}}}. \quad (5.18)$$

where σ_{N_2} and $\sigma_{^3\text{He}}$ are the cross sections for N_2 and ^3He respectively. These cross sections can be obtained using data taken with reference cells which were filled with pure N_2 and ^3He gas separately. The densities of the N_2 gas and the ^3He gas in the main target cell, n_{N_2} and $n_{^3\text{He}}$, can be obtained from the cell filling density information. During E06-010, three ^3He target cells were used. Table 5.10.1 shows the filling densities of ^3He and N_2 in these cells in the units of amagats¹. The density of N_2 in the target cell was also verified by taking scattering data. The idea is to compare the yield from the nitrogen elastic peak in the reference cell, which has a known density, to the yield from the nitrogen elastic peak in a polarized ^3He cell.

$$n_{N_2}^{polcell} = \frac{Y_{N_2}^{elastic}}{Y_{N_2}^{elastic}} n_{N_2}^{refcell}. \quad (5.19)$$

¹An amagat is a unit of number density. It is defined as the number of ideal gas molecules per unit volume at 1 atm (= 101.325 kPa) and 0°C (= 273.15 K)

Table 5.6: The filling densities of ^3He and N_2 in the target cells. The uncertainty for ^3He was 2% and for N_2 it was 5% (relative).

Target Cell	^3He density (amagats)	N_2 density (amagats)
Maureen	7.52	0.106
Brady	7.87	0.11
Astral	8.08	0.11

For this measurement the data were taken at ^3He elastic kinematics where the nitrogen elastic peak can also be observed. We can further reduce the systematic uncertainties in Eq. (5.19) by changing the pressure of the nitrogen in the reference cell and using the slope of the N_2 pressure curve (yield vs. pressure) to determine the nitrogen number density in the ^3He target cell.

5.11 ^3He Nuclear Corrections - Extraction of Neutron Information

The properties of the free nucleons are modified by various effects inside the nucleus. These effects include fermi motion, nuclear binding, spin depolarization, and nuclear shadowing. Therefore, we need a method to extract the neutron information from the measured ^3He asymmetries. A standard approach, in the DIS region, used by many experiments in the past [78][79][80] is to use an effective nucleon polarization method [81][82][83]. In this method the measured ^3He asymmetry is expressed as,

$$A_{^3\text{He}} = 2p_p f_p A_p + p_n f_n A_n \quad (5.20)$$

where $f_{(p)n}$ is the proton(neutron) "dilution" factors and $p_{(p)n}$ is the effective polarization of the protons (neutrons) inside the ^3He nuclei. They are given by [82]

$$p_n = 0.86 \pm 0.02 \quad \text{and} \quad p_p = 0.028 \pm 0.004. \quad (5.21)$$

These effective polarizations are obtained using ^3He wave functions constructed from the nucleon-nucleon potentials.

Recently, S. Scopetta *et.al.* [18] have extended this calculation to the semi-inclusive DIS process which involves fragmentation functions along with the parton distribution functions.

In particular, a calculation was done to show the validity of the effective polarization method to extract the neutron single spin asymmetries (both Collins and Sivers asymmetries) using a transversely polarized ^3He target in the same kinematic region as E06-010. The calculation was performed in the frame work of the impulse approximation (IA) which assumes that in the SIDIS process the hard probe interacts with single nucleon and there are no further interactions with the recoiling nuclear system. The other assumption is that the internal structure of the nucleon is not modified when it is in the nuclear medium, rather it is same as a free nucleon.

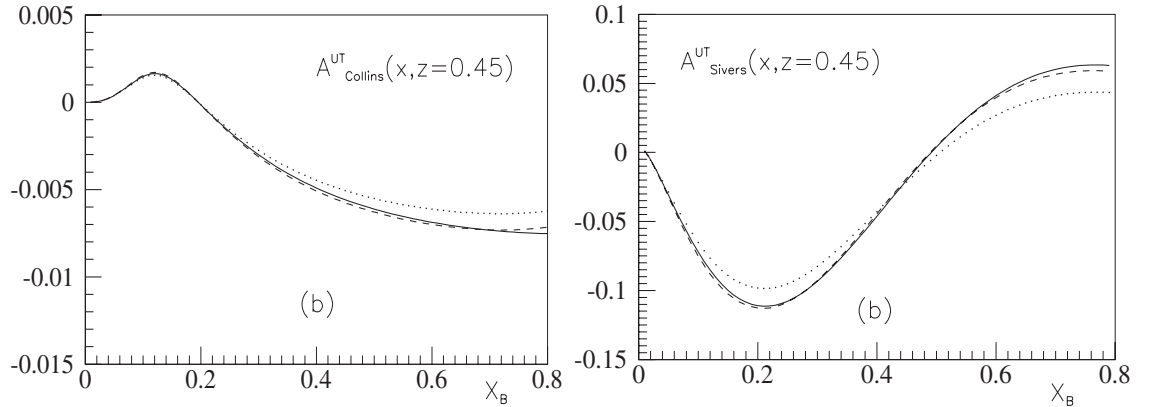


Figure 5.24: The left(right) plot shows the model calculation of the neutron Collins(Sivers) asymmetry for π^- meson (solid curve). The dashed curve shows the asymmetry extracted from Eq.(5.20) and dotted curve shows result when the proton polarization is ignored in Eq.(5.20). This figure is reproduced from Ref. [18]

Figure 5.24 shows the model calculation for the neutron Collins and Siver asymmetries for negatively charged pions at $z=0.45$, a value which is very close to our experimental value. The solid curve corresponds to the direct neutron calculation whereas the dashed curve shows the result using Eq.(5.20). The dotted curve shows the result if the proton polarization is ignored in Eq.(5.20). The same calculations can be directly extended to the positive pion asymmetries. It is clear from the plot that the difference between the solid curve and the dashed curve is at a few percent level. Therefore, it is safe to use the effective polarization approach to extract the neutron asymmetries from ^3He .

Although these calculations were done in the impulse approximation framework, the effects of nuclear shadowing and final state interactions(FSI), in principle, cannot be ignored in the case of SIDIS processes. However, it is worth noting that the nuclear shadowing effect is more pronounced in the small Bjorken x region. This experiment probes the valence quark

region ($0.1 < x < 0.4$). Therefore, the effect from nuclear shadowing is ignored. The FSI cannot be completely ignored in the SIDIS processes, since we detect the outgoing hadron (unlike the inclusive DIS process), especially, at these Q^2 values ($Q^2 < 3 \text{ GeV}^2$ for E06-010). However, due to the large energy fraction of the pion ($z = 0.5$) and an outgoing pion momentum of 2.35 GeV^2 , the effects of FSI are neglected. More studies are needed to fully understand these effects in SIDIS processes.

CHAPTER 6: RESULTS AND OUTLOOK

In this chapter we will present the results of the Collins and Sivers asymmetries for positive pions obtained from a ${}^3\text{He}$ target. Then we will show the extracted Collins and Sivers moments for the neutron from the $n^\uparrow(e, e'\pi^+)X$ SIDIS reaction. The Collins and Sivers moments presented here are close to the final results. The study on major systematic uncertainties are finished, but there are still some other systematic studies that are currently being carried out, and the effect of these are not expected to change the results in any significant way. They will be discussed towards the end of this chapter.

Along with these main results, the inclusive single hadron asymmetries from the ${}^3\text{He}^\uparrow(e, h^{+/-})X$ reaction in both spectrometers (BigBite and HRS) will be presented. The BigBite spectrometer on the right side of the beam has large angular and momentum coverage, therefore the asymmetries are presented as function of hadron momentum in the BigBite spectrometer, whereas the HRS on the left side of the beam has a very narrow angular and momentum coverage, therefore only one value of the asymmetry is presented for the inclusive hadron channel at a momentum of 2.35 GeV. For the inclusive hadron asymmetry results, only statistical errors are shown. The systematic studies are currently being studied.

6.1 HRS Inclusive Hadron Single Spin Asymmetries

In this section the preliminary HRS inclusive hadron asymmetries are presented. In the inclusive hadron process, ${}^3\text{He}^\uparrow(e, h^{+/-})X$, only the produced hadron is detected in the spectrometer. The target single spin asymmetry for this type of measurement is given by

$$A_{raw} = \frac{1}{P} \frac{Y_+ - Y_-}{Y_+ + Y_-} \quad (6.1)$$

where $+$ and $-$ represent the two opposite target spin directions and P is the polarization. As discussed in the section 3.1, data was taken with two target spin configurations - "transverse" and "vertical". Figure 6.1 shows the simplified diagram of these two configurations. Here \vec{k}_1 , \vec{k}_2 , and \vec{S}_T are the vectors corresponding to the initial electron momentum, the produced hadron momentum, and the target spin, respectively. Also, the spin angle (ϕ_S^h) in this process is given by the angle between the planes formed by the $\vec{k}_1 \times \vec{k}_2$ and $\vec{k}_1 \times \vec{S}_T$.

Figure 6.2 shows the inclusive asymmetries for π^+ and π^- mesons, and protons at

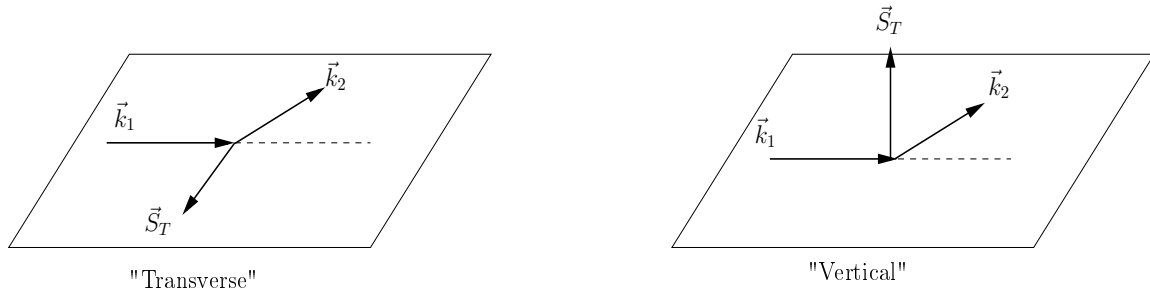


Figure 6.1: The left(right) panel shows the transverse(vertical) target spin configurations, where the incoming electron (\vec{k}_1), the outgoing hadron(\vec{k}_2), and the spin vectors(\vec{S}_T) are shown.

$P_h = 2.35$ GeV. These are corrected for the target polarization but not corrected for the N_2 dilution. The error bars represent only the statistical uncertainty. The systematic uncertainties are currently being studied. There is a clear non-zero asymmetry observed when the target spin is "vertical". In this case, the π^+ and π^- meson asymmetries have opposite signs and the proton asymmetry has the same sign as the π^+ asymmetry, indicating a quark flavor dependence. In the "transverse" configuration, all the asymmetries are zero within the statistical uncertainties. Due to small acceptance of the HRS and the average ϕ_S^h being close to zero, the asymmetries are expected to be zero in this configuration. Moreover, due to the small acceptance we cannot study the P_T , the transverse momentum of the outgoing hadron, dependence of these asymmetries in the HRS. The average P_T for this measurement is about 0.65 GeV.

6.2 BigBite Inclusive Hadron Single Spin Asymmetries

In this section the BigBite inclusive hadron asymmetries are presented. Since there was no possibility to separate different hadron species in the BigBite spectrometer, the asymmetries are presented as charged hadron asymmetries. However, the hadron production in this kinematics is mostly dominated by pions. Kaon production is expected to be very small at these energies. We observed that a significant fraction of the event sample consisted of photons, which were mainly produced by the decay of π^0 mesons produced in the target. The inclusive photon asymmetry is also presented which reflects the π^0 asymmetry.

Figure 6.3 shows the asymmetry for the negatively charged hadrons and Figure 6.4 is for the positively charged hadrons in the two target spin configuration mentioned earlier.

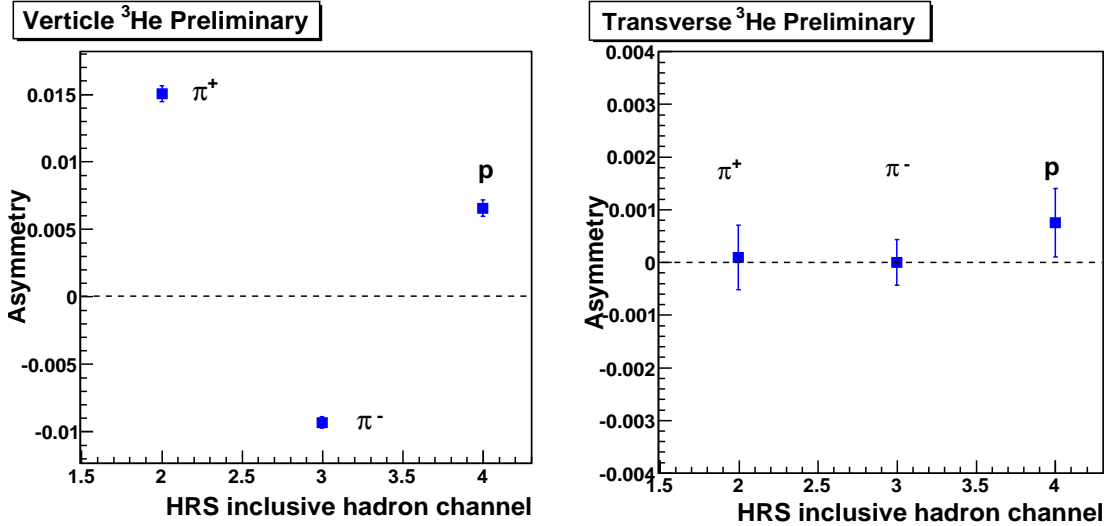


Figure 6.2: The left(right) panel shows the inclusive hadron asymmetry in the HRS for "vertical" ("transverse") spin configuration corrected for the target polarization. These asymmetries are not corrected for N_2 dilution. The error bars indicate the statistical uncertainty. The study of the systematic uncertainties is currently underway.

The asymmetries were corrected with the target polarization but not for the N_2 dilution. The error bars represent only the statistical uncertainty. As discussed in section 3.3.1, two different triggers, T1 and T6, were used in the BigBite spectrometer to take the singles data. Although both triggers were constructed using the same detector signals, one at lower threshold (T1) and the other at higher threshold (T6), the data they sampled were completely different due to high prescale factors. The black and red points indicate the asymmetries obtained from the two triggers.

For a given hadron, the asymmetries in the HRS and in the BigBite spectrometer should have opposite signs, since the HRS was on the left side of the beam and BigBite on the right side. Our observation of the asymmetry sign is consistent with this expectation. For example, in the "vertical" target spin case, the observed asymmetry in the HRS for π^+ meson is positive (Figure 6.2) and that for the BigBite spectrometer it is negative (Figure 6.4). Here, it is assumed that the positive hadrons in the BigBite spectrometer is dominated by π^+ meson production. Similarly the negative hadrons are dominated by π^- mesons. In addition to this, as in the case of the HRS, we observe opposite signs for positively and negatively charged hadron asymmetries in the BigBite spectrometer.

Since the BigBite spectrometer has much larger angular acceptance than the HRS, we can observe a ϕ_S^h angular dependence of the asymmetry. The data from both target spin

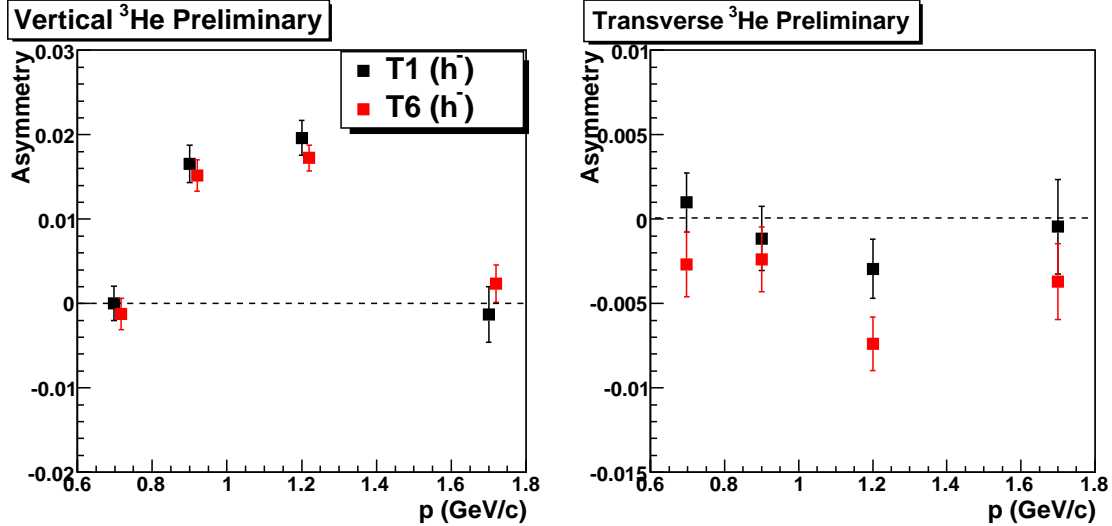


Figure 6.3: The two panels show the asymmetries in the inclusive ${}^3\text{He}e^\dagger(e, h^-)X$ reaction. Corrections due to N_2 dilution have not been applied.

configurations was combined and the resultant asymmetries were fitted with an angular modulation of the form,

$$A_{3\text{He}}(\phi_S^h) = a_0 \sin(\phi_S^h) \quad (6.2)$$

where $a_0 = \langle \sin(\phi_S^h) \rangle$ is the amplitude of the asymmetry moment. Figure 6.5 shows the asymmetries obtained for the negative hadrons, positive hadrons, and photons as function of the hadron's momentum. We observed large negative asymmetries for the photons, which most likely carries the π^0 asymmetries.

Although, the HRS has a very small angular acceptance, an attempt was made to fit the asymmetry from the HRS to the same angular modulation that was described earlier. Figure 6.6 shows the result of this fit. It shows the asymmetry moment obtained for π^+ and π^- mesons and protons. These moments are not corrected for the N_2 dilutions. A general observation from Figs. 6.5 and 6.6 is that the signs of the asymmetry moments for the π^+ and π^- mesons in the HRS are consistent with that of the BigBite spectrometer h^+ and h^- particles, respectively. We can compare this result with the analyzing power A_N obtained in the FANL E704 experiment, where $p^\dagger p$ collisions were used to measure the inclusive hadron asymmetry [84]. A_N had opposite signs for oppositely charged hadrons, as observed in this experiment. Moreover, for A_N , the π^0 and π^+ mesons have the same sign, which is again consistent with what we observe in our experiment, assuming the photon carries the π^0 asymmetry. Further studies on the P_T and x_F dependence of the observed

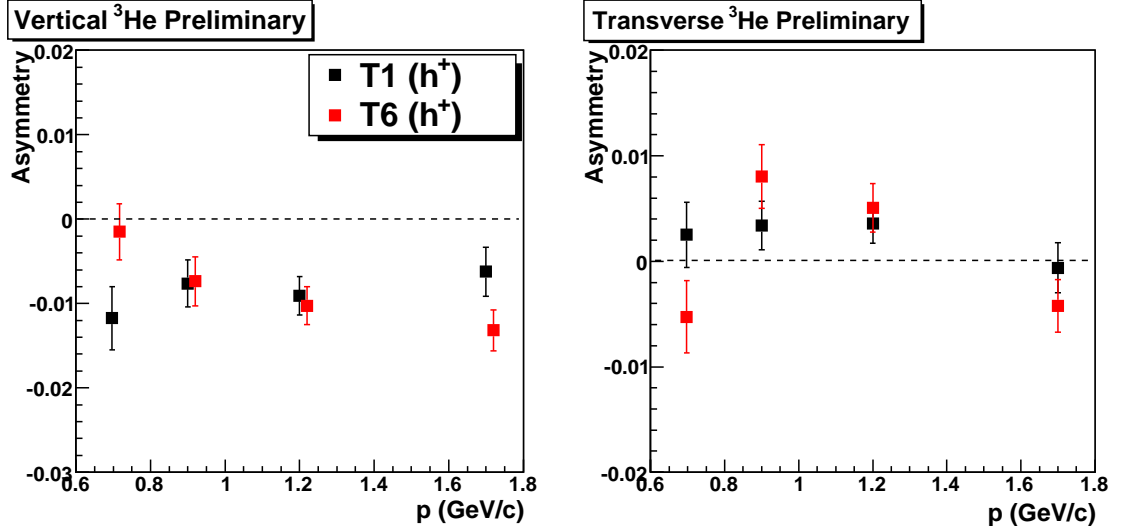


Figure 6.4: The two panels shows the asymmetries in the inclusive ${}^3\text{He}e^\dagger(e, h^+)X$ reaction. Corrections due to N_2 dilution have not been applied.

inclusive hadron asymmetries in this experiment are shown in [12].

6.3 Single Spin Asymmetry Results for Semi-Inclusive DIS in the $n^\uparrow(e, e'\pi^+)X$ Reaction

In this section the target SSA in the coincidence channel $n^\uparrow(e, e'\pi^+)X$ are presented. The cuts used for selecting the SIDIS events are described in chapter 5. Initially, the data was divided into five bins in the BigBite momentum, from 0.6 GeV to 2.2 GeV. The asymmetry was calculated in each momentum bin, corrected only for the target polarization. Figure 6.7 shows the π^+ asymmetry as a function of BigBite momentum for two different target spin configurations. Differently colored points correspond to the asymmetries obtained using pass-3 and pass-4¹ data with variations in the PID and acceptance cuts. It should be noted here that the full corrections for the BigBite shower and preshower degradation were included only in pass-4.

¹The raw data is processed in several iterations during the data analysis, each time refining detector calibrations and saved variables. Each such iteration is known as a “pass”.

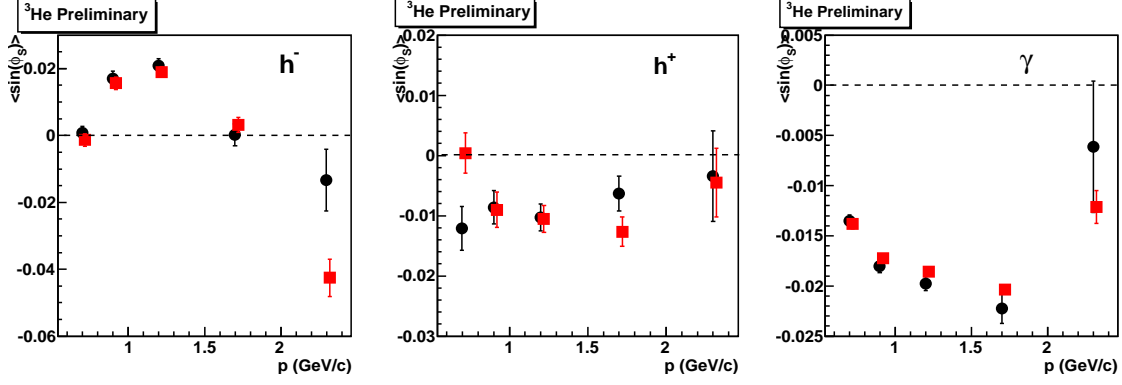


Figure 6.5: BigBite singles asymmetries obtained from the angular modulation $\langle \sin(\phi_S^h) \rangle$ for negative(left) hadrons, positive(center) hadrons, and photons(right). The error bars represent the statistical uncertainty. The systematic errors are not shown as they are currently under study.

6.3.1 Angular Modulation: Extraction of Asymmetry Moments

As discussed in section 3.1, the measured single spin asymmetries, neglecting the sub-leading twist terms, are proportional to three terms with angular modulations given by,

$$A_{UT}(\phi_h, \phi_S) = A_{UT}^{\sin(\phi_h + \phi_S)} \sin(\phi_h + \phi_S) + A_{UT}^{\sin(\phi_h - \phi_S)} \sin(\phi_h - \phi_S) + A_{UT}^{\sin(3\phi_h - \phi_S)} \sin(3\phi_h - \phi_S), \quad (6.3)$$

where the terms with angular modulation $\sin(\phi_h + \phi_S)$, $\sin(\phi_h - \phi_S)$, and $\sin(3\phi_h - \phi_S)$ are known as Collins, Sivers, and Pretzelosity terms [85], respectively.

In order to separate the asymmetry moments, the data were first binned into several two-dimensional (2D) bins of ϕ_S and ϕ_h . The raw asymmetry was computed in each of these 2D bins taking the target polarization into account, and then fitted with the function given by Eq. (6.3). Fig 6.8 shows the result of this fit. The black points indicate the result obtained from using all three terms in Eq. (6.3), whereas the red and magenta points show the result obtained from using only the first two terms with $\sin(\phi_h + \phi_S)$ and $\sin(\phi_h - \phi_S)$ modulation. Two different fitting procedures were used - (M) refers to a fit based on the "MINUIT2" minimization routine, and (F) refers to the normal two-dimensional fitting procedure with two terms. In the MINUIT2 fit there is the possibility to exclude the angular bins with very low statistics. The results from both procedures, "M" and "F", agree when only two terms are used in the fit. The statistical uncertainty becomes large when all three terms are taken into account. This is due to the fact that there is limited angular coverage in $\phi_S - \phi_h$ for this experiment [12].

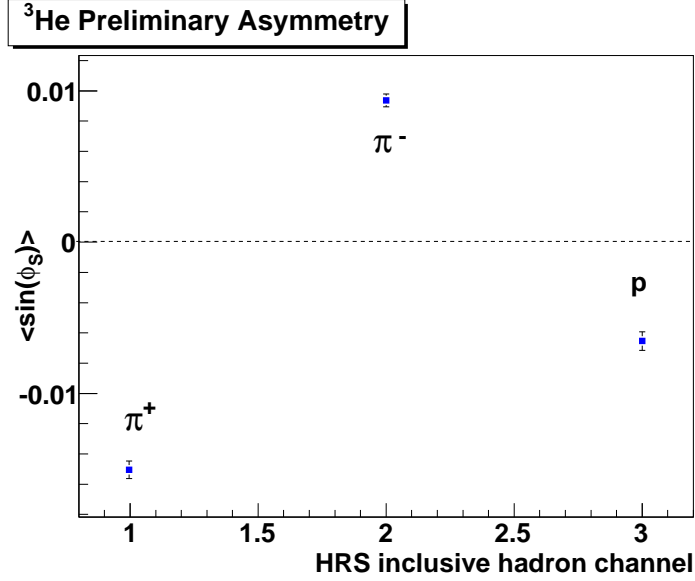


Figure 6.6: HRS singles asymmetries obtained from the angular modulation $\langle \sin(\phi_S^h) \rangle$ for π^+ and π^- mesons and protons, at $P_h=2.35$ GeV. The error bars represent the statistical uncertainty. The systematic errors are not shown.

6.3.2 Nitrogen Dilution Correction

The raw ^3He asymmetry moments extracted in the previous section need to be corrected for the N_2 dilution to obtain the ^3He physics asymmetry. The procedure to extract the N_2 dilution factor is discussed in section 5.10. The study was done by X. Qian from Duke University. The corrected asymmetry is

$$A_{3\text{He}}^{\text{raw}} = P_{3\text{He}} f_{\text{N}_2} A_{3\text{He}}^{\text{phy}}. \quad (6.4)$$

where f_{N_2} is the nitrogen dilution factor given by the Eq. (5.18). The target polarization ($P_{3\text{He}}$) is already taken into account while computing the raw asymmetry moments. In the calculation of f_{N_2} , the charge and pressure normalized yield from the N_2 and ^3He gases are obtained from the reference cell data. The dilution factors were obtained in all four x -bins separately for each of the three target cells. Figure 6.9 summarizes the nitrogen dilution factors for all three target cells. The error bars represent the quadrature sum of the statistical and systematic uncertainties. The systematic uncertainties include, uncertainties in the filling density of ^3He ($\sim 2\%$) and N_2 ($\sim 5\%$), uncertainties in the reference cell pressure (~ 1 psig), and radiative corrections due to small differences in the target cell wall thicknesses.

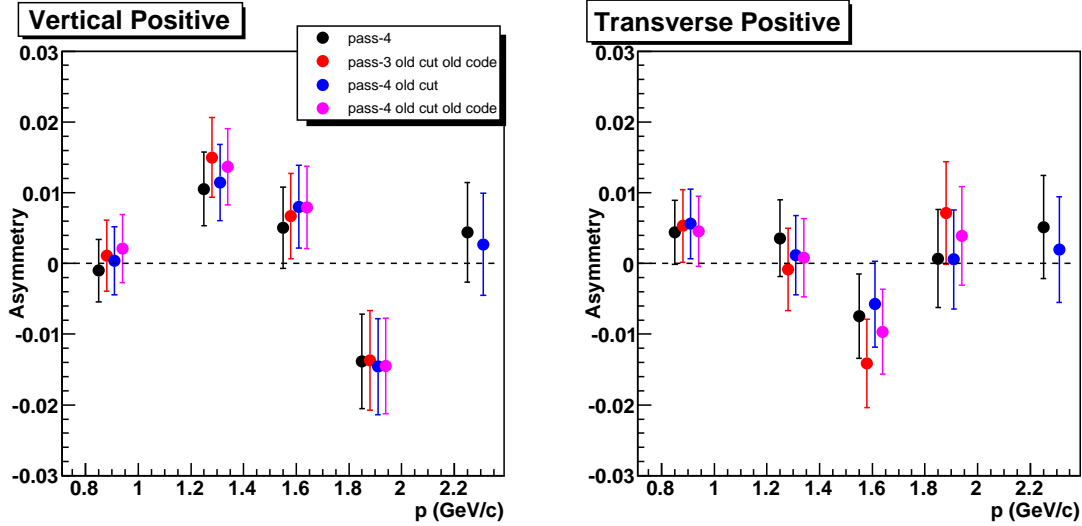


Figure 6.7: The left (right) panel shows the measured SSA in the ${}^3\text{He}(e, e'\pi^+)X$ channel when target spin is vertical (transverse). Different colors indicate the same data but with variations in the PID and acceptance cuts. "pass-4" is the most recent data used for the analysis. The error bars show only the statistical uncertainty [12].

6.3.3 Systematic Uncertainties

The major systematic uncertainties associated with the extracted ${}^3\text{He}$ asymmetry moments are presented below. The summary of all the systematic uncertainties is listed in Table 6.2 at the end.

- Negative Pion Contamination to the DIS Electron Sample:** In section 5.7.1 the contamination of π^- mesons to the BigBite electron sample was discussed. This type of background introduces a systematic uncertainty in the coincidence ${}^3\text{He}(e, e'\pi^+)X$ channel. In order to determine the level of uncertainty, the $\sin(\phi_h + \phi_S)$ and $\sin(\phi_h - \phi_S)$ asymmetry moments for the ${}^3\text{He}^\uparrow(e, \pi^-\pi^+)X$ reaction were computed by selecting π^- events in the BigBite spectrometer instead of electrons, in coincidence with π^+ events in the HRS. The difference between the central value of the asymmetry moments computed for the ${}^3\text{He}^\uparrow(e, e'\pi^+)X$ and the ${}^3\text{He}^\uparrow(e, \pi^-\pi^+)X$ event samples, weighted by the contamination fraction (given in Table 5.4), determines the systematic uncertainty. Fig 6.10 shows the level of SSA in the ${}^3\text{He}^\uparrow(e, \pi^-\pi^+)X$ channel in two target spin states. The systematic uncertainty was found to be between 0.1% to 2.5% depending on the x -bin.
- Photon-induced Electron Contamination:** The systematic uncertainty associ-

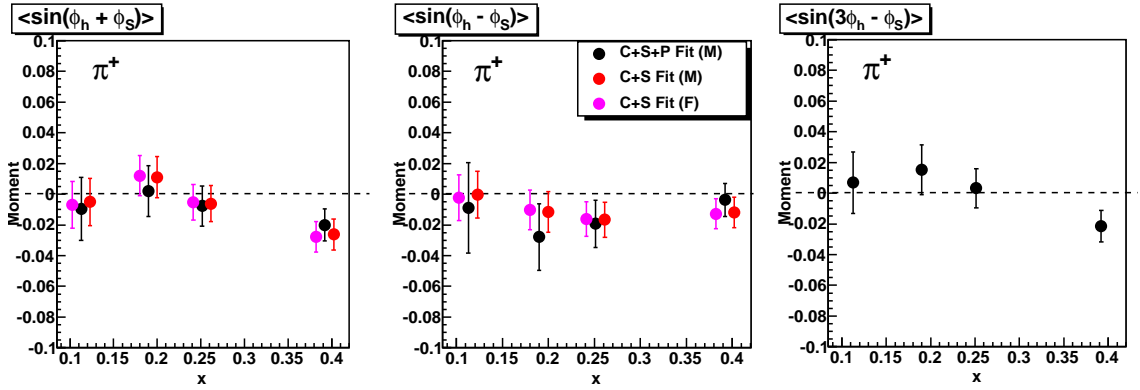


Figure 6.8: ${}^3\text{He}\uparrow(e, e'\pi^+)X$ asymmetry moments obtained from fitting the Collins (left), Siverson(right), and Pretzelosity(right) angular modulations to the measured raw asymmetry. The error bars represent the statistical uncertainty.

ated with the photon-induced electron contamination, discussed in section 5.7.2, was also determined in the same way as the π^- meson contamination. In this case, the asymmetry moments were computed for ${}^3\text{He}\uparrow(e, \gamma\pi^+)X$ and the central values were compared with the ${}^3\text{He}\uparrow(e, e'\pi^+)X$ moments, after weighting with the corresponding photon-induced electron contamination fraction (given in Table 5.5). The systematic uncertainties for this background were found to be between 6% to 32% depending on the x bin. The lowest x bin has largest the uncertainty. Fig 6.11 shows the level of asymmetry in the ${}^3\text{He}\uparrow(e, \gamma\pi^+)X$ channel for the two target spin states.

- **Yield Drift:** The gain drop observed on the BigBite preshower and shower detectors (see section 4.5) lead to a slow drift in the measured yield for the ${}^3\text{He}\uparrow(e, e'\pi^+)X$ reaction, since these detectors were used for triggering the electron. The drift in the yields can lead to false asymmetries, thereby contaminating the physics asymmetry. However, the target spin-flip sequence was independent of the detector signals and hence not correlated to the changes in the detectors. Therefore any false asymmetry generated due to drift in the yield is expected to be small. A study was performed [12] to estimate the systematic uncertainty arising from this effect and it was found to be a maximally 11% of the statistical uncertainty.
- **Systematics Due to Other Angular Modulation Terms:** The asymmetry moments presented in this thesis have been extracted using a 2D fit containing only two leading-twist terms with angular modulations $\sin(\phi_h + \phi_S)$ and $\sin(\phi_h - \phi_S)$. But

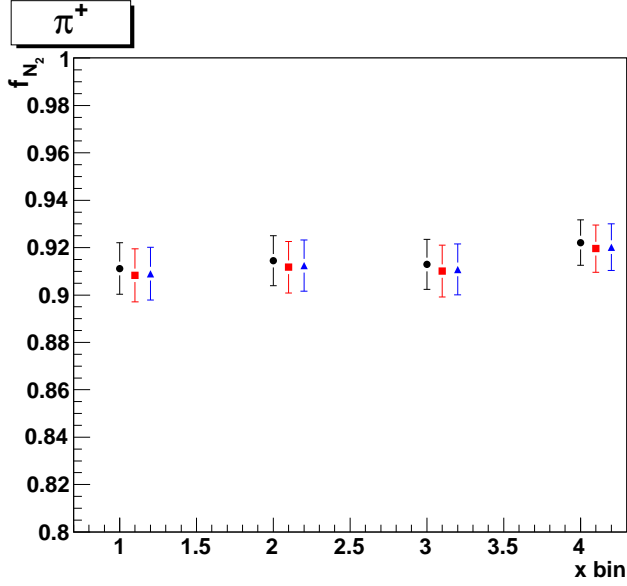


Figure 6.9: Nitrogen dilution factors are shown in each x bin. Different colors indicate the dilution factors for the three different target cells [12].

there are a total of five terms in the expression of the cross-section for unpolarized beam and transversely polarized target (see Eq. (2.45)). Two of them are higher-twist terms and rest the are leading-twist. There can be systematic error due the exclusion of these terms from the 2D fit. The main systematic effect can come from the omission of third leading twist term with an angular modulation of $\sin(3\phi_h - \phi_S)$ (Pretzelosity [85]). The contribution from the higher twist terms is assumed to be small. In addition to this, the contributions from the terms arising due to a small component of longitudinal polarization (A_{UL} term) need to be accounted for. Since the denominator of the asymmetry contains the differential cross section for the unpolarized target and beam, these terms also need to be included in the systematic studies. A preliminary study of these effects is done in [12]. Here we summarize the systematic errors due to all the above mentioned angular terms in Table 6.1.

Other sources of systematic uncertainties include target polarization, target density fluctuations, single track cut on the HRS and kaon contamination in the pion sample. A complete study of the systematics uncertainties is in progress. Here we show the major systematic uncertainties in Table 6.2.

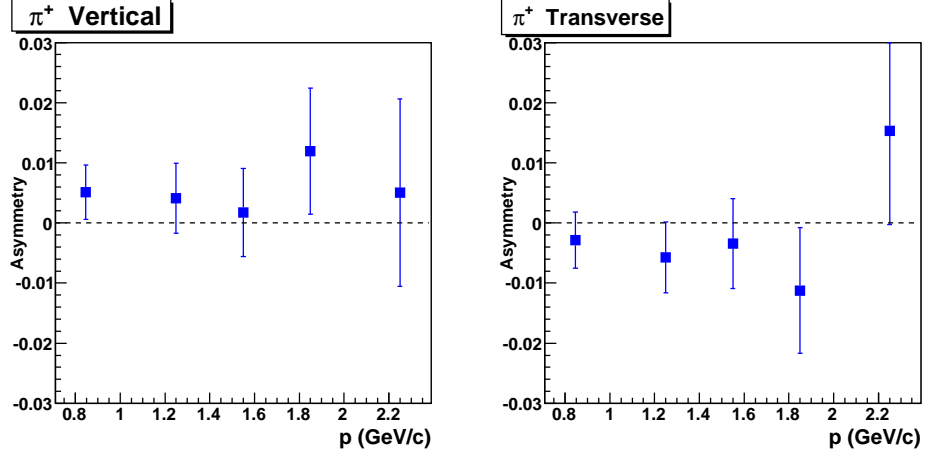


Figure 6.10: The left(right) panel shows the SSA in ${}^3\text{He}\uparrow(e, \pi^-\pi^+)X$ channel in vertical(transverse) target spin configuration.

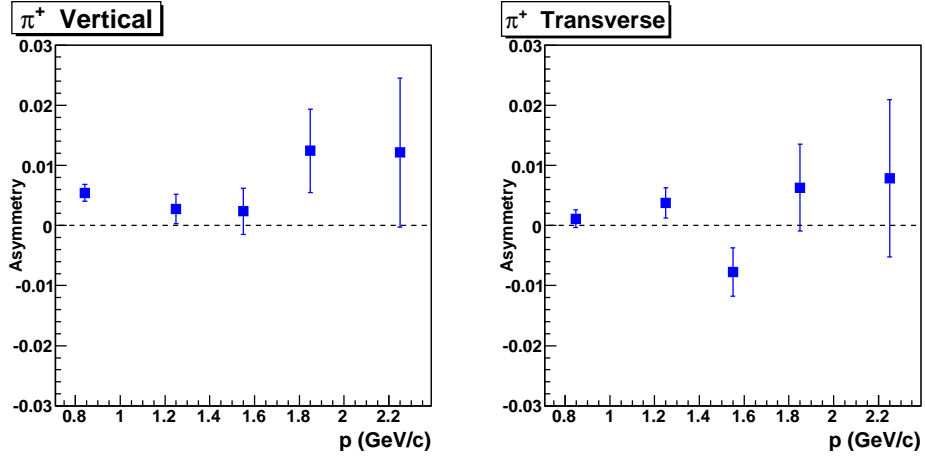


Figure 6.11: The left(right) panel shows the SSA in the ${}^3\text{He}\uparrow(e, \gamma\pi^+)X$ channel in the vertical(transverse) target spin configuration.

6.3.4 Single Spin Asymmetries Results for ${}^3\text{He}$

The asymmetry moments obtained from the 2D fit using the Collins and Sivers terms are shown in Fig 6.12. This result is for the ${}^3\text{He}\uparrow(e, e'\pi^+)X$ reaction. The error bars represent the statistical uncertainty and the combined systematic uncertainty from all sources is shown as a red band at the bottom of the plot. The solid curve shows a theoretical prediction from Anselmino *et al.* [19][20].

From the plot it is clear that the result is dominated by the statistical errors. Except in the high x bin for the Collins moment, all other points are consistent with zero within the experimental errors.

Table 6.1: A summary of the systematic uncertainties due to exclusion of other angular terms in the fit to extract the Collins and Sivers moments. The neutron asymmetries(second column) were estimated using the preliminary proton results. The ^3He asymmetries were estimated using combined neutron and proton results. The effect of different angular terms for the Collins/Sivers moments are shown in the last two columns.

Angular term	Neutron π^+	^3He π^+	Collins π^+	Sivers π^+
$\sin(3\phi_h + \phi_S)$	-	-	14-68%	24-124%
$\sin(\phi_S)$	5%	0.7%	24-42%	25-43%
$\sin(2\phi_h + \phi_S)$	2%	$2.8e^{-3}$	8-10%	23-28%
A_{LU} leakage	3%	$5.2e^{-3}$	<0.1%	<0.1%
Cahn $\cos(\phi_h)$	5%	5%	2-9%	1-7%
Boer-Mulder $\cos(2\phi_h)$	5%	5%	1-3%	1-8%

6.3.5 Preliminary SSA on the Neutron

The extraction of neutron information from the measured ^3He physics asymmetries has been discussed in section 5.11. We use the *effective polarization* approach where the experimentally measured ^3He asymmetry can be written as

$$A_{3He} = 2p_p f_p A_p + p_n f_n A_n, \quad (6.5)$$

$$A_n = \frac{A_{3He} - 2p_p f_p A_p}{p_n f_n} \quad (6.6)$$

where p_p and p_n are the effective polarizations of the proton and neutron in the ^3He nucleus. f_p and f_n are the proton and neutron "dilution factors". A_p and A_n are the physics asymmetries corresponding to the proton and the neutron. The unpolarized cross-section of ^3He can be written as,

$$\sigma_U^{3He} = 2\sigma_U^p + \sigma_U^n, \quad (6.7)$$

and we can define the quantities f_p and f_n and f_{H_2} as,

$$f_p = \frac{\sigma_U^p}{2\sigma_U^p + \sigma_U^n}, \quad f_n = \frac{\sigma_U^n}{2\sigma_U^p + \sigma_U^n}, \quad f_{H_2} = 1 - \frac{\sigma_U^{H_2}}{2\sigma_U^p + \sigma_U^n}. \quad (6.8)$$

Using Eqs. (6.7) and (6.8) we can rewrite Eq. (6.9) as,

$$A_n = \frac{A_{3He} - p_p(1 - f_{H_2})A_p}{p_n f_{H_2}}, \quad (6.9)$$

where $p_p = 0.86 \pm 0.02$ and $p_n = -0.028 \pm 0.004$ (see [82]) and the proton asymmetry (A_p) can be estimated by a theory calculation with input from the information on the proton

Table 6.2: Systematic uncertainties associated with the various sources in the ${}^3\text{He}^\uparrow(e, e'\pi^+)X$ reaction. σ_{stat} is the statistical uncertainty and "relative" indicates uncertainties with respect to the central value.

Source	Systematic Uncertainty (in the units of σ_{stat})
BigBite Photon-induced e^- Cont.	0.32, 0.19, 0.06, 0.05
BigBite π^- Cont.	0.01 - 0.025
Vertex Cut	0.17
Yield Drift	0.11, 0.02, 0.02, 0.02
Bin Centering	0.13
HRS kaon Cont.	0.04
HRS Single Track Cut	0.015
Target Density	0.021
Target Polarization	5% (relative)
N_2 Dilution	0.3% - 0.6% (relative)

asymmetries from the HERMES experiment. Fig 6.13 shows the predictions of the Collins and Sivers moments for the proton and the neutron calculated by Anselmino *et al.*[19][20].

The dilution factor f_{H_2} can be computed either from the data or from the model calculation. From the data, f_{H_2} can be determined by calculating the ratio of the unpolarized cross sections of H_2 and ${}^3\text{He}$ using the reference cell data. In the model calculation a naïve x - z separation between the parton distribution function (PDF) and the fragmentation function (FF) is assumed in calculating the SIDIS cross-section ratio. The values of f_{H_2} used in this extraction procedure are shown in [12].

The preliminary neutron results for both the Collins and Sivers moments obtained from this method are shown in Fig 6.14. The error bars show the statistical uncertainty and the red band on the bottom shows the total systematic uncertainty. The solid magenta curve is a theory prediction from Anselmino *et al.* [19][20], the solid black curve is a prediction from Ma *et al.*[21][86], and the red curve is from Pasquini *et al.*[22].

The extracted neutron results suggest that the Collins moment is consistent with zero within the experimental errors and agree with the theory predictions, except for the highest x bin. The Sivers moments are not as large as predicted by the theory calculations. But the Sivers moment shows a clear trend favoring negative values. A summary of the absolute statistical and systematic errors in each Bjorken x bin is shown in Table 6.3 for both the Collins and Sivers moments. The experimental results are dominated by statistical errors

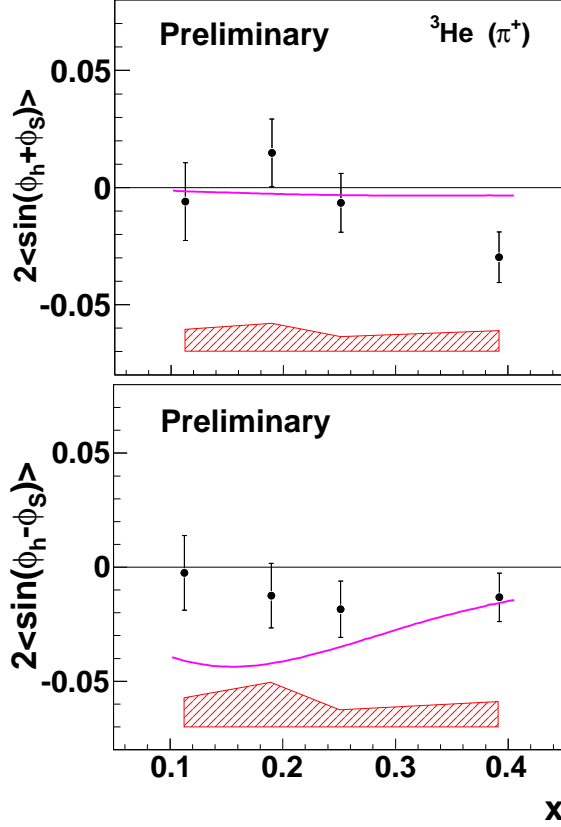


Figure 6.12: Preliminary results for the Collins and Sivers moments obtained for π^+ mesons on ${}^3\text{He}$. The error bars represent the statistical uncertainty and the red band shows the total systematic uncertainty. A theory prediction is shown by the solid curve [19][20].

and a more precise measurements are needed in terms of both statistics and systematics to clearly demonstrate a non-zero Sivers moment for the π^+ meson produced on neutrons.

The prediction for the Collins moment from Anselmino *et al.* is based on a global fit to the SIDIS data from the HERMES and COMPASS experiments, together with the $e^+e^- \rightarrow h_1 h_2 X$ data from the Belle experiment. They fit the data by assuming a simple parametrization, such that the transversity distribution obeys the Soffer bound, and simultaneously extract the Collins fragmentation function along with the transversity distribution function. The prediction for the Sivers moment is also based on a fit to the SIDIS data using a simple parametrization of the x dependence of the unknown Sivers function. In these fits they assume the factorization of the distribution and fragmentation functions. The prediction for the Collins moments from Ma *et al.* is based on a model for the transver-

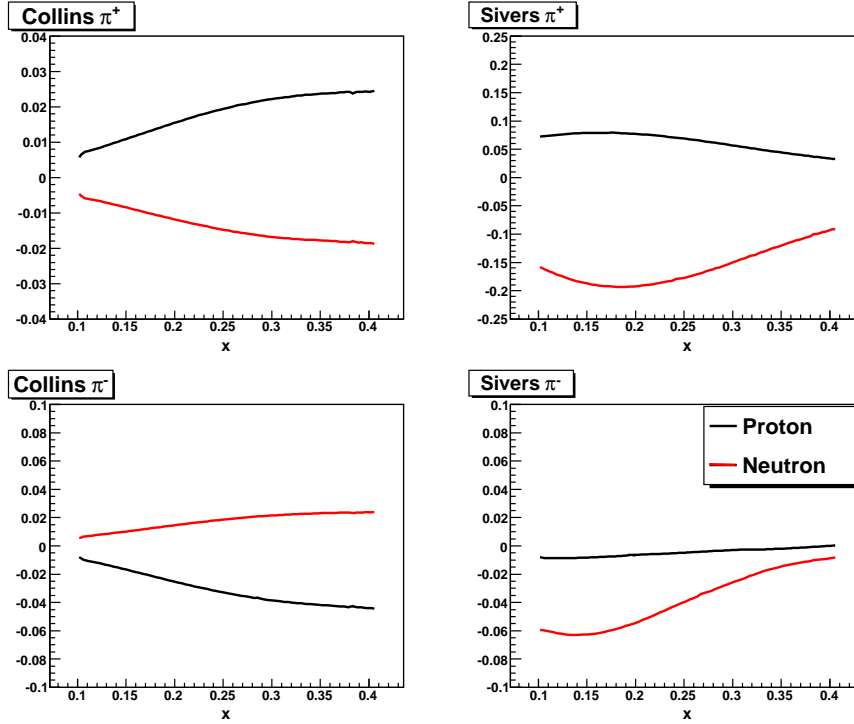


Figure 6.13: Theory calculations for proton and neutron Collins and Sivers moments by Anselmino *et al.* [19][20]

sity distribution and they use the same parametrization for the Collins fragmentation as Anselmino *et al.* [19][20]. Pasquini *et al.* calculate the transversity distribution function evolved to leading order using light-cone wavefunctions, and a parametrization used for the unpolarized distribution function in the denominator for the asymmetry (see Eq (2.61)) to predict the Collins moments [22].

Contributions to the Sivers asymmetries can come from two mechanisms – one due to the quark orbital angular momentum (L_q) and other due to the gluon orbital angular momentum (L_g). S. J. Brodsky and S. Gardner in their work [87] suggest that a flip in sign of the Sivers moment for π^+ production from neutron with respect to that observed on the proton will indicate relatively small contribution from L_g mechanism compared to the L_q mechanism. This is due to the distinct isospin structure of the L_g mechanism compared to the L_q mechanism, as discussed in Ref. [87]. Indeed, the results presented in this work for Sivers moment support this argument. The π^+ Sivers asymmetry on neutron is favoring a negative value (Figure 6.14), while that on the proton from the HERMES experiment is clearly a positive value (see Figure 2.13).

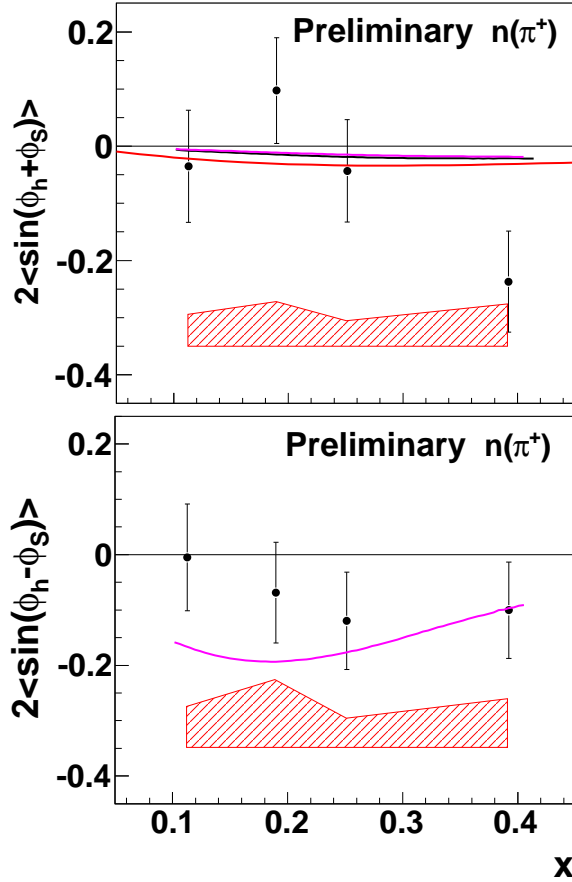


Figure 6.14: Preliminary results on the Collins and Sivers moments obtained for π^+ on the neutron. The error bars represent the statistical uncertainty and the red band shows the systematic errors. The solid magenta curve is a theory prediction from Anselmino *et al.*[19][20], the solid black curve is a prediction from Ma *et al.*[21], and the red curve is from Pasquini [22]

Work on Monte Carlo studies using SIMC² is being carried out to fully understand the systematic uncertainties associated with bin centering and various particle contamination. For example, contamination from diffractive ρ meson production. In addition to this, the systematics associated with the radiative effects have to be estimated. Both the incoming lepton or scattered lepton can emit real photons in a QED radiative process. This process changes the event kinematics and needs to be corrected with the momentum of the emitted photon. Not only the kinematical variables x and Q^2 are affected, but also the spin angle ϕ_S and the hadron angle ϕ_h , since z axis is defined by the virtual photon direction. For

²SIMC is a standard Hall-C Monte Carlo for coincidence reactions.

Table 6.3: A summary of the statistical and systematic errors in each Bjorken x bin for the Collins (columns 2 and 3) and Sivers moments (columns 4 and 5).

x -bin	$2\langle \sin(\phi_h + \phi_S) \rangle$		$2\langle \sin(\phi_h - \phi_S) \rangle$	
	Stat. Error (absolute)	Sys. Error (absolute)	Stat. Error (absolute)	Sys. Error (absolute)
0.113	9.8%	5.5%	9.6%	7.5%
0.190	9.2%	7.7%	9.1%	12.4%
0.251	8.9%	4.3%	8.8%	5.3%
0.392	8.8%	7.4%	8.7%	8.7%

the HERMES experiment in similar kinematics, it was estimated that the systematic uncertainty due to radiative effects was about 5% [2]. So, for this experiment it is expected to be of the same order. Presently these studies are also being carried out, but the effects are expected to be small and will not change the results in any significant way.

6.4 Summary and Future Studies

Experiment E06-010 took data from October 2008 until February 2009 on a transversely polarized ^3He target. We have presented a detailed description of the instrumentation and the detectors that were used in the experiment, and the procedures involved in calibrating these detectors. The physics data analysis which includes the selection of SIDIS events from the data using kinematical cuts, determining the background particle contamination and associated false asymmetries, and a procedure to extract the neutron information from the measured ^3He asymmetries have been discussed.

Collins and Sivers moments of π^+ mesons produced on neutrons have been presented for the first time. The neutron results were obtained by measuring single spin asymmetries in the SIDIS reaction $^3\text{He}e^\uparrow(e, e'\pi^+)X$ in a kinematical range of $0.19 < x < 0.34$ and $1.77 < Q^2 < 2.73 \text{ GeV}^2$. The Collins moments are consistent with zero within experimental uncertainties except for the highest x bin (around $x=0.4$) which shows a negative amplitude. The Sivers moments shows a systematic trend towards negative amplitudes, although not as large as predicted by the theory. These results along with the π^- meson results presented in [14] provide a vital input to the extraction of the transversity and Sivers distribution functions of different quark flavors. The results presented in this work are complementary to the two experiments that currently contain all our experimental knowledge on the Collins and Sivers moments - the HERMES experiment using a proton target [33][34] and the COMPASS experiment using both the proton and the deuteron targets [35][36].

Two new experiments have been proposed to run in Hall A after the Jefferson Lab 12 GeV energy upgrade. The first experiment (PR09-018) uses the BigBite spectrometer and a new large acceptance Super BigBite spectrometer as a hadron arm to measure the SSA in SIDIS reactions using a transversely polarized ^3He target [88]. The second experiment (PR12-09-014) uses a solenoid detector (SoLID) with a full 2π azimuthal angle coverage to measure the SSA on a transversely polarized ^3He target [89]. Due to its full angular coverage this experiment can provide data in four dimensions (x, z, P_T and Q^2) for the Collins, Sivers, and Pretzelosity[85] asymmetries. These two experiments can provide high precision data which can help in a much more precise determination of transversity and Sivers distribution functions.

Appendix A: CONVENTIONS

The following conventions are used in this thesis.

- The metric tensor $g^{\mu\nu}$ is given by

$$g^{\mu\nu} = g_{\mu\nu} = \begin{pmatrix} 1 & 0 & 0 & 0 \\ 0 & -1 & 0 & 0 \\ 0 & 0 & -1 & 0 \\ 0 & 0 & 0 & -1 \end{pmatrix} \quad (\text{A.1})$$

- The totally anti-symmetric matrix $\epsilon_{\mu\nu\alpha\beta}$ is normalized such that,

$$\epsilon^{0123} = -\epsilon_{0123} = +1 \quad (\text{A.2})$$

- A generic four-vector A^μ is written in Cartesian contravariant components, as

$$A^\mu = (A^0, A^1, A^2, A^3) = (A^0, \vec{A}) \quad (\text{A.3})$$

- The light-cone components of A^μ are defined as

$$A^\pm = \frac{1}{\sqrt{2}}(A^0 \pm A^3), \quad (\text{A.4})$$

and in the components A^μ can be written as

$$A^\mu = (A^+, A^-, \vec{A}_\perp). \quad (\text{A.5})$$

- γ -matrices: The Dirac matrices in the chiral representation are defined as

$$\gamma^0 = \begin{pmatrix} 0 & \mathbf{1} \\ \mathbf{1} & 0 \end{pmatrix}, \quad \gamma^i = \begin{pmatrix} 0 & -\sigma^i \\ \sigma^i & 0 \end{pmatrix}, \quad i = 1, 2, 3 \quad (\text{A.6})$$

where σ_i are the usual Pauli matrices. We defined

$$\gamma^5 = \gamma_5 = i\gamma^0\gamma^1\gamma^2\gamma^3 = \begin{pmatrix} \mathbf{1} & 0 \\ 0 & -\mathbf{1} \end{pmatrix} \quad (\text{A.7})$$

- The scalar product of the γ matrices and any four-vector A is defines as

$$\not{A} \equiv \gamma^\mu A_\mu = \gamma^0 A^0 - \gamma^1 A^1 - \gamma^2 A^2 - \gamma^3 A^3. \quad (\text{A.8})$$

BIBLIOGRAPHY

- [1] Particle Data Group, Phys. Lett. **B 667**, 1 (2008).
- [2] L. L. Pappalardo, Ph.D. thesis, Universita degli Studi di Ferrara, 2008.
- [3] V. Barone, A. Drago, and P. G. Ratcliffe, Phys. Rep. **359**, 1 (2002).
- [4] M. Diefenthaler, arXiv:0706.2242 (hep-ex) (2007).
- [5] M. Anselmino *et al.*, arXiv:0805.2677(hep-ph) (2008).
- [6] C. Collaboration, arXiv:0802.2160 (2008).
- [7] J. Alcorn *et al.*, Nucl. Instrum. Meth. A **522**, 294 (2004).
- [8] A. S. Kolarkar, Ph.D. thesis, University of Kentucky, 2007.
- [9] Y. Qiang, *Private communication*.
- [10] C. Dutta, *Private communication*.
- [11] J. Huang, Polarized ^3He target spin-flip system, https://hallaweb.jlab.org/wiki/index.php/Online_Spin_Flip.
- [12] X. Qian, Ph.D. thesis, Duke University, 2010.
- [13] A. Gavalya, *Private communication*.
- [14] C. Dutta, Ph.D. thesis, University of Kentucky, 2010.
- [15] Y. Zhang, *Private communication*.
- [16] J. Huang, *Private communication*.
- [17] K. de Jager and G. R. (Editors), Hall- A Annual Report 2009, <http://hallaweb.jlab.org/publications/AnnualReports/AnnualReport2009.pdf>.
- [18] S. Scopetta, Phys. Rev. **D 75**, 054005 (2007).
- [19] M. Anselmino *et al.*, Phys. Rev. **D 75**, 054032 (2007).
- [20] M. Anselmino *et al.*, Phys. Rev. **D 71**, 074006 (2005).

- [21] B.-Q. Ma and I. Schmidt, J. Phys. G **24**, L71 (1998).
- [22] S. Boffi, A. V. Efremov, B. Pasquini, and P. Schweitzer, Phys. Rev. **D 79**, 094012 (2009).
- [23] M. Gell-Mann, Phys. Lett. **8**, 214 (1964).
- [24] G. Zweig, CERN preprint **TH-401,TH-412**, (1964).
- [25] J. D. Bjorken, Phys. Rev. **179**, 1547 (1969).
- [26] R. Feynman, Phys. Rev. Lett. **23**, 1415 (1969).
- [27] J. Ashman *et al.* (EMC Collaboration), Phys. Lett. **B 206**, 364 (1988).
- [28] J. Ashman *et al.* (EMC Collaboration), Nucl. Phys. **B 328**, 1 (1989).
- [29] M. Burkardt, A. Miller, and W.-D. Nowak, arXiv:0812.2208 (2008).
- [30] J. P. Ralston and D. E. Soper, Nucl. Phys. **B 152**, 109 (1979).
- [31] S. J. Brodsky, D. S. Hwang, and I. Schmidt, Phys. Rev. Lett. **530**, 99 (2002).
- [32] M. Burkardt, Phys. Rev. **D 66**, 114005 (2002).
- [33] A. Airapetian *et al.* (HERMES Collaboration), Phys. Rev. Lett. **103**, 152002 (2009).
- [34] A. Airapetian *et al.* (HERMES Collaboration), Phys. Rev. Lett. **94**, 012002 (2005).
- [35] M.G. Alekseev *et al.* (COMPASS Collaboration), arXiv:1005.5609 (2010).
- [36] V. Yu. Alexakhin *et al.* (COMPASS Collaboration), Phys. Rev. Lett. **94**, 202002 (2005).
- [37] M. Anselmino, A. Efremov, and E. Leader, Phys. Rept. **A 261**, 1 (1995).
- [38] F. E. Close, Rep. Prog. Phys. **42**, 1285 (1979).
- [39] Y. L. Dokshitzer, Sov. Phys. JETP **46**, 641 (1977).
- [40] V. N. Gribov and L. N. Liptov, Sov. J. Nucl. Phys **15**, 675 (1972).
- [41] L. N. Liptov, Sov. J. Nucl. Phys **20**, 94 (1975).
- [42] G. Altarelli and G. Parisi, Nucl. Phys. **B 126**, 298 (1977).

- [43] R. L. Jaffe, arXiv:hep-ph/9602236 (1996).
- [44] A. V. Manohar, arXiv:hep-ph/9204208 (1992).
- [45] R. L. Jaffe, arXiv:hep-ph/9710465 v2 **2**, (1997).
- [46] R. L. Jaffe and X. Ji, Nucl. Phys. **B 375**, 527 (1992).
- [47] M. Stratmann, Z. Phys., C **60**, 763 (1993).
- [48] H. Kim, M. V. Polyakov, and K. Goeke, Phys. Lett. **B 387**, 577 (1996).
- [49] M. Wakamatsu and T. Kubota, Phys. Rev. **D 60**, 034020 (1999).
- [50] M. Fukugita, Y. Kuramashi, M. Okawa, and A. Ukawa, Phys. Rev. Lett. **75**, 2092 (1995).
- [51] S. Aoki, M. Doui, T. Hatsuda, and Y. Kuramashi, Phys. Rev. **D 56**, 433 (1997).
- [52] J. Soffer, Phys. Rev. Lett. **74**, 1292 (1995).
- [53] D. Sivers, Phys. Rev. **D 41**, 83 (1990).
- [54] C. J. Bebek *et al.*, Phys. Rev. Lett. **30**, 624 (1973).
- [55] G. Drews *et al.*, Phys. Rev. Lett. **41**, 1433 (1978).
- [56] J. C. Collins, Nucl. Phys. **B 396**, 161 (1993).
- [57] A. Bacchetta, U. D'Alesio, and M. Diehl, Phys. Rev. **D 70**, 117504 (2004).
- [58] A. Bacchetta *et al.*, JHEP **0702**, 093 (2007).
- [59] A. Bacchetta, Ph.D. thesis, Vrije Universiteit, 2002, arXiv:hep-ph/0212025.
- [60] J. Collins and A. Metz, Phys. Rev. Lett. **93**, 252001 (2004).
- [61] J. Collins, Phys. Lett. **B 536**, 43 (2002).
- [62] Z.-B. Kang and J.-W. Qiu, Phys. Rev. Lett. **103**, 172001 (2009).
- [63] X. Ji, J. Ma, and F. Yuan, Phys. Rev. **D 71**, 034005 (2005).
- [64] X. Ji, J. Ma, and F. Yuan, Phys. Lett. **B 597**, 299 (2004).

- [65] T. Navasardyan *et al.*, Phys. Rev. Lett. **98**, 022001 (2007).
- [66] M. Jones, Technical report, Jefferson Lab, (unpublished) (unpublished).
- [67] H. A. beam and polarimeters, <http://hallaweb.jlab.org/equipment/beam.html>.
- [68] P. H. Solvignon, Ph.D. thesis, Temple University, 2006.
- [69] A. P. Serebrov *et al.*, Phys. Rev. **C 78**, 035505 (2008).
- [70] W. Happer, Rev. Mod. Phys. **44**, 169 (1972).
- [71] E. Babcock, I. Nelson, S. Kadlecek, B. Driehuys, L. W. Anderson, F. W. Hersman, and T. G. Walker, Phys. Rev. Lett. **91**, 123003 (2003).
- [72] A. Abragam, *Principles of nuclear magnetism, The Intl. Series of Monographs on Physics* (Oxford Science Publications, 1983).
- [73] A. S. Barton, N. R. Newbury, G. D. Cates, B. Driehuys, H. Middleton, and B. Saam, Phys. Rev. **A 49**, 2766 (1994).
- [74] CODA, CEBAF Online Data Acquisition System, <https://coda.jlab.org>.
- [75] X. Qian, Y. Qiang, K. Allada, and Y. Wang, Internal Report: Separation of Collins and Sivers Asymmetry from E06-010 data: Blue Team Report, E-LOG ID 267.
- [76] T. W. Donnelly and A. S. Raskin, *Ann. Phys.* **169**, 247 (1986).
- [77] S. Model, <http://gwdac.phys.gwu.edu>.
- [78] X. Zheng, Ph.D. thesis, MIT, 2002.
- [79] K. M. Kramer, Ph.D. thesis, The College of William and Mary, 2003.
- [80] V. A. Sulkosky, Ph.D. thesis, The College of William and Mary, 2007.
- [81] J. L. Friar *et al.*, Phys. Rev. **C 42**, 2310 (1990).
- [82] C. Ciofi degli Atti *et al.*, Phys. Rev. **C 48**, 968 (1993).
- [83] F. Bissey *et al.*, Phys. Rev. **C 64**, 024004 (2001).
- [84] FANL E704 Collaboration, Phys. Lett. **B 264**, 462 (1991).

- [85] J. She, J. Zhu, and B.-Q. Ma, Phys. Rev. **D 79**, 054008 (2009).
- [86] B. Sun *et al.*, Eur. Phys. J. **C 65**, 163 (2009).
- [87] S. J. Brodsky and S. Gardner, Phys. Lett. **B 643**, 22 (2006).
- [88] S. B. Wojtsekhowski, E. Cisbani, G. Cates, and G. Franklin, "Measurement of the Semi-Inclusive π and K electro-production in DIS regime from transversely polarized ^3He target with the SBS & BB spectrometers in Hall A", JLAB approved experiment E09-018.
- [89] S. J.-P. Chen, H. Gao, X. Jiang, J.-C. Peng, and X. Qian, "An update to PR12-09-014: Target Single Spin Asymmetry in Semi-Inclusive Deep-Inelastic ($e, e'\pi^{+/-}$) Reaction on a Transversely Polarized ^3He Target at 8.8 and 11 GeV", JLAB approved experiment E10-006.

VITA

Kalyan C. Allada

- **Date and place of birth:**

- December 24, 1978; Hyderabad, India

- **Educational institutions attended and degrees awarded:**

- Osmania University, India, M.Sc (Physics) 2001.

- University of Hyderabad, India, M.Tech (Computational Techniques in Physics) 2003.

- University of Kentucky, Ph.D. 2010(expected).

- **Professional positions held:**

- Research Assistant, University of Kentucky, 2005-2010

- Teaching Assistant, University of Kentucky, 2003-2005

- **Scholastic and professional honors:**

- 2009-10 Jefferson Science Associates/Jefferson Lab Graduate Fellowship.

- **Professional Publications:**

1. Hard Photodisintegration of a Proton Pair, I. Pomerantz *et al.*, Phys. Lett. **B684**, 106 (2010), arXiv:0908.2968.

2. The proton elastic form factor ratio $\mu = G_E^p/G_M^p$ at low momentum transfer, G. Ron *et al.*, Phys. Rev. Lett. **99**, 202002 (2007), arXiv:0706.0128.

3. "Polarization Observables in Deuteron Photodisintegration below 360 MeV", J. Glister *et al.*, arXiv:1003.1944